



ScuDo

Scuola di Dottorato ~ Doctoral School
WHAT YOU ARE, TAKES YOU FAR



Doctoral Dissertation
Doctoral Program in Energy Engineering (30th Cycle)

Analysis of Advanced Air and Fuel Management Systems for Future Automotive Diesel Engine Generations

Andrea Piano

* * * * *

Supervisor

Prof. Federico Millo

Doctoral Examination Committee:

Prof. Agostino Gambarotta, Università degli studi di Parma

Prof. Carlo Nazareno Grimaldi, Università degli studi di Perugia

Prof. Michael Bargende, Universität Stuttgart

Prof. Carlo Beatrice, Istituto Motori – Consiglio Nazionale delle Ricerche

Prof. Jan Macek, Czech Technical University in Prague

Politecnico di Torino

June 5, 2018

This thesis is licensed under a Creative Commons License, Attribution - Noncommercial - NoDerivative Works 4.0 International: see www.creativecommons.org. The text may be reproduced for non-commercial purposes, provided that credit is given to the original author.

I hereby declare that, the contents and organisation of this dissertation constitute my own original work and does not compromise in any way the rights of third parties, including those relating to the security of personal data.

.....
Andrea Piano
Turin, June 5, 2018

Summary

The increasingly demanding targets in terms of CO₂ reduction and the more stringent emission regulations are pushing the OEMs to the adoption of engine technologies left so far for innovation. Looking forward to next years, a not negligible increase in Diesel engines cost to meet the CO₂ targets is expected, with a significant impact on market penetration in the near future. But Diesel engines are going to cost more and more not only because of CO₂ emission targets, but also because of pollutant emission limits. In order to fully exploit the potential of the abovementioned innovative technologies, numerical simulation can play a fundamental role by allowing the creation of a kind of a virtual test rig where evaluating the impact of design modifications.

Within this context, this work has the aim of evaluating the potential of the Variable Valve Actuation (VVA) in terms of both engine efficiency and aftertreatment thermal management improvements. Moreover, since development trends in modern Common Rail fuel injection systems (FIS) show dramatically increasing capabilities in terms of number of injection events per engine cycle as well as the modulation and shaping of the injection rate, an optimization analysis of the injection parameters was carried out in order to also fully exploit the potential of innovative FIS in terms of fuel consumption and combustion noise minimization.

More in detail, in Chapter 2, the characteristics of the engine selected as test cases will be presented: a EURO 6 passenger car 1.6l 4-cylinder Diesel engine was chosen for the analysis, equipped with a latest generation of Common Rail fuel injector. Since the aim of the preliminary analysis was to develop the virtual test rig where the potential of innovative engine concepts could be evaluated, the 1D-CFD fuel injector and engine models were built and coupled in a commercially available software, GT-SUITE. More specifically, a numerical model of a pressure-balanced Common-Rail injector was calibrated and validated on several single injection events in a wide range of rail pressures and energizing times (ETs), as well as on advanced multi-injection strategies, featuring up to 5 consecutive events with very short dwell time allowing hydraulic fusion. The numerical results were compared with experimental injection rate curves acquired at the Perugia University proprietary test bench. The tested multi-injection patterns were very challenging for

the model in terms of capability to capture the injector dynamic behavior. Although, the results are satisfactory and show a good response even for very close injections. After that, the fuel injector model was coupled with the complete engine model, featuring the predictive combustion model DIPulse, developed by Gamma Technologies. The accuracy with which the coupled models predict the actual behavior of the engine, in terms of in-cylinder pressure, combustion related parameters and NO_x emissions, was satisfactory since the model is able to reproduce with high accuracy the combustion process at different loads, engine speeds, rail pressures and injection patterns.

After the definition of the 1D-CFD model as a virtual test rig, two different analysis were carried out concerning the optimization of both the air management and fuel injection systems, exploring the potential of the application of a fully flexible valve actuation, and the fuel injection pattern optimization.

The VVA application on the selected engine will be the subject of Chapter 3, that will be divided in 2 main topics: the evaluation and identification of the best VVA strategies to be implemented in order to, on one hand, increase the engine efficiency and to, on the other hand, speed up the aftertreatment system warm up. Regarding the first topic (engine efficiency improvement), the following 3 techniques were scrutinized under steady state operating conditions, representative of the low load-low speed region of the engine map which is typically exploited in urban driving conditions:

- Late Intake Valve Closure (LIVC) – The retarded closure of the inlet valve could enable Miller cycle, in which the effective compression ratio is smaller than the effective expansion ratio.
- Late Exhaust Valve Opening (LEVO) – Retarding EVO timing could result in a higher expansion work collected by the piston than the standard timing.
- Variable Exhaust Valve Timing (VVT) – The exhaust valve timing can be adjusted to maximize the expansion work at each engine speed.

Then, the most promising technique in terms of fuel consumption reduction in steady state analysis without exceeding the baseline Brake Specific engine-out NO_x emissions, was simulated under transient conditions, for evaluating its BSFC reduction potential over the whole Worldwide harmonized Light vehicles Test Cycle (WLTC).

As far as the aftertreatment warm up is concerned, the following 3 different VVA techniques were scrutinized in the same steady state conditions of the previous analysis, since they are representative of the first 300 s of WLTC, chosen as cold phase of the driving cycle:

- Early Exhaust Valve Opening (EEVO) – Advancing EVO timing results in a higher exhaust pressure and temperature than the standard valve timing, but with a non-negligible fuel penalty, due to the reduced expansion work collected by the piston.
- Variable Exhaust Valve Timing (VVT) – By advancing EV timing the same effect of EEVO can be obtained and higher in-cylinder residuals amount can be achieved. Retarding EV timing, the overlap between exhaust and intake valve lifts increases and a higher amount of internal EGR can be achieved.
- Exhaust Valve reOpening (EVrO) – The secondary opening of the EV when the IV is open produces an efficient recirculation of the burned gas from the previous engine cycle to the in-cylinder charge.

Since all the 3 abovementioned VVA strategies allowed achieving significant increases in the exhaust gas temperature, with generally negligible or acceptable fuel penalties, they were evaluated in transient condition over the whole WLTC, focusing on the aftertreatment monolith wall temperature increment in the first 300 s of the WLTC.

Moving to the fuel injection pattern optimization, the analysis will be presented in Chapter 4, in which 3 different optimization approaches and their pros and cons will be analyzed. The aim of the optimization process was to minimize Brake Specific Fuel Consumption (BSFC) and Combustion Noise (CN) without exceeding the Brake Specific NO_x (BSNO_x) baseline value for 3 different steady state engine operating conditions, proved to be representative of a typical type approval driving cycle. Instead of using a detailed engine model, a simplified configuration was built in GT-SUITE: it consists of a single cylinder with valves, injection system, intake and exhaust ports and runners, and a control unit able to maintain the engine load constant, to adjust the injection strategy and swirl level. The effect of friction is taken into account by means of a Chen Flynn model, with the pressure-dependent term limited to the first order. Moreover, the simplified engine model features the DIPulse combustion model to predict combustion

phenomena and NO_x emission within the cylinder, and a user subroutine for combustion noise evaluation. The simplified configuration allowed a reduction of an order of magnitude in terms of computational time, while maintaining an high accuracy in replicating the real engine operating conditions. Several independent variables were introduced into the process, mainly related to the injection pattern (number of injection events, SOI, ETs, Dwell Times DTs, rail pressure) , as well as the EGR rate. More in detail, the following approaches were used in this analysis:

- Full Factorial Design of Experiments (DoE) – It allows a definition of a complete space of results by analyzing the whole domain defined by each independent variable level.
- Single-Objective – It is able to perform a minimization or maximization of a single output, as fuel consumption or combustion noise, or of a so-called objective function, which can be a combination of a certain number of outputs.
- Multi-Objective – Differently from the Single-optimization, this approach allows the simultaneously minimization or maximization of several dependent variables, as fuel consumption and combustion noise.

For Single- and Multi-Objective problems the Non-dominated Sorting Genetic Algorithm (NSGA-III) was used obtaining significant improvements in terms of BSFC and CN by adopting digitalized close pilot events with respect to the DoE analysis, also highlighting relevant computational time savings for the optimization process.

Acknowledgment

I would like to acknowledge General Motors – Global Propulsion Systems for sponsoring my PhD scholarship. I would also like to convey my gratitude to Dr. Francesco C. Pesce, Mr. Davide Di Nunno and Mr. Alessandro Gallone for providing me their valuable suggestions.

My special thanks to Prof. Lucio Postriotti and his research group in Perugia University for performing the remarkable experimental analysis of the complete fuel injection system.

I wish to thank Gamma Technologies LLC for the incomparable contribution on my research activity and for hosting me in its headquarters in 2016. My gratitude is also extended to Mr. Shawn Harnish and the entire team of Hydraulics and Fuel Injection in Westmont for providing frequent support and step-by-step guidance in my simulation work.

I would also like to express my sincere thanks to POWERTECH Engineering for sharing their valuable expertise. Particularly, I owe deeply grateful to Mr. Andrea Bianco for the precious technical help in the setup of 3D-CFD analysis.

Contents

List of Tables	III
List of Figures.....	V
Abbreviations.....	XVII
Introduction.....	1
Preliminary analysis.....	9
2.1 Engine test case.....	9
2.2 Fuel injector test case.....	12
2.2.1 Experimental test.....	13
2.2.2 1D-CFD model.....	18
Results – Single injection event.....	24
Results – Multiple injection events.....	29
2.3 Coupling between engine and fuel injector models.....	32
2.3.1 DIPulse combustion model	33
2.3.2 Combustion and emission results.....	38
2.3.3 Complete engine model results	41
I part: Air management system analysis	45
3.1 CO2 reduction potential.....	46
3.1.1 K-points selection.....	48
3.1.2 Simulation setup.....	49
3.1.3 Late Intake Valve Closure.....	50
3.1.4 Late Exhaust Valve Opening	56
3.1.5 Variable Exhaust Valve Timing.....	59
3.2 Warmup improvement potential	62
3.2.1 K-points selection.....	64
3.2.2 Simulation setup.....	64
3.2.3 Early Exhaust Valve Opening.....	66

3.2.4	Variable Exhaust Valve Timing.....	72
3.2.5	Exhaust Valve reOpening	76
3.3	Summary of the results	82
II part:	Fuel injection system optimization	87
4.1	Simulation setup	88
4.2	Optimization process	91
4.2.1	DoE approach.....	91
4.2.2	Single-Objective approach	95
4.2.3	Multi-Objective approach	99
4.2.4	Summary of the results.....	102
	Conclusions.....	109
	References.....	113
	Appendix A1 - Combustion process modelling: sensitivity analysis to DIPulse calibration parameters.....	121
	Appendix A2 - Combustion process modelling: sensitivity analysis to engine control parameters.....	123

List of Tables

Table 1.1 – Estimated costs of emissions control technologies for European light duty vehicle (assuming 1.5L 4-cylinder) [18]	7
Table 2.1 – Main features of the B16DTH engine	10
Table 2.2 – ISO4113 fluid properties	17
Table 2.3 – Geometrical and hydraulic parameters for the tested nozzles.....	17
Table 2.4 – R-squared related to Nozzle A results [43]	26
Table 2.5 – R-squared related to Nozzle B results [43]	28
Table 3.1 – Selected key-points for steady state analysis – CO2 reduction [81]	48
Table 3.2 – Characteristics of the selected vehicle for transient analysis [81]	48
Table 3.3 – Selected key-points for steady state analysis – WU improvement [89].....	64
Table 3.4 – Comparison between 0 and 80 CA deg of reOpening phase with 3.0 mm as maximum lift – 1000 RPM X 2 bar BMEP [89]	80
Table 4.1 – Selected key-points for injection optimization	88
Table 4.2 – Full Factorial DoE settings [106]	92
Table 4.3 – Genetic Algorithm settings [121].....	97
Table 4.4 – Optimization results [121].....	103

List of Figures

Figure 1.1 – ‘Der Spiegel’ covers [8,9].....	2
Figure 1.2 – Comparison of global CO2 regulations for passenger car [10]	2
Figure 1.3 – Sales-weighted type-approval CO2 emissions from EU lower medium passenger cars by fueling technology. Pie charts indicate the market share of gasoline, Diesel and hybrid vehicles in each year [11]	3
Figure 1.4 – Monthly Diesel shares of new car registrations in France, Germany, Italy, Spain, and the UK [12]	4
Figure 1.5 – Vehicle sales forecast in UE market made by FEV [15]	5
Figure 1.6 – Vehicle sales forecast in US market made by Fuels Institute [16]	5
Figure 1.7 – Estimates of direct manufacturing cost per percent fuel consumption reduction in 2025 [17]	6
Figure 1.8 – Estimated costs of emissions control technologies for European light duty vehicle from Euro 4 to Euro 6 (assuming 1.5L 4-cylinder) [18].....	7
Figure 2.1 – Engine friction losses comparison [20]	11
Figure 2.2 – In-vehicle performance comparison between 2.0l and 1.6l Diesel engines [20].....	11
Figure 2.3 – BSFC comparison – 2000 RPM X 2 bar BMEP [20]	12
Figure 2.4 – Sound power level comparison [20]	12
Figure 2.5 – Bosch CRI2-20	12
Figure 2.6 – Valve opening area difference between innovative pressure-balanced valve (left) and traditional poppet valve(right) [27]	13
Figure 2.7 – Silicon methodology for internal geometry detection [30].....	14
Figure 2.8 – Bosch CRI2-20: from scan to CAD 3D [31]	15
Figure 2.9 – Experimental single injection test matrix for Nozzle A and Nozzle B.....	17
Figure 2.10 – Current injection operations investigated for Nozzle A [43]....	18
Figure 2.11 – Electromagnetic valve model [31].....	19
Figure 2.12 – Control valve model [31].....	20
Figure 2.13 – Control chamber model [31].....	20

Figure 2.14 – Mass flow rate versus square root of the pressure drop for the Z-Hole orifice [28].....	21
Figure 2.15 – Mass flow rate versus square root of the pressure drop for the A-Hole orifice [28].....	21
Figure 2.16 – Needle mechanics model [31].....	23
Figure 2.17 – Main hydraulic network model [31]	24
Figure 2.18 – Experimental (dashed) and simulated (solid) injection rates for six rail pressure values tested – Nozzle A [43].....	25
Figure 2.19 – EMI curves comparison between experiments (black dashed) and simulation results (red solid) for Nozzle A.....	26
Figure 2.20 – Average error for each rail pressure related to Nozzle A results	26
Figure 2.21 – Experimental (dashed) and simulated (solid) injection rates for six rail pressure values tested – Nozzle B [43].....	27
Figure 2.22 – EMI curves comparison between experiments (black dashed) and simulation results (red solid) for Nozzle B.....	28
Figure 2.23 – Average error for each rail pressure related to Nozzle B results	28
Figure 2.24 – Experimental (black dashed) and simulated (red solid) injection rates for standard double pilot strategy at rail pressure equal to 400 bar – Nozzle A [43].....	29
Figure 2.25 – Experimental (black dashed) and simulated (red solid) injection rates for standard double pilot strategy at rail pressure equal to 1000 bar – Nozzle A [43].....	29
Figure 2.26 – Experimental (black dashed) and simulated (red solid) injection rates for single + close pilot strategy at rail pressure equal to 400 bar – Nozzle A [43].....	30
Figure 2.27 – Experimental (black dashed) and simulated (red solid) injection rates for single + close pilot strategy at rail pressure equal to 1000 bar – Nozzle A [43].....	30
Figure 2.28 – Experimental (black dashed) and simulated (red solid) injection rates for double + close pilot strategy at rail pressure equal to 400 bar – Nozzle A [43].....	30
Figure 2.29 – Experimental (black dashed) and simulated (red solid) injection rates for double + close pilot strategy at rail pressure equal to 1000 bar – Nozzle A [43].....	31

Figure 2.30 – Experimental (black dashed) and simulated (red solid) injection rates for triple pilot + main + after strategy at rail pressure equal to 400 bar – Nozzle A [43].....	31
Figure 2.31 – Example of Injection Rate Map.....	33
Figure 2.32 – Engine model CPU increase factor due to adding detailed injector model	33
Figure 2.33 – Test matrix	38
Figure 2.34 – DIPulse combustion model results – Experimental (black) and predicted (red) in-cylinder (solid) and burn rate (dashed) comparisons, injection mass flow rate (green dashed)	39
Figure 2.35 – DIPulse combustion model results - Combustion parameters: IMEP (top-left), in-cylinder maximum pressure (top-right), crank angle of maximum pressure (bottom-left), crank angle at 50% fuel burned (bottom-right).....	40
Figure 2.36 – DIPulse combustion model results – Experimental (black) and predicted (red) in-cylinder (solid) and burn rate (dashed) comparisons, injection mass flow rate (green dashed) – 2000 RPM X 8.7 bar BMEP	40
Figure 2.37 – DIPulse combustion model results – Simulated (red) and experimental (black) emissions comparison: NO _x (left) and SOOT emission (right)	40
Figure 2.38 – Experimental and simulated BMEP (left) and BSFC (right) comparison for the entire engine map.....	41
Figure 2.39 – Experimental and simulated volumetric efficiency comparison for the entire engine map	41
Figure 2.40 – Experimental and simulated compressor outlet (left) and turbine inlet (right) pressure comparison for the entire engine map.....	42
Figure 2.41 – Experimental and simulated compressor outlet (left) and turbine inlet (right) temperature comparison for the entire engine map	42
Figure 2.42 – FMEP trend at different coolant temperature – 5 bar BMEP engine load.....	43
Figure 2.43 – Comparison between experimental (black dashed) and simulated (red solid) normalized fuel consumption over WLTC.....	44
Figure 3.1 – Engine operating conditions over the WLTC driving cycle (blue) and selected key-points (red) on the engine map.....	48
Figure 3.2 – Full factorial DoE grid for VVA analysis.....	49
Figure 3.3 – Example of response surface for delta BSNO _x (a), and delta BSFC (b) obtained from full factorial DoE of EGR and VGT parameters settings for a	

given exhaust valve lift profile and geometrical compression ratio: the dashed area represents the region in which the baseline NOx emission levels are exceeded and which cannot therefore be considered as suitable solutions. – 1500 RPM X 2 bar BMEP [81].....50

Figure 3.4 – LIVC lift profiles tested [81]51

Figure 3.5 – Delta BSFC at different LIVC actuations for 2 bar (left) and 5 bar (right) engine load – 1000 RPM [81].....52

Figure 3.6 – Delta BSFC at different LIVC actuations for 2 bar (left) and 5 bar (right) engine load – 1500 RPM [81].....52

Figure 3.7 – Delta BSFC at different LIVC actuations for 2 bar (left) and 5 bar (right) engine load – 2000 RPM [81].....52

Figure 3.8 – Peak firing pressure and friction losses (top), heat transfer losses and air-to-fuel ratio (center), maximum temperature and heat transfer coefficient (bottom), compression ratio equal to 15.5 at different LIVC angle – 1000 RPM X 2 bar BMEP (left) and 1000 RPM X 5 bar BMEP (right) [81]53

Figure 3.9 – logP-logV (left) and in-cylinder temperature (right) for baseline (black) and LIVC60 (red) actuations54

Figure 3.10 – Swirl ratio (left) and turbulent kinetic energy – TKE (right) for baseline (black) and LIVC60 (red) actuations54

Figure 3.11 – Normalized cumulated fuel consumption respect to the baseline value, in transient simulation for baseline (black dashed) and LIVC60 (red) actuations [81].....55

Figure 3.12 – Percentage of LIVC engine operating conditions on the total fuel consumption over WLTC [81].....56

Figure 3.13 – LEVO lift profiles tested [81].....56

Figure 3.14 – Delta BSFC (top), Delta PMEP (center) and Delta IMEP360 (bottom) at different LEVO actuations for 2 bar (left) and 5 bar (right) engine loads – 1000 RPM [81]57

Figure 3.15 – Delta BSFC (top), Delta PMEP (center) and Delta IMEP360 (bottom) at different LEVO actuations for 2 bar (left) and 5 bar (right) engine loads – 1500 RPM [81]58

Figure 3.16 – Delta BSFC (top), Delta PMEP (center) and Delta IMEP360 (bottom) at different LEVO actuations for 2 bar (left) and 5 bar (right) engine loads – 2000 RPM [81]58

Figure 3.17 – Effect of LEVO: difference between exhaust and intake pressures (top), PMEP (center) and Rack Position (bottom) for LEVO20, 40, 60 (red circle, blue square, green diamond, respectively).....	59
Figure 3.18 – Zoom @ BDC for LogP-LogV diagram for 3 different LEVO actuations	59
Figure 3.19 – VVT lift profiles tested [81]	60
Figure 3.20 – Delta BSFC (top), Delta PMEP (center) and Delta IMEP360 (bottom) at different EV timings for 2 bar (left) and 5 bar (right) engine loads – 1000 RPM [81]	61
Figure 3.21 – Delta BSFC (top), Delta PMEP (center) and Delta IMEP360 (bottom) at different EV timings for 2 bar (left) and 5 bar (right) engine loads – 1500 RPM [81]	61
Figure 3.22 – Delta BSFC (top), Delta PMEP (center) and Delta IMEP360 (bottom) at different EV timings for 2 bar (left) and 5 bar (right) engine loads – 2000 RPM [81]	62
Figure 3.23 – Engine operating conditions over the first 300 s of WLTC driving cycle (blue) and selected key-points (red) on the engine map.....	64
Figure 3.24 – Example of response surface for delta BSNOx (top), delta Exhaust Turbine Outlet temperature (center) and delta BSFC (bottom) obtained from full factorial DoE of EGR and VGT parameters settings for a given exhaust valve lift profile and geometrical compression ratio: the dashed area represents the region in which the baseline NOx emission levels are exceeded and which cannot therefore be considered as suitable solutions – 1000 RPM X 2 bar BMEP [89]...	65
Figure 3.25 – EEVO lift profiles tested [89].....	67
Figure 3.26 – Delta Exhaust Temperature (top) and delta BSFC (bottom) at different EEVO actuations for 2 bar (left) and 5 bar (right) engine load – 1000 RPM [89].....	68
Figure 3.27 – Delta Exhaust Temperature (top) and delta BSFC (bottom) at different EEVO actuations for 2 bar (left) and 5 bar (right) engine load – 1500 RPM [89].....	68
Figure 3.28 – Delta Exhaust Temperature (top) and delta BSFC (bottom) at different EEVO actuations for 2 bar (left) and 5 bar (right) engine load – 2000 RPM [89].....	68
Figure 3.29 – Engine split losses between 3 different compression ratios (16.0, 15.5 and 17.5) for EEVO 20 configuration – 1000 RPM x 2 bar BMEP	69

Figure 3.30 – Engine split losses between 3 different compression ratios (16.0, 15.5 and 17.5) for EEVO 20 configuration – 1000 RPM x 5 bar BMEP	69
Figure 3.31 – Top: thermal exhaust power at turbine outlet in transient simulations for baseline (black) and EEVO60 (red) actuations. Bottom: relative delta between VVA and baseline thermal power – First 300 s of WLTC [89]	70
Figure 3.32 – Normalized cumulated fuel consumption respect to the baseline value, in transient simulations for baseline (black) and EEVO60 (red) actuations [89].....	71
Figure 3.33 – Top: DOC monolith temperature in transient simulations for baseline (black) and EEVO60 (red) actuations. Bottom: normalized cumulated fuel consumption respect to the baseline value, in transient simulations for baseline (black) and EEVO60 (red) actuations – First 300 s of WLTC	71
Figure 3.34 – VVT lift profiles tested [89]	72
Figure 3.35 – Delta Exhaust Temperature (top) and delta BSFC (bottom) at different EV timings for 2 bar (left) and 5 bar (right) engine load – 1000 RPM [89]	73
Figure 3.36 – Delta Exhaust Temperature (top) and delta BSFC (bottom) at different EV timings for 2 bar (left) and 5 bar (right) engine load – 1500 RPM [89]	73
Figure 3.37 – Delta Exhaust Temperature (top) and delta BSFC (bottom) at different EV timings for 2 bar (left) and 5 bar (right) engine load – 2000 RPM [89]	73
Figure 3.38 – Residual gas percentage at different EV timings - 1000 RPM X 2 bar BMEP [89].....	74
Figure 3.39 – Top: thermal exhaust power at turbine outlet in transient simulations for baseline (black), VVT-30 (red solid) and VVT+56 (red dashed) actuations. Bottom: relative delta between VVAs and baseline thermal power – First 300 s of WLTC [89]	74
Figure 3.40 – Normalized cumulated fuel consumption respect to the baseline value, in transient simulations for baseline (black) VVT-30 (red solid) and VVT+56 (red dashed) actuations. [89].....	75
Figure 3.41 – Top: DOC monolith temperature in transient simulations for baseline (black), VVT-30 (red solid) and VVT+56 (red dashed) actuations. Bottom: normalized cumulated fuel consumption respect to the baseline value, in transient simulations for baseline (black) and VVAs (red) actuations – First 300 s of WLTC	75

Figure 3.42 – EvrO lift profiles tested: maximum lift is the peak value of the secondary lift [89].....	77
Figure 3.43 – EvrO lift profiles tested: reOpening phase is the angle between the closure of the main EV lift and the opening of the re-breathing [89].....	77
Figure 3.44 – Delta exhaust temperature and delta BSFC at different EVrO actuations with only iEGR (left) and iEGR+LPEGR (right) configurations – 1000 RPM X 2 bar BMEP [89]	78
Figure 3.45 – Delta exhaust temperature and delta BSFC at different EVrO actuations with only iEGR (left) and iEGR+LPEGR (right) configurations – 1500 RPM X 2 bar BMEP [89]	78
Figure 3.46 – Delta exhaust temperature and delta BSFC at different EVrO actuations with only iEGR (left) and iEGR+LPEGR (right) configurations – 2000 RPM X 2 bar BMEP [89]	78
Figure 3.47 – Delta exhaust temperature and delta BSFC at different EVrO actuations with only iEGR (left) and iEGR+LPEGR (right) configurations – 1000 RPM X 5 bar BMEP [89]	79
Figure 3.48 – Delta exhaust temperature and delta BSFC at different EVrO actuations with only iEGR (left) and iEGR+LPEGR (right) configurations – 1500 RPM X 5 bar BMEP [89]	79
Figure 3.49 – Delta exhaust temperature and delta BSFC at different EVrO actuations with only iEGR (left) and iEGR+LPEGR (right) configurations – 2000 RPM X 5 bar BMEP [89]	79
Figure 3.50 – Top: thermal exhaust power at turbine outlet in transient simulations for baseline (black) and EVrO 3.0 mm X 80 CA (red) actuations. Bottom: relative delta between VVA and baseline thermal power – First 300 s of WLTC [89]	80
Figure 3.51 – Normalized cumulated fuel consumption respect to the baseline value, in transient simulations for baseline (black) and EVrO 3.0 mm X 80 CA (red) actuations. [89].....	81
Figure 3.52 – Top: DOC monolith temperature in transient simulations for baseline (black) and EVrO 3.0 mm X 80 CA (red) actuations. Bottom: normalized cumulated fuel consumption respect to the baseline value, in transient simulations for baseline (black) and VVAs (red) actuations – First 300 s of WLTC.....	81
Figure 3.53 – LIVC60 steady state results in terms of BSFC difference on the engine map.....	82

Figure 3.54 – EEVO60 steady state results in terms of exhaust temperature difference on the engine map.....	83
Figure 3.55 – VVT-30 steady state results in terms of exhaust temperature difference on the engine map.....	84
Figure 3.56 – EVrO (3.0 mm X 80 CA deg) steady state results in terms of exhaust temperature difference on the engine map	85
Figure 3.57 – WLTC results for warmup improvement strategies: aftertreatment monolith temperature @ 300 s WLTC (top), delta fuel consumption difference @ 300 s (center) and @ end of WLTC (bottom).....	85
Figure 4.1 – Detailed engine model [106].....	89
Figure 4.2 – Reduced engine model [106]	89
Figure 4.3 – Detailed (red) and reduced (green) engine model configuration comparison for selected key-points: CPU time (left), BSFC (right)	90
Figure 4.4 – GT-SUITE and experimental combustion noise comparison. Engine map points in blue, key-points in red [106].....	90
Figure 4.5 – DoE results in normalized BSFC – BSNO _x – CN space. Grey planes represents the maximum and minimum BSNO _x level allowed. [106].....	93
Figure 4.6 – DoE post-processed results: BSNO _x level within 5% of the baseline value [106].....	93
Figure 4.7 – DoE results: baseline (black) and optimized (red) in-cylinder pressure (top), burn rate (center) and injection rate (bottom) – Left column: 1500 RPM X 2 bar BMEP; Center column: 1500 RPM X 5 bar BMEP, Right column: 2000 RPM X 8 bar BMEP	94
Figure 4.8 – DoE results: baseline (black) and optimized (red) BSFC factor and CN factor – Left column: 1500 RPM X 2 bar BMEP; Center column: 1500 RPM X 5 bar BMEP, Right column: 2000 RPM X 8 bar BMEP	95
Figure 4.9 – Single-Objective results: objective function values for each iteration [121]	98
Figure 4.10 – Single-Objective results: baseline (black) and optimized (blue) in-cylinder pressure (top), burn rate (center) and injection rate (bottom) – Left column: 1500 RPM X 2 bar BMEP; Center column: 1500 RPM X 5 bar BMEP, Right column: 2000 RPM X 8 bar BMEP [121]	98
Figure 4.11 – Detail on objective function results. Top: objective function value; Center: BSFC; Bottom: Combustion Noise – 2000 RPM X 8 bar BMEP [121]	99

Figure 4.12 – Single-Objective results: baseline (black) and optimized (blue) BSFC factor and CN factor – Left column: 1500 RPM X 2 bar BMEP; Center column: 1500 RPM X 5 bar BMEP, Right column: 2000 RPM X 8 bar BMEP...	99
Figure 4.13 – Multi-Objective optimization results in the BSFC-Combustion Noise space – Left column: 1500 RPM X 2 bar BMEP; Center column: 1500 RPM X 5 bar BMEP, Right column: 2000 RPM X 8 bar BMEP [121].....	101
Figure 4.14 – Multi-Objective results: baseline (black) and optimized (green for minimum BSFC, orange for minimum combustion noise) in-cylinder pressure (top), burn rate (center) and injection rate (bottom) – Left column: 1500 RPM X 2 bar BMEP; Center column: 1500 RPM X 5 bar BMEP, Right column: 2000 RPM X 8 bar BMEP [121].....	101
Figure 4.15 – Multi-Objective results: baseline (black) and optimized (green for minimum BSFC, orange for minimum combustion noise) BSFC factor and CN factor – Left column: 1500 RPM X 2 bar BMEP; Center column: 1500 RPM X 5 bar BMEP, Right column: 2000 RPM X 8 bar BMEP	102
Figure 4.16 – Optimization process results: baseline (black) and optimized (red for DoE, blue for DoE, green for minimum BSFC, orange for minimum combustion noise) BSFC factor and CN factor – Left column: 1500 RPM X 2 bar BMEP; Center column: 1500 RPM X 5 bar BMEP, Right column: 2000 RPM X 8 bar BMEP [121]	103
Figure 4.17 – Split power losses for the best injection strategy for each optimization approach. Engine operating point: 1500 RPM X 2 bar BMEP [121]	104
Figure 4.18 – In-cylinder pressure (top), burn rate (center) and in-cylinder temperature (bottom) comparisons for the best injection strategy for each optimization approach. Engine operating point: 1500 RPM X 2 bar BMEP [121]	104
Figure 4.19 – Split power losses for the best injection strategy for each optimization approach. Engine operating point: 1500 RPM X 5 bar BMEP [121]	105
Figure 4.20 – In-cylinder pressure (top), burn rate (center) and in-cylinder temperature (bottom) comparisons for the best injection strategy for each optimization approach. Engine operating point: 1500 RPM X 5 bar BMEP [121]	105

Figure 4.21 – Split power losses for the best injection strategy for each optimization approach. Engine operating point: 2000 RPM X 8 bar BMEP [121]	106
Figure 4.22 – In-cylinder pressure (top), burn rate (center) and in-cylinder temperature (bottom) comparisons for the best injection strategy for each optimization approach. Engine operating point: 2000 RPM X 8 bar BMEP [121]	106
Figure 4.23 – Computational time for the optimization process considering Full Factorial DoE and Multi-Objective (or Single-Objective) optimization approaches (referred to simulations distributed on a single core, Intel i7-6700 3.4 GHz processor) [121]	107
Figure A1.1 – Sensitivity analysis for different multipliers values using predictive DIPulse combustion model: Entrainment Rate Multiplier (top left), Ignition Delay Multiplier (top right), Premixed Combustion Rate Multiplier (bottom left), Diffusion Combustion Rate Multiplier (bottom right) – Engine operating point: 2000 RPM X 2 bar BMEP	122
Figure A1.2 - Sensitivity analysis for different multipliers values using predictive DIPulse combustion model: Entrainment Rate Multiplier (top left), Ignition Delay Multiplier (top right), Premixed Combustion Rate Multiplier (bottom left), Diffusion Combustion Rate Multiplier (bottom right) – Engine operating point: 3000 RPM X FL bar BMEP	122
Figure A2.1 – DIPulse combustion model results @ 5 different EGR rates – Experimental (black) and predicted (red) in-cylinder (solid) and burn rate (dashed) comparisons, injection mass flow rate (green dashed) – 1500 RPM X 8 bar BMEP	123
Figure A2.2 – DIPulse combustion model results @ 5 different SOI – Experimental (black) and predicted (red) in-cylinder (solid) and burn rate (dashed) comparisons, injection mass flow rate (green dashed) – 1500 RPM X 8 bar BMEP	124
Figure A2.3 – DIPulse combustion model results @ 5 different Boost Pressure levels – Experimental (black) and predicted (red) in-cylinder (solid) and burn rate (dashed) comparisons, injection mass flow rate (green dashed) – 1500 RPM X 8 bar BMEP	124
Figure A2.4 – DIPulse combustion model results - Combustion parameters: IMEP (top-left), in-cylinder maximum pressure (top-right), crank angle of maximum pressure (bottom-left), crank angle at 50% fuel burned (bottom-right) for	

boost pressure (red circle), EGR rate (blue square) and SOI (green diamond) sweeps 125

 Figure A2.5 – DIPulse combustion model results – NO_x (left) and SOOT emission (right) comparison for boost pressure (red circle), EGR rate (blue square) and SOI (green diamond) sweeps 125

 Figure A2.6 – NO_x emission comparison – Zoom on low NO_x zone..... 126

Abbreviations

ACEA	European Automobile Manufacturers' Association
AT	Aftertreatment
BDC	Bottom Dead Center
BEV	Battery Electric Vehicle
BMEP	Brake Mean Effective Pressure
BSFC	Brake Specific Fuel Consumption
BSNO _x	Brake Specific NO _x
CA	Crank Angle
CAA	Clean Air Act
CAD	Computer-Aided Design
CAE	Computer-Aided Engineering
CARB	California Air Resources Board
CFD	Computational Fluid Dynamics
CI	Compression Ignition
CN	Combustion Noise
CNF	Combustion Noise Factor
CPU	Central Processing Unit
CR	Compression Ratio
CT	Computed Tomography
DAE	Differential Algebraic Equation
DOC	Diesel Oxidation Catalyst
DoE	Design of Experiments

DT	Dwell Time
ECU	Electronic Control Unit
EEA	European Environment Agency
EEVO	Early Exhaust Valve Opening
EGR	Exhaust Gas Recirculation
EIVC	Early Intake Valve Closure
EMI	Einspritzmengenindikator
ET	Energizing Time
EU	European Union
EV	Exhaust Valve
EVO	Exhaust Valve Opening
EVrO	Exhaust Valve reOpening
FC	Fuel Consumption
FIS	Fuel Injection System
FL	Full Load
FMEP	Friction Mean Effective Pressure
FRM	Fast Running Model
GA	Genetic Algorithm
GM	General Motors
HCCI	Homogeneous Charge Compression Ignition
HD	Heavy Duty
HT	Heat Transfer
ICCT	International Council on Clean Transportation
iEGR	internal EGR
IMEP	Indicated Mean Effective Pressure
IMEP360	High Pressure Indicated Mean Effective Pressure
ISFC360	High Pressure Indicated Specific Fuel Consumption
IV	Intake Valve

IVC	Intake Valve Closure
KBA	Kraftfahrt-Bundesamt
LEVO	Late Exhaust Valve Opening
LHV	Lower Heating Value
LIVC	Late Intake Valve Closure
LP	Low Pressure
LPEGR	Low Pressure EGR
MDE	Medium Diesel Engine
MFB50	Crank Angle at 50% Mass Fraction Burned
MO	Multi-Objective
NCGA	Neighborhood Cultivation Genetic Algorithm
NEDC	New European Driving Cycle
NSGA	Non-dominated Sorting Genetic Algorithm
NVH	Noise – Vibration – Harshness
ODE	Ordinary Differential Equation
OEM	Original Equipment Manufacturer
PHEV	Plug-in Hybrid Electric Vehicle
PID	Proportional-Integral-Derivative
PM	Particulate Matter
PMEP	Pumping Mean Effective Pressure
PWM	Pulse-Width Modulation
RDE	Real Driving Emissions
RPM	Revolutions Per Minute
R&D	Research and Development
SO	Single-Objective
SOI	Start Of Injection
TDC	Top Dead Center
TKE	Turbulence Kinetic Energy

TST	Two-Stage Turbocharger
UK	United Kingdom
US EPA	United States Environmental Protection Agency
VGT	Variable Geometry Turbine
VVA	Variable Valve Actuation
VVT	Variable Valve Timing
VW	Volkswagen
WLTC	Worldwide harmonized Light vehicles Test Cycle
WU	Warm Up

Chapter 1

Introduction

September 18th, 2015. After more than 1 year of emissions tests that involved ICCT, CARB, West Virginia University, Phillip A. Brooks (Director of Air Enforcement Division, US EPA) signed a Notice of Violation addressed to Mr. David Geanacopoulos (Executive Vice President Public Affairs and General Counsel, Volkswagen Group of America, Inc) and to Mr. Stuart Johnson (General Manager of Engineering and Environmental Office, Volkswagen Group of America, Inc), in which EPA stated that “*VW manufactured and installed defeat device in certain model year 2009 through 2015 light-duty vehicles equipped with 2.0 liter engines. These defeat devices bypass, or render inoperative elements of the vehicles’ emission control system that exist to comply with CAA emission standards*” [1]. In that day, the solution became the problem, ‘clean Diesel’ (as claimed by the AUDI 2010 Super Bowl commercial [2]) became ‘dirty Diesel’: in other words, Diesel engine became something to defeat [3–5]. Without going through details, in the next days, the VW declaration regarding the 11 millions of vehicles equipped with the defeat device followed the official guilt admission by Mr. Winterkorn (AD, Volkswagen Group) and his resignation. Since 8.5 million over the total of 11 million of vehicles were in European zone, the Diesel fever crossed the Atlantic Ocean and arrived in Europe: in 2 months KBA (Kraftfahrt-Bundesamt) defined a recall plan available for the 28 EU countries, that consisted in a ECU software update and a flow transformer installation.

In the last 2 years and half, this scandal, known as Dieselgate, involved the more important car manufacturers (i.e. PSA, FCA, BMW, Daimler) as well as the main suppliers (i.e. BOSCH), leading the public opinion to the idea that something hidden and dirty is behind the automotive industry, mainly related to Diesel engines production. As an example of this, in Figure 1.1, 2 Der Spiegel magazine cover are reported.

The last (hopefully) but not the least (unfortunately), in January 2018, New York Times revealed that the 3 major German carmakers (Volkswagen, Daimler and BMW) financed the research who involved monkeys to test the Diesel exhaust

gas effect on health [6]. After that, the Süddeutsche Zeitung reported that same tests were also carried out on 25 young and healthy human beings: the experiments, carried out at an institute of the University Clinic Aachen, involved the group having to breathe in varying different concentrations of nitric oxide after which they were physically examined for any side-effects [7]. In their point of view, these studies had the aim to show that modern Diesel technology were clean and had solved the problem of excess emissions linked to a range of lung ailments. However, they intensified a backlash against Diesel in Europe once more.



Figure 1.1 – ‘Der Spiegel’ covers [8,9]

So, does it still make sense to talk about Diesel engine applied to passenger car? Is it necessary to continue the development of these engines? In the framework previously introduced, the answers at these two questions become self-evident and useless. However, a more detailed analysis is needed.

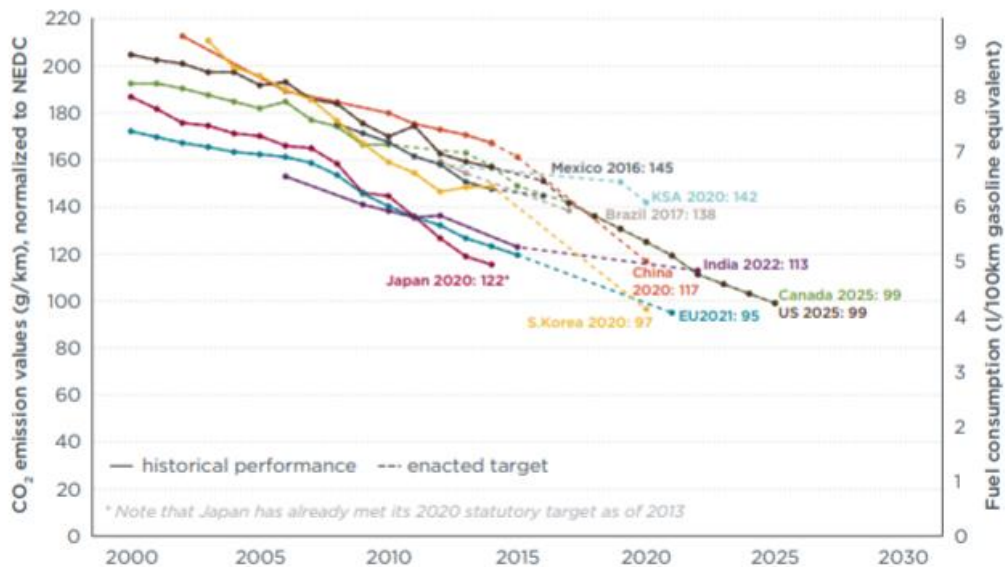


Figure 1.2 – Comparison of global CO2 regulations for passenger car [10]

First of all, CO₂ emission targets. In the international context, the EU has historically been a front-runner with respect to vehicle emission targets. In recent years, however, most large economies have set converging CO₂ emission targets for new vehicles [10]. Figure 1.2 provides a comparison of the EU CO₂ passenger car standards with similar regulations around the world, converting all regulatory programs to the NEDC test cycle. The EU passenger car standard of 95 g/km for 2020 (effectively 2021) can be compared to similar targets for the US (93 g/km for 2025 passenger cars), Japan (105 g/km by 2020), and China (117 g/km by 2020).

The plot in Figure 1.3 shows the sales weighted average CO₂ emissions for the lower-medium vehicle segment, the one with the highest market share recently in Europe: the blue line represents gasoline vehicles, red line is for Diesel vehicles and purple is for hybrids electric vehicles. The green dashed line is the European average CO₂ emission target to be reached in 2021. From this plot, it is clear how Diesel engines helped in achieving the CO₂ targets in last years. This results was achieved thanks to their higher efficiency compared to gasoline engines, but also to their market penetration.

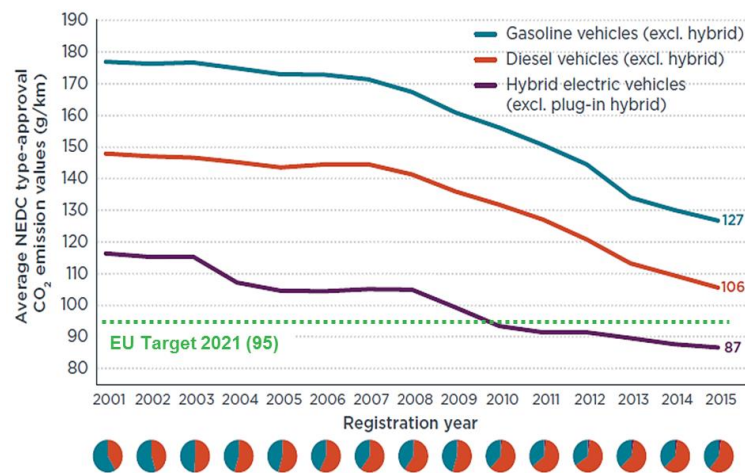


Figure 1.3 – Sales-weighted type-approval CO₂ emissions from EU lower medium passenger cars by fueling technology. Pie charts indicate the market share of gasoline, Diesel and hybrid vehicles in each year [11]

After Dieselgate, something changed. The share of Diesel vehicles among new car registrations in the EU decreased from a peak of 55% in 2011 to 49% in 2016, and recent data indicate that Diesel shares continued to fall in 2017 and early 2018 as depicted in Figure 1.4 where Diesel shares of new car registrations in France, Germany, Italy, Spain, and the United Kingdom from January 2012 to December 2017 are shown [12]. These five countries are the largest Diesel markets in the EU, obtaining a Diesel share fell from 56% in 2012 to 45% of passenger car sales. In 2017 alone, the Diesel share declined by 5 percentage points or more in all markets but this did not happen in Italy [12].

The direct consequence of market share highlighted in Figure 1.4 is reported by EEA in [13] and ACEA in [14]: an increase in CO₂ emissions coupled with a rise in gasoline sales was measured, since 2010 when monitoring starting under current

EU legislation. Erick Jonnaert, ACEA Secretary General, stated “*The shift from Diesel to petrol – together with the relatively low market penetration of alternative powertrains – is now having a tangible impact on the CO2 performance of Europe’s new car fleet. Looking ahead, this will pose serious challenges to meeting future CO2 targets.*” More in detail, the EEA data can be summarized in the following list as reported in [13].

- New cars sold in 2017 emitted on average 118.5 g CO₂/km, a slight increase of 0.4 g/km compared to 2016.
- For the first year since monitoring started, petrol cars became the most sold vehicles in the EU, constituting almost 53 % of sales. Diesel cars made up 45 % of the new registrations. Compared to 2016, the registrations of Diesel cars decreased in all EU Member States except in Italy (+0.6 %) and in Denmark (+6.9 %). The biggest decrease of Diesel cars was registered in Greece and Luxemburg (-19 % and -17 %). The countries with the highest proportions of Diesel sales included Ireland (65 %) and Portugal (61 %), Italy (56 %).
- The difference between average fuel efficiency of petrol cars (121.6 g CO₂/km) and Diesel cars (117.9 g CO₂/km) is reducing compared to 2016. The average fuel efficiency of petrol cars has been constant in the last two years; whereas the fuel-efficiency of Diesel cars has worsened, compared to 2016 (116.8 g CO₂/km).

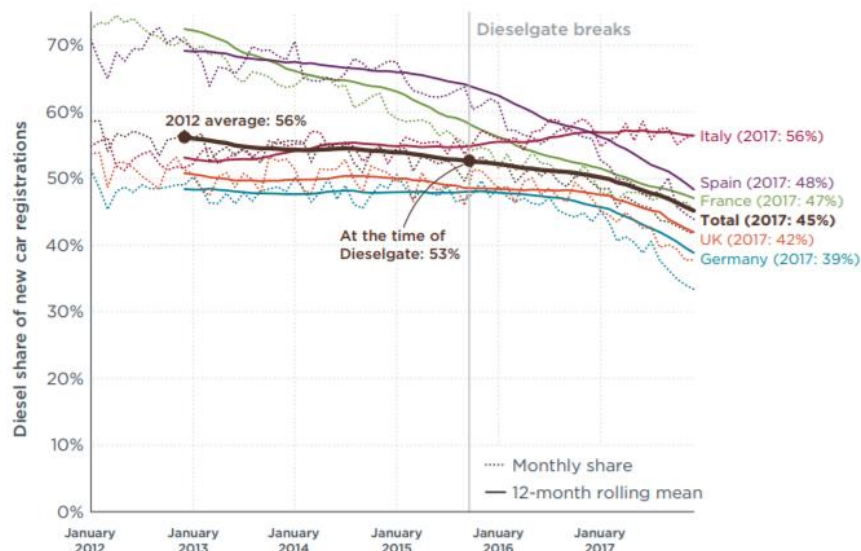


Figure 1.4 – Monthly Diesel shares of new car registrations in France, Germany, Italy, Spain, and the UK [12]

Another important point in the EEA analysis is that the sales of plug-in hybrid electric vehicles (PHEV) and battery-electric vehicles (BEV) continued to increase, last year by 42 %. However, the share of these categories in the new fleet remains low (1.5 %). In detail, around 97 000 BEV were registered in 2017, a 51 % increase

compared to 2016, while sales of new PHEVs increased by 35 %.The largest number of BEV were registered in France (more than 26 110 vehicles) and Germany (more than 24 350 vehicles) and the UK (more than 13 580 vehicles).

And what about future? The answer can be divided in 2 parts: firstly, the CO2 targets must be reached very soon (3-4 years) and Diesel powertrains play a key role in the OEM strategies to meet tighter standards, since the modern Diesel powertrains keep the advantage in terms of efficiency despite more complex emissions controls system. Secondly, if the time horizon is postponed to the next 20 years, the trend may change due to the higher BEV and PHEV market penetration. However, by looking Figure 1.5, where the vehicle sales forecast proposed by FEV is shown, it is clear that Diesel powertrains will have a not negligible market penetration (25%).

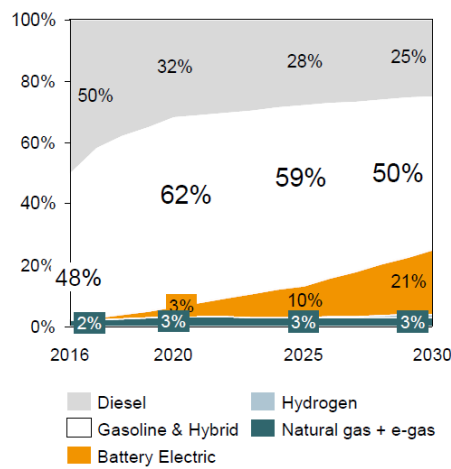


Figure 1.5 – Vehicle sales forecast in UE market made by FEV [15]

This results is also confirmed by the vehicle sales forecast in US market made by Fuel Institute in Figure 1.6. The sales graphics demonstrate that in the proposed scenario, gasoline and Diesel-powered vehicles are projected to lose modest market share.

This means that the optimization of Diesel powertrains is nowadays needed and it will remain necessary for the next years.

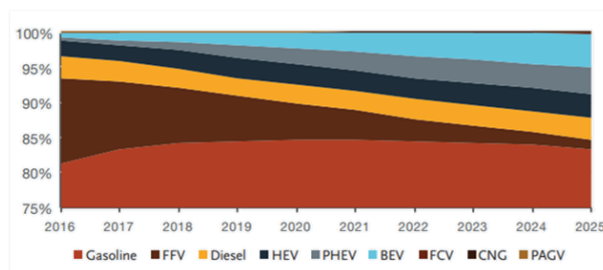


Figure 1.6 – Vehicle sales forecast in US market made by Fuels Institute [16]

As already stated, most countries all around the world are pushing towards a reduction of CO2 emissions, in particular for the automotive sector. Looking forward to next years, ICCT in [17] proposed that an increase in Diesel engines cost

to meet the CO2 targets is expected, as depicted by Figure 1.7, in which is showing Diesel engine manufacturing cost as function of fuel consumption reduction. For example, to achieve a 20% fuel consumption reduction with an advanced Diesel engine, an increase in manufacturing cost of roughly 2000\$ compared to a standard Diesel engine should be expected. And this could have an impact on Diesel market penetration in the near future. Moreover, Figure 1.7 shows that the future diesels are expected to cost less with respect to a full hybrid configuration. The costs are lower because of less expensive emission control systems and improved engine components. Adding the costs and benefits of a 48V mild hybrid system and electric supercharging (orange box) leads to slightly higher costs per percent reduction in fuel consumption, but average total costs remain lower than for full hybrids [17].

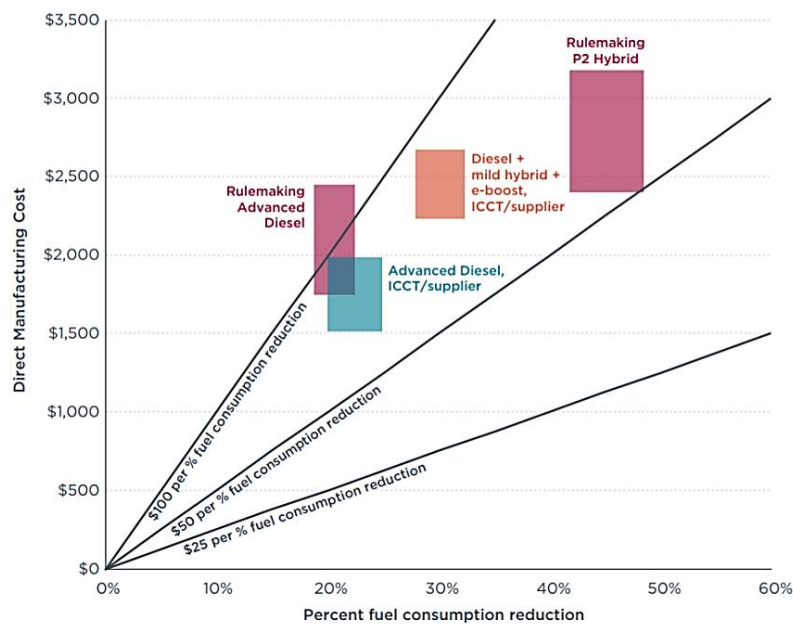


Figure 1.7 – Estimates of direct manufacturing cost per percent fuel consumption reduction in 2025 [17]

However, Diesel engines are going to cost more and more not only because of CO2 emission targets, but also because of pollutant emissions regulations. As known, there is a worldwide trend in setting tighter limits, but, in order to reach them, the introduction of new technologies is needed and linked to a cost increment. ICCT in [18], proposes a summary study in which the cost of technology is presented for each European regulatory level. These results are summarized in Figure 1.8, and reported in detail in Table 1.1. As it can be seen from Figure 1.8, the red zone represents costs related to engine-out emission controls, blue is for aftertreatment system costs and green is for R&D costs. Going from Euro 5 to Euro 6 most part of the cost increase was due to the aftertreatment system technology. If this trend will be confirmed also for the next generation of Diesel engines, again it could have an impact on market penetration.

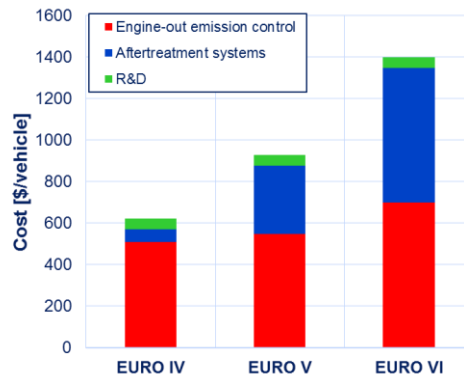


Figure 1.8 – Estimated costs of emissions control technologies for European light duty vehicle from Euro 4 to Euro 6 (assuming 1.5L 4-cylinder) [18]

Table 1.1 – Estimated costs of emissions control technologies for European light duty vehicle (assuming 1.5L 4-cylinder) [18]

Regulation	EURO 1	EURO 2	EURO 3	EURO 4	EURO 5	EURO 6
Year	1992	1996	2000	2005	2009	2014
Regulated Pollutants	NOx+HC PM CO	NOx+HC PM CO	NOx PM CO	NOx PM CO	NOx PM CO	NOx PM CO
Emission levels [g/km]	1.13 0.18 3.16	0.7 0.08 1	0.5 0.05 0.64	0.25 0.025 0.5	0.18 0.005 0.5	0.08 0.0045 0.5
Engine-out emissions control	\$30	\$114	\$364	\$508	\$548	\$699
AT systems	\$0	\$0	\$62	\$62	\$328	\$648
Fixed costs (R&D, cert.)	\$26	\$26	\$51	\$51	\$51	\$51
Total costs	\$56	\$140	\$476	\$621	\$927	\$1398

This very complex context are pushing the OEMs to the adoption of engine technologies left so far for innovation. Looking forward to next years, a not negligible increase in Diesel engines cost to meet the CO₂ targets pollutant emissions limits. In order to fully exploit the potential of the abovementioned ‘left in the closet’ technologies, numerical simulation can play a fundamental role by allowing the creation of a kind of a virtual test rig, giving as outputs the combustion related parameter, the pollutant emissions and the combustion noise. Therefore, this work has the aim of evaluating the potential of the Variable Valve Actuation in terms of both engine efficiency and aftertreatment thermal management improvements. Moreover, since development trends in modern Common Rail fuel injection systems show dramatically increasing capabilities in terms of number of injection events per engine cycle as well as the modulation and shaping of the injection rate, an optimization analysis of the injection parameters was carried out in order to minimize fuel consumption and combustion noise.

Chapter 2

Preliminary analysis

Part of the work described in this Chapter was also previously published in the following publications.

- Piano, A., Boccardo, G., Millo, F., Cavicchi, A. et al., "Experimental and Numerical Assessment of Multi-Event Injection Strategies in a Solenoid Common-Rail Injector," SAE Int. J. Engines 10(4):2129-2140, 2017, <https://doi.org/10.4271/2017-24-0012>.
- Piano, A., Millo, F., Postriotti, L., Biscontini, G. et al., "Numerical and Experimental Assessment of a Solenoid Common-Rail Injector Operation with Advanced Injection Strategies," SAE Int. J. Engines 9(1):565-575, 2016, <https://doi.org/10.4271/2016-01-0563>.
- Sapio, F., Piano, A., Millo, F., and Pesce, F., "Digital Shaping and Optimization of Fuel Injection Pattern for a Common Rail Automotive Diesel Engine through Numerical Simulation," SAE Technical Paper 2017-24-0025, 2017, <https://doi.org/10.4271/2017-24-0025>.
- Piano, A., Millo, F., Boccardo, G., Rafigh, M. et al., "Assessment of the Predictive Capabilities of a Combustion Model for a Modern Common Rail Automotive Diesel Engine," SAE Technical Paper 2016-01-0547, 2016, <https://doi.org/10.4271/2016-01-0547>.

2.1 Engine test case

The selected test case is the 1.6l 4L CDTI Ecotec Diesel engine, developed by General Motors (GM) and introduced in the market in 2013. This engine was the first Diesel from GM to comply the EURO 6 emissions legislations setting ‘benchmarks for refinement, performance and environmental compatibility’, as claimed by Dr. Thomas Sedran [19].

The global development of the engine, in which more than 1000 engineers were involved, can be divided in 3 main parts: the core engineering, in GM Global Propulsion System in Turin, the vehicle integration and calibration, in GM in

Russelsheim, and the production process in Szentgotthárd (Hungary). The in-vehicle integration was properly standardized in order to support 6 different brand, 6 global platforms, and over 70 specific applications. [20]

The selected engine was available in a range of power outputs, among which the so-called B16DTH was selected. The main features of the engine are highlighted in Table 2.1.

Table 2.1 – Main features of the B16DTH engine

Engine type	DI Turbocharged Diesel Euro 6
Engine architecture	4-cylinder in line, 4 valves per cylinder with double overhead camshafts
Displacement	1598 cm^3
Stroke x Bore	80.1 mm x 79.7 mm
Compression Ratio	16:1
Cylinder block / Bedplate	Semi-closed deck aluminium block (precision sand casting) and aluminium bedplate (die cast)
Turbocharger	Single-stage with VGT
Fuel Injection System	Common Rail with solenoid injectors (2000 bar maximum injection pressure)
EGR circuit	High Pressure
Maximum Torque	100 kW @ 4000 RPM
Maximum Power	320 Nm @ 2000 RPM

The main characteristics of the selected engine are briefly summarized as follows [20]:

- Combustion system – a shallow-dish bowl profile was chosen for improving the spray propagation in moderate swirl conditions, for increasing the EGR tolerance and the good thermal behaviour at high load engine conditions. The low-pressure drop inlet ports includes swirl flaps for optimizing the in-cylinder air motion.
- Fuel Injection system – the Common Rail system includes 8-hole latest generation solenoid injectors with a maximum injection pressure of 2000 bar and it is able to guarantee up to 10 injection pulses per engine cycle.
- Engine architecture – the aluminium cylinder block and bedplate support up to 180 bar as peak firing pressure inside the cylinder and were designed to have up to 1.4 kg/kW engine weight-to-power ratio.
- Lubrication system – it consists of variable displacement oil pump that can regulates between 2 different pressure levels depending on the operating conditions, and a dedicated piston cooling jets oil gallery controlled by the ECU through a solenoid valve. This system is able to reduce the friction losses in partial load and to improve the lubrication in high load conditions. This results is confirmed by Figure 2.1, in

which the friction losses of the selected engine is compared with other 36 production Diesel engines.

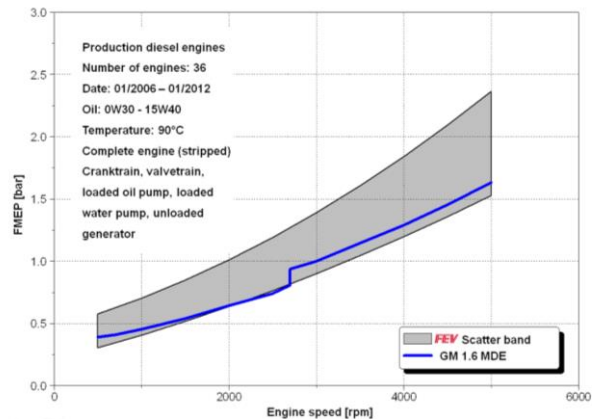


Figure 2.1 – Engine friction losses comparison [20]

- Cooling system – it features a switchable water pump with an electromagnetic clutch that provide a transversal flow through the cylinder head water jacket.

The 1.6l Diesel engine is an effective result of a right downsizing approach from the previous 2.0l engine family. This is also confirmed by the results in Figure 2.2 where the CO₂ emission along NEDC as a function of the elasticity is plotted for 2 different engine versions (TST for Two Stage Turbocharger, VGT for Single Stage Turbocharger with VGT): the 1.6l engine is able to provide similar results in terms of elasticity but with a significant improvements in terms of fuel consumption, with a reduction of about 25%.

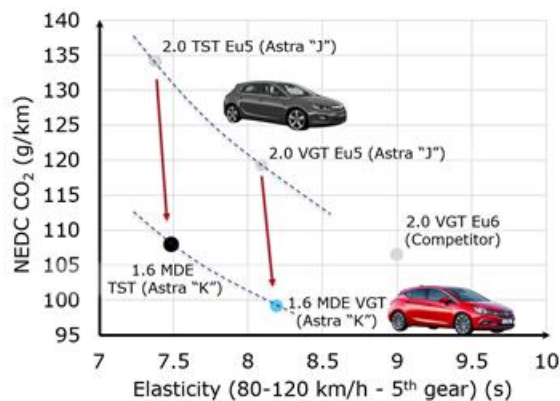


Figure 2.2 – In-vehicle performance comparison between 2.0l and 1.6l Diesel engines [20]

Moreover, the engine downsizing combined with the optimized abovementioned features leads to a relevant improvement in terms of engine efficiency, especially at low load of the engine map, as shown in Figure 2.3, where the BSFC at 2000 RPM X 2 bar BMEP engine operating condition is depicted in comparison with the scatter band of 39 benchmarked engines.

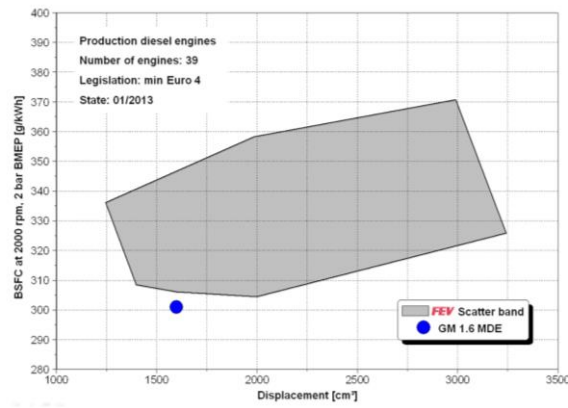


Figure 2.3 – BSFC comparison – 2000 RPM X 2 bar BMEP [20]

In addition, this engine sets benchmark for NVH since the noise radiation of base engine components was minimized thanks to several design optimization loops with CAE simulation tools, as well as the in-cylinder combustion noise. This result is clearly shown in Figure 2.4: the GM engine is always in the lower part of the scattered band related to benchmarked engines.

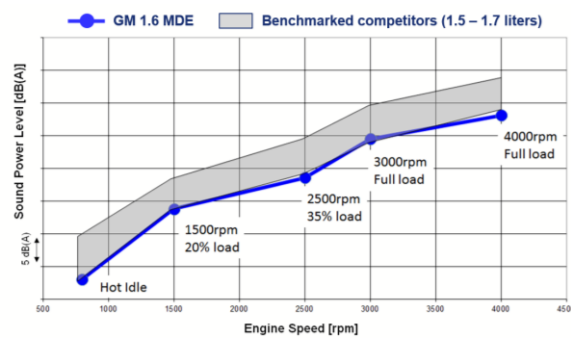


Figure 2.4 – Sound power level comparison [20]

2.2 Fuel injector test case

As far as fuel injection system is concerned, in this work a latest generation of solenoid Common Rail injector, Bosch CRI2-20, was selected as shown Figure 2.5.

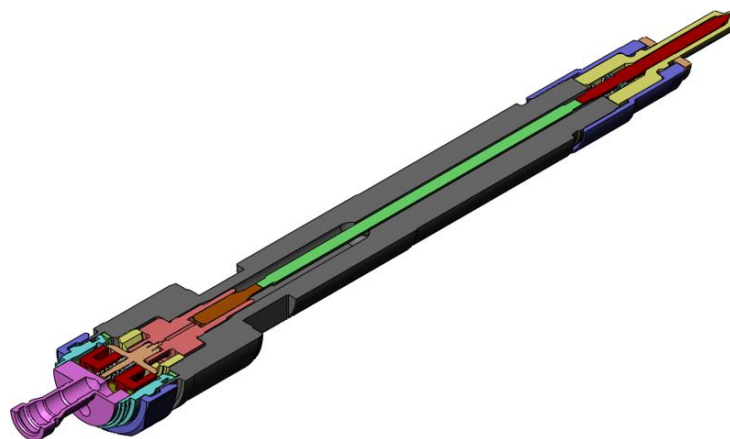


Figure 2.5 – Bosch CRI2-20

The new generation of solenoid injector developed by Bosch, are built with a fast-switching solenoid valve allowing a high degree of freedom in the injection pattern definition thanks to 10 individual injections with short injection dwell time, per power cycle. These multiple injections simultaneously enable the fuel consumption, pollutant emissions and noise reductions [21–25]. The increasing need of higher injection pressure to meet the emissions standard, made necessary the pressure-balanced pilot valve introduction: this innovative design allows the injection pressure increase without the injection performance worsening caused by both spring preload and electromagnetic force increment in a traditional poppet valve [26]. The difference in terms of valve opening area is shown in Figure 2.6.

In addition, the CRI2-20 generation has an integrated high-pressure volume that reduces pressure pulsations and also increases hydraulic efficiency through reduced return flow [21].

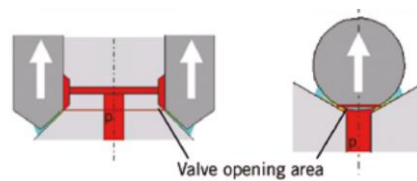


Figure 2.6 – Valve opening area difference between innovative pressure-balanced valve (left) and traditional poppet valve(right) [27]

As the present final goal is developing a design tool for the Fuel Injection System (FIS) operating in part load conditions typical of driving cycles, the 1D fuel injector model was developed and tuned focusing on complex injection strategies. As a matter of fact, although several papers are present in literature concerning the development of 1D models for Diesel injectors [28–30], unfortunately only partial validations of such models are generally presented: the reported validations are often carried out for relatively long injection events, which are only moderately interesting for the implementation of advanced, multi-event injection strategies currently used for automotive applications. Differently, in this case the injection system was operated in several multi-injection strategies, at different rail pressure values. The results obtained at the hydraulic bench (injection rate profiles and rail pressure profiles) were used to tune the 1D injector model, obtaining a satisfactory accuracy of the predicted injection rate profiles also with complex, reduced dwell-time actuation strategies [31].

2.2.1 Experimental test

Since in order to validate the 1D injector model, in addition to all the main geometric characteristics of the injector, experimental hydraulic data are required mainly in terms of rail pressure time history and solenoid current profile (inputs to the model) and injection rate curve (to be compared with the model main output). The experimental facilities which were exploited to this end will be described in detail in next paragraphs.

Internal geometry detection

The detection of the internal geometry of the injector is needed to obtain a good geometric characterization. Nozzle, Z-hole and A-hole are the critical parts of the injector where cavitation can appear and, consequently, a precise detection has to be done [32]. In literature, the most used technique for the evaluation of geometric parameters, consists of the use of special silicone to obtain a mold of the physical part. Then, using a Scanning Electron Microscope, pictures are obtained and processed by means of CAD software. [30,33–37]. The process could be divided in 3 consecutive steps:

1. Realization of silicon mold – the internal part of the injector must be properly cleaned since the fuel could interact with the silicone. Usually, the silicone used for these measurements is vinyl-polysiloxane with a hardness of shore 8: it could be stretched without suffering any permanent deformation and it does not adhere to the wall. [37]
2. Imaging with the Scanning Electron Microscope – electron microscope is used to take pictures of the sample and requires materials that conducts electricity, therefore the process includes gold coating of the mold ($1\ \mu m$ thickness) [37].
3. Treatment of the pictures and determination of the characteristic dimensions – The pictures obtained with the electron microscope have a reference dimension that leads to use a CAD software with a proper scale factor for obtaining the actual dimensions of the internal parts [37].

The described silicone methodology is shown in Figure 2.7.

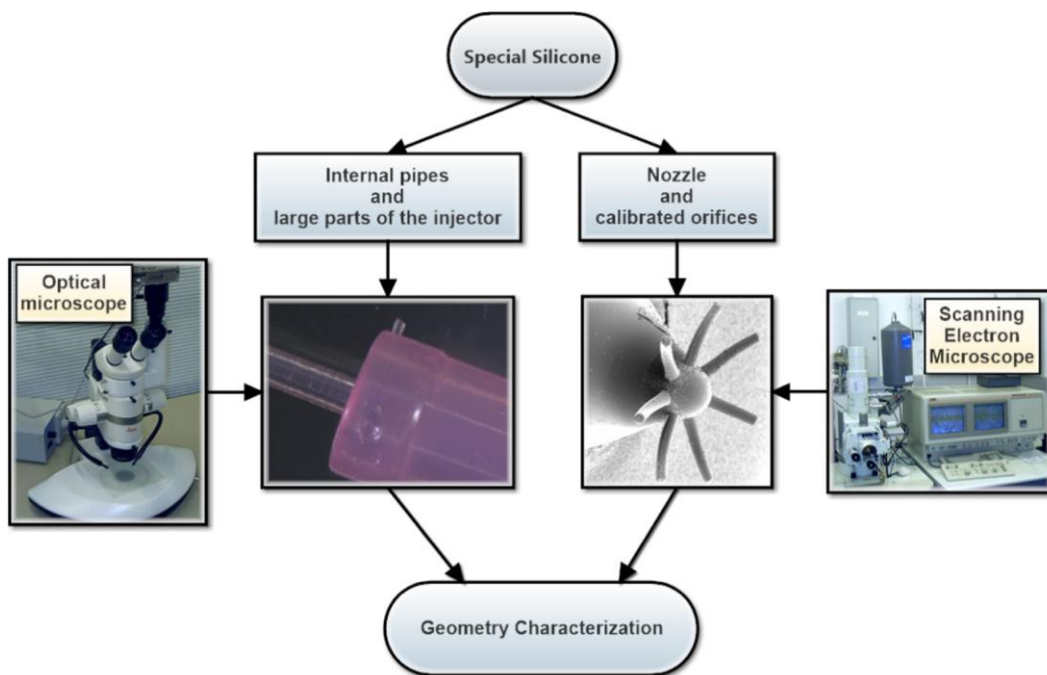


Figure 2.7 – Silicone methodology for internal geometry detection [30]

In this work a different methodology was adopted: more specifically, a 3D Computed Tomography (CT) of the injector was carried out. This technique is nowadays among the most advanced available in the industry; CT is a completely non-destructive and non-contact method for obtaining three-dimensional representation of the scanned object both externally and internally. A CT scanner consists of an x-ray emitting source, a positioning system, a detector and electronic and computational devices for data acquisition and elaboration. The principles are described below: radiographic images of the part are acquired from different angles; then, combining together all the acquired images, a virtual slice through the part is reconstructed. When different consecutive slices are computed, a 3D visualization is obtained. The reason why it was decided to use this technique is that it has many advantages with respect to traditional dimensional measuring systems, especially in terms of reduced measuring time, including scanning, reconstruction and analysis time [38,39]. An example of the images of the injector obtained through CT is reported in Figure 2.8.

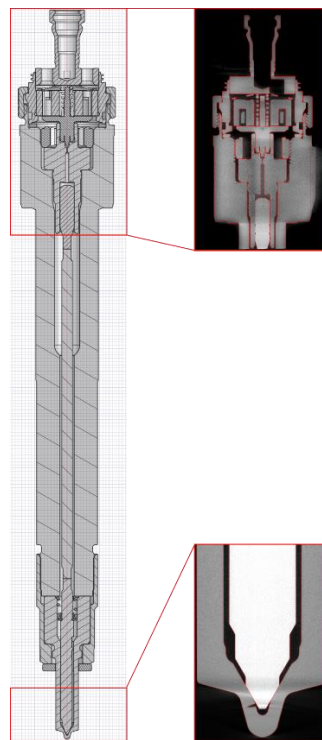


Figure 2.8 – Bosch CRI2-20: from scan to CAD 3D [31]

Injection analyzer

The experimental hydraulic data used to tune and validate the GT-SUITE 1D model of the solenoid injector were obtained at Perugia University SprayLab by a proprietary STS Injection Analyzer. This instrument is designed to simultaneously measure both the global injected volume and the injection rate time history (along with other dynamic signals such as rail pressure, injector current, needle lift) in a given operating condition. The operating condition is defined by the rail pressure level and by the injector actuation strategy, based on $2n-1$ parameters (with n ET

values and n-1 DT values); the instrument can vary any of the 2n-1 parameters to analyze the system behavior. The mean injected volume and the dynamic signals are acquired in the same batch of consecutive injection events, allowing both the mean behavior and the shot-to-shot dispersion evaluation. In case of multi-injections strategy, the injected volume from the single injection events can also be derived.

The injection rate measurement by the STS Injection Analyzer is based on the Zeuch's Method, i.e. the injection in a closed, fixed volume chamber filled with the same injected fluid. At the injection occurrence, the injected volume ΔV is forced to enter the measuring chamber, in which before the injection event the P_{base} level (50 bar in this campaign) is maintained, causing its pressure to rise according to Equation 1:

$$\Delta P = \frac{k}{V} \Delta V \quad \text{Eq. 1}$$

where k is the fluid Bulk Modulus and V is the measuring chamber volume.

Differentiating Equation 1 allows the injection rate evaluation (Equation 2):

$$\dot{Q} = \frac{dV}{dt} = \frac{V}{k} \frac{dP}{dt} \quad \text{Eq. 2}$$

The pressure history in the measuring chamber, along with the fluid temperature, is detected by a piezo-resistive sensor (Kistler 4075 A100). At the end of each injector actuation cycle, the globally injected volume is evacuated from the measurement chamber by a fast acting solenoid valve in order to re-set the P_{base} pressure level for the next injection cycle. The fluid escaping the Injection Analyzer flows through a Coriolis mass flow meter (Siemens Sitrans CF 2100, accuracy $\pm 0.5\%$ of the actual reading in the range 0.1-4 kg/h) to measure the mean injected mass and the fuel density over an assigned set of injector actuation cycles. Further, the mass flow meter allows a continuous instrument calibration overcoming the difficulties in determining the fluid bulk modulus in the actual operating conditions. More details about the STS Injection Analyzer are reported in [40,41]. The rail supply was provided by a CP1H Bosch pump driven by an electric motor, with a transmission ratio set to simulate a 2100 engine rpm operation. A pickup on the pump shaft triggered the pulse train generation for the injection system, with an injection phasing to the pump TDC analogous to the engine operation. The rail pressure is set by a two-way, PWM-modulated inlet metering valve controlled by a self-developed PID strategy. In stand-by (no injection) conditions, a rail pressure ripple within the minimum between 2% of the set point and 10 bar was obtained. The rail was submerged in an oil-heated vessel so as to regulate the fuel temperature in the rail-injector pipe @ 40 ± 1 °C with all the injection pressure levels and injection strategies. The used fluid for the experimental test is a commercial, ISO4113 compliant Diesel pump test fluid [42]. The properties of ISO4113 are highlighted in Table 2.2.

Table 2.2 – ISO4113 fluid properties

Carbon content	86.2 w%
Hydrogen content	13.5 w%
Lower Heating Value, LHV	42.84 MJ/kg
Cetane number (ISO 5165-98)	51.2
Density @ 15°C	837.5 kg/m ³
Viscosity @ 40°C	2.681 mm ² /s
Surface tension @ 20°C	30.4 mN/m

Dataset

In order to assess the robustness and the predictive capability of the model, two different nozzles, the main characteristics of which are reported in Table 2.3, were tested and simulated.

Table 2.3 – Geometrical and hydraulic parameters for the tested nozzles

Element	Holes number	Nominal diameter	Flow number
-	-	mm	cm ³ /30s @Δp=100 bar
Nozzle A	7	0.139	390
Nozzle B	8	0.114	340

The experimental activity was carried out in 2 different steps: firstly, the experimental injection rate profiles and injected volumes along with rail pressure profiles were acquired in several single event injector operation strategies (as shown in Figure 2.9) for the two nozzle highlighted in Table 2.3; secondly, multi-event and unconventional driving strategies for obtaining the injection rate shaping were tested (in Figure 2.10) on Nozzle A.

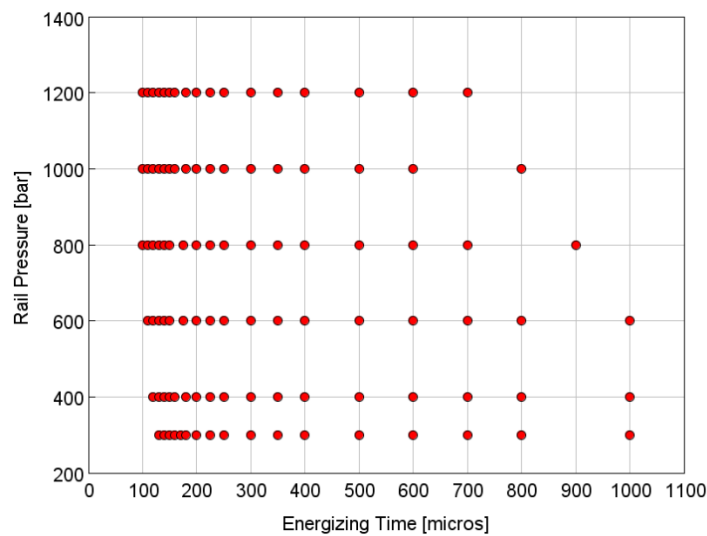


Figure 2.9 – Experimental single injection test matrix for Nozzle A and Nozzle B

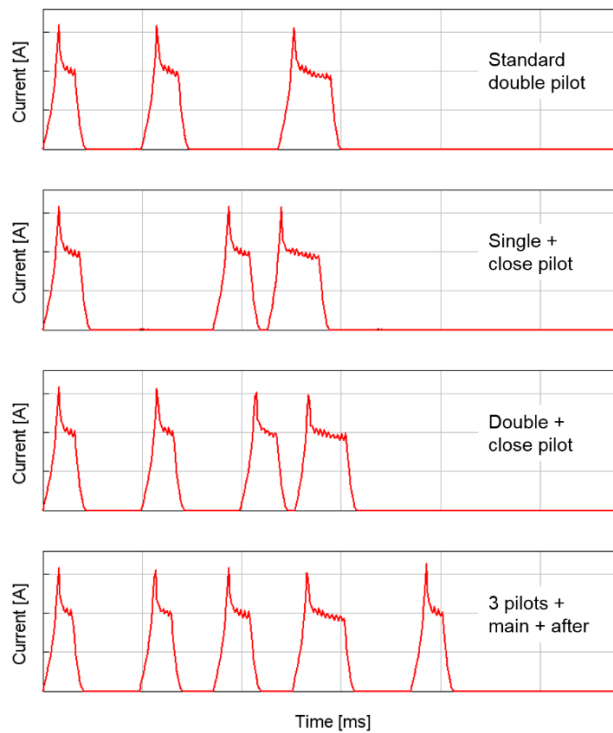


Figure 2.10 – Current injection operations investigated for Nozzle A [43]

2.2.2 1D-CFD model

Different approaches for the simulation of the injection system can be found in literature and they are referred to 3 different modelling techniques:

- 3D-CFD – this approach is mainly focused on a detailed simulation of the fluid domain. It cannot be used for simulations that have to take into account coupling among different physical subsystems.
- 1D-CFD – Navier-Stokes, Newton and Maxwell equations are computed to model fluid, mechanical and electromagnetic parts of the whole circuit.
- Bond graph – the system is reduced to a network of 0D elements. This 0D schematization produces only ODEs and DAEs.

Among the abovementioned options, the 1D-CFD approach, by means of GT-SUITE simulation software, was chosen for the following reasons: differently from 3D-CFD it has the capability to model the entire fuel injection system thanks to multi-domain approach; differently from Bond Graph, it is able to provide a physically based representation of phenomena. Moreover, the detailed 1D-CFD injector model could be coupled with DIPulse, predictive combustion modelling developed by Gamma Technologies, for a comprehensive engine modelling, from injector command to engine-out pollutant emissions.

GT-SUITE is a simulation tool for design and analysis of engine and vehicle system and components [19]. It is capable of modeling the coupled behavior of hydraulic and mechanical components, and it is also able to study steady-state and

transient response. GT-SUITE is based on one-dimensional, compressible, unsteady fluid dynamics and multi-body dynamics. Moreover, flow and heat transfer in the piping and volumes can be modelled, as well as mass dynamics. As it can be seen in the next sections, the flow solver includes models for cavitation, frequency dependent friction, species transport and non-equilibrium aeration everywhere in the system. [44,45].

Electromagnetic Valve

The solenoid model is built from electric and magnetic primitives representing the electromagnetic system: a current source, a coil, radial and axial magnetic components, and the air gap between the solenoid and armature. The model solves for the magnetic flux induced by current in the coil. This flux passes through the magnetic circuit, generating a force on the armature according to the flux and air gap, as shown in Figure 2.11, where the flux is represented by a dashed red line.

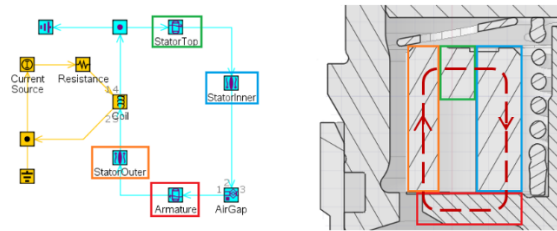


Figure 2.11 – Electromagnetic valve model [31]

In addition, the air gap between the armature and the stator is modelled considering the geometrical data. As a result, it gives a mechanical force directly connected to the armature and proportional to the squared magnetic flux φ , as shown in Equation 3.

$$F = \frac{dR}{dx} \frac{\varphi^2}{2} \quad \text{Eq. 3}$$

Where R is the reluctance that is proportional to the gap length x and inversely proportional to the equivalent cross sectional area of the air gap A_{eq} . (Equation 4)

$$R = \frac{x}{\mu_0 A_{eq}} \quad \text{Eq. 4}$$

μ_0 = Permeability of free space

Control Valve

The performance of a servo driven injector is mainly ruled by the control valve, typically a solenoid actuated valve. The fluid-structure interaction of the valve is modelled using the 1D mechanic library and some fluid-mechanical sub-models, as shown in . The valve-seat region was modelled by two fluid mechanical templates

with opposed pressure forces. As Figure 2.12 shows, two different templates were used to model correctly the valve-seat region of the valve, one to model the interaction between flow and mechanical system, while the other one to calculate the change in flow area as a function of the lift of the poppet, the pressure force on the poppet and the redistribution of the attached volumes. For the latter, a linear variation of the pressure acting in the flapper seat area was assumed.

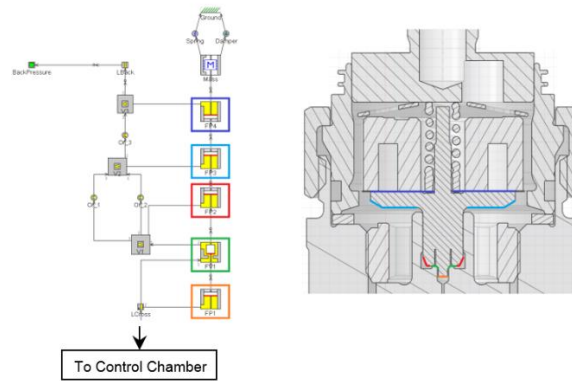


Figure 2.12 – Control valve model [31]

Control Chamber

As known, the needle motion results from an imbalance of the pressure forces acting on the needle. This imbalance results from a reduction of the pressure in the control chamber which is initiated by opening the control valve. When the control valve is opened, fuel drains from the high pressure at the inlet of the injector, through the inlet orifice into the control chamber, and through the outlet orifice to the low pressure downstream of the control valve. Once the control valve is fully open, the design of these orifices has a significant impact on the pressure in the control chamber and therefore the imbalance of forces on the needle. The large pressure drop across these orifices can cause cavitation so care is required to investigate the flow through them. The proposed control chamber model in GT-SUITE is presented in Figure 2.13.

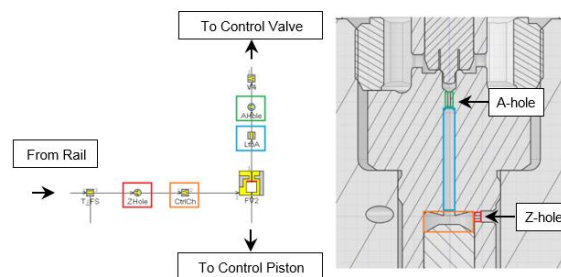


Figure 2.13 – Control chamber model [31]

The geometry of the inlet and outlet holes strongly affects the dynamic behaviour of the needle. As a result, the control volume orifice of the injector need to be hydraulically characterized. An example of a possible experimental setup for

the characterization of the flow through these controlling orifices was proposed by Salvador et al. [28].

Z-Hole

The Computed Tomography of the injector shows a conical section of the orifice. In this case, the sub-model adopted to evaluate the discharge coefficient of the inlet orifice, does not consider the cavitation phenomenon. This hypothesis is consistent with hydraulic characterization made by Salvador et al., where the mass flow rate has a linear behaviour with the square root of the pressure as highlighted by Figure 2.14 [28].

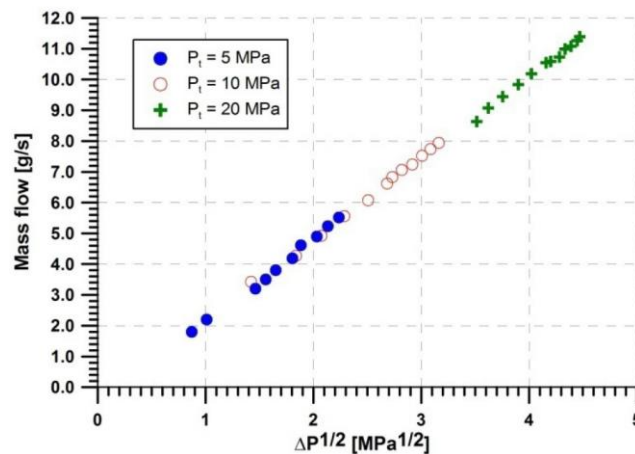


Figure 2.14 – Mass flow rate versus square root of the pressure drop for the Z-Hole orifice [28]

A-Hole

As opposed to the Z-hole, the A-hole has not a conical section but a cylindrical one. Moreover, from the hydraulic characterization, a different behavior can be seen in Figure 2.15 [28]: there is a value of pressure drop above which the mass flow rate is constant and the orifice cavitates.

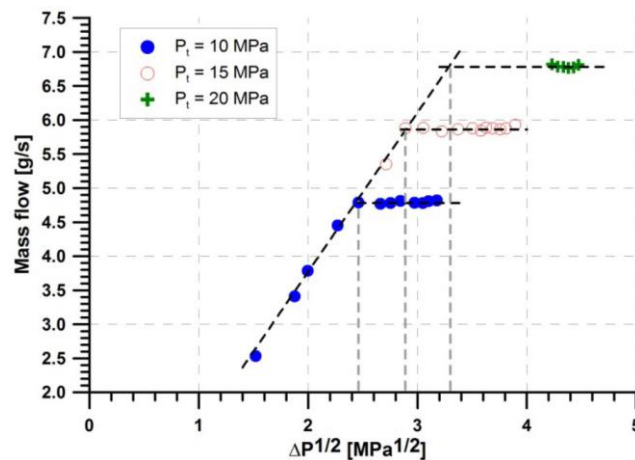


Figure 2.15 – Mass flow rate versus square root of the pressure drop for the A-Hole orifice [28]

The discharge coefficient was therefore estimated by means of the GT-SUITE sub-model for liquid flow through an orifice, including cavitation effects, based on Sarre et al. work [46]. The transition into cavitation is defined by a critical cavitation number and the discharge coefficient will be a constant value for no cavitation and calculated based on the cavitation number in cavitating regime. The cavitation number K is defined in Equation 5 [44,46].

$$K = \frac{p_1 - p_v}{p_1 - p_2} \quad \text{Eq. 5}$$

where p_1 is the pressure upstream of the orifice, p_2 is the pressure downstream of the orifice, and p_v is the vapour pressure of the fluid. The onset of cavitation is specified by the critical cavitation number. If the cavitation number is lower than the critical cavitation number, the orifice is cavitating and the discharge coefficient will be calculated as defined in Equation 6 [44,46].

$$C_d = C_c \sqrt{K} \quad \text{Eq. 6}$$

where C_c is the contraction coefficient, defined in Equation 7 [44,46].

$$C_c = \left[\left(\frac{1}{0.61} \right)^2 - 11.4 \cdot \frac{R}{D} \right]^{-0.5} \quad \text{Eq. 7}$$

in which $\frac{R}{D}$ is the ratio of the inlet radius to the orifice diameter. The contraction coefficient is limited to be ≤ 1 . If $K \geq K_{crit}$, there is no cavitation and the discharge coefficient is calculated as defined in Equation 8 [44,46].

$$C_d = C_c \sqrt{K_{crit}} \quad \text{Eq. 8}$$

Given the impossibility to measure R (inlet radius of the orifice) with the 3D CT resolution, the Contraction Coefficient was considered similar to the value found in literature [28].

Control piston and needle mechanics

The pressure force acting on the control piston is calculated with a dedicated sub-model that determines the pressure force using the upstream and downstream pressures. The pressure acting on the needle varies due to the design of the nozzle and the tight fit of the needle in the nozzle. In order to accurately model the pressure force on the needle, the flow path through the nozzle is modelled using fluid volumes and pipes. In particular the needle poppet valve is modelled by calculating the flow area through the valve based on the position of the mass attached to it. The valve's discharge coefficient is determined based on the Reynolds number of the

flow through the valve. The volume changes due to the poppet motion are also taken into account.

The high-pressure fuel acting on the control piston and needle leads to significant axial deformation of their bodies given the small needle lifts in injectors. This is taken into account by separating each body into two masses connected by a spring and a damper as shown in Figure 2.16. The spring represents the axial stiffness of the body and the damper accounts for material damping.

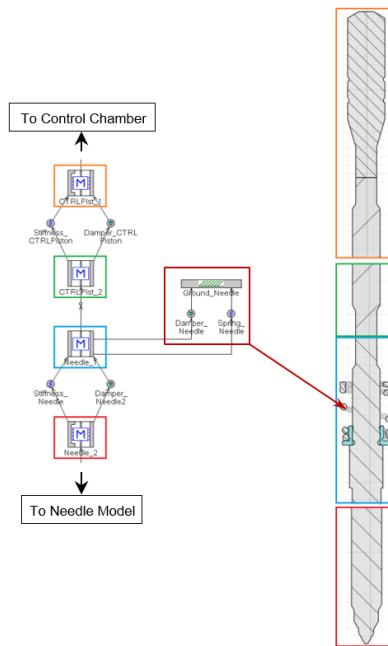


Figure 2.16 – Needle mechanics model [31]

Hydraulic network

Explicit solver is used for time integration of the fluid dynamics, adopting short time steps in order to capture high frequency events, since the wave dynamics can significantly affect the hydraulic behaviour of the injector and because a short time scale is desired in terms of injection rate profile respect to crank angle.

As far as the friction and the heat transfer settings for the flow circuit are concerned, it is worth to mention that, while typical friction models are based on Moody chart fits, in an unsteady flow, as in this case, a model that adapts to the amplitude and frequency of the flow pulsations is needed. Usually this model is called frequency-dependent and considers that the friction and heat transfer are enhanced due to boundary layer regrowth [44].

The main hydraulic network is shown in Figure 2.17, where the connections with the mechanical parts of the injector body are shown with a black row.

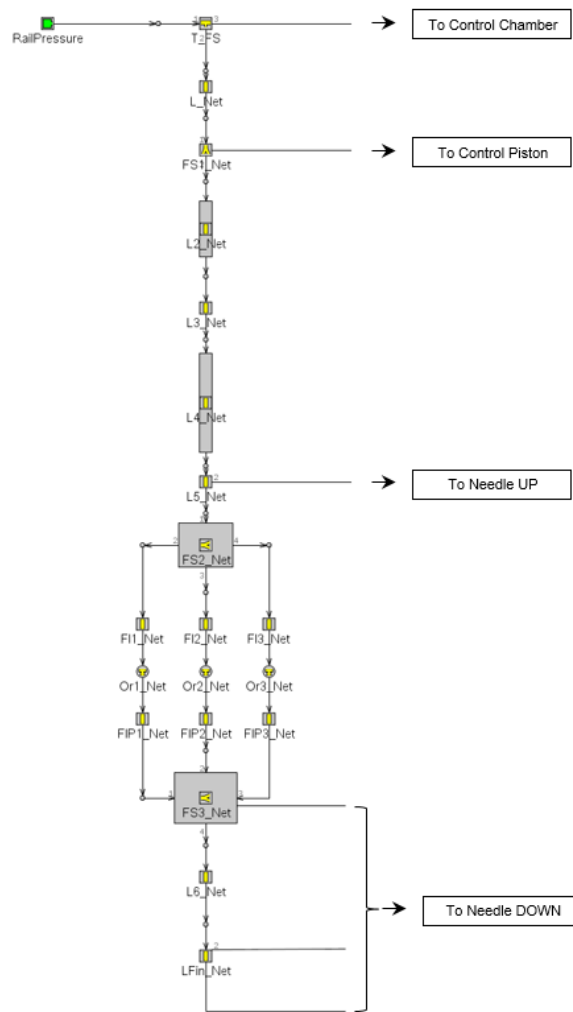


Figure 2.17 – Main hydraulic network model [31]

Results – Single injection event

Concerning the instantaneous volumetric flow rate, the experimental and simulated profiles comparison for each rail pressure is shown in Figure 2.18 for Nozzle A and Figure 2.21 for Nozzle B. In the figures the dashed line is the experimental injection rate, while in solid line the simulation result. A high level of accuracy was achieved in replicating the behaviour of the injector for each rail pressure level: the start and the end of the injection are accurately predicted and also the transient phase of the injection, like the opening and the closing slopes. Moreover, the peak injection rate value is predicted with very high precision.

As a consequence, also in terms of total injected quantity, the model predictive capability can be considered more than satisfactory for all the analyzed injector control profiles. The EMI curve results, where the total injected quantity is a function of energizing time and rail pressure, are shown in Figure 2.19 (Nozzle A) and in Figure 2.22 (Nozzle B). The new model is able to predict the total injected quantity with high accuracy for each rail pressure, where the red curve almost overlaps the experimental curve. Also the slope of the curves is very well predicted by the 1D-CFD model.

In order to quantify the error in the injection rate prediction, the average error was defined (Equation 9).

$$\% Error_i = \frac{Q_{inj,i SIM} - Q_{inj,i EXP}}{Q_{inj,i EXP}} \cdot 100 \quad \text{Eq. 9}$$

$Q_{inj,i SIM}$ = total injected quantity from simulations for i^{th} injection
 $Q_{inj,i EXP}$ = total injected quantity from experiments for i^{th} injection

The Equation 9 evaluates the percentage error in terms of total injected quantity respect to the experiments. This value is useful to obtain an estimate of the error in the total injected quantity, without any consideration about the shape of the injection rate or the timing.

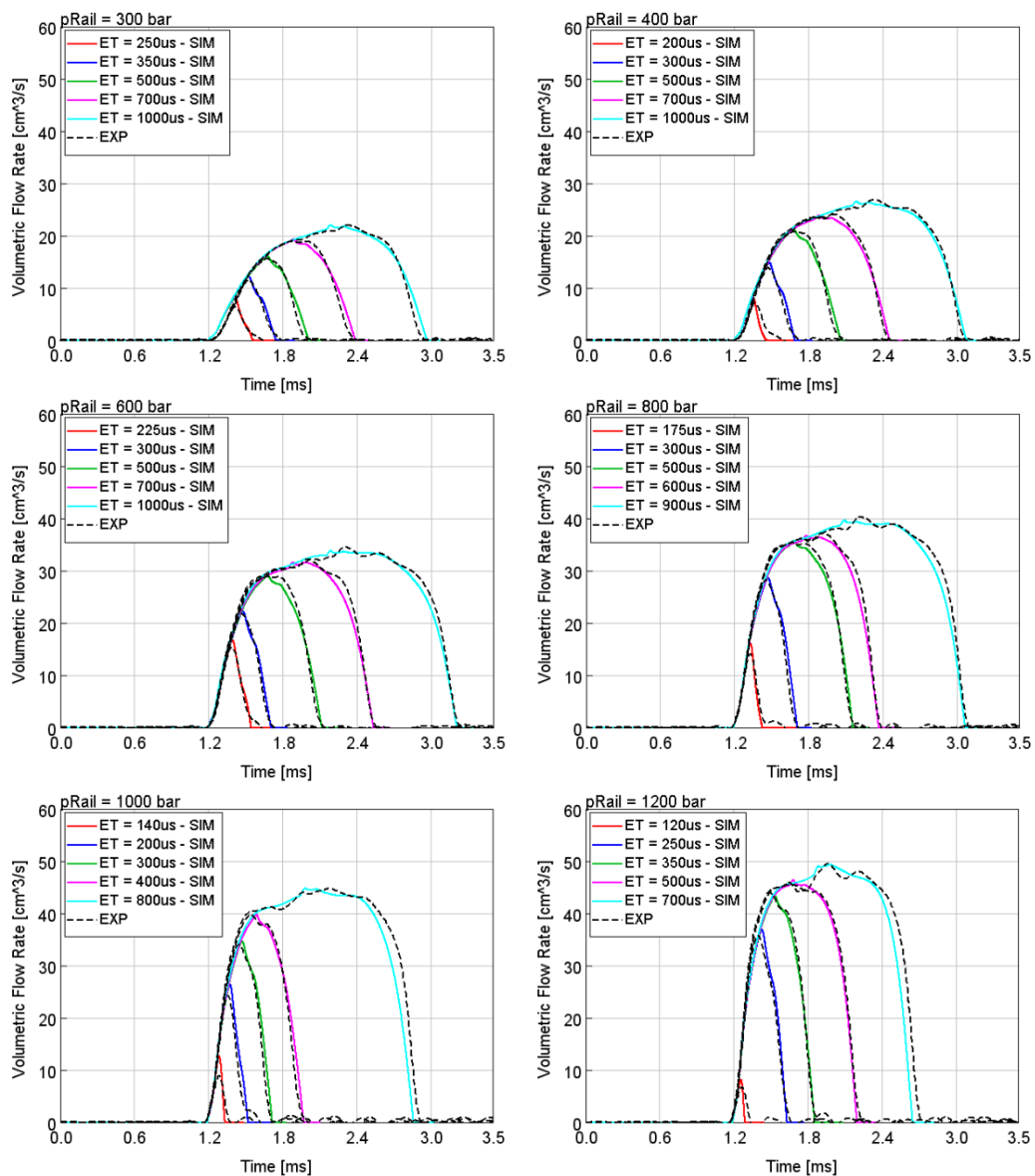


Figure 2.18 – Experimental (dashed) and simulated (solid) injection rates for six rail pressure values tested – Nozzle A [43]

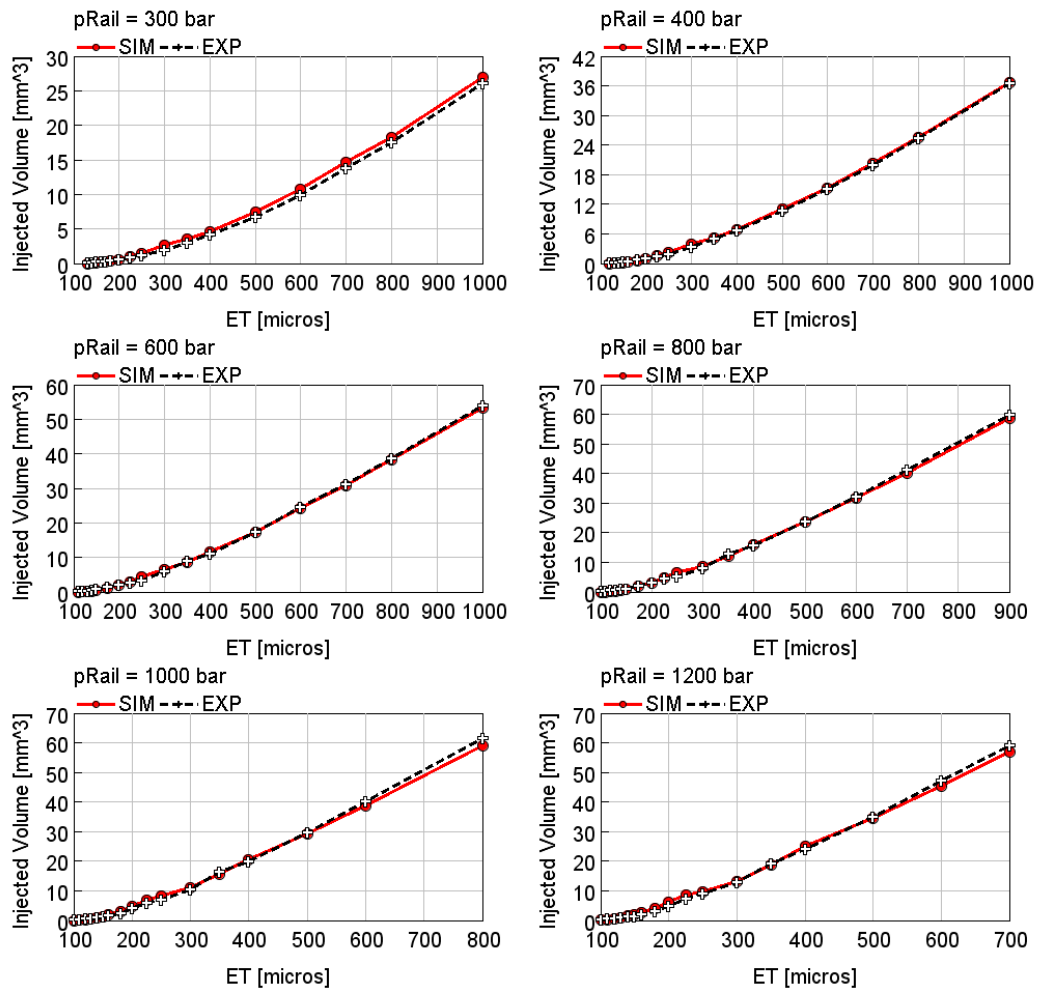


Figure 2.19 – EMI curves comparison between experiments (black dashed) and simulation results (red solid) for Nozzle A

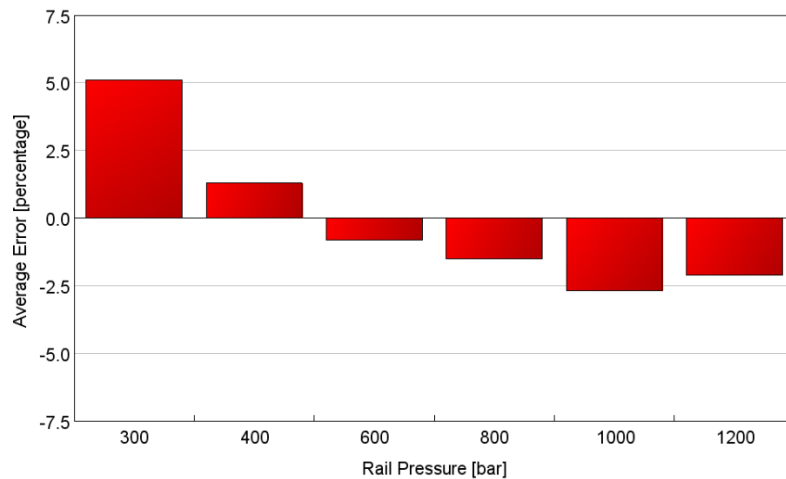


Figure 2.20 – Average error for each rail pressure related to Nozzle A results

Table 2.4 – R-squared related to Nozzle A results [43]

	R-squared					
	300 bar	400 bar	600 bar	800 bar	1000 bar	1200 bar
Nozzle A	0.999	0.999	0.999	0.999	0.998	0.998

The average percentage error (Eq. 9) related to the EMI curves, for each rail pressure, is shown in the histograms in Figure 2.20 and Figure 2.23, for Nozzle A and B respectively. As it can be seen, the error on the entire rail pressure range is in the $\pm 5\%$ band; obtaining a deviation between the highest and the lowest error values is highly contained, confirming the robustness of the 1D-CFD injector model.

The R-squared comparison for the EMI curve previously defined is shown in Table 2.4 (Nozzle A) and Table 2.5 (Nozzle B): this result gives a measure of how well the observed outcomes can be replicated by the model. The two models provide a R-squared very close to 1 for each level of the tested rail pressure.

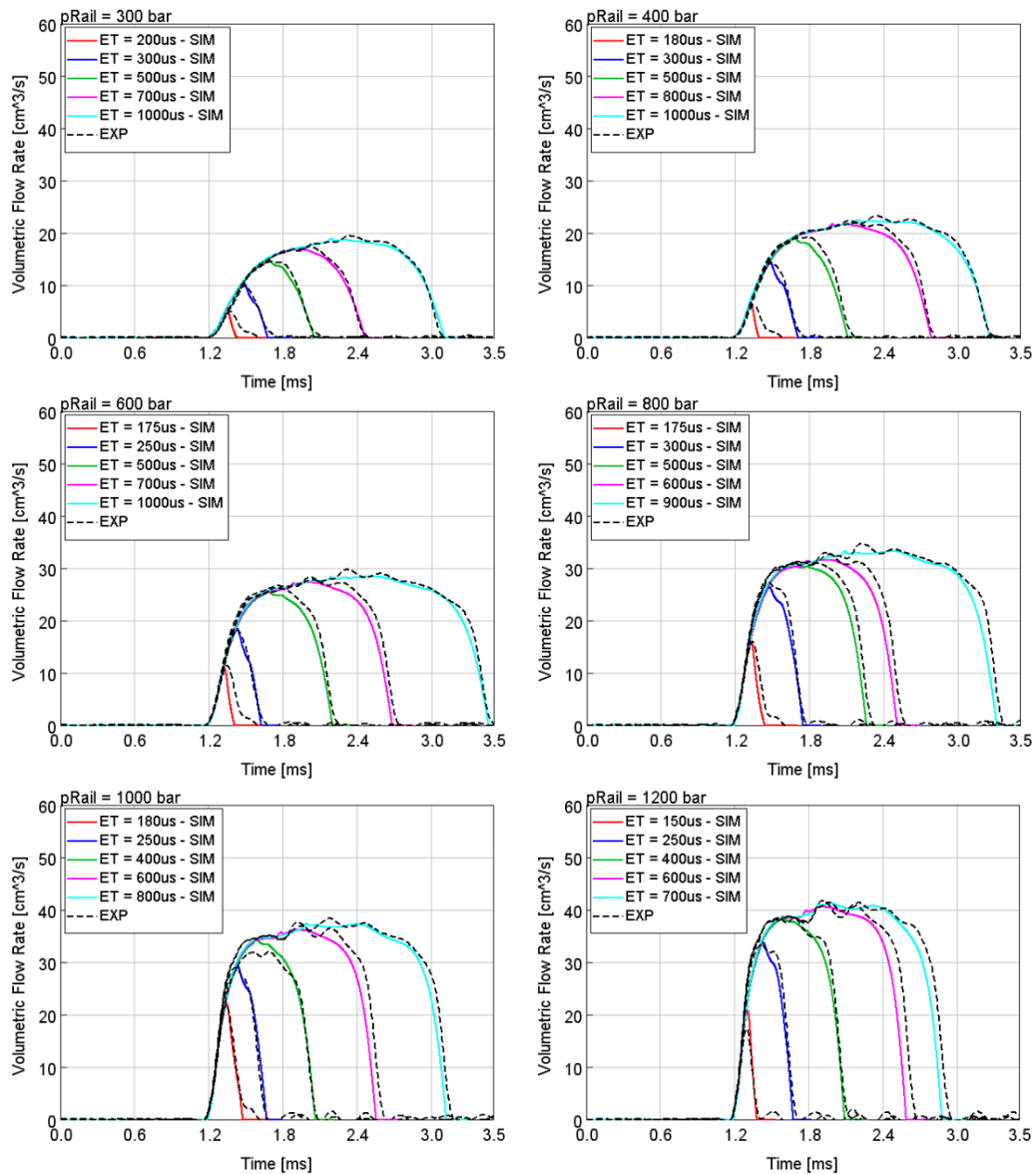


Figure 2.21 – Experimental (dashed) and simulated (solid) injection rates for six rail pressure values tested – Nozzle B [43]

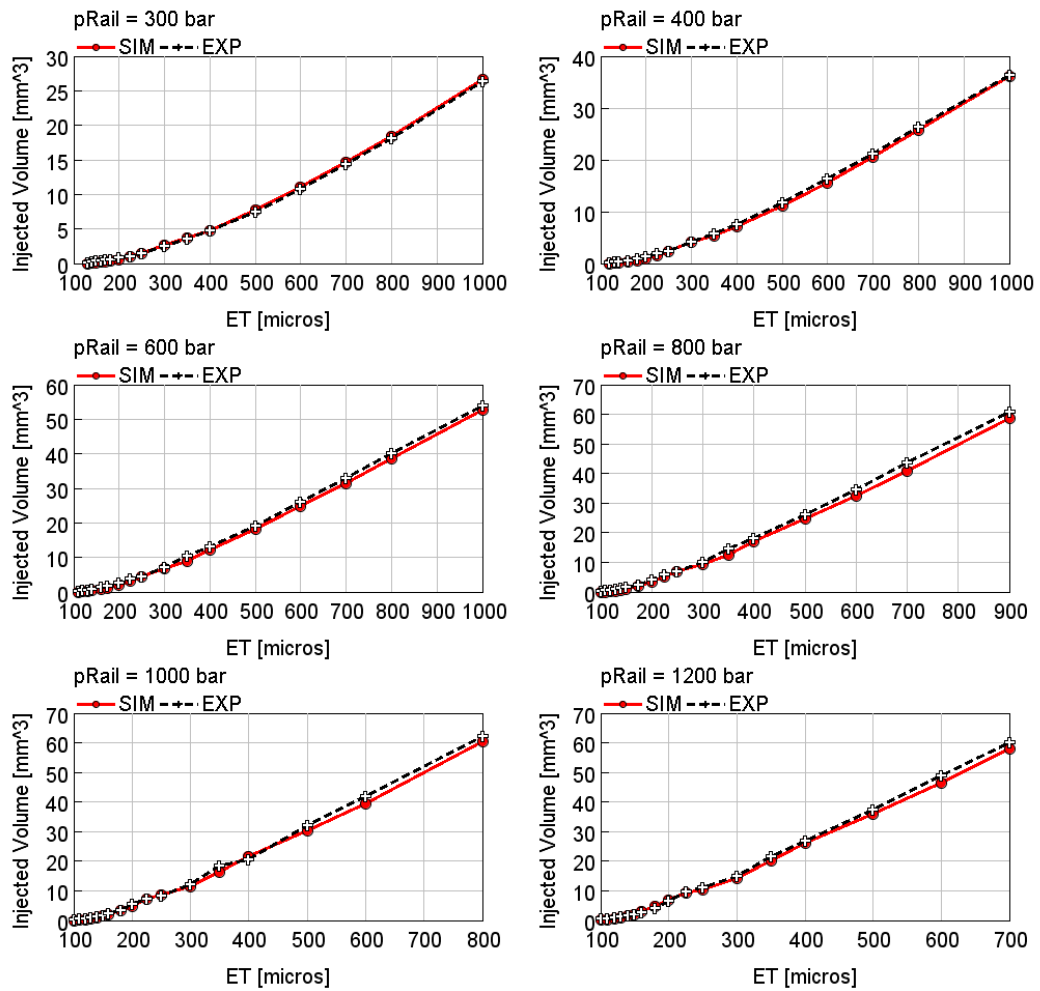


Figure 2.22 – EMI curves comparison between experiments (black dashed) and simulation results (red solid) for Nozzle B

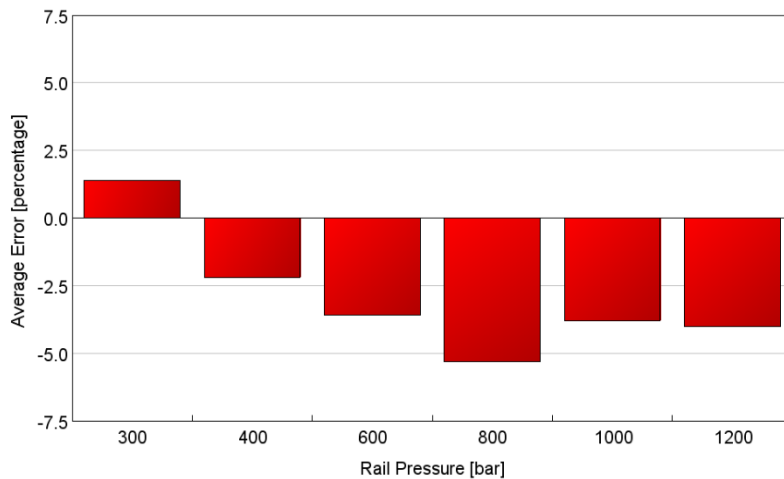


Figure 2.23 – Average error for each rail pressure related to Nozzle B results

Table 2.5 – R-squared related to Nozzle B results [43]

	R-squared					
	300 bar	400 bar	600 bar	800 bar	1000 bar	1200 bar
Nozzle B	1.000	1.000	0.999	0.999	0.998	1.000

Results – Multiple injection events

The model built was validated against an extensive experimental dataset of close double pilot and multi-pilot injection patterns with almost zero dwell time between two consecutive injection events. Figure 2.24 and Figure 2.25 show the results in terms of comparison between experimental and simulated injection rate for standard double pilot strategy. The accuracy with which the model predicts the injection rate confirms that the injector dynamic is fully captured. The model is able to predict the correct timing and to capture the pulse to pulse interaction at 2 different rail pressure levels. Figure 2.26, Figure 2.27, Figure 2.28, Figure 2.29, show the close pilot effect with single or double pilot injection results. As in the previous case, the accuracy in the prediction of the injection profile is more than satisfactory for both the rail pressure levels.

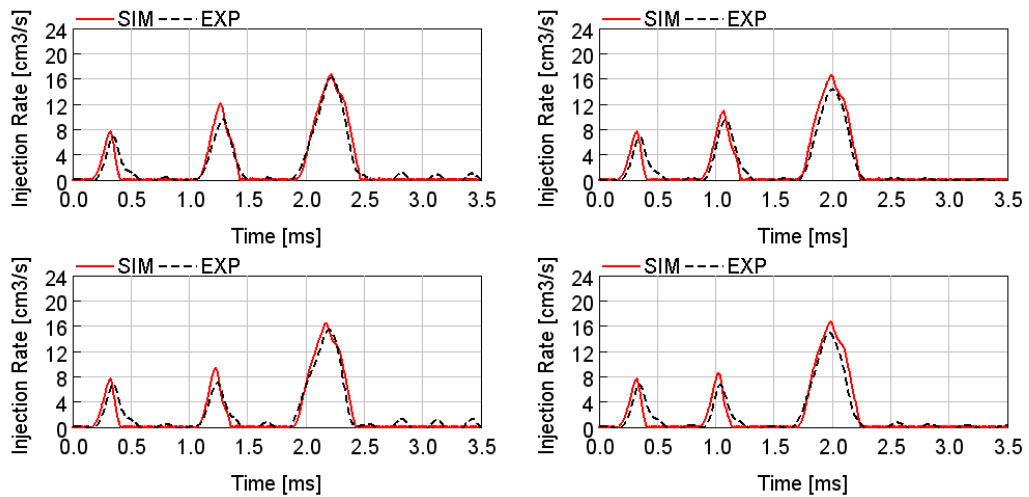


Figure 2.24 – Experimental (black dashed) and simulated (red solid) injection rates for standard double pilot strategy at rail pressure equal to 400 bar – Nozzle A [43]

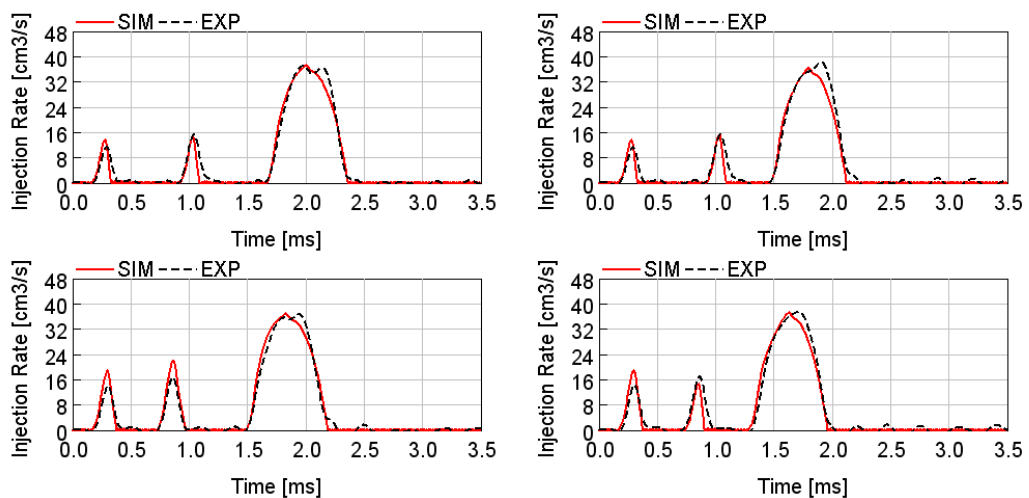


Figure 2.25 – Experimental (black dashed) and simulated (red solid) injection rates for standard double pilot strategy at rail pressure equal to 1000 bar – Nozzle A [43]

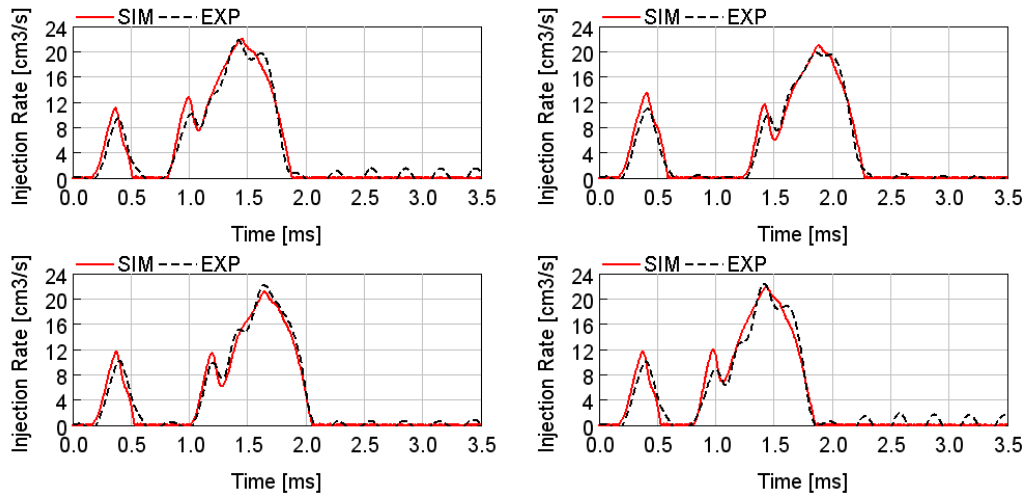


Figure 2.26 – Experimental (black dashed) and simulated (red solid) injection rates for single + close pilot strategy at rail pressure equal to 400 bar – Nozzle A [43]

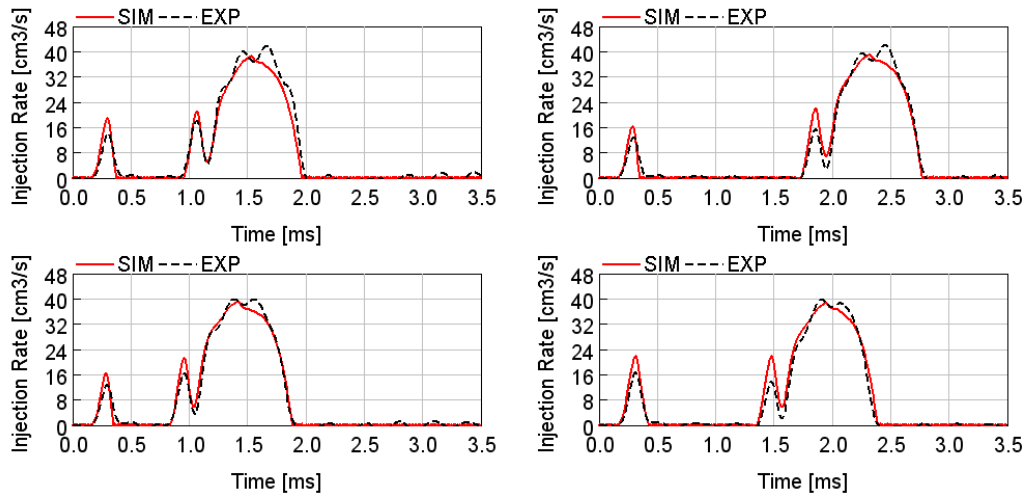


Figure 2.27 – Experimental (black dashed) and simulated (red solid) injection rates for single + close pilot strategy at rail pressure equal to 1000 bar – Nozzle A [43]

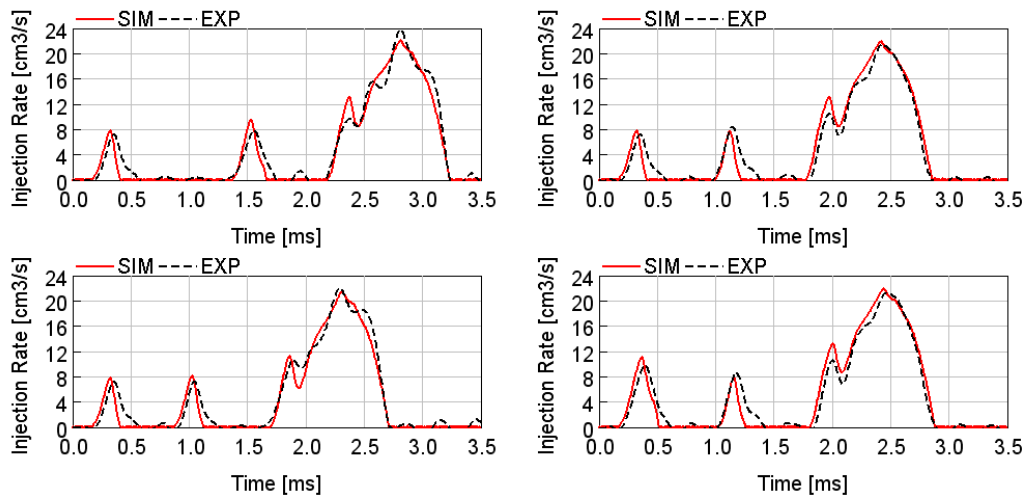


Figure 2.28 – Experimental (black dashed) and simulated (red solid) injection rates for double + close pilot strategy at rail pressure equal to 400 bar – Nozzle A [43]

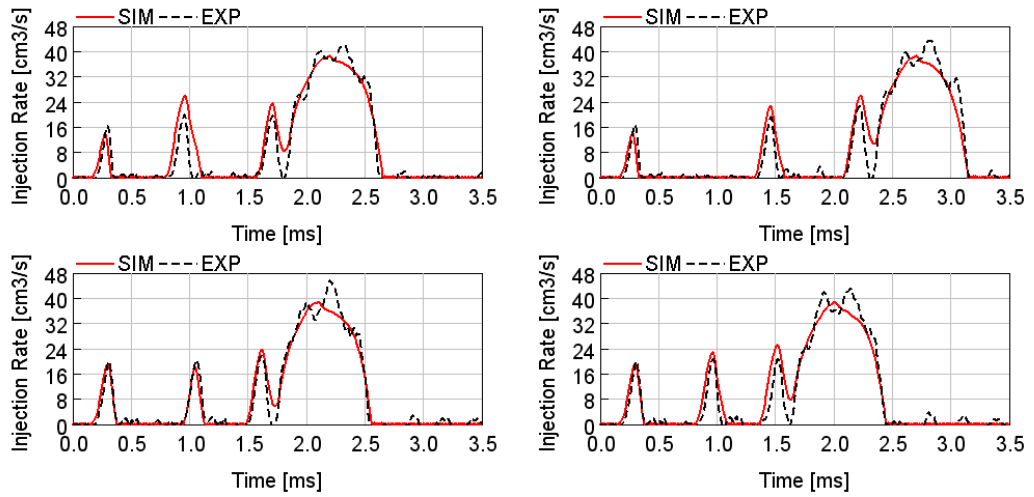


Figure 2.29 – Experimental (black dashed) and simulated (red solid) injection rates for double + close pilot strategy at rail pressure equal to 1000 bar – Nozzle A [43]

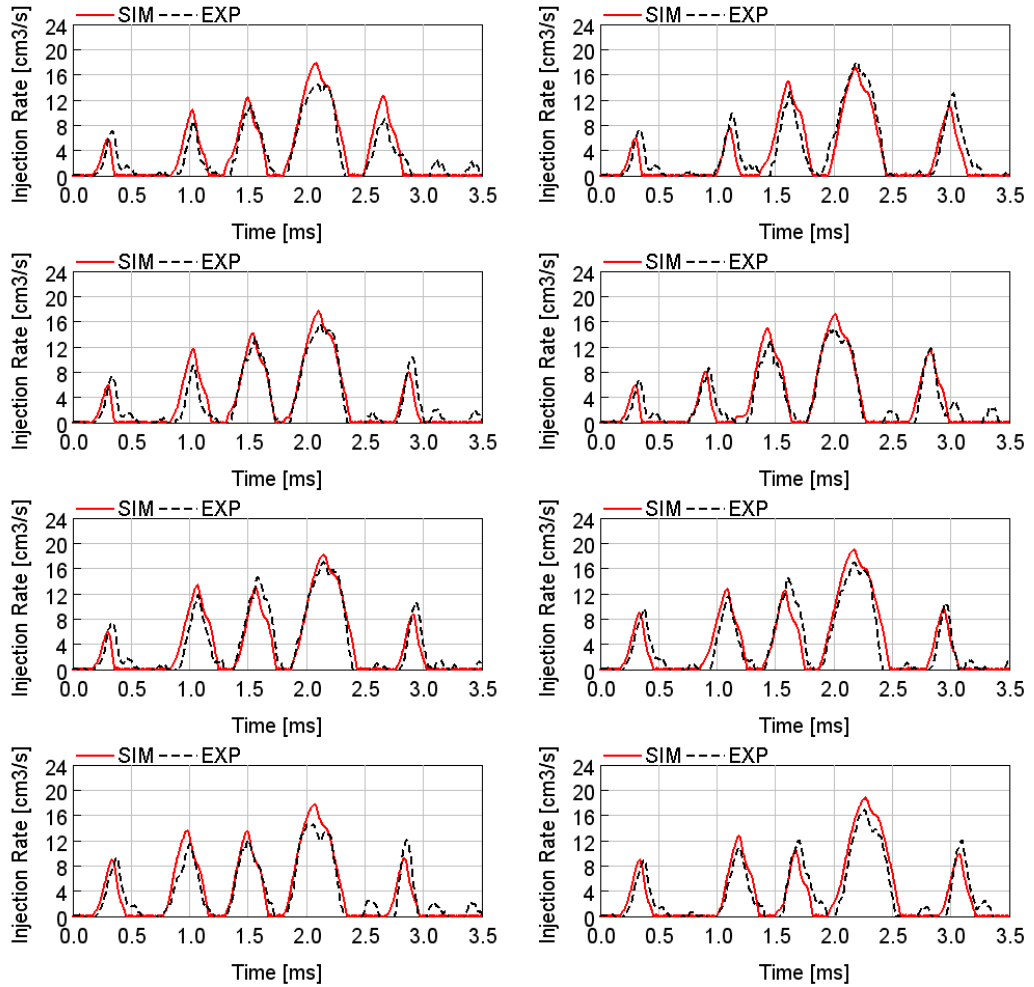


Figure 2.30 – Experimental (black dashed) and simulated (red solid) injection rates for triple pilot + main + after strategy at rail pressure equal to 400 bar – Nozzle A [43]

Also for the multi-pilot patterns (Figure 2.30) the comparison between the experimental and simulated volumetric injection rates shows a more the satisfactory accuracy of the model in predicting the actual behavior of the ballistic injector even

with injection strategies characterized by reduced DT values between consecutive events.

2.3 Coupling between engine and fuel injector models

GT-SUITE is able to directly integrate the detailed injector to the cylinder in a complete engine model. As known, compressible liquids typically require much smaller time steps than gases. Without special logic, the addition of a hydraulic circuit to the engine model would greatly reduce the time step in the gas circuit. As reported by Gamma Technologies, there are several options for injector and engine models integration [45,47].

- Circuits technology –A proper logic in GT-SUITE effectively splits the two circuits and allows each of them to take their own time steps. This means that the engine circuit can take its large time steps and then wait for the liquid circuit to synchronize. The end result is that the total simulation time for an integrated injector and engine should be roughly equal to the sum of both models run individually.
- Slave injectors – if cylinder to cylinder variation is not important, CPU time can be reduced copying the profile from 1 detailed injector and shifting it based on firing order for the other injectors.
- Skip cycle – since the injector circuit is computationally expensive, it is possible to run the injector model for 1 cycle, and use it for all remaining cycles for reaching convergence criteria.
- Partial cycles – the CPU time reduction is allowed by running only portion of cycle when injection appears, in order to capture the effect of the cylinder pressure on the injection rate as well.
- Injection Rate Map – as shown in Figure 2.31, Injection Rate Map is a map of injection profiles as a function of rail pressure and energizing time. Each point of the map contains only a single pulse. each pulse is looked up independently when multiple injections are simulated. In other words, this approach does not capture pulse to pulse interactions between consecutive injection events. The Injection Rate Map interpolates between profiles, making it a good option any time it is not possible to measure or simulate profiles for all operating points that will be simulated in the engine model.

In the following analysis, the Injection Rate Map was used for the injection rate definition since in the trade-off between accuracy and computational time, the focus was set on the CPU time reduction (it will be more clear in Chapter 3). As highlighted in Figure 2.32, this approach causes an increment of the total CPU time of about 10%. The previously developed injector model was used in order to define an Injection Rate Map.

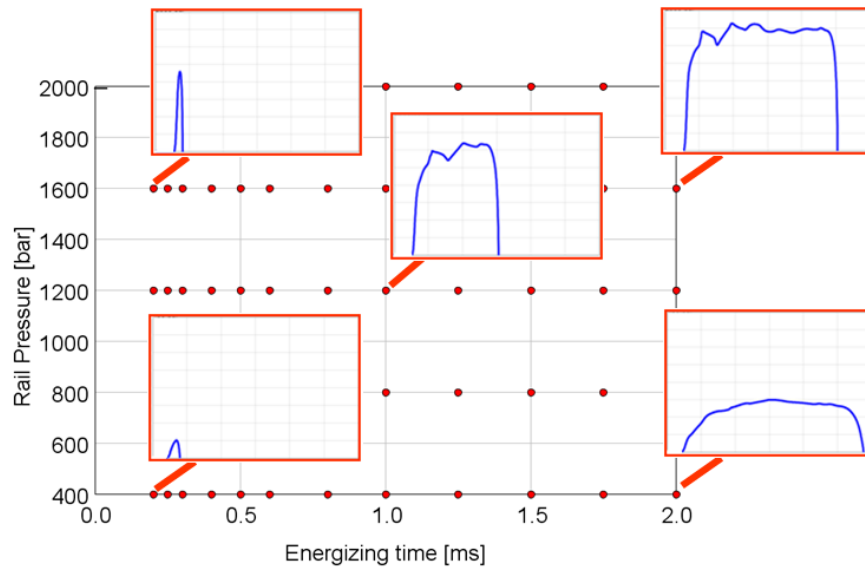


Figure 2.31 – Example of Injection Rate Map

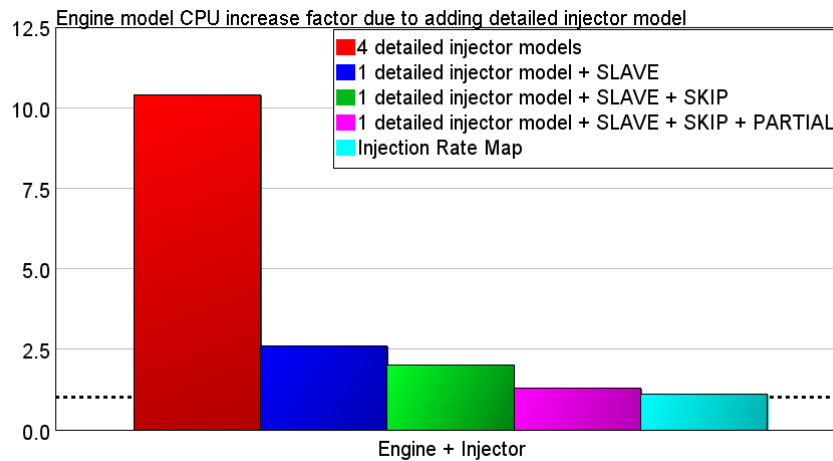


Figure 2.32 – Engine model CPU increase factor due to adding detailed injector model

2.3.1 DIPulse combustion model

In GT-SUITE there are multiple options available to model the combustion process. More specifically the different methodologies can be divided as follows [45]:

- non-predictive combustion model – the model imposes a burn rate as a function of crank angle. This prescribed burn rate will be followed regardless of the conditions in the cylinder, assuming that there is sufficient fuel available in the cylinder to support the burn rate. Therefore, the burn rate will not be affected by factors such as residual fraction or injection timing. This may be appropriate as long as the intended use of the model is to study a variable which has little effect on the burn rate. For example, a model built to study the influence of intake manifold runner length on volumetric efficiency or a model built to study the acoustic performance of different muffler designs would

not require any prediction of burn rate. In these cases, the variables of interest have a minimal effect on the burn rate. However, a non-predictive model may not be a good choice when the intended use of the model is to study a variable that has a direct and significant effect on the burn rate. In that case, a predictive or semi-predictive combustion model is a more appropriate choice so the burn rate will respond appropriately to a change in the variable of interest. For example, a model built to study the influence of injection timing and profile in a Diesel engine would require predictive capability to obtain any meaningful results, because the burn rate itself is a strong function of the injection quantities.

- predictive combustion model – in this case the combustion is an output of the engine model. Predictive combustion models attempt to model the important physics in the combustion process in order to predict the combustion burn rate. This implies that the model should automatically adjust to changing conditions (engine speed, EGR rate, etc.) with no change in model inputs. It requires calibration to measurement data in order to provide accurate results.
- semi-predictive combustion model – it is sensitive to the significant variables that influence combustion rate, and responds appropriately to changes in those variables, but does not use any physical models to predict that response. Instead, these models utilize a non-predictive (e.g. Wiebe) methodology where the combustion burn rate is imposed, with lookups or other methods to calculate the proper Wiebe parameters based on the significant input variables.

Regarding Diesel engine, Gamma Technologies developed the Direct-Injection Diesel Multi-Pulse Model, called DIPulse. It is able to predict the combustion rate and the associated emissions for direct-injection Diesel engine with single and multi-pulse injection events. The basic approach of this model is to track the fuel as it is injected, evaporates, mixes with surrounding gas, and burns. As such an accurate injection profile is absolutely required to achieve meaningful results; in addition, each contiguous injection event is defined as an injection pulse and is tracked separately from all other pulses. Any number of pulses may be injected, and there is no inherent distinction made between pilot, main, or post injection pulses.

The cylinder contents are discretized into three thermodynamic zones, each with their own temperature and composition. The main unburned zone contains all cylinder mass at IVC, the spray unburned zone contains injected fuel and entrained gas, and the spray burned zone contains combustion products. The DIPulse model also includes several submodels which simulate the relevant physical processes taking place during injection and combustion as reported in [45].

- **Entrainment**

As the spray penetrates, it slows down as the surrounding unburned and burned gases are entrained into the pulse. The intermixing of pulses

occurs through entrainment. The position and velocity of each packet are determined using an empirical correlation for spray tip penetration described in [48,49]. In which, the spray tip length S is described by the Equation 10:

$$S = \begin{cases} u_{inj}t \left[1 - \frac{1}{16} \left(\frac{t}{t_b} \right)^8 \right] & \frac{t}{t_b} \leq 1 \\ u_{inj}t_b \frac{15}{16} \left(\frac{t}{t_b} \right)^{0.5} & \frac{t}{t_b} \geq 1 \end{cases} \quad \text{Eq. 10}$$

Where, the breakup time t_b is defined by the Equation 11, and the velocity at injector nozzle by equation 12.

$$t_b = 4.351 \sqrt{\frac{2\rho_l}{\rho_g} \frac{d_n}{C_d u_{inj}}} \quad \text{Eq. 11}$$

$$u_{inj} = C_d \sqrt{\frac{2\Delta P}{\rho_l}} = \frac{\dot{m}_{inj}}{A_n \rho_l} \quad \text{Eq. 12}$$

- t = time
- \dot{m}_{inj} = injection mass flow rate
- A_n = injector nozzle area
- d_n = injector nozzle diameter
- C_d = injector nozzle discharge coefficient
- ρ_l = liquid fuel density
- ρ_g = gaseous fuel density
- ΔP = pressure drop across injector nozzle

The entrainment rate is determined by applying conservation of momentum and can be modified by the Entrainment Rate Multiplier C_{ent} , defined in Equation 13 as a function of u that is the velocity at spray tip (Equation 14).

$$\frac{dm}{dt} = -C_{ent} \frac{m_{inj} u_{inj}}{u^2} \frac{du}{dt} \quad \text{Eq. 13}$$

$$u = \frac{dS}{dt} \quad \text{Eq. 14}$$

- **Evaporation**

Droplet evaporation is modeled with a coupled solution of heat and mass transfer which appropriately accounts for both diffusion-limited and boiling-limited evaporation [50,51].

- **Ignition**

The mixture in each pulse undergoes an ignition delay modeled with an Arrhenius expression which can be modified by the Ignition Delay Multiplier C_{ign} . The ignition delay (Equation 15) is calculated separately for each pulse based on the conditions within the pulse, and accounts for entrainment and evaporation within the pulse as well as pulse-to-pulse interactions.

$$\tau_{ign} = C_{ign}\rho^{-2}e^{\left(\frac{3000}{T}\right)}[O_2]^{-0.5} \quad \text{Eq. 15}$$

$[O_2]$ = oxygen concentration
 T = pulse temperature
 ρ = pulse gas density

- **Premixed combustion**

When a pulse ignites, the mixture present at that time is set aside for premixed combustion. The rate of this combustion is assumed to be kinetically-limited and can be modified by the Premixed Combustion Rate Multiplier C_{pm} , as defined in Equation 16.

$$\frac{dm_{pm}}{dt} = C_{pm}m_{pm}k(t - t_{ign})^2 f([O_2]) \quad \text{Eq. 16}$$

t_{ign} = time at ignition
 m_{pm} = premixed mass
 k = Turbulent kinetic energy

- **Diffusion combustion**

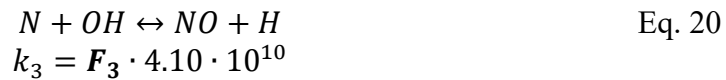
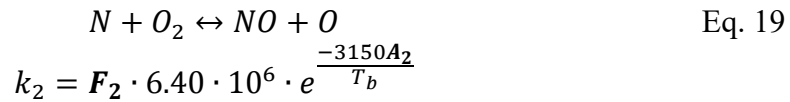
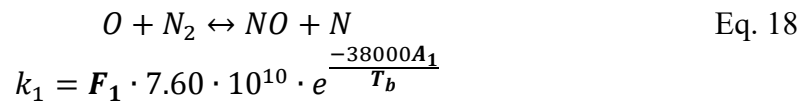
After a pulse ignites, the remaining unmixed fuel and entrained gas in the pulse continue to mix and burn in a primarily diffusion-limited phase. The rate of this combustion can be modified by the Diffusion Combustion Rate Multiplier C_{df} as shown in Equation 17. Diffusion combustion rate is reduced at high loads (long injection duration) due to spray-wall and spray-spray interactions.

$$\frac{dm}{dt} = C_{df}m \frac{\sqrt{k}}{\sqrt[8]{V_{cyl}}} f([O_2]) \quad \text{Eq. 17}$$

V_{cyl} = cylinder volume

Realistically, predictive combustion models include assumptions and simplifications, and therefore will require some calibration of the physical constants to best match the specific combustion system. The goal of a predictive combustion model calibration process is to find the single set of model constants that will provide the best possible match to a wide variety of operating points.

DIPulse model is also able to predict the NOx and soot emissions thanks to proper submodels. The formation of NOx during combustion is predicted based on the extended Zeldovich mechanism [25] which includes the N2 oxidation, N oxidation and OH reduction reactions described by Equations 18, 19 and 20, respectively.



The NOx emission model uses 6 calibration multipliers: the NOx Calibration Multiplier multiplies the NOx concentration output of the model, while the other 5 are the Arrhenius constants of the abovementioned equations.

- F_1 = N₂ oxidation rate multiplier
- F_2 = N oxidation rate multiplier
- F_3 = OH reduction rate multiplier
- A_1 = N₂ oxidation activation temperature multiplier
- A_2 = N oxidation activation temperature multiplier
- T_b = burned sub-zone temperature

As far as soot concentration prediction is concerned, the Modified Hiroyasu model [52,53] was applied. “Soot Formation Multiplier” and “Soot Burnup Multiplier” give the opportunity to control the soot evolution and oxidation, respectively.

The experimental data used for this activity includes a set of operating points covering the entire engine map (337 engine points), a set of EGR, rail pressure, start of injection and boost pressure sweeps measured in 7 operating points representative of a typical driving cycle. The total operating points available for the activity are shown in Figure 2.33. Among more than 500 points, only 28 operating conditions were selected for the calibration process, 13 of which at full load and 15 at part load operating conditions.

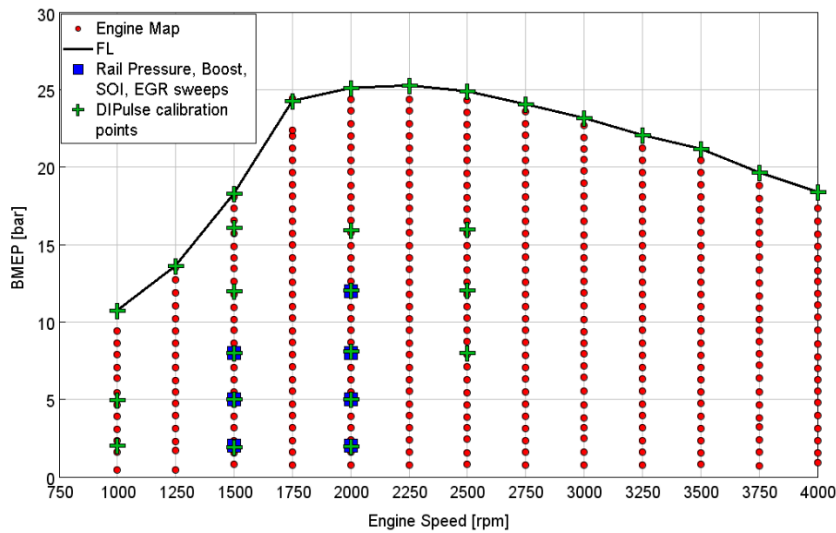


Figure 2.33 – Test matrix

2.3.2 Combustion and emission results

After a proper calibration process, in which the 4 constants of DIPulse model highlighted in Equation 13, 15, 16 and 17 were defined, a good agreement was obtained in replicating the combustion process. More specifically, as it can be seen from Figure 2.34, a satisfactory agreement between the predicted (red line) and experimental (black line) in-cylinder pressure and burn rate can be observed: the pilot injections and main injection pulses are well captured by the DIPulse combustion model.

The good agreement is also confirmed in Figure 2.35, where the comparison between experimental and predicted combustion parameters, as IMEP, peak pressure, crank angle at peak pressure and MFB50 for the Engine map point, is shown. As it can be seen, the model predicts the IMEP with an error lower than 5%; as well as the MFB50 predicted by the DIPulse shows a more than satisfactory agreement with the experimental data, with an error smaller than 5 CA deg for most of the engine points. Regarding the crank angle of peak pressure, few points show a not satisfactory agreement, since the predicted value is much lower respect to the experimental one: this is due to the fact that the retarded SOI calibration for NOx reduction leads to a double peak in the in-cylinder pressure trace. In these cases, as shown in Figure 2.36, the pressure level at the end of compression stroke has a similar value with respect to the maximum pressure reached during combustion. So, a slight difference in pressure trace (as highlighted in Figure 2.36) causes an high error in the detection of the crank angle at maximum pressure.

Also the emissions level can be well predicted by the DIPulse. Figure 2.37 – left shows a more than satisfactory accuracy in the prediction of the NOx concentration. Same accuracy were not obtained for SOOT emission prediction, requiring a more detailed 3D-CFD approach for the quantification of SOOT emission.

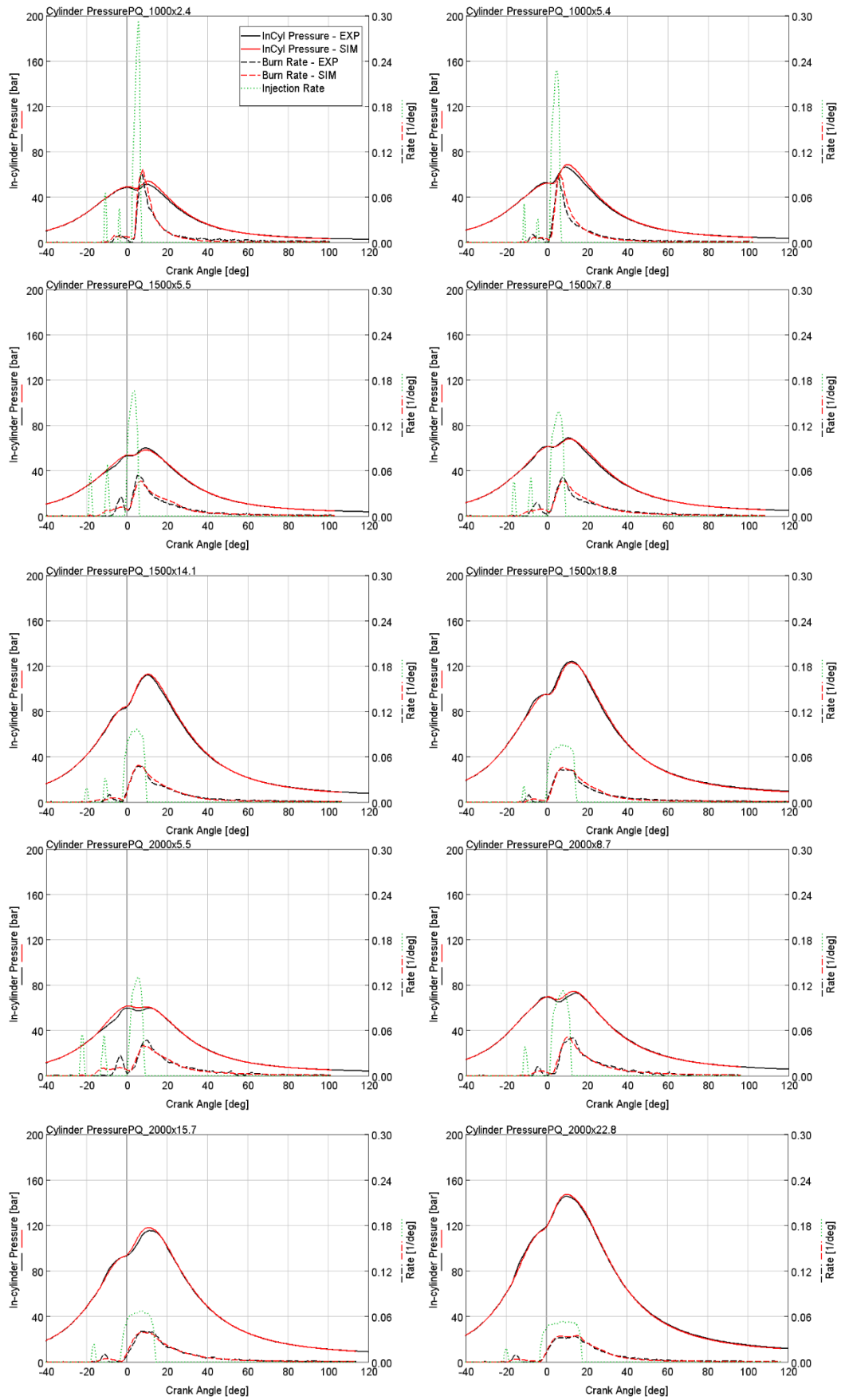


Figure 2.34 – DIPulse combustion model results – Experimental (black) and predicted (red) in-cylinder (solid) and burn rate (dashed) comparisons, injection mass flow rate (green dashed)

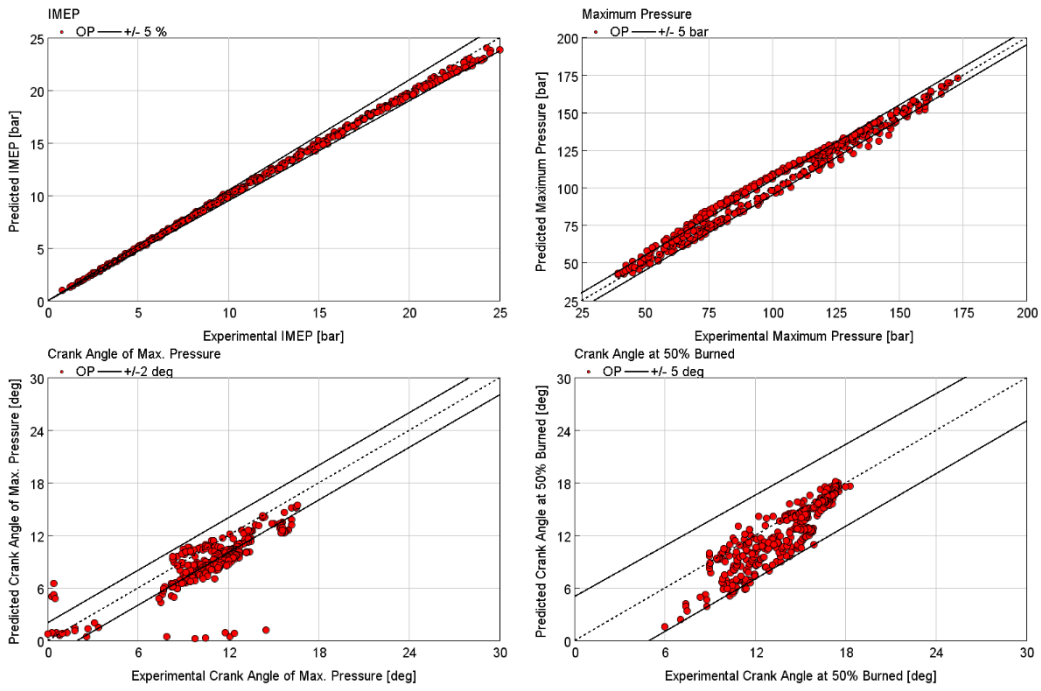


Figure 2.35 – DIPulse combustion model results - Combustion parameters: IMEP (top-left), in-cylinder maximum pressure (top-right), crank angle of maximum pressure (bottom-left), crank angle at 50% fuel burned (bottom-right)

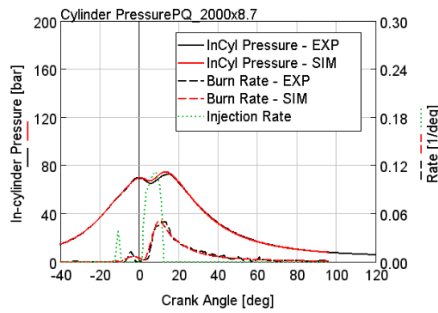


Figure 2.36 – DIPulse combustion model results – Experimental (black) and predicted (red) in-cylinder (solid) and burn rate (dashed) comparisons, injection mass flow rate (green dashed) – 2000 RPM X 8.7 bar BMEP

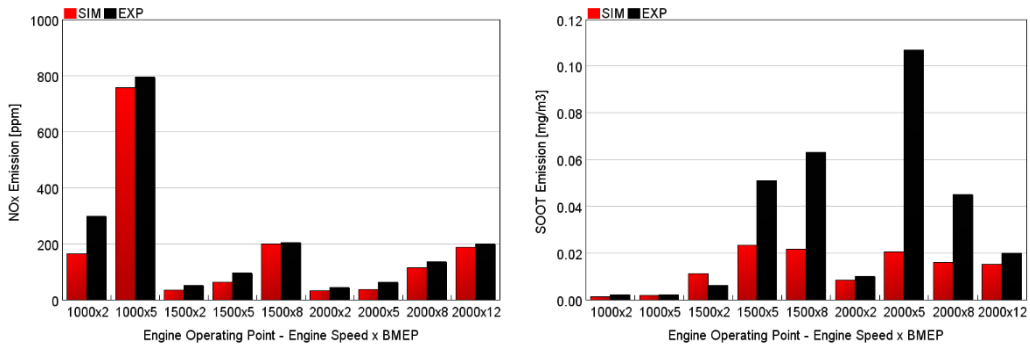


Figure 2.37 – DIPulse combustion model results – Simulated (red) and experimental (black) emissions comparison: NOx (left) and SOOT emission (right)

2.3.3 Complete engine model results

After calibrating the DIPulse combustion model through the CPOA, the model was implemented in the full engine model, replacing the previously used non-predictive combustion model, which employs experimentally measured burn rates. In the following figures (Performance in Figure 2.38, Flow in Figure 2.39, Pressure in Figure 2.40, Temperature in Figure 2.41) the comparison between the experimental data and the simulation results are reported for the full engine model. It should be noticed that the comparison was extended to more than 300 engine operating points, over the entire engine operating map.

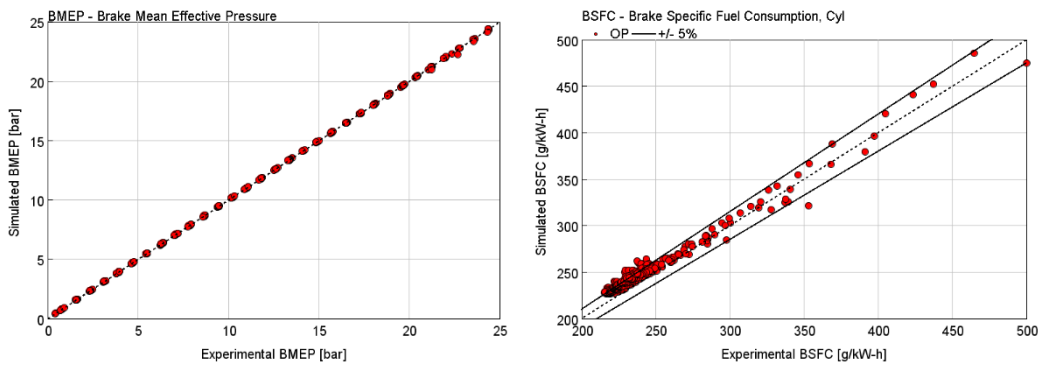


Figure 2.38 – Experimental and simulated BMEP (left) and BSFC (right) comparison for the entire engine map

- **BMEP** (Figure 2.38 – left) – Since a controller was put in place to meet the BMEP target controlling the injected quantity by adjusting the duration of the main injection, the simulated BMEP always matches the measured value.
- **BSFC** (Figure 2.38 – right) – The model predicts with good accuracy the fuel consumption showing an average error lower than 4%. Significant errors are present at low load engine operating conditions (below 1 bar BMEP) which are characterized by experimental high dispersion. For these conditions, a very small error in FMEP gives high error in BSFC.

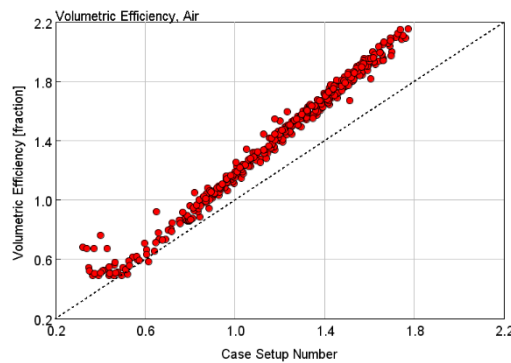


Figure 2.39 – Experimental and simulated volumetric efficiency comparison for the entire engine map

- **Volumetric efficiency** (Figure 2.39) – Significant discrepancies between the simulated and the experimental results can be noticed. However, since pressure and temperature levels in the intake manifold are predicted with good accuracy, as it will be shown in the following section, the experimental mass flow rates do not appear to be always consistent with the other measurements.
- **EGR fraction** – since the EGR target map was not provided, the setpoints for the whole engine map had to be extrapolated from a limited dataset coming from other measurements.

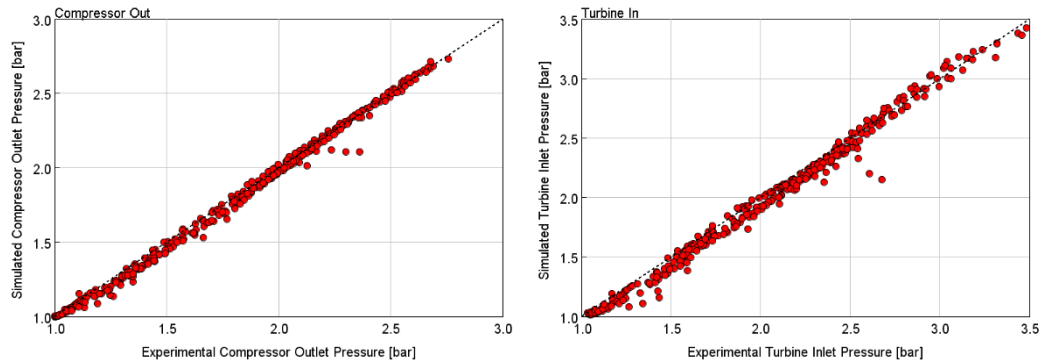


Figure 2.40 – Experimental and simulated compressor outlet (left) and turbine inlet (right) pressure comparison for the entire engine map

- **Compressor Outlet Pressure** (Figure 2.40 – left) – In the simulation model the compressor outlet pressure is controlled by the acting on the VGT controller: therefore the simulated Compressor Outlet pressure should always match the corresponding experimental value.
- **Turbine Inlet Pressure** (Figure 2.40 – right) – The model predicts the turbine inlet pressure with very good accuracy.

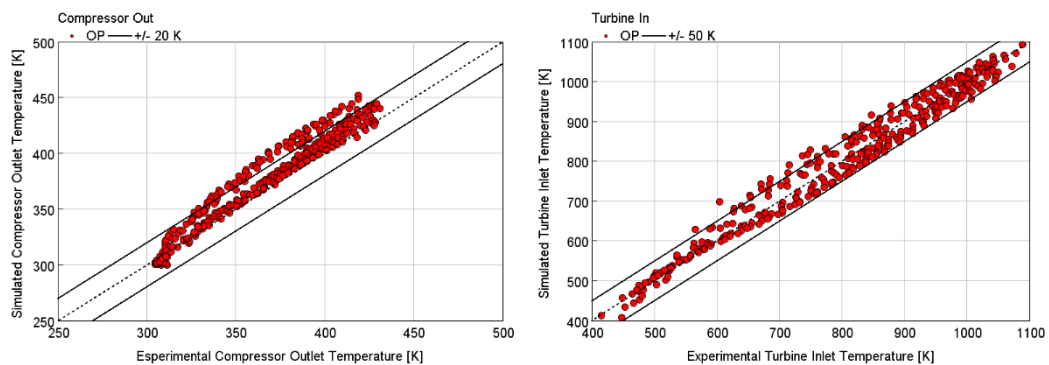


Figure 2.41 – Experimental and simulated compressor outlet (left) and turbine inlet (right) temperature comparison for the entire engine map

- **Compressor Outlet Temperature** (Figure 2.41 – left) – The compressor outlet temperature predictions probably suffer from some turbocharger map inaccuracies and is not well matched for all the operating points. However this should not affect the in-cylinder

calculations since the temperature downstream of the intercooler is imposed to be equal to the experimental value.

- **Turbine Inlet Temperature** (Figure 2.41 – right) – Turbine inlet temperature is very well matched despite it is normally a very critical parameter to meet with a 1D-CFD code due to the complex heat loss process in the exhaust port, exhaust manifold and turbine volute.

A more detailed analysis of the DIPulse results can be found in Appendix A1 and A2. Appendix A1 is focused on the effects of the DIPulse calibration parameters on the combustion results: the analysis was carried out considering a variations of $\pm 10\%$ and $\pm 30\%$ (with respect to the optimized values) of each parameters while keeping all the other parameters constant. Appendix A2 reports the DIPulse results considering a sensitivity analysis on engine control parameters (as EGR rate, SOI, or boost pressure) as highlighted in Figure 2.33.

After the calibration and the validation of the detailed engine model in steady state conditions, it was reduced to a Fast Running Model (FRM) in order to be used for transient analysis, as the simulation of typical type approval driving cycles. The developed FRM model operates with a computational time 3 times slower with respect to real time and consists of:

- ECU controls in order to change engine calibration during the transient simulation, for example as a function of cooling water temperature or valve actuations.
- Thermal masses of pistons, liners, cylinder head and turbine for taking into account the thermal inertia in cold start conditions.
- Estimated friction losses based on Chen Flynn model as a function of cooling water temperature, as shown in Figure 2.42.

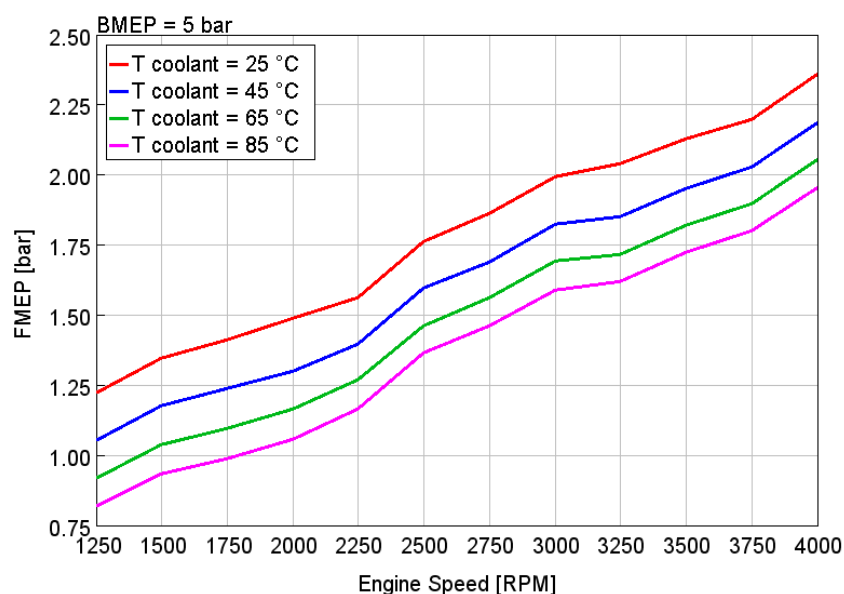


Figure 2.42 – FMEP trend at different coolant temperature – 5 bar BMEP engine load

The comparison between the experimental and simulated normalized fuel consumption along the WLTC is shown in Figure 2.43. The FRM 1D model underestimates the total fuel consumption of about 4%. This difference is mainly due to the difference in the first part of the driving cycle and the estimated Chen Flynn model at low coolant temperature may introduce errors in the prediction of real behavior. Nevertheless, the accuracy of the 1D model remains satisfactory, and the results of the simulated WLTC was taken as reference for the next analysis.

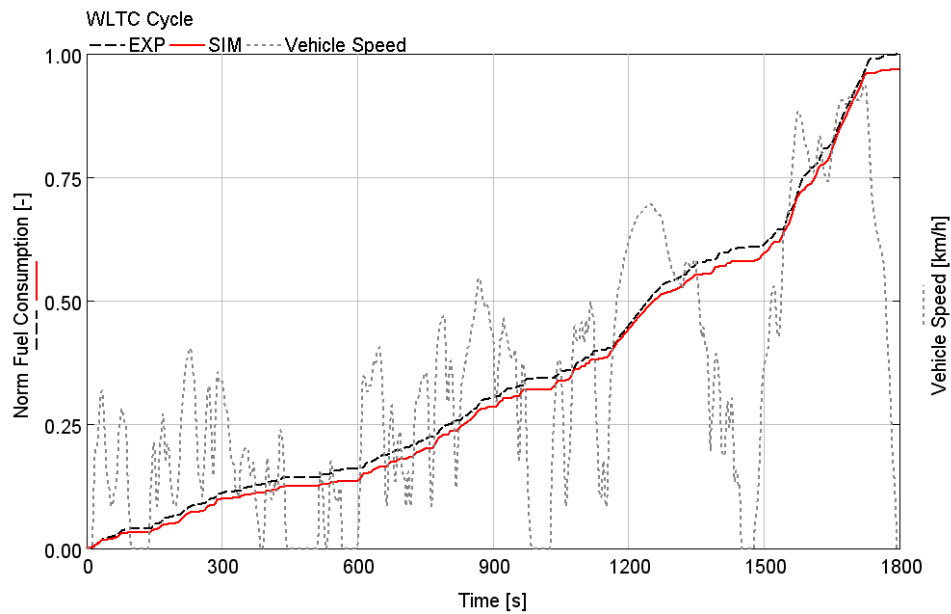


Figure 2.43 – Comparison between experimental (black dashed) and simulated (red solid) normalized fuel consumption over WLTC

As already stated, the accuracy with which the 1D engine model coupled with the injector model predicts the actual behavior of the system is more than satisfactory. In other words, a kind of virtual test rig was built in GT-SUITE, thanks to which the air management and fuel injection systems optimization, presented in the next chapters, was performed.

Chapter 3

I part: Air management system analysis

Part of the work described in this Chapter was also previously published in the following publications.

- Piano, A., Millo, F., Di Nunno, D., and Gallone, A., " Numerical Assessment of the CO₂ Reduction Potential of Variable Valve Actuation on a Light Duty Diesel Engine," SAE Technical Paper 2018-37-0006, 2018, <https://doi.org/10.4271/2018-37-0006>.
- Piano, A., Millo, F., Di Nunno, D., and Gallone, A., "Numerical Analysis on the Potential of Different Variable Valve Actuation Strategies on a Light Duty Diesel Engine for Improving Exhaust System Warm Up," SAE Technical Paper 2017-24-0024, 2017, <https://doi.org/10.4271/2017-24-0024>.

As already stated in the Introduction, the future generation of Diesel engines must achieve 2 different goals: on one hand, there is the increasing need of efficiency improvements; on the other hand, the more stringent emissions regulations push the car manufacturer to produce low emissions vehicles. In this very complex context, an advanced and fully flexible air management system is becoming highly desirable for modern Diesel engines since it can help the engine development with the aims of reduce CO₂ emission and improve the exhaust aftertreatment efficiency.

Differently from gasoline engines, where Variable Valve Actuation (VVA) is a well-established technique largely adopted in series production, variable air management systems in Diesel engines have not achieved considerable market penetration. However, their benefits are summarized as follows.

- Low-speed torque improvement retarding Exhaust Valve Opening (EVO) timing as suggested by Tai et al. [54]. Retarded EVO after

Bottom Dead Center (BDC) results in an increase in turbine power (higher pressure pulses) and, consequently, in an air-to-fuel ratio increment, although with a significant Brake Specific Fuel Consumption (BSFC) penalty in steady state condition because of higher pumping losses and residuals within the cylinder. However, the BSFC penalty due to this technique can be negligible in the overall driving-cycle fuel consumption, due to the very short time spent at full load at very low engine speed. Same effect can be achieved by advancing EVO [55].

- Fuel consumption reduction. Engine efficiency improvement can be achieved by optimizing EVO timing at each engine speed, or enabling Miller cycle obtaining higher thermodynamic efficiency with a very high geometric compression ratio. [25,56–59]
- Emission reduction. Theoretically, adjusting IVC with a flexible valve actuation leads to an air–fuel ratio increase and a consequent soot reduction. Another effect is related to the reduced effective compression ratio by early or late IVC to obtain lower compression pressure, combustion temperature, and NO_x. [60–63] Negative valve overlap, intake valve pre-opening during the intake stroke, or exhaust valve post-opening during the intake stroke, could enable internal EGR, as effective way for reducing engine-out emissions. [62,64]
- Turbulence modulation within the cylinder. Gas motion level can be adjusted by using unequal intake valve lifts thus enhancing the swirl motion in order to reduce soot formation at low speed). [56] Thanks to the adoption of VVA, the redundant air control valve (intake and exhaust throttle) could be eliminated, simplifying the overall engine system. [56]
- Advanced combustion modes enabling, such as Homogeneous Charge Compression Ignition (HCCI). VVA can provide variable effective compression ratio, charge composition and temperature control required for such advanced combustion modes. [65–67]
- Aftertreatment system performance improvement. An additional opening of the exhaust valve during the intake stroke, or an early EVO could provide higher exhaust temperature that can speed-up the warm up of the aftertreatment system since to the higher in-cylinder residuals [68–70].

3.1 CO₂ reduction potential

Among the abovementioned benefits, in this paragraph the impact of VVA on engine efficiency improvements was analyzed. Even if the traditional belief was that the Diesel engine may benefit less from VVA in engine breathing performance compared with the gasoline engine due to the un-throttled operation and to a much lower rated speed that results in a not so severe valve timing trade-off, it should be noted that the expectation on the percentage fuel economy improvement should be

different for gasoline and Diesel engines because the Diesel engine is largely used in heavy-duty applications where even a small percentage of fuel economy gain is valuable for a large fleet. [56]

Some investigations focused on fuel consumption reduction can be found in literature and are reported as follows. [71–76]

More in detail, in 1996, Stebler et al. performed a numerical and experimental investigation on the application of Miller cycle in order to reduce the engine-out NO_x for a 9-cylinder turbocharged Diesel engine for stationary use. While power output and fuel consumption were slightly improved, NO_x emissions could be reduced up to 20% thanks to the adoption of an early intake valve closure. [77]

Schutting et al., in [78], analyzed the shift of the Intake Valve Closure (IVC), applied to a turbocharged Diesel engine with the aim of achieving a NO_x reduction. The authors concluded that Miller or Atkinson cycles are appropriate techniques for NO_x reduction, without disadvantages in particles, HC, CO and fuel consumption. The potential is almost exclusively limited by the capabilities of the charging system. However, compared to external exhaust gas recirculation, no advantages could be found leading the authors to state that the application of Miller- or Atkinson-cycle to a Diesel engine does not make sense at the moment, if an Exhaust Gas Recirculation (EGR) system is applied.

Rinaldini et al. in [79] explored the potential of Miller cycle applied to an 2.8 L 4-cylinder turbocharged Diesel engine. More specifically, the authors found that a reduction NO_x emissions from 20% to 30% can be achieved for five different engine operating conditions in the low-load and low-speed zone, with an average fuel consumption worsening of about 2%.

EGR coupled with Miller cycle for a Heavy-Duty (HD) Diesel engine was experimentally analyzed by Guan et al. in [80]. the results demonstrated that the combination of the EGR and Miller cycle can lead to minimum impact on the smoke emission and fuel economy (thanks to a higher fuel injection pressure) while achieving lower engine-out NO_x emissions (about 70%).

In the next sub-paragraphs a simulation study is presented evaluating the impact of both Intake and Exhaust VVA on the fuel consumption of the selected engine. Numerical simulations were carried out by means of the 1D-CFD engine model described in Chapter 1. In this analysis, the following three different techniques were scrutinized in order to assess their potential in terms of efficiency improvements:

- Late Intake Valve Closure (LIVC) – The retarded closure of the intake valve could enable Miller cycle, in which the effective compression ratio is smaller than the effective expansion ratio.
- Late Exhaust Valve Opening (LEVO) – Retarding EVO timing could result in a higher expansion work collected by the piston than the standard timing.
- Exhaust Valve Phasing (VVT) – The exhaust valve timing can be adjusted to maximize the expansion work at each engine speed.

3.1.1 K-points selection

The simulation study was divided in 2 steps: first of all, a steady state analysis was performed on 6 selected engine operating conditions, representative of a typical type approval driving cycle; then, the best VVA strategies were evaluated under transient conditions over the WLTC cycle. Regarding the selection of the steady state conditions, a fuel consumption evaluation of the single operating point over the WLTC was carried out. In Figure 3.1, the 6 selected key-points are highlighted in red circle, in which the percentage weight on total fuel consumption is shown.

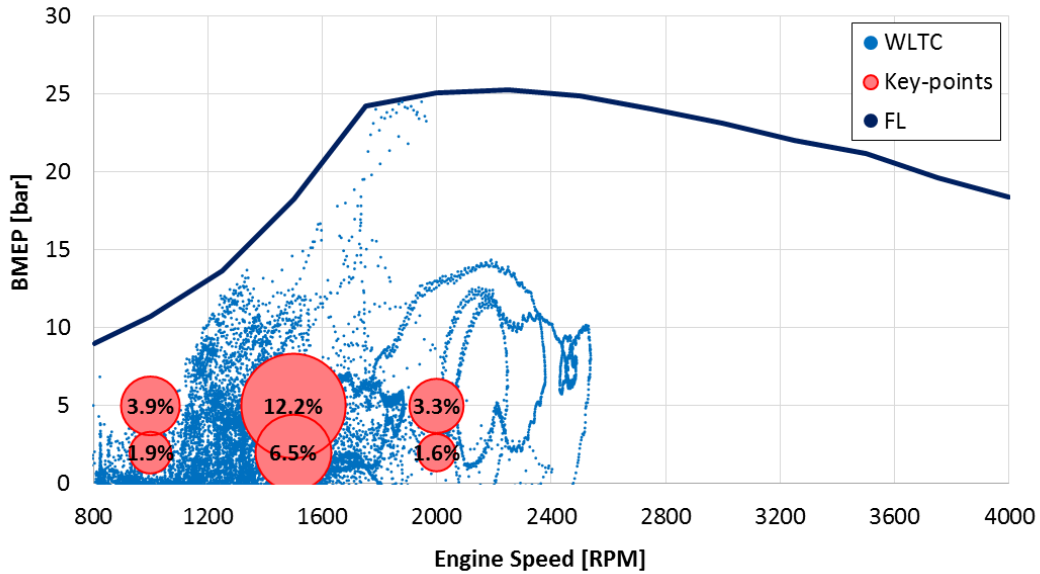


Figure 3.1 – Engine operating conditions over the WLTC driving cycle (blue) and selected key-points (red) on the engine map

For the sake of clarity, the selected key-points are also listed in Table 3.1. As it can be seen, the points are related to the Low Speed – Low Load engine operating conditions. The selected vehicle for the transient simulation is an European C-Segment, the characteristics of which are highlighted in Table 3.2.

Table 3.1 – Selected key-points for steady state analysis – CO₂ reduction [81]

Engine Speed [RPM]	BMEP [bar]
1000	2.0, 5.0
1500	2.0, 5.0
2000	2.0, 5.0

Table 3.2 – Characteristics of the selected vehicle for transient analysis [81]

Euro car segment	C-Segment
Kerb mass	1280 kg
Traction Power @ 100 km/h	13.1 kW

3.1.2 Simulation setup

The previously developed 1D-CFD engine model, featuring DIPulse predictive combustion model and an integrated fuel injector model, was used in order to evaluate the VVA potential in terms of CO₂ reduction. Since the adoption of non-conventional valve lift profiles may require significant adjustments in terms of boost pressure and EGR levels, different VGT positions and EGR valve openings were explored for each engine key-point in combination with different exhaust and intake valve lifts. Moreover, since the different tested VVA lifts can also imply significant variations in terms of effective compression and expansion ratios, two different geometrical compression ratios (CR 15.5 and CR 17.5) were considered. To this aim, a full factorial Design of Experiments (DoE) was performed, by varying the turbine rack position and the opening of the EGR valve (both of them from totally closed to totally opened). For each combination of the design and calibration parameters of the DoE, the MFB50 was maintained equal to the baseline value by adjusting the injection timing while keeping unchanged all the other parameters of the injection pattern (number of injection pulses, Energizing Time, Dwell Time and rail pressure), as the ECU control works. The full factorial DoE, shown in Figure 3.2, was repeated for each combination of VVA lift and engine key point resulting in more than 1500 different combinations for each VVA strategy. Then, the DoE results were post-processed in order to identify the combination between boost pressure and EGR rate which could minimize the fuel consumption without exceeding the NO_x emissions of the baseline settings for each valve lift profile and each engine compression ratio. An example of the response surfaces of the DoE for Brake Specific NO_x (BSNO_x) and BSFC are shown in Figure 3.3 (top and bottom respectively), where the Rack Position represents the VGT opening that varies from 0 (totally closed) to 1 (totally open). The dashed areas represent the region in which the baseline NO_x levels are exceeded and which cannot be therefore considered as suitable solutions. The optimal combination of the DoE parameters corresponds therefore to the minimum BSFC level achieved outside from the dashed areas where the baseline NO_x emissions level are exceeded.

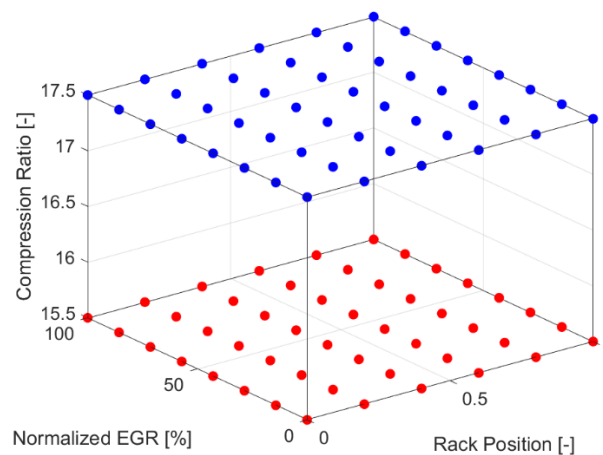


Figure 3.2 – Full factorial DoE grid for VVA analysis

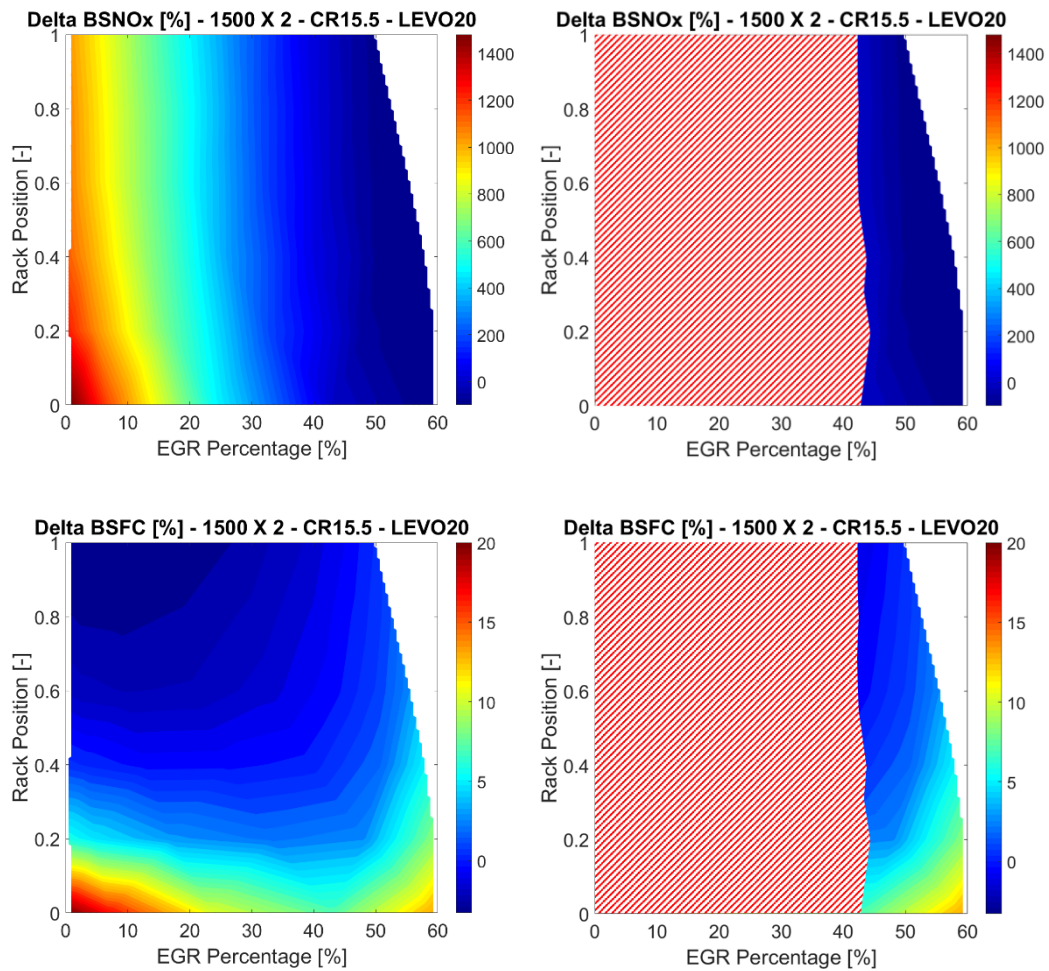


Figure 3.3 – Example of response surface for delta BSNOx (a), and delta BSFC (b) obtained from full factorial DoE of EGR and VGT parameters settings for a given exhaust valve lift profile and geometrical compression ratio: the dashed area represents the region in which the baseline NOx emission levels are exceeded and which cannot therefore be considered as suitable solutions. – 1500 RPM X 2 bar BMEP [81]

3.1.3 Late Intake Valve Closure

LIVC was chosen to enable Miller cycle with the aim of fuel consumption reduction. Thanks to the “Millerization” of the working cycle, significant theoretical results can be achieved as explained as follows.

- Lowered effective compression ratio, without reducing the expansion ratio, to enable the so-called over-expanded cycle and improve the thermodynamic efficiency [25].
- As a consequence of the previous bullet, a temperature reductions at the end of compression stroke can be achieved, resulting in NOx emissions reduction. Or, as alternative, the lower temperature at TDC allows a SOI advancing with benefit in terms of BSFC, keeping constant the NOx level. It is worth to say that Miller cycle could reduce NOx due to lower

compression temperature, but SOOT emissions may significantly increase because of the lowered air-to-fuel ratio.

- The peak cylinder pressure could be reducing by lowering the effective compression ratio, leading to a mechanical friction losses reduction.

In the ideal case study, Miller cycle could be enabled with LIVC or EIVC, without any substantial difference. This does not happen in the real cycle in which for each actuation different behavior can be highlighted. From the point of view of the intake valve throttling, in EIVC the intake valves must start to close when the delta between the cylinder pressure and the charge pressure is significant. However, LIVC consists of a backflow of charge from the cylinder into the intake manifold that inherently involves throttling losses [82]. By the way, in both actuations a reduction of pumping losses with respect to the conventional valve lift can be seen [83]. As far as heat transfer is concerned, LIVC results in in-cylinder charge pushed back into the intake manifold. This air was previously heated in the cylinder and, after be pushed back, it is stored in the intake port until the next cycle resulting in a higher in-cylinder temperatures during the intake stroke (reduction in gas density) and in the first degrees of compression stroke [56]. However other issue concerns with EIVC: on one hand the reduction of in-cylinder air motion and turbulent mixing [84]; on the other hand the required shorter valve event could be an issue in mechanical cam design due to the constraints of valvetrain dynamics [56].

For these reasons, LIVC was chosen for enabling Miller Cycle. Figure 3.4 shows three different valve lifts analyzed in this study with intake valve closure at 20, 40, 60 crank angle degrees later than the baseline.

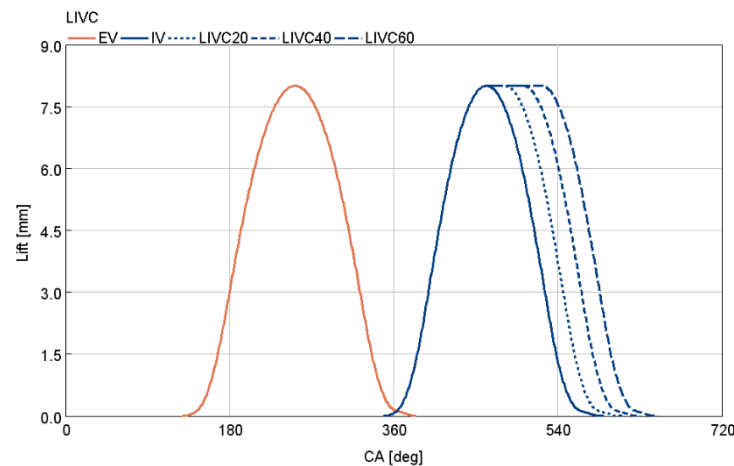


Figure 3.4 – LIVC lift profiles tested [81]

Steady-state analysis

Figure 3.5, Figure 3.6, Figure 3.7 show the results of the steady-state analysis in the engine key-points listed in Table 3, in terms of delta BSFC, as a function of LIVC angle. As Figure 3.5, Figure 3.6, Figure 3.7 highlight, LIVC allows efficiency improvements only at lower load and the larger the lift profile, the higher the BSFC benefit. However, the trend becomes opposite at higher load.

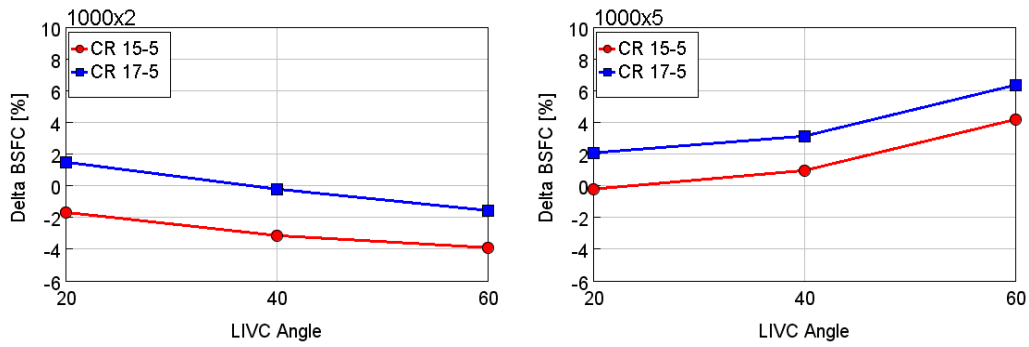


Figure 3.5 – Delta BSFC at different LIVC actuations for 2 bar (left) and 5 bar (right) engine load – 1000 RPM [81]

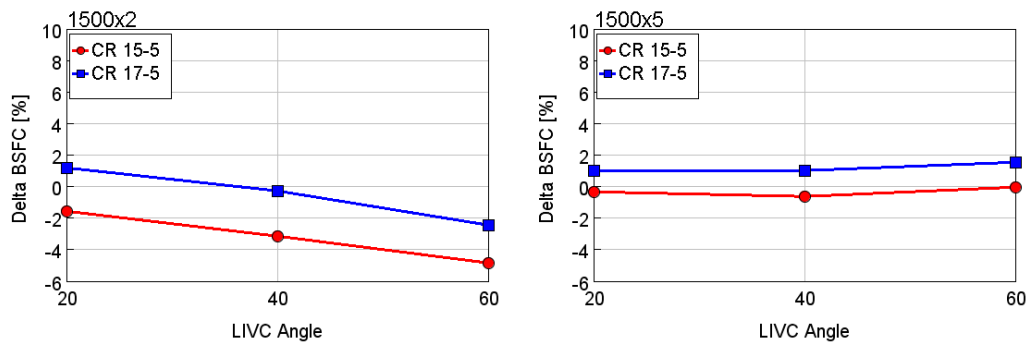


Figure 3.6 – Delta BSFC at different LIVC actuations for 2 bar (left) and 5 bar (right) engine load – 1500 RPM [81]

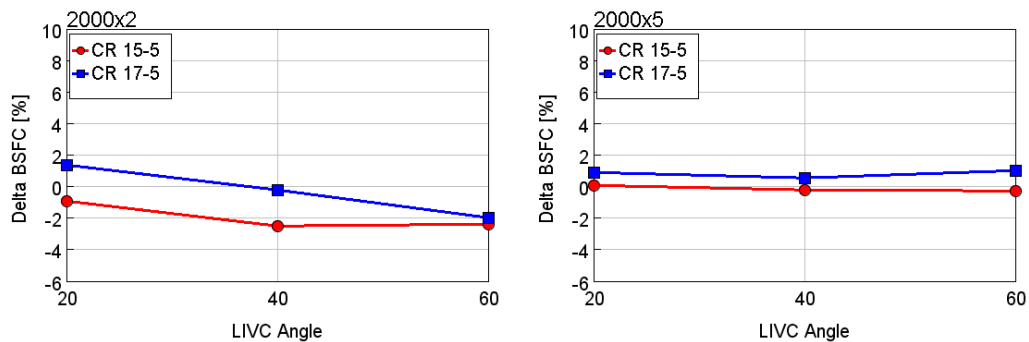


Figure 3.7 – Delta BSFC at different LIVC actuations for 2 bar (left) and 5 bar (right) engine load – 2000 RPM [81]

In Figure 3.8 – top, the peak firing pressure is plotted: since Chen Flynn model is used to predict friction losses as a function of maximum pressure, the resulted FMEP reduces retarding the intake valve closure, leading to a BSFC reduction at lower load. At higher load, LIVC allows a reduction in maximum pressure as well but the friction reduction does not lead to BSFC benefit. As shown in Figure 3.8 – center, this happens because the heat transfer losses increase by retarding the closure of the intake valve, since the turbocharger system cannot recover the amount of air lost, causing a reduction in air-to-fuel ratio. The air-to-fuel reduction happens at lower load as well, but on the contrary it leads to a reduction in heat transfer losses. This result can be explained by plotting the maximum temperature reached in the engine cycle and the heat transfer coefficient, averaged in the

compression and expansion strokes (Figure 3.8 – bottom). As expected, for both loads, retarding the intake valve closure the heat transfer coefficient reduces, since it is a function of pressure level and overall turbulence within the cylinder. On the contrary, retarding the intake valve closure the maximum temperature increases, because of the reduced air-to-fuel ratio. But, at lower load the increase in temperature is offset by a reduction in the heat transfer coefficient; on the contrary at higher load, the maximum temperature increment is an order of magnitude higher respect to the heat transfer coefficient reduction, causing a heat transfer losses increment.

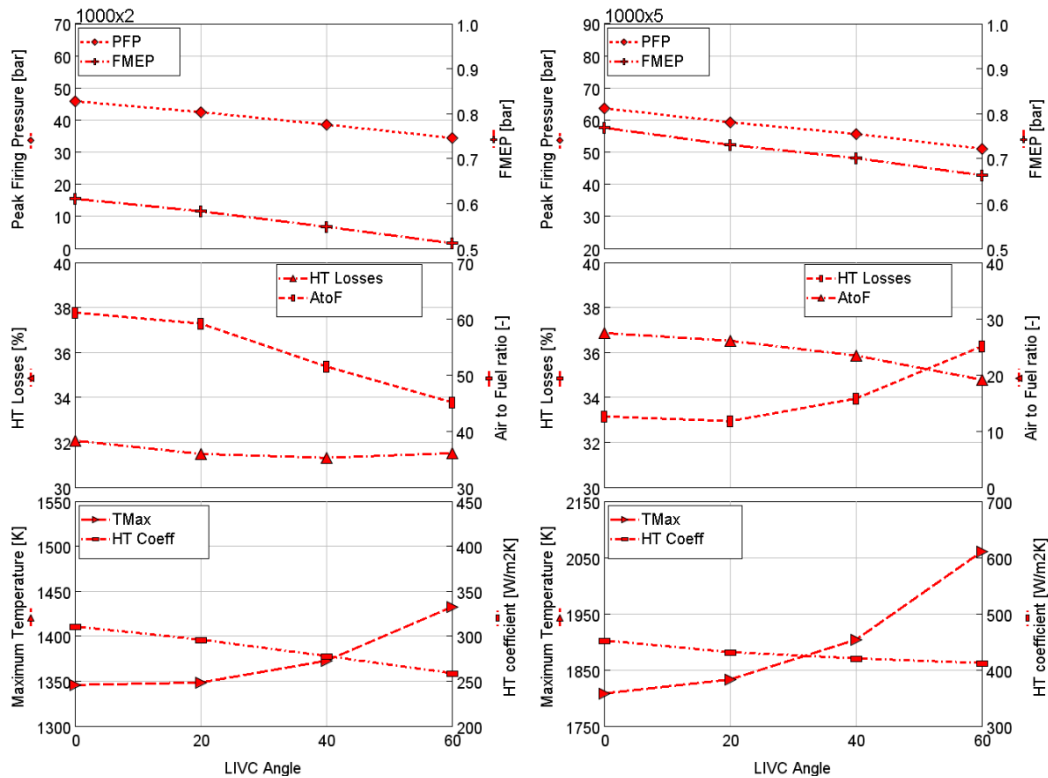


Figure 3.8 – Peak firing pressure and friction losses (top), heat transfer losses and air-to-fuel ratio (center), maximum temperature and heat transfer coefficient (bottom), compression ratio equal to 15.5 at different LIVC angle – 1000 RPM X 2 bar BMEP (left) and 1000 RPM X 5 bar BMEP (right) [81]

Regarding the HT coefficient shown in Figure 3.8 – bottom, in these analysis the WoschniGT model was used for the heat transfer coefficient evaluation, since the measured swirl data was not available. Moreover, the GT variation of Woschni correlation takes into account that the HT changes during the valve opening event: more specifically, HT coefficient is increased by the inflow and backflow velocities through the intake and exhaust valves, respectively. It is worth to say that, theoretically the GT flow model could be the best choice considering the fact that by retarding the IVC the turbulence level may change, causing a HT coefficient variation.

In order to validate this choice, a 3D-CFD cylinder cold flow analysis was carried out in CONVERGE CFD Software to evaluate the turbulence level in both baseline and LIVC60 actuations. The effect of LIVC is shown in Figure 3.9, where logP-logV diagram and in-cylinder temperature were highlighted for both the

actuators: considering LIVC60, since the IV remains open after BDC, the effective compression stroke starts in delay respect to the baseline actuation reaching lower pressure and temperature values at TDC (end of compression stroke).

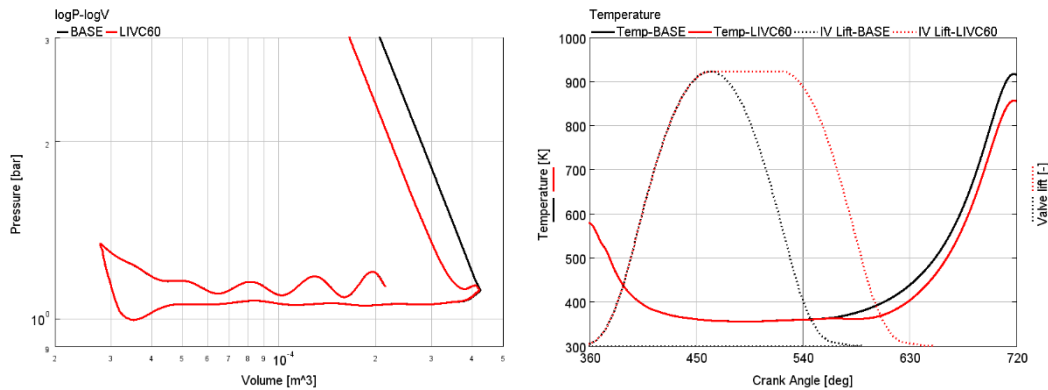


Figure 3.9 – logP-logV (left) and in-cylinder temperature (right) for baseline (black) and LIVC60 (red) actuators

Moreover, the turbulence analysis is shown in Figure 3.10: it is worth to point out that retarding the IV closure causes a slight swirl ratio reduction, keeping almost constant the TKE level within the cylinder. This results confirms that the choice of WoschniGT is consistent, and the model is able to correctly predict the HT coefficient variation due to different IV actuators.

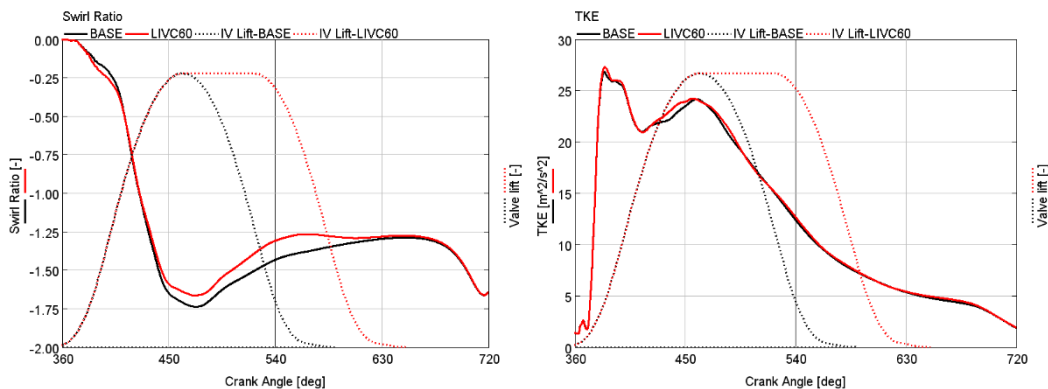


Figure 3.10 – Swirl ratio (left) and turbulent kinetic energy – TKE (right) for baseline (black) and LIVC60 (red) actuators

Transient analysis

Finally, a transient analysis was carried out in order to highlight the impact of the LIVC technique in terms of BSFC reduction along the whole WLTC. The engine calibrations to be used for the WLTC in terms of EGR rate and boost pressure were defined on the basis of the DoE steady state analysis. A proper switch was set in order to change the baseline calibration to the LIVC one when VVA is actuated. More specifically, the valve lift actuation was set in order to change the lift during 1 engine cycle using these approaches: concerning VVA actuation, a map of different valve profiles as a function of engine speed and fuel quantity was

defined. The switch from conventional to non-conventional valve lift is done using the data from the nearest point without any interpolation between data points. On the contrary, EGR rate, injection timing and boost pressure are actuated using a linear interpolation among different engine operating conditions in the driving cycle.

Figure 3.5, Figure 3.6, Figure 3.7 show that the best LIVC profiles in terms of BSFC reduction are the most retarded one. For this reason, LIVC60 was selected to be evaluated in transient analysis and its actuation was limited in the low load zone (BMEP ≤ 2 bar) of the engine map.

The result in terms of normalized cumulated fuel consumption along the driving cycle is shown in Figure 3.11, where the LIVC result (red line) is compared with the baseline actuation (black dashed line). Differently from the steady state analysis, no significant benefits were found in transient analysis, with a BSFC reduction lower than 1%.

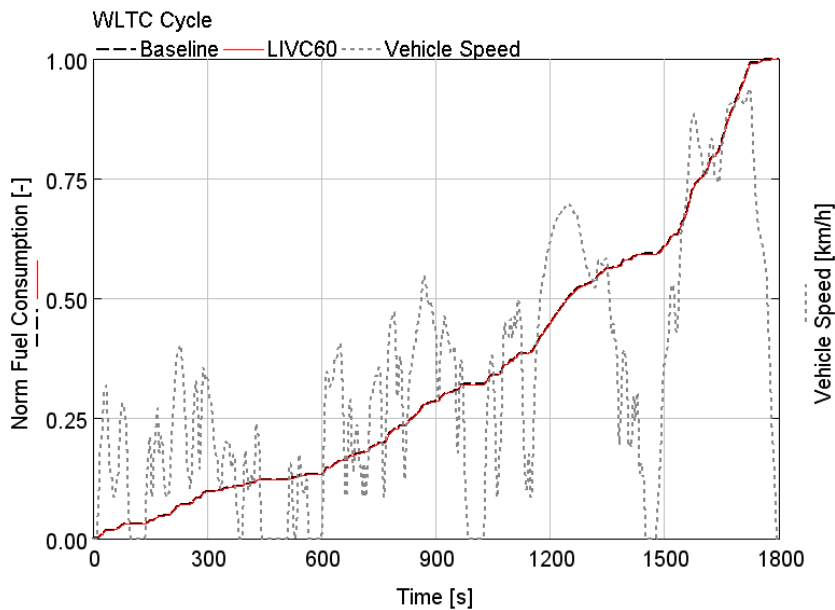


Figure 3.11 – Normalized cumulated fuel consumption respect to the baseline value, in transient simulation for baseline (black dashed) and LIVC60 (red) actuations [81]

This result can be explained by analyzing Figure 3.12, in which the percentage of the part load conditions in which LIVC60 was actuated (BMEP ≤ 2 bar) on the total fuel consumption is shown. In other words, even if LIVC may result in significant efficiency improvements in steady state analysis, its actuation is limited to a part load zone that has a low impact on the total fuel consumption over the driving cycle.

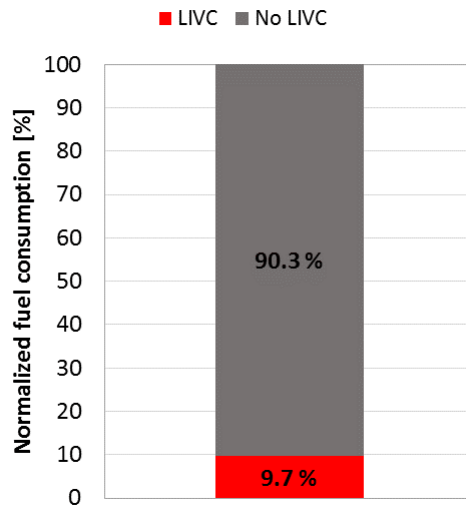


Figure 3.12 – Percentage of LIVC engine operating conditions on the total fuel consumption over WLTC [81]

3.1.4 Late Exhaust Valve Opening

A fast opening lift of the exhaust valve is usually desirable in order to retard the EVO timing for improving BSFC. Moreover, an exhaust valve faster opening may also reduce the blow-down flow losses increasing the energy available at turbine inlet, especially needed at low engine speed where the variable geometry turbine is usually closed. However, a retarded EVO timing results in high pumping losses, especially at high engine speeds when the engine air flow rate is high.[56]

As Figure 3.13 shows, in this analysis three different valve lifts on both exhaust valves with exhaust valve opening at 20, 40, 60 crank angle degrees later than the baseline were considered. The modified valve profiles were obtained a priori without any consideration about the design of the valve lift, such as limitations on maximum acceleration or maximum jerk of the valve profile.

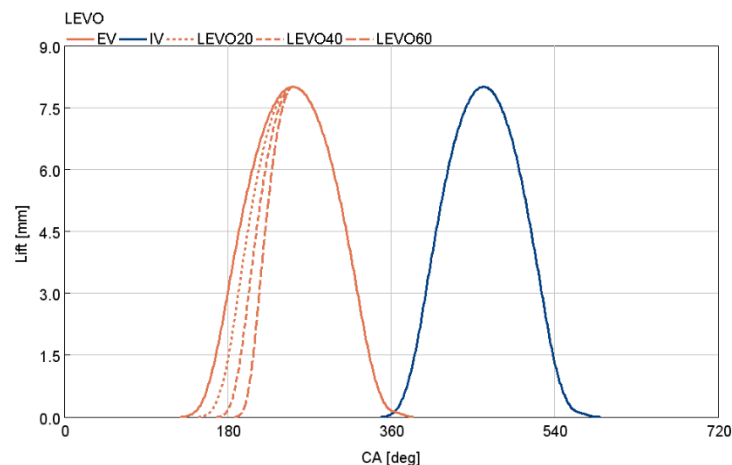


Figure 3.13 – LEVO lift profiles tested [81]

Steady-state analysis

As Figure 3.14 – top, Figure 3.15 – top and Figure 3.16 – top show, no significant benefits could be achieved in terms of BSFC reduction with any of the investigated valve lift profiles, thus suggesting that the increase in the expansion work (Figure 3.14 – bottom, Figure 3.15 – bottom and Figure 3.16 – bottom) is offset by the increase of the pumping work at the beginning of the exhaust stroke (Figure 3.14 – center, Figure 3.15 – center and Figure 3.16 – center). To better clarify this effect, LEVO results were shown in Figure 3.17 for 1000 RPM X 5 bar BMEP engine load. At constant Rack Position, the difference between exhaust and intake pressure does not reflect the corresponding PMEP trend for each LEVO configuration. Therefore, the PMEP increase should be addressed to another effect. In fact, by looking at Figure 3.18, where the LogP-LogV diagram is shown for the LEVO actuations, it is immediately clear that a retarded opening of the EV causes an increase in pressure inside the cylinder during the initial part of the exhaust stroke. This effect results in an increment of pumping losses.

Furthermore, regarding the analyzed compression ratios, it is worth to point out that the higher CR gives higher BSFC for two main reasons: on one hand, increasing the CR, the in-cylinder maximum pressure increases, giving higher friction losses; on the other hand, increasing the CR results in higher charge temperature and, consequently, higher heat transfer losses. Moreover, at constant engine speed, at higher load, the impact of higher friction losses is reduced and the gap between the blue curve (higher CR) and the red one (lower CR) is significantly reduced, as shown by Figure 3.14 – top, Figure 3.15 – top and Figure 3.16 – top.

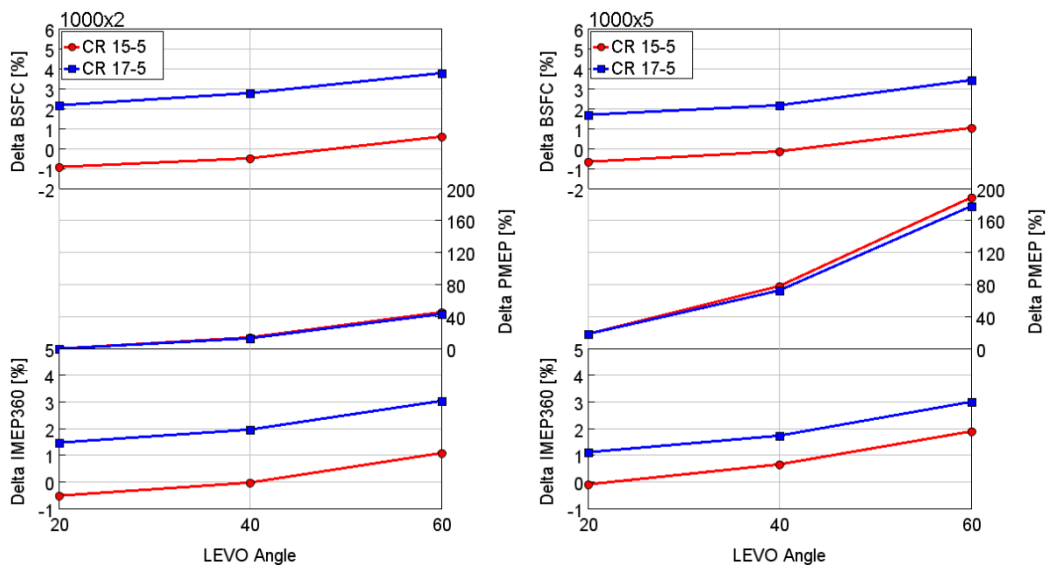


Figure 3.14 – Delta BSFC (top), Delta PMEP (center) and Delta IMEP360 (bottom) at different LEVO actuations for 2 bar (left) and 5 bar (right) engine loads – 1000 RPM [81]

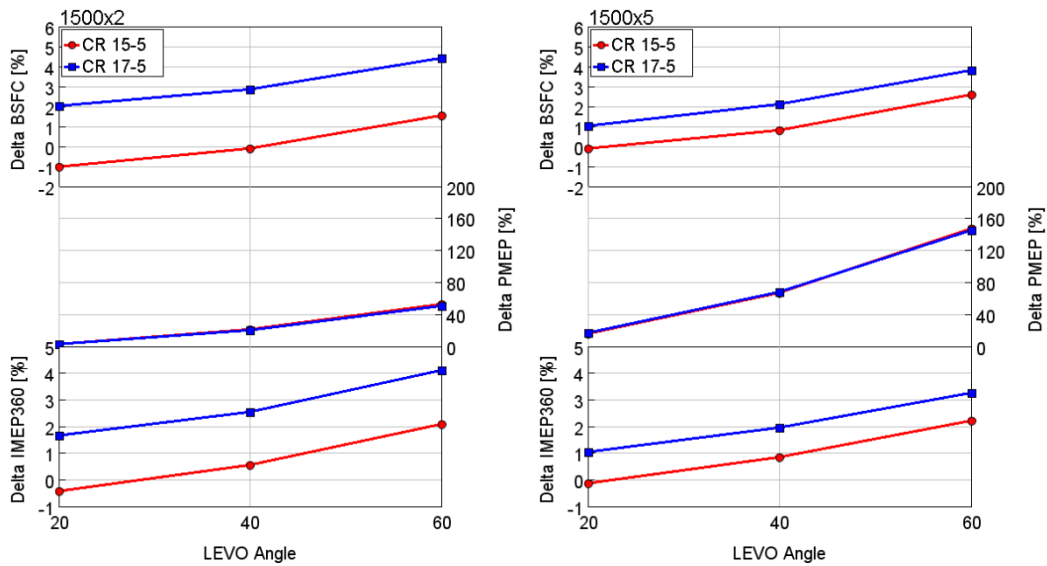


Figure 3.15 – Delta BSFC (top), Delta PMEP (center) and Delta IMEP360 (bottom) at different LEVO actuations for 2 bar (left) and 5 bar (right) engine loads – 1500 RPM [81]

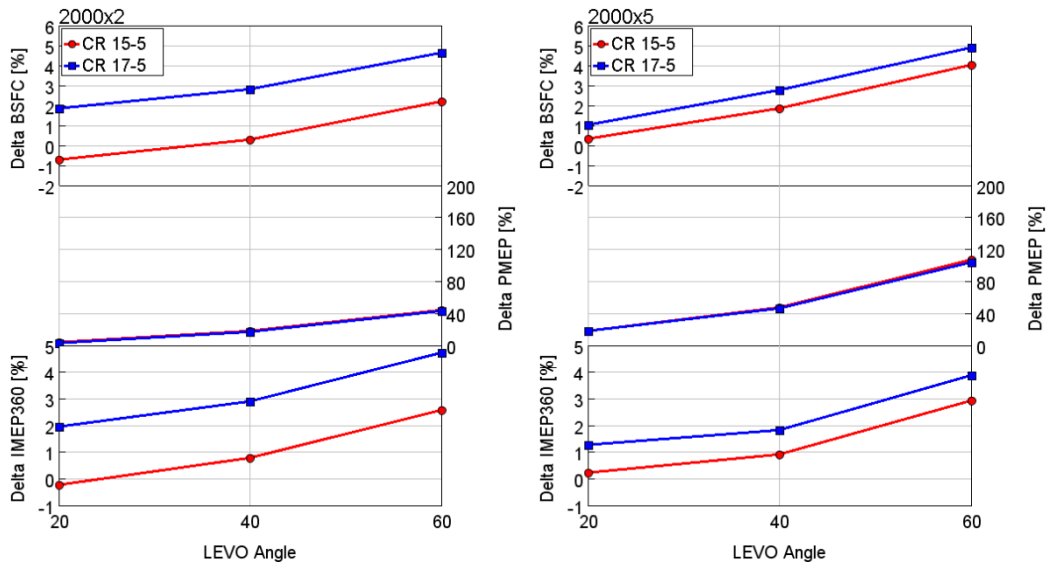


Figure 3.16 – Delta BSFC (top), Delta PMEP (center) and Delta IMEP360 (bottom) at different LEVO actuations for 2 bar (left) and 5 bar (right) engine loads – 2000 RPM [81]

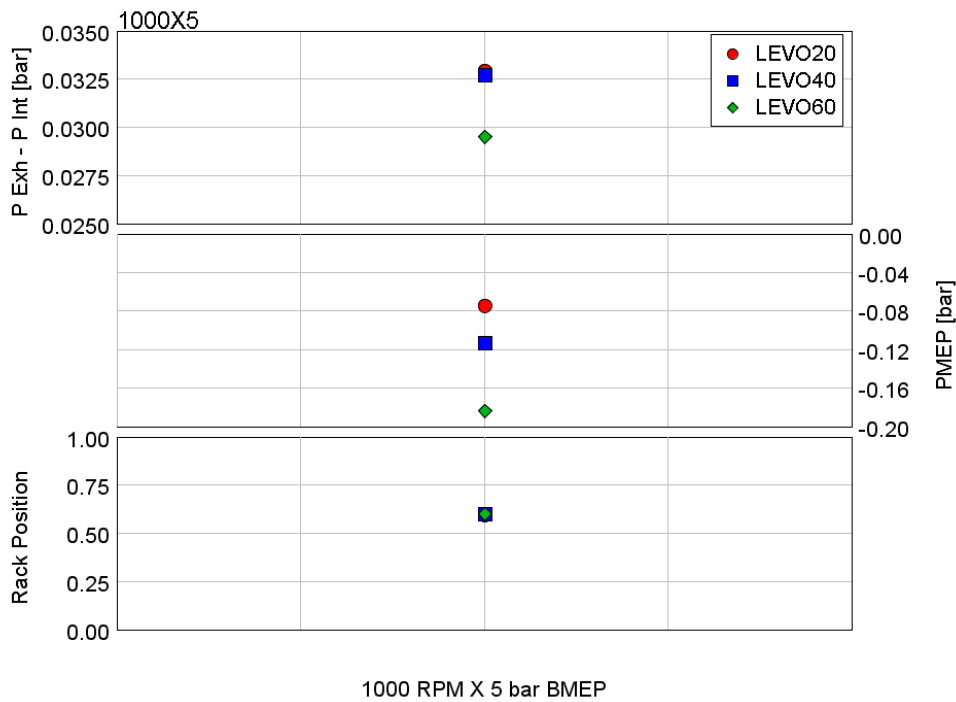


Figure 3.17 – Effect of LEVO: difference between exhaust and intake pressures (top), IMEP (center) and Rack Position (bottom) for LEVO20, 40, 60 (red circle, blue square, green diamond, respectively)

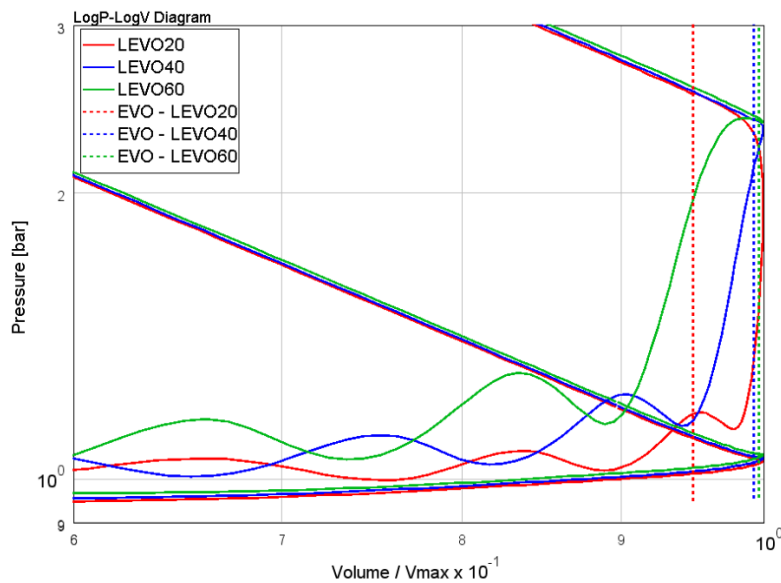


Figure 3.18 – Zoom @ BDC for LogP-LogV diagram for 3 different LEVO actuations

3.1.5 Variable Exhaust Valve Timing

The optimum selection of the exhaust valve opening and closure is usually determined by the need of increasing volumetric efficiency and decreasing pumping losses to reduce BSFC and it is a trade-off between high and low speeds requirements. VVA could give the capability to adjust the optimum timing for efficiency improvements at each engine speed.

The tested valve lift profiles (-12, -6, +6, +12 CA deg) are shown in Figure 3.19, where sign ‘-’ means advancing the profile with respect to the baseline timing and sign ‘+’ means retarding the profile with respect to the baseline timing. The different valve timings were actuated for both the exhaust valves.

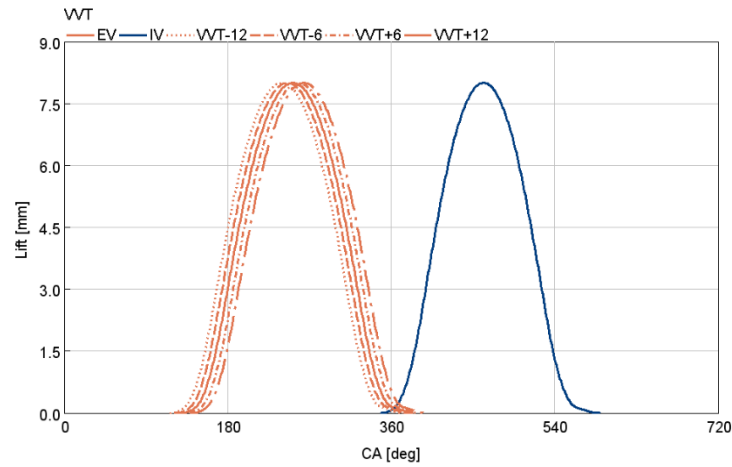


Figure 3.19 – VVT lift profiles tested [81]

Steady-state analysis

The results of the steady-state analysis are shown in Figure 3.20, Figure 3.21 and Figure 3.22 for the selected engine key-points in Table 3.

As Figure 3.20 – top, Figure 3.21 – top and Figure 3.22 – top show, no significant benefits could be achieved in terms of BSFC reduction with any of the investigated valve lift phasings, nor by advancing the EVO (to achieve higher temperature at the turbine inlet) nor retarding the EVO (to increase the expansion work). The results of retarded EVO with exhaust valve phasing are in agreement with the LEVO results, which were discussed in the previous paragraph. More specifically, the higher expansion work (Figure 3.20 – bottom, Figure 3.21 – bottom and Figure 3.22 – bottom) is offset by the increase of the pumping work at the beginning of the exhaust stroke (Figure 3.20 – center, Figure 3.21 – center and Figure 3.22 – center).

Furthermore, as previously highlighted for LEVO technique, it is worth to point out that the higher CR gives higher BSFC. Moreover, at constant engine speed, at higher load, the impact of higher friction losses is reduced and the gap between the blue curve (higher CR) and the red one (lower CR) is significantly reduced, as shown by Figure 3.20 – top, Figure 3.21 – top and Figure 3.22 – top.

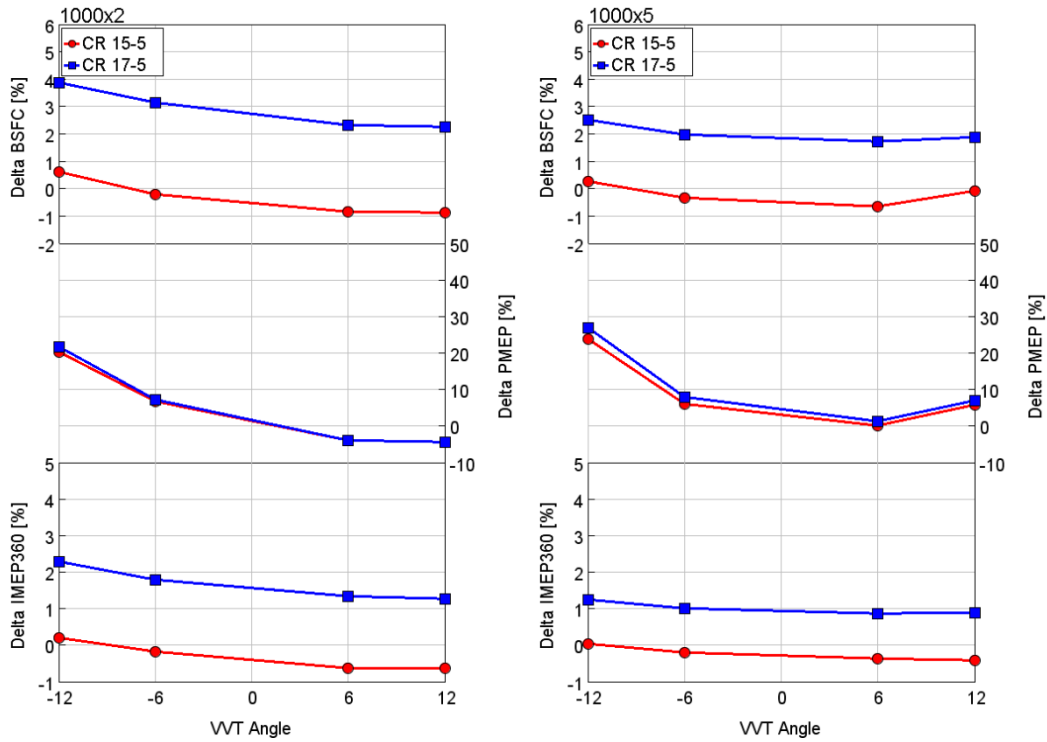


Figure 3.20 – Delta BSFC (top), Delta PMEP (center) and Delta IMEP360 (bottom) at different EV timings for 2 bar (left) and 5 bar (right) engine loads – 1000 RPM [81]

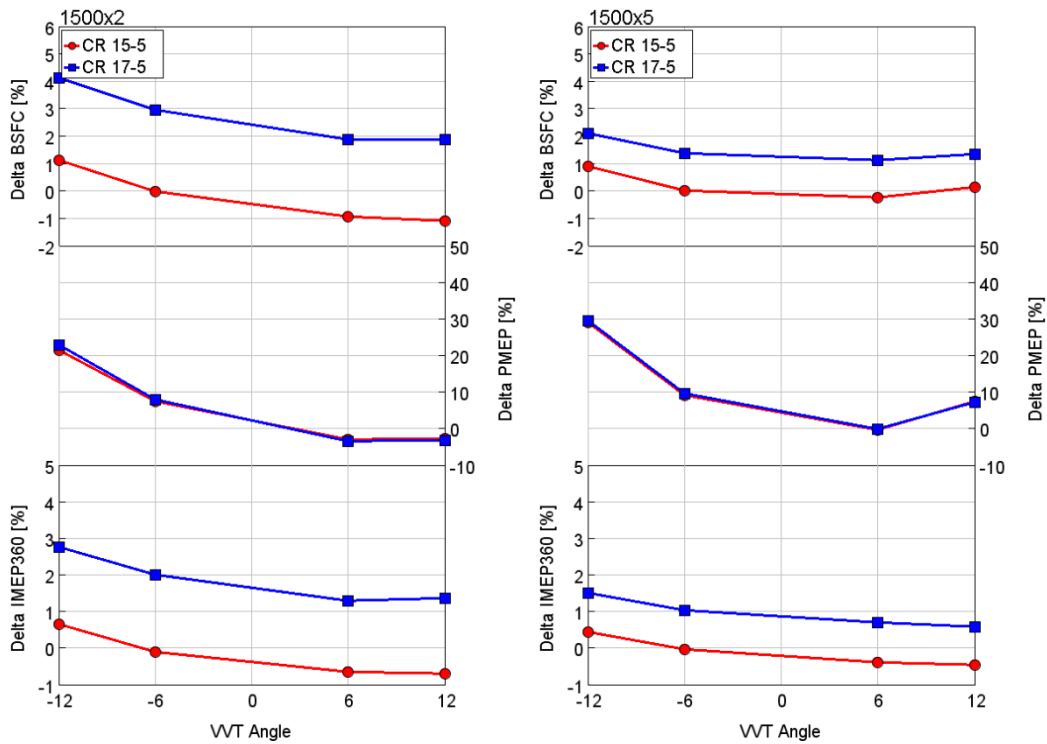


Figure 3.21 – Delta BSFC (top), Delta PMEP (center) and Delta IMEP360 (bottom) at different EV timings for 2 bar (left) and 5 bar (right) engine loads – 1500 RPM [81]

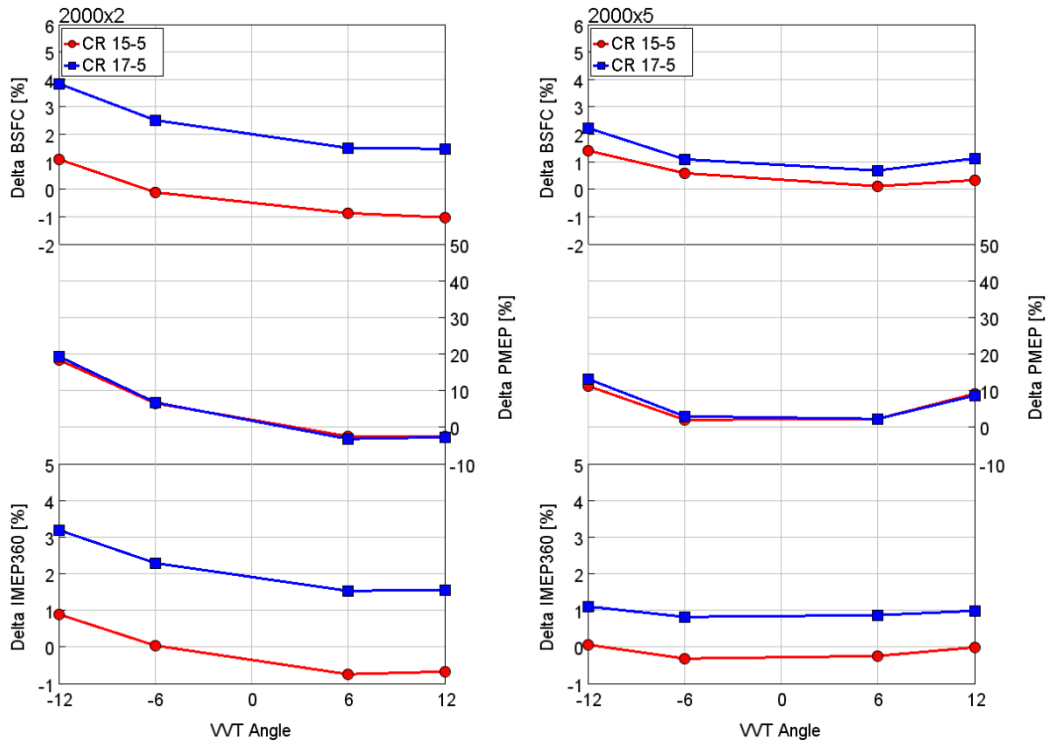


Figure 3.22 – Delta BSFC (top), Delta PMEP (center) and Delta IMEP360 (bottom) at different EV timings for 2 bar (left) and 5 bar (right) engine loads – 2000 RPM [81]

3.2 Warmup improvement potential

Among the VVA benefits listed in the first section of this paragraph, it was stated that VVA can accelerate the warm up of the AT system after cold start. In this context, the VVA on the exhaust valves can be a key technology for increasing AT system temperatures after cold start and during warm up. The application of VVA with this aim has been analyzed from different points of views over the last years.

Brauer, Diezemann et al. conducted an investigation on a single cylinder engine with a secondary opening of the EV obtaining an exhaust gas temperature increase and a reduction of the engine-out emissions in cold low-load operation [70]. Brauer, Pohlke et al., in [69], presented a simulation study on a conventional, single stage boosted 2.0L passenger car Diesel engine with the objective to reduce exhaust AT heat-up time thanks to a secondary exhaust valve lift. The same VVA features were assessed for their ability to increase full load torque at low engine speed thanks to scavenging. Two different VVA technologies proposed by Schaeffler were explored, the UniAir system and a multiple switching concept with a switchable roller finger follower. As a result, the two solutions give similar internal EGR (iEGR) rates, exhaust temperatures, BSFC values and air to fuel ratios at low engine speed.

In a recent publication, Gonzalez and Di Nunno presented a one-dimensional computational method combined with experimental bench tests for analyzing the performance of a 4-cylinder Diesel engine using iEGR through a secondary lift of the exhaust valve. The results of this technology was compared with the use of

multiple after injections: the implementation of iEGR was found to be beneficial compared with the use of multiple after injections only, because of the need for less added fuel to provide the same exhaust gas temperature increase [68].

Some OEMs (Original Equipment Manufacturers) have introduced VVA on passenger car Diesel engines using different valve lift strategies and hardware solutions. The Mazda SkyActiv-D 2.2L Diesel engine adopts a re-breathing of the EV thanks to a switchable roller finger follower, in order to stabilize combustion after engine start and to accelerate the AT heat-up [85].

Jaguar Land Rover implemented an exhaust side cam phaser combined with a cooled low-pressure EGR system on its new 2.0L Diesel engine: this design enables more rapid catalyst heating, further minimizing harmful emissions during the critical warm up phase [86].

Deppenkemper et al. in [87,88] developed an holistic 1D engine simulation approach for the modelling of full-transient engine operation allowing the analysis of future engine concepts. The authors present the application of variable valve train on a passenger car Diesel engine, and the heating potential according to an efficient engine and exhaust gas thermal management was evaluated. The results are compared to a conventional multi-event injections or retarded SOI heating strategies in terms of a faster aftertreatment light-off and benefits in CO₂ emissions. In this work, a cylinder deactivation or an exhaust re-opening event could provide up to 5-10% CO₂ reduction under RDE conditions that comply with the EURO 6d legislation limit.

As already done for the CO₂ reduction analysis, in this paragraph a simulation study is presented evaluating the impact of Exhaust Valve VVA on the exhaust temperature of the selected Diesel engine. Moreover, numerical simulations were carried out by means of the integrated model introduced in the preliminary analysis, featuring the predictive combustion model (DIPulse) to properly evaluate the impact of different VVA strategies on the combustion process. In this analysis, the following three different techniques were scrutinized in order to assess their potential in terms of accelerating the aftertreatment warm up:

- Early Exhaust Valve Opening (EEVO) - Advancing EVO timing results in a higher exhaust pressure and temperature than the standard valve timing.
- Exhaust Valve Phasing (VVT) - By advancing EV timing the same effect of EEVO can be obtained and higher in-cylinder residuals amount can be achieved. Retarding EV timing, the overlap between exhaust and intake valve lifts increases and a higher amount of internal EGR can be achieved.
- Exhaust Valve reOpening (EVrO) - The secondary opening of the EV when the IV is open produces an efficient recirculation of the burned gas from the previous engine cycle to the in-cylinder charge.

3.2.1 K-points selection

As a reference, the first 300 s were chosen as representative of the cold phase of the WLTC where the potential of VVA on exhaust aftertreatment warmup was evaluated. Also in this case 6 key-points were selected for evaluating the impact of different valve actuations in steady state conditions.

Differently from the CO₂ reduction case, the engine conditions for the first 300 s were time-weighted. In Figure 3.1, the 6 selected key-points are highlighted in red circle, in which the percentage weight on total cold phase duration is shown.

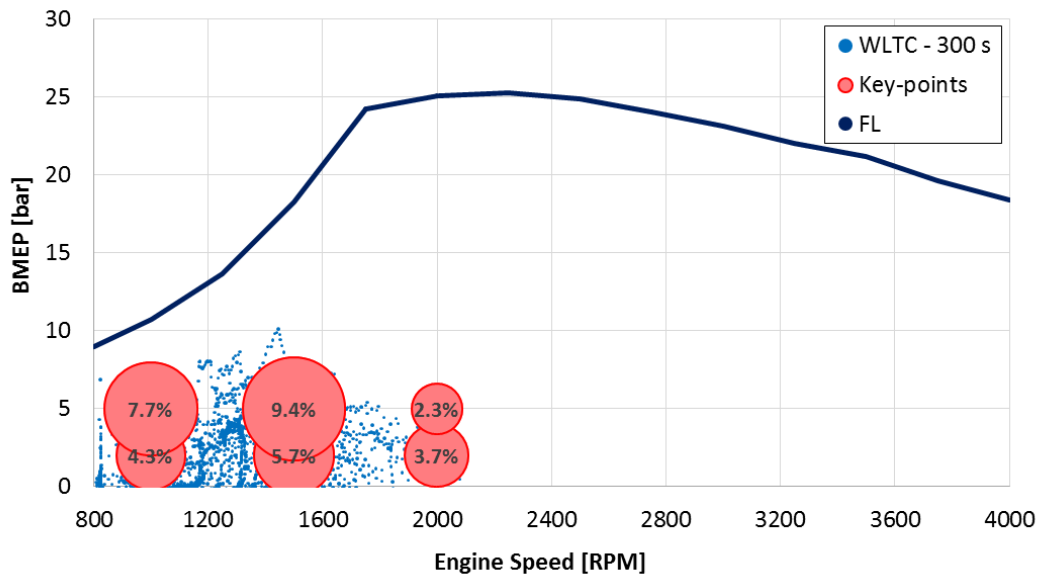


Figure 3.23 – Engine operating conditions over the first 300 s of WLTC driving cycle (blue) and selected key-points (red) on the engine map

The selected key-points are also listed in Table 3.3. As it can be seen, the points are related to the Low Speed – Low Load engine operating conditions.

Table 3.3 – Selected key-points for steady state analysis – WU improvement [89]

Engine Speed [RPM]	BMEP [bar]
1000	2.0, 5.0
1500	2.0, 5.0
2000	2.0, 5.0

Also in this case, the selected vehicle for the transient simulation is an European C-Segment, the characteristics of which are highlighted in Table 3.2.

3.2.2 Simulation setup

Since the adoption of non-conventional valve lift profiles may require significant adjustments in terms of boost pressure and EGR levels, different VGT

positions and EGR valve openings were explored for each engine key-point in combination with different exhaust valve lifts. Moreover, since the different tested VVA lifts can also imply significant variations in terms of effective expansion ratio, two different geometrical compression ratios (CR 15.5 and CR 17.5) were considered.

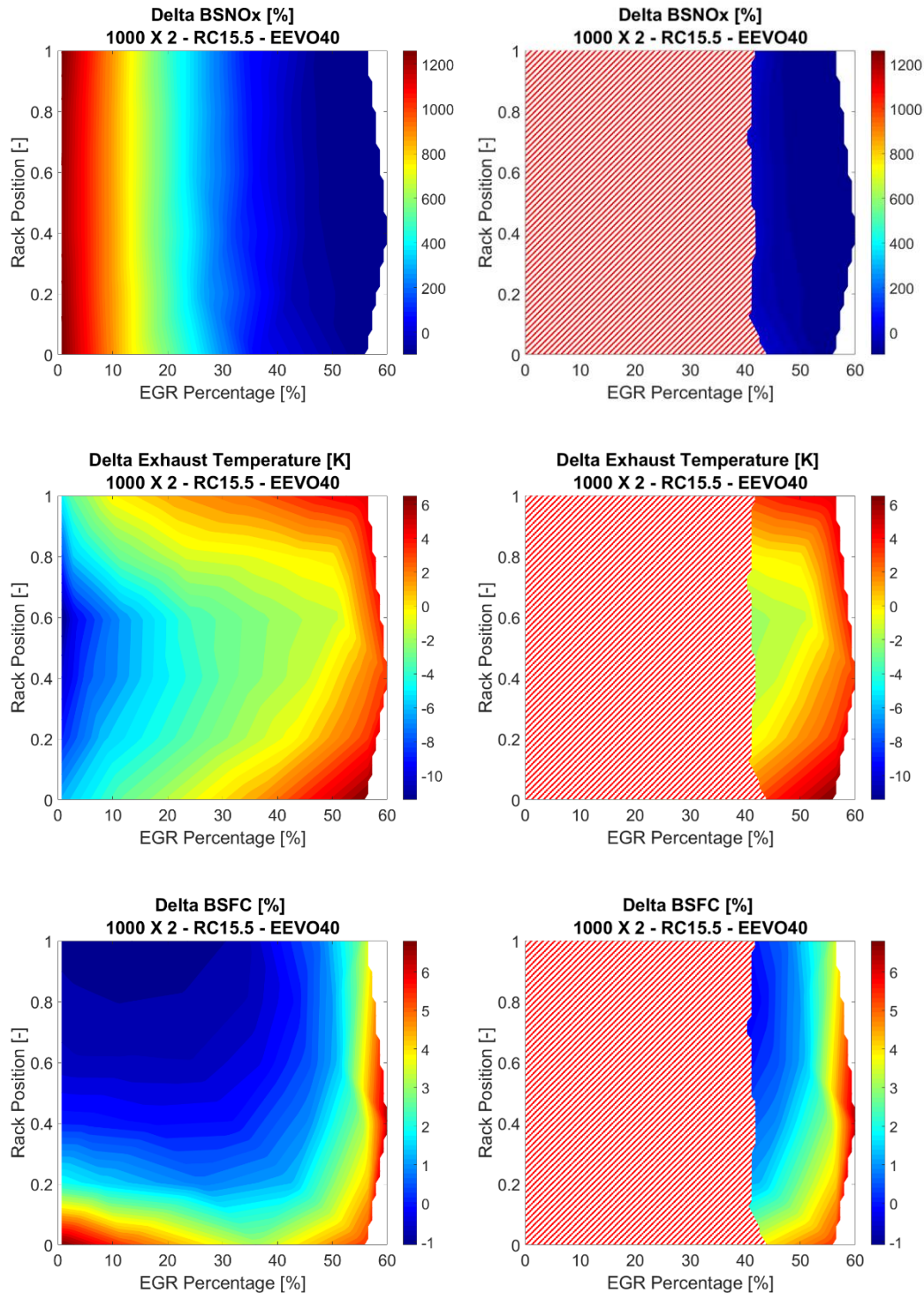


Figure 3.24 – Example of response surface for delta BSNOx (top), delta Exhaust Turbine Outlet temperature (center) and delta BSFC (bottom) obtained from full factorial DoE of EGR and VGT parameters settings for a given exhaust valve lift profile and geometrical compression ratio: the dashed area represents the region in which the baseline NOx emission levels are exceeded and which cannot therefore be considered as suitable solutions – 1000 RPM X 2 bar BMEP [89]

To this aim, a full factorial Design of Experiments (DoE) was performed, by varying the turbine rack position and the opening of the EGR valve (both of them from totally closed to totally opened). For each combination of the design and calibration parameters of the DoE, the MFB50 was maintained equal to the baseline value by adjusting the injection timing while keeping unchanged all the other parameters of the injection pattern (number of injection pulses, Energizing Time, Dwell Time and rail pressure), as the ECU control works. Then, the DoE results were post-processed in order to identify the combination between boost pressure and EGR rate which could maximize the exhaust temperature (at turbine outlet) without exceeding the NO_x emissions of the baseline settings for each valve lift profile and each engine compression ratio. An example of the response surfaces of the DoE for Brake Specific NO_x (BSNO_x), exhaust temperature and BSFC are shown in Figure 3.24 (top, center and bottom respectively), where the Rack Position represents the VGT opening that varies from 0 (totally closed) to 1 (totally open). The dashed areas represent the region in which the baseline NO_x levels are exceeded and which cannot be therefore considered as suitable solutions. The optimal combination of the DoE parameters (shown with a black star in Figure 4b and 4c) corresponds therefore to the maximum exhaust temperature level achieved outside from the dashed areas where the baseline NO_x emissions level are exceeded with an acceptable BSFC worsening. The full factorial DoE was repeated for each combination of exhaust valve lift and engine compression ratio.

3.2.3 Early Exhaust Valve Opening

In order to maximize engine performance, the optimum EVO is usually a balance between the work obtained during the expansion stroke and the pumping losses during the exhaust stroke. Advancing EVO results in exhaust pressure and temperature levels higher than those obtained with the standard valve timing. Although the exhaust temperature increases, a lower expansion work is collected by the piston, and a higher fuel flow rate is required for obtaining the same performance. Moreover, a further negative impact of EEVO could be related to the higher in-cylinder pressure against which the exhaust valves have to open: as a consequence, the valve driving system could absorb more power with respect to the baseline valve lift. The losses in the valve mechanism (hydraulic or cam-driven) could hence become more significant with earlier EVO [56]. A detailed investigation on the valve faces net force should therefore be carried out in order to evaluate this effect.

It is worth to point out that Gonzalez et al. in [68] proposed some drawbacks related to this technique: because of the higher pressure in the exhaust port, EEVO could have a negative impact on the engine noise acting as a practical limit for this actuation.

As Figure 3.25 shows, in this analysis four different valve lifts on both EVs with EVO at 20, 40, 60 and 90 crank angle degrees before the baseline were considered.

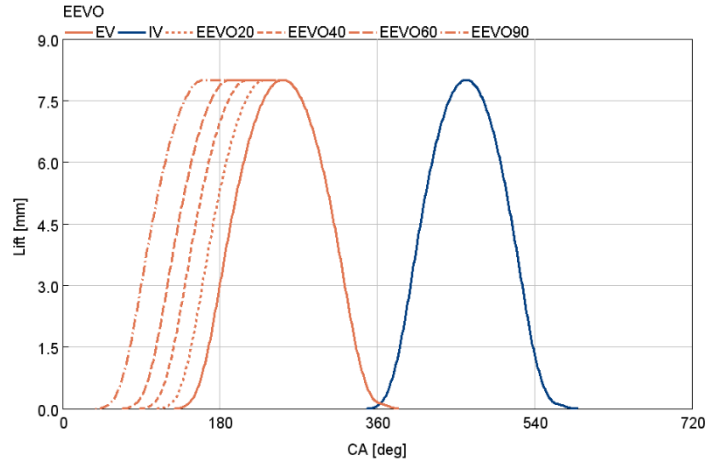


Figure 3.25 – EEVO lift profiles tested [89]

Steady-state analysis

The results obtained from the EEVO analysis are shown in Figure 3.26, Figure 3.27 and Figure 3.28 for the 6 engine key-points listed in Table 3.3, in terms of exhaust temperature and BSFC differences. More in details they are expressed by Equation 21 and Equation 22, respectively:

$$\text{Delta Exhaust Temperature} = T_{exh_{VVA}} - T_{exh_{Baseline}} \quad \text{Eq. 21}$$

$$\text{Delta BSFC} = \frac{BSFC_{VVA} - BSFC_{Baseline}}{BSFC_{Baseline}} \cdot 100 \quad \text{Eq. 22}$$

Where, ‘VVA’ subscript defines the EEVO actuation, and ‘Baseline’ subscript is related to the baseline valve lift. The exhaust temperature in Equation 21 is the mean value of the gas temperature averaged on the basis of the mass flow rate over an engine cycle, expressed by Equation 23:

$$T_{exh} = \frac{\int \dot{m} T dt}{\int \dot{m} dt} \quad \text{Eq. 23}$$

Where:

$$\begin{aligned} T &= \text{exhaust gas temperature} \\ \dot{m} &= \text{exhaust mass flow rate} \end{aligned}$$

As shown by Figure 3.26, Figure 3.27, Figure 3.28, advancing the EVO increases the exhaust temperature due to the reduced expansion in the cylinder; on the other hand, the lower expansion work gives higher BSFC, confirming the expected results. Furthermore, as far as the compression ratio is concerned, Figure 3.18, Figure 3.19, Figure 3.20 show that the higher compression ratio gives lower improvements in terms of exhaust temperature due to the higher expansion ratio.

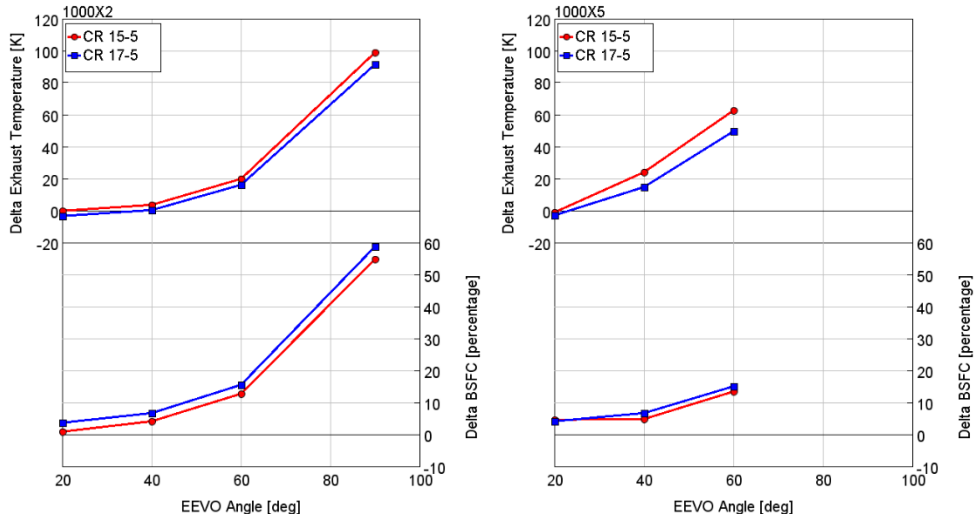


Figure 3.26 – Delta Exhaust Temperature (top) and delta BSFC (bottom) at different EEVO actuations for 2 bar (left) and 5 bar (right) engine load – 1000 RPM [89]

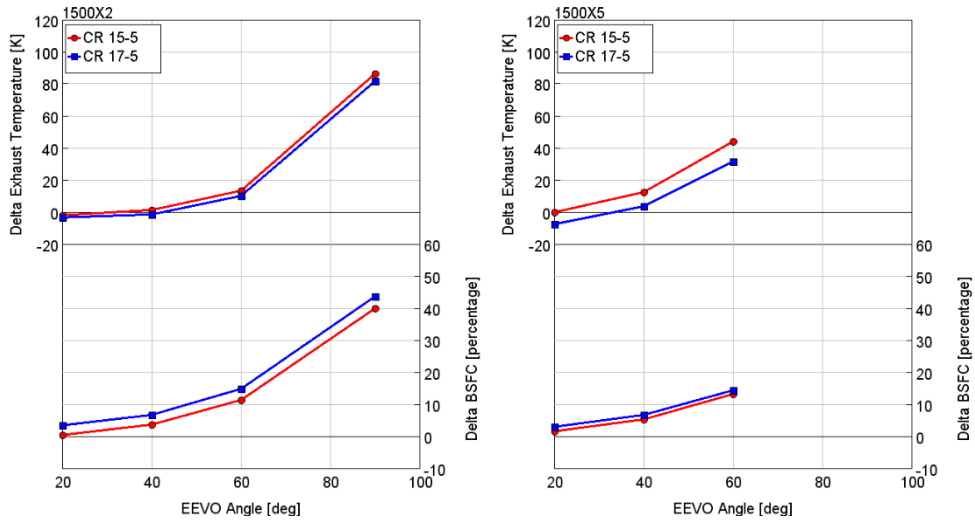


Figure 3.27 – Delta Exhaust Temperature (top) and delta BSFC (bottom) at different EEVO actuations for 2 bar (left) and 5 bar (right) engine load – 1500 RPM [89]

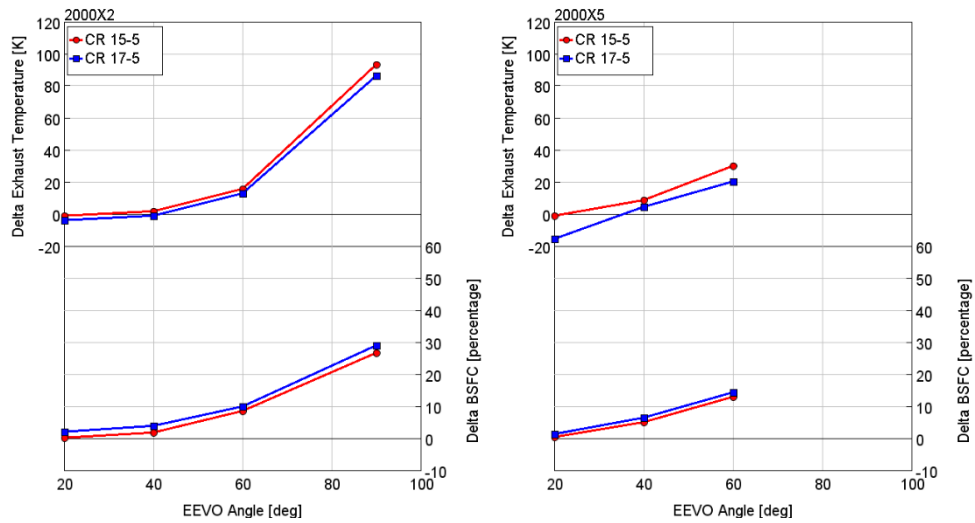


Figure 3.28 – Delta Exhaust Temperature (top) and delta BSFC (bottom) at different EEVO actuations for 2 bar (left) and 5 bar (right) engine load – 2000 RPM [89]

In addition, CR 17.5 gives higher BSFC for two reasons: on one hand, the higher CR gives higher maximum in-cylinder pressure and, consequently, higher friction losses; on the other hand, at the same time higher CR gives higher charge temperature and higher heat transfer losses (split losses in Figure 3.29 and Figure 3.30). Increasing the load, (X 5 bar BMEP in Figure 3.26 – right, Figure 3.27 – right, Figure 3.28 – right), the impact of the friction losses is reduced and the red and green curves are almost superimposed. This is confirmed from Figure 3.30 where the split losses for the case 1000 RPM X 5 bar BMEP– EEVO 20 is shown.

In Figure 3.29 is possible to point out the effect on heat transfer value of different compression ratios, but also the lower percentage related to the exhaust enthalpy term of CR 17.5 respect to the CR 16.0 that can explain the delta exhaust temperature lower than 0 in Figure 3.26 (Case 1000 RPM X 2 bar BMEP – EEVO 20 – CR 17.5).

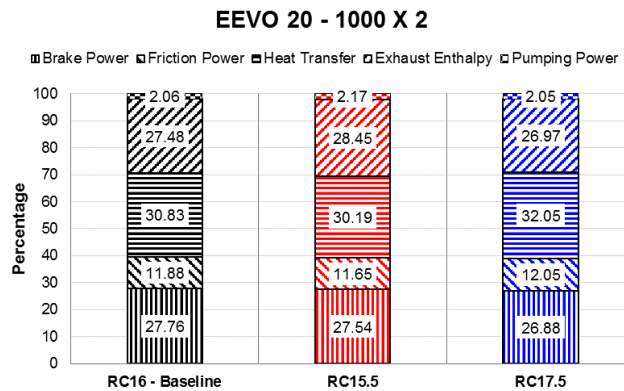


Figure 3.29 – Engine split losses between 3 different compression ratios (16.0, 15.5 and 17.5) for EEVO 20 configuration – 1000 RPM x 2 bar BMEP

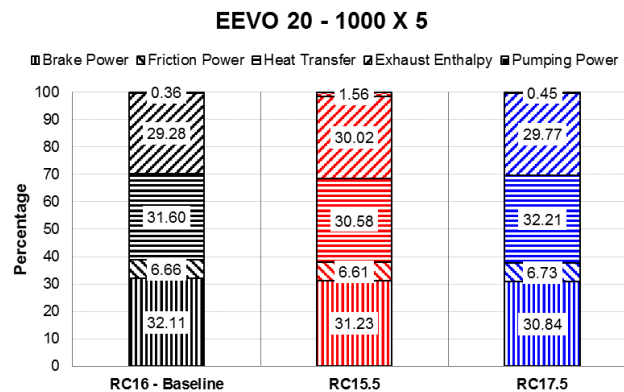


Figure 3.30 – Engine split losses between 3 different compression ratios (16.0, 15.5 and 17.5) for EEVO 20 configuration – 1000 RPM x 5 bar BMEP

Transient analysis

A transient analysis was carried out in order to highlight the impact of the EEVO techniques in terms of exhaust temperature differences and BSFC penalties along the whole WLTC. The engine calibrations to be used for the WLTC in terms of EGR fraction and boost pressure were defined on the basis of the DoE steady

state analysis. A proper switch was set in order to change the baseline calibration to the EEVO-oriented one when VVA is actuated. More specifically, the valve lift actuation was set in order to change the lift during 1 engine cycle using these approaches: concerning VVA actuation, a map of different valve profiles as a function of engine speed and fuel quantity was defined. The switch from conventional to non-conventional valve lift is done using the data from the nearest point without any interpolation between data points. On the contrary, EGR percentage, injection timing and boost pressure are actuated using a linear interpolation among different engine operating conditions in the driving cycle.

Figure 3.18, Figure 3.19, Figure 3.20 show that the 90 CA shift in advance of the EVO produces the largest increases in exhaust temperature, but with unacceptable penalties in terms of BSFC (in some cases, about 50% more than the baseline value). For this reason, the EEVO60 with CR 15.5 was chosen for the WLTC simulation as the best compromise between temperature increment and BSFC worsening. As a reference, the first 300 s were chosen as representative of the cold phase of the WLTC: the EEVO technique was actuated during this phase for low load operating points below 5 bar BMEP as suggested by the steady state results.

In Figure 3.31, the exhaust thermal power of baseline and EEVO actuations (top) and the difference between them are shown in order to highlight the effect on the total exhaust gas power that flows through the AT system.

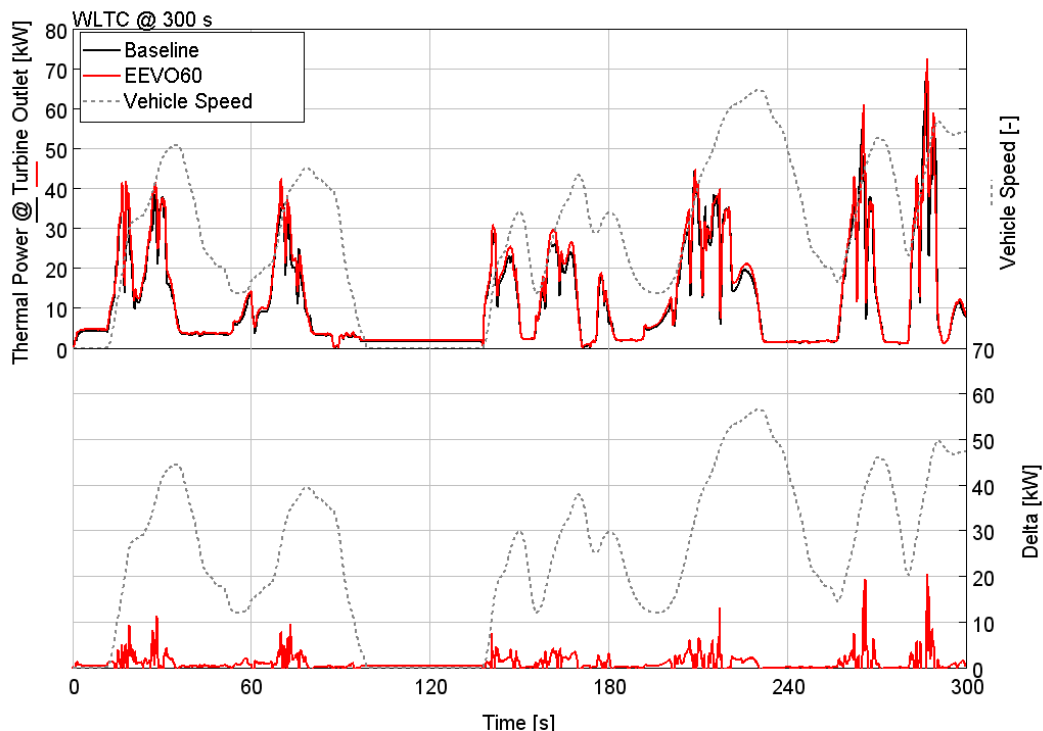


Figure 3.31 – Top: thermal exhaust power at turbine outlet in transient simulations for baseline (black) and EEVO60 (red) actuations. Bottom: relative delta between VVA and baseline thermal power – First 300 s of WLTC [89]

Figure 3.32 shows the comparison between the baseline and the EEVO60 fuel consumption: as it can be seen from the figure, the BSFC penalty after 300 s is

8.2%, but at the end of the cycle it is about 1%, without exceeding the baseline NOx emission value.

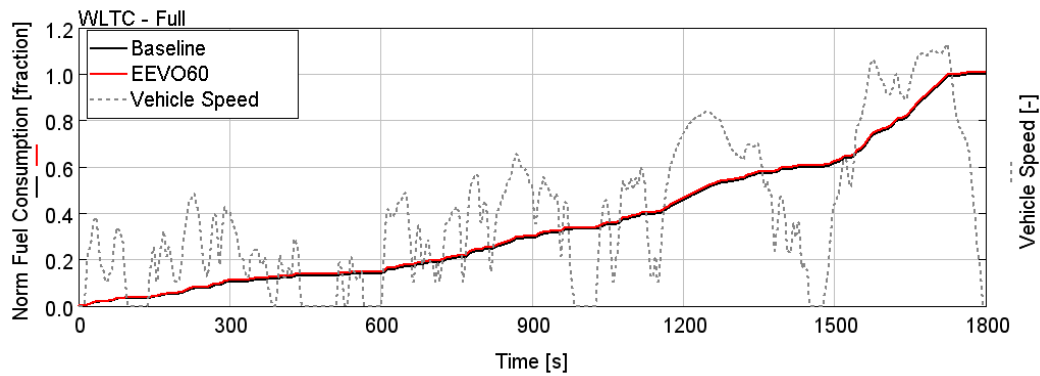


Figure 3.32 – Normalized cumulated fuel consumption respect to the baseline value, in transient simulations for baseline (black) and EEVO60 (red) actuations [89]

A simulation analysis of the AT system was also carried out in order to assess the warm up of the Diesel Oxidation Catalyst (DOC) monolith, calibrated and validated in [90–92]. The exhaust gas flow rate was imposed as a boundary condition at the inlet of the monolith in order to evaluate the effect of the thermal inertia of the monolith, since previous work had shown that the monolith temperature is the dominant parameter for the light-off [90]. However, it should be pointed out that the effect of CO and HC oxidation on DOC was not taken into account, since these emissions could not be modelled with a 1D simulation code.

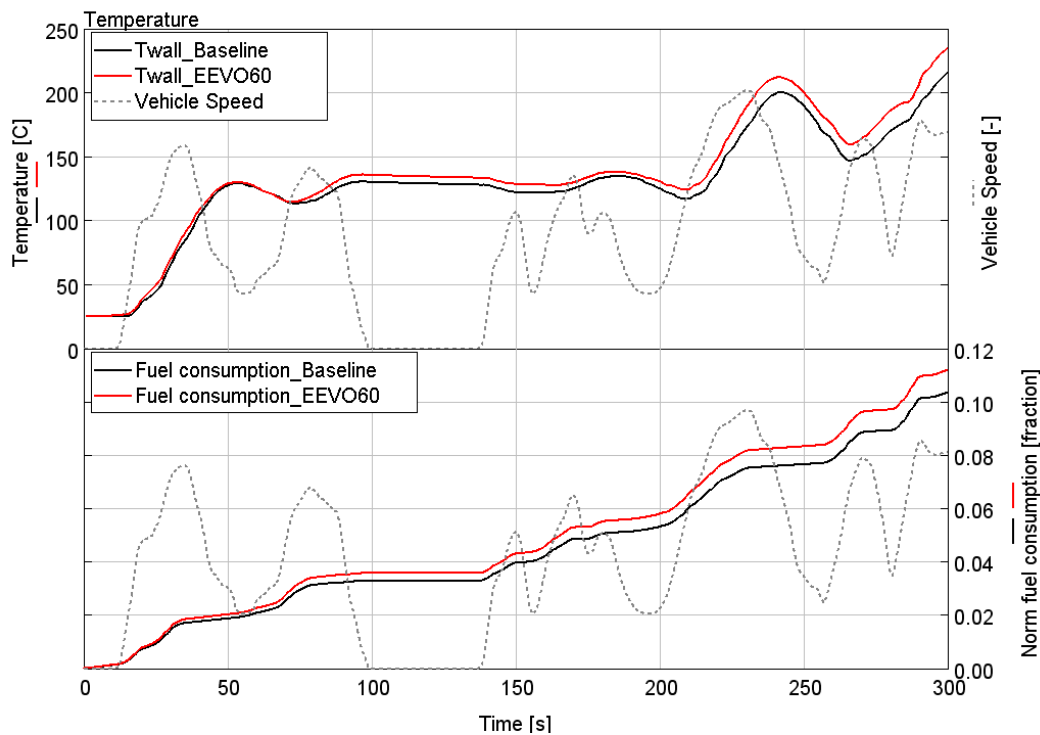


Figure 3.33 – Top: DOC monolith temperature in transient simulations for baseline (black) and EEVO60 (red) actuations. Bottom: normalized cumulated fuel consumption respect to the baseline value, in transient simulations for baseline (black) and EEVO60 (red) actuations – First 300 s of WLTC

In Figure 3.33 – top, DOC monolith temperature trend for baseline and EEVO60 actuations (and the relative normalized fuel consumption, bottom) for the first 300 s of WLTC. As shown, after 300 s, the increase in monolith temperature is equal to about 20°C.

3.2.4 Variable Exhaust Valve Timing

The same approach adopted for the assessment of the EEVO technique was used for obtaining the best configuration for the exhaust phasing. The reference exhaust valve timing was both advanced (no overlap between the valves but higher exhaust temperature due to the higher temperature of the gas) and retarded (increasing the overlap and the residual in-cylinder fraction), with a total number of 7 different timings. The tested valve lift profiles (-30, -20, -12, -6, +6, +12, +56 CA deg) are shown in Figure 3.34, where sign ‘-’ means advancing the baseline timing and sign ‘+’ means retarding the baseline timing.

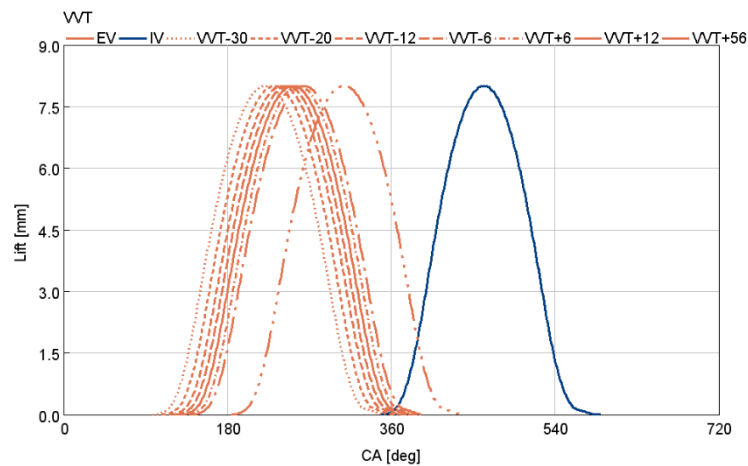


Figure 3.34 – VVT lift profiles tested [89]

Steady-state analysis

The results obtained from the Exhaust Phasing analysis are shown in Figure 3.35, Figure 3.36, and Figure 3.37 for the 6 engine key-points highlighted in Table 3.3, in terms of exhaust temperature (Equation 21) and BSFC difference (Equation 22).

Thanks to the adoption of the exhaust phasing, higher exhaust temperatures could be obtained. The highest values are obtained with the most advanced timing (high in-cylinder temperature thanks to the higher level of residual gas with respect to the baseline timing, as Figure 3.38 shows) and retarded timing (large overlap allows iEGR). Finally, it should be pointed out that the adoption of the most retarded timing (56 CA deg) is not feasible with the current combustion chamber, since it would require a 5 mm valve pocket in the piston head.

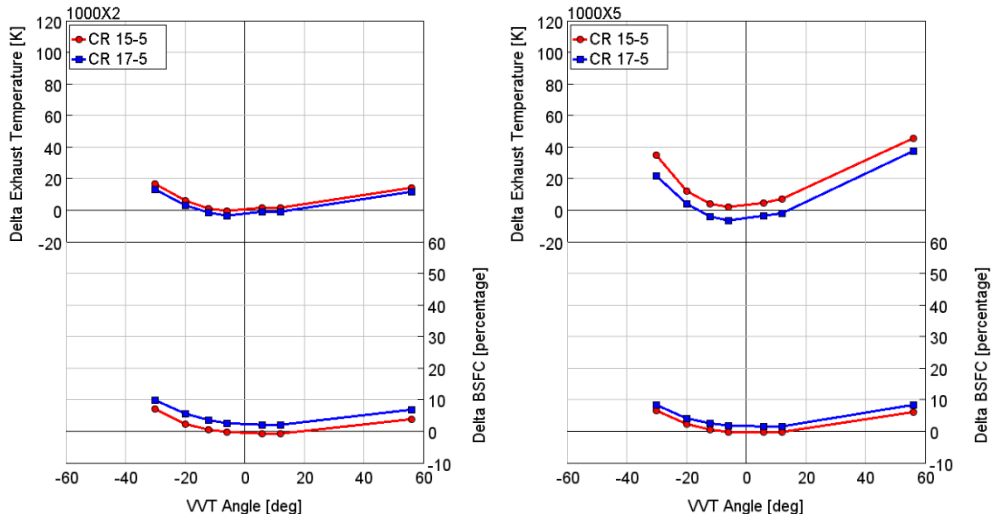


Figure 3.35 – Delta Exhaust Temperature (top) and delta BSFC (bottom) at different EV timings for 2 bar (left) and 5 bar (right) engine load – 1000 RPM [89]

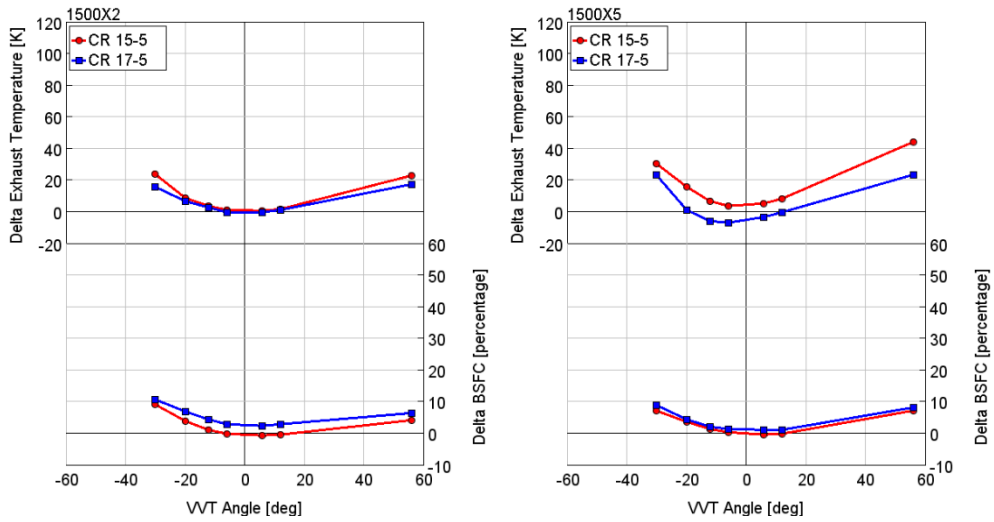


Figure 3.36 – Delta Exhaust Temperature (top) and delta BSFC (bottom) at different EV timings for 2 bar (left) and 5 bar (right) engine load – 1500 RPM [89]

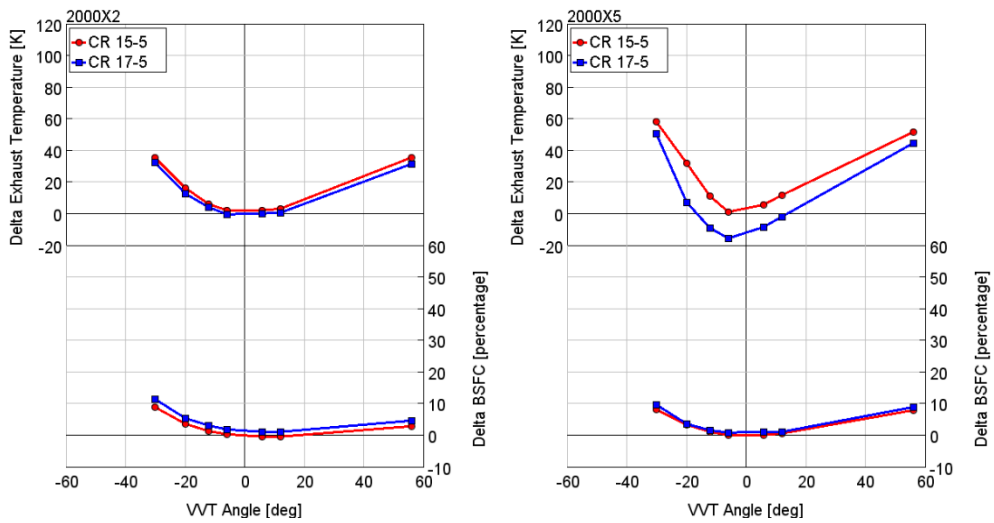


Figure 3.37 – Delta Exhaust Temperature (top) and delta BSFC (bottom) at different EV timings for 2 bar (left) and 5 bar (right) engine load – 2000 RPM [89]

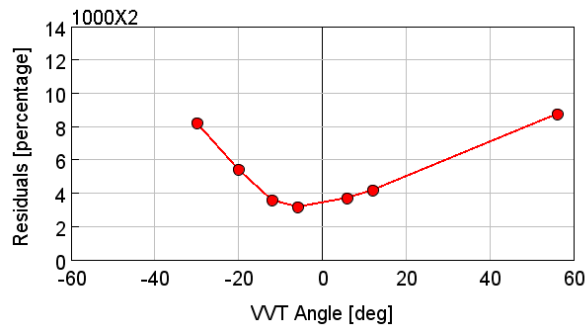


Figure 3.38 – Residual gas percentage at different EV timings - 1000 RPM X 2 bar BMEP [89]

Transient analysis

As Figure 3.35, Figure 3.36, and Figure 3.37 show, only 2 phasing values (-30, +56 CA) were chosen for WLTC simulations as the most promising lifts for obtaining high exhaust temperature values. Also in this case, the transient simulations were carried out considering the 15.5 CR because it can provide higher exhaust gas temperature with respect to the 17.5 CR.

As for the EEVO, the main results are shown in the following figures: Figure 3.39 shows the thermal power of the gas at turbine outlet and the relative delta between the two VVA timings and the baseline, Figure 3.40 the cumulated fuel consumption normalized with respect to the baseline value, and Figure 3.41 the AT simulation results in terms of aftertreatment monolith temperature and normalized fuel consumption for the first 300 s.

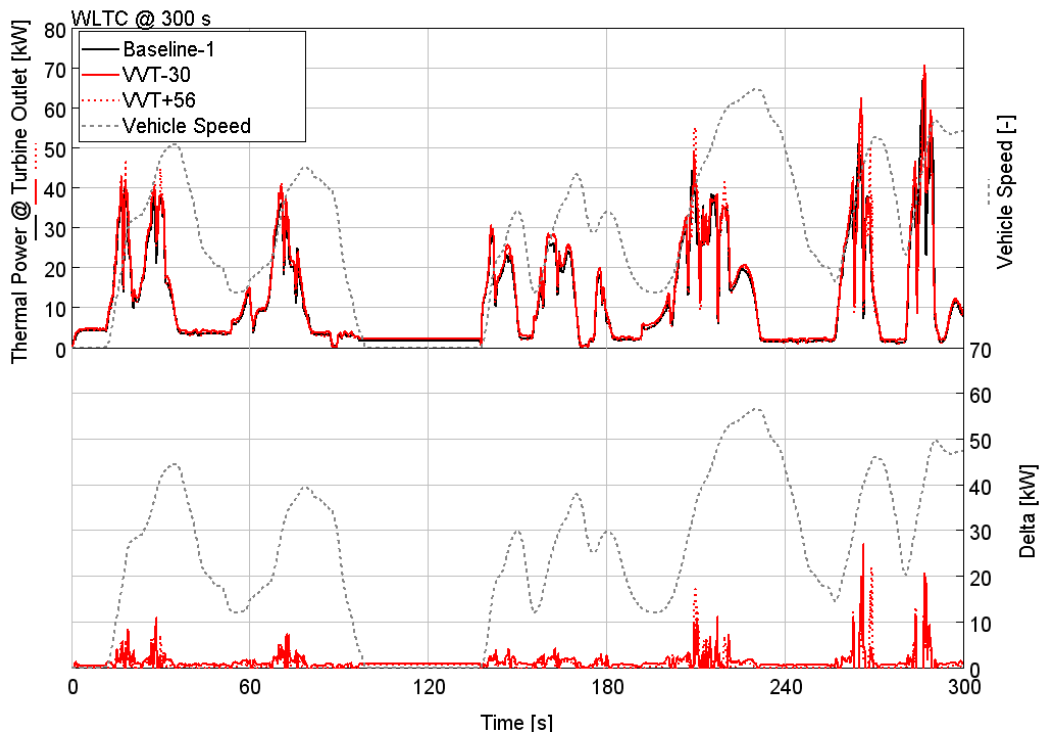


Figure 3.39 – Top: thermal exhaust power at turbine outlet in transient simulations for baseline (black), VVT-30 (red solid) and VVT+56 (red dashed) actuations. Bottom: relative delta between VVAs and baseline thermal power – First 300 s of WLTC [89]

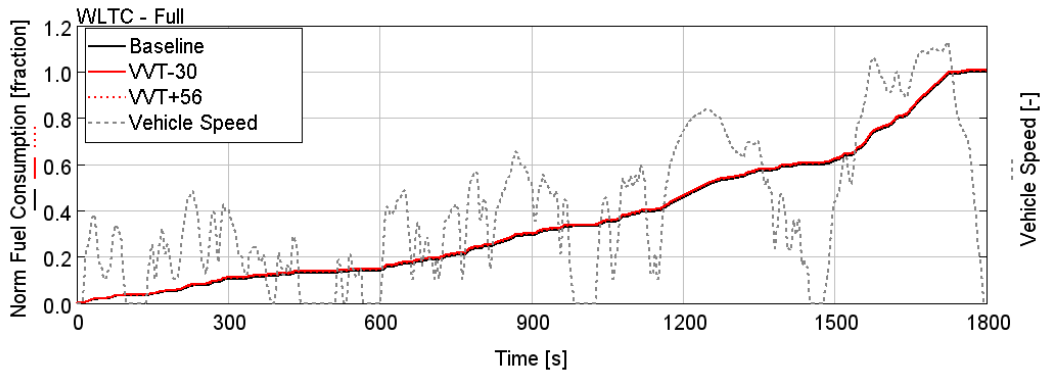


Figure 3.40 – Normalized cumulated fuel consumption respect to the baseline value, in transient simulations for baseline (black) VVT-30 (red solid) and VVT+56 (red dashed) actuations. [89]

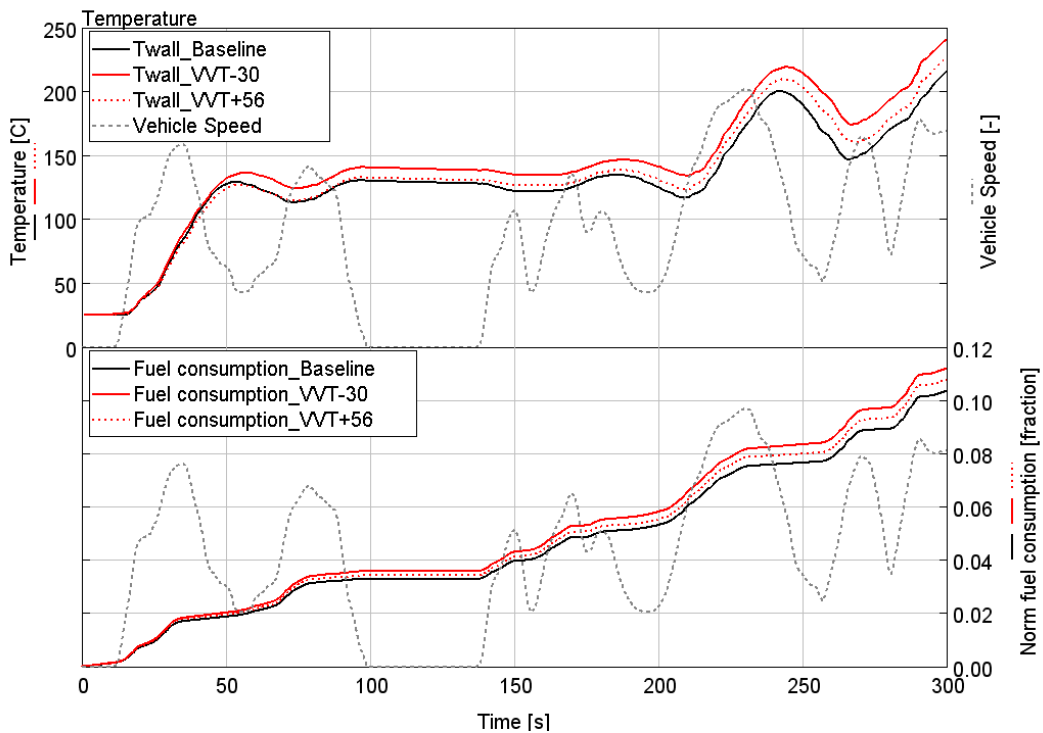


Figure 3.41 – Top: DOC monolith temperature in transient simulations for baseline (black), VVT-30 (red solid) and VVT+56 (red dashed) actuations. Bottom: normalized cumulated fuel consumption respect to the baseline value, in transient simulations for baseline (black) and VVAs (red) actuations – First 300 s of WLTC

Keeping constant the level of NO_x emissions for both timings with respect to the baseline, it is possible to increase the exhaust temperature at the turbine outlet, and consequently the thermal power for accelerating the warm up of the exhaust system. From the AT system simulation results, shown in Figure 3.41, advancing is more effective than retarding, leading to a temperature increase of about 25°C after 300 s instead of a limited increase of 10 °C only. Also in this case the effects of HC and CO oxidation on the DOC temperature were not taken into account.

The fuel penalty related to timing +56 is about 4.1% after 300 s and about 0.5% at the end of WLTC. Regarding timing -30, the fuel penalty is about 8.2% after 300 s and about 1% at the end of the cycle, as for the EEVO analysis. This value is significantly lower than the estimate under steady state operating conditions (which

was about 10%): this is due to the fact that the VVA lift is actuated for the initial 300 s only, and for some engine operating conditions only, which are impacting on the overall fuel consumption over the whole cycle by about 8%. The steady state trend for the two timings is confirmed by the transient analysis, where the -30 has an higher fuel consumption with respect to the +56 timing.

3.2.5 Exhaust Valve reOpening

Internal EGR can increase the exhaust gas temperature and reduce engine-out emissions thanks to a charge composition control achieved by an exhaust valve post-lift during the intake stroke or an intake valve pre-lift during the exhaust stroke [56,64,68,93,94]. In this analysis, the first approach was selected for evaluating the impact of the technique on the exhaust gas temperature and on fuel consumption since in literature it seems to be the more effective strategies in internal EGR exploitation .

In this context, Millo et al. in [62] presented a comparison between the two abovementioned different iEGR solutions for a small Diesel engine: by experimental analysis, the post-opening of the EV, although giving lower iEGR fraction, was shown to produce an higher reduction in NO_x, suggesting that the lower temperatures of the EGR play an important role. The post-opening lift respect to the IV pre-opening highlighted a potential reduction of NO_x of about 13% on the operating points representative of the ECE-40 driving cycle, without any detrimental effects on fuel consumption and soot emissions.

This result is also confirmed by Benajes et al. [95]: using as reference an inline six-cylinder engine, they found that the intake pre-lift event produced lower EGR rate than the exhaust reOpening event. Moreover, they stated that the internal EGR rate was influenced more by the engine speed than the load, and the higher engine speed the higher EGR rate is produced. Regarding the turbulence level within the cylinder, they found that the exhaust reOpening significantly reduces the swirl ratio, while the intake pre-lift does not.

The reOpening was evaluated by Edwards et al in [84] as well, founding that the selected strategy gives higher cylinder charge temperature with respect to the intake pre-lift.

Steady-state analysis

For this technique a different approach in terms of EV profile selection was used: for each key-point highlighted in Table 3.3, 36 different combinations of maximum lift of EV reOpening and phasing respect to the main EV closure timing were analyzed, as shown in Figure 3.42 (maximum reOpening lift variation) and Figure 3.43 (reOpening phase variation).

For EVrO evaluation, two different EGR configurations were simulated: one considering the iEGR only thanks to the reOpening (the high pressure EGR valve is closed and the NO_x target is reached only by the residual mass fraction from the exhaust port), the other one with iEGR in combination with a low pressure EGR

(LPEGR) in order to obtain a more extended zone in the engine map where EVrO could be helpful. For each of these simulations, a different DoE analysis was performed: in the case of iEGR, only the rack position was changed in order to reach a proper value of boost pressure as well as a suitable backpressure for recirculating hot exhaust gases; when combining the iEGR with the LPEGR, the DoE was instead focused on turbine rack position and EGR valve variations.

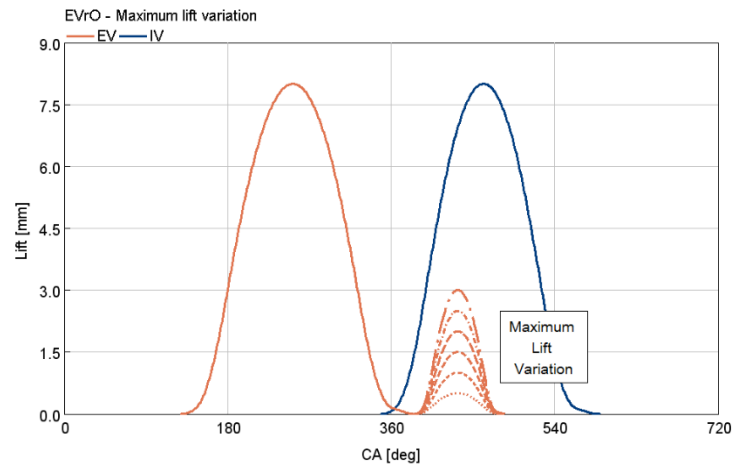


Figure 3.42 – EvrO lift profiles tested: maximum lift is the peak value of the secondary lift [89]

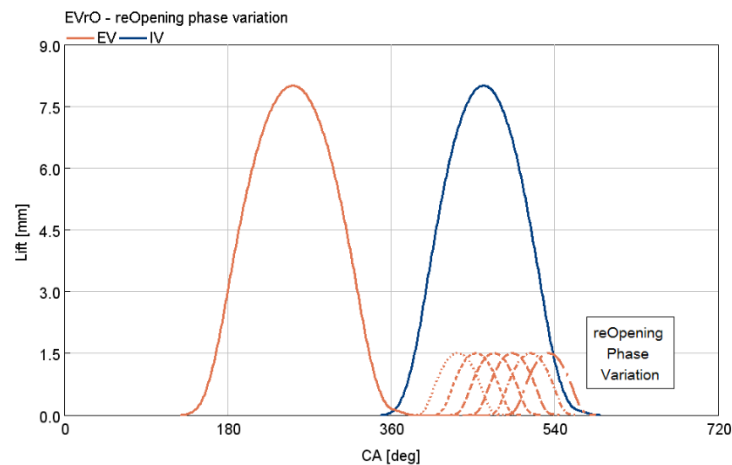


Figure 3.43 – EvrO lift profiles tested: reOpening phase is the angle between the closure of the main EV lift and the opening of the re-breathing [89]

In Figure 3.44, Figure 3.45, Figure 3.46, Figure 3.47, Figure 3.48 and Figure 3.49 the results in terms of delta exhaust temperature (Equation 21) and delta BSFC (Equation 22) are shown. The response surfaces have on X-axis the value (in mm) of the secondary EV lift peak and on Y-axis the angle interval (in deg) between the closure of the main EV event and the opening of the re-breathing. The results show an increment in terms of exhaust temperature by using the EV re-breathing that is always linked to an higher BSFC, as expected. Moreover, by blending the external and the internal EGR, it is possible to extend the zone in the engine map where the EVrO can be used. On the other hand, at low load by using a LPEGR the exhaust temperature increment is lower respect to the iEGR-only strategy, but with lower fuel penalties.

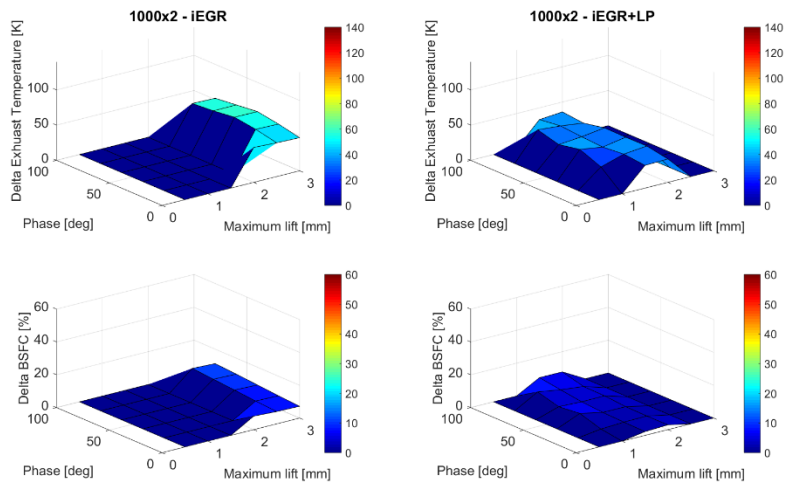


Figure 3.44 – Delta exhaust temperature and delta BSFC at different EVrO actuations with only iEGR (left) and iEGR+LPEGR (right) configurations – 1000 RPM X 2 bar BMEP [89]

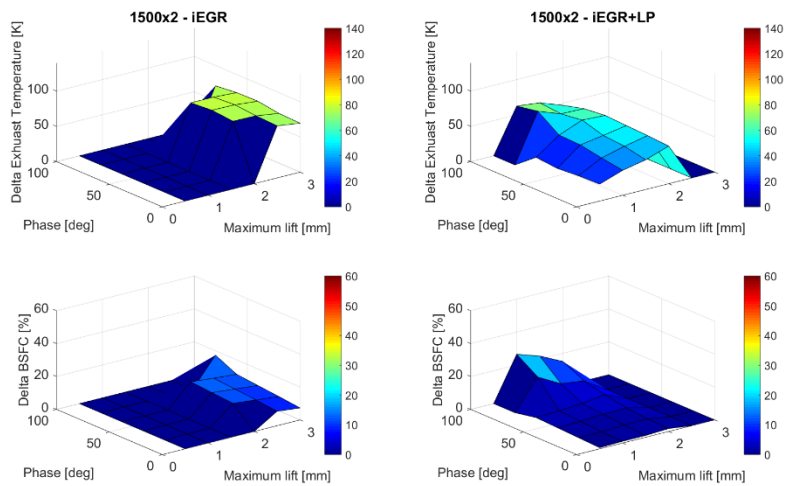


Figure 3.45 – Delta exhaust temperature and delta BSFC at different EVrO actuations with only iEGR (left) and iEGR+LPEGR (right) configurations – 1500 RPM X 2 bar BMEP [89]

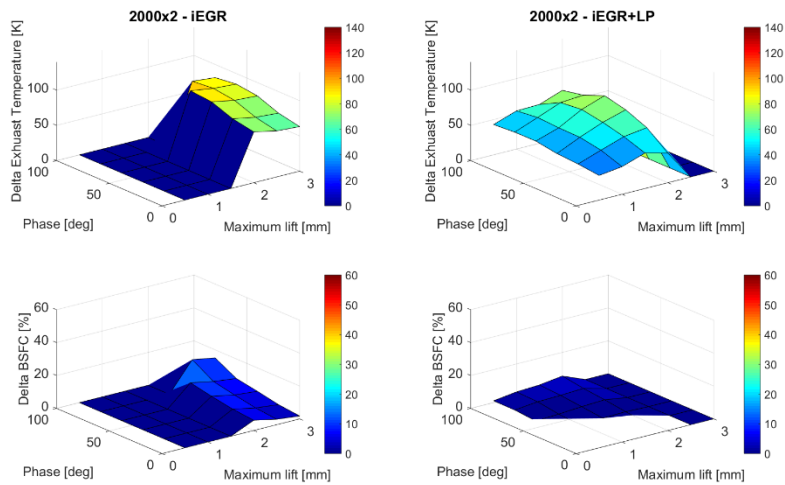


Figure 3.46 – Delta exhaust temperature and delta BSFC at different EVrO actuations with only iEGR (left) and iEGR+LPEGR (right) configurations – 2000 RPM X 2 bar BMEP [89]

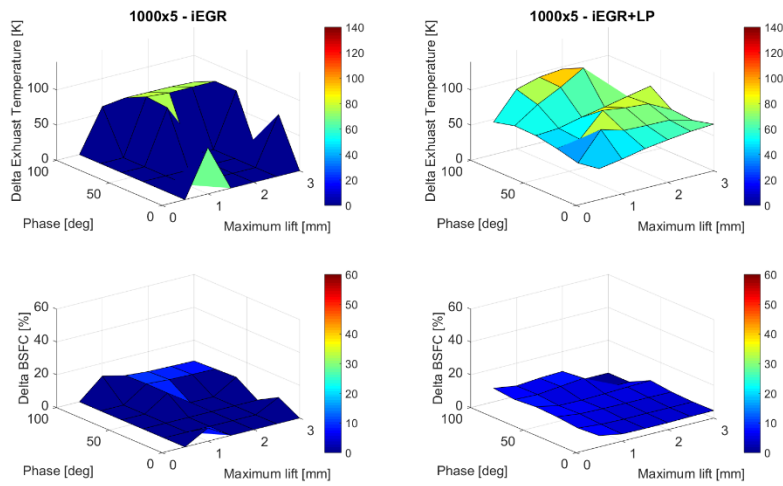


Figure 3.47 – Delta exhaust temperature and delta BSFC at different EVrO actuations with only iEGR (left) and iEGR+LPEGR (right) configurations – 1000 RPM X 5 bar BMEP [89]

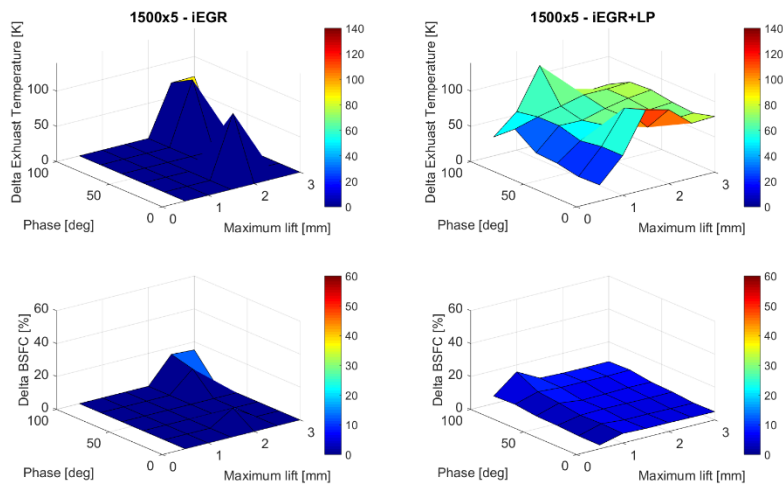


Figure 3.48 – Delta exhaust temperature and delta BSFC at different EVrO actuations with only iEGR (left) and iEGR+LPEGR (right) configurations – 1500 RPM X 5 bar BMEP [89]

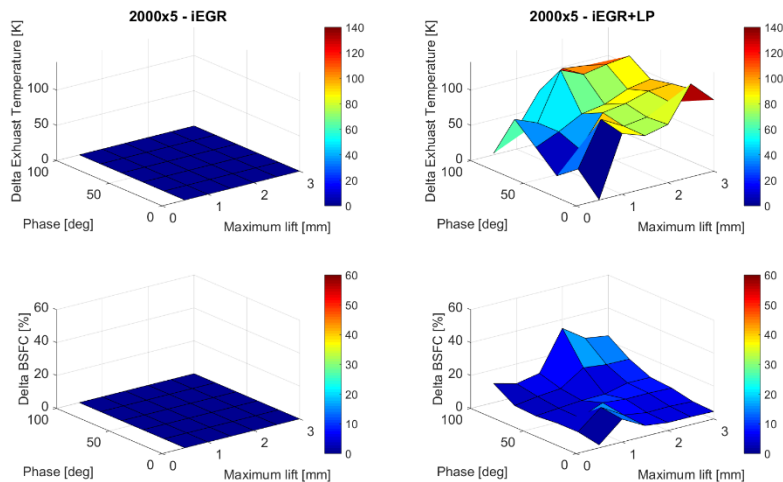


Figure 3.49 – Delta exhaust temperature and delta BSFC at different EVrO actuations with only iEGR (left) and iEGR+LPEGR (right) configurations – 2000 RPM X 5 bar BMEP [89]

As it can be seen clearly from the results the reOpening phase for the iEGR-only configuration has a significant impact on BSFC at constant re-breathing lift peak: a more detailed cylinder pressure analysis has shown that this phasing effect is caused by the PMEP worsening and not by the heat transfer increment. As an example, Table 3.4 shows the simulation results for the 1000 RPM X 2 bar BMEP engine point and 3.0 mm lift at two different phase levels: the high pressure ISFC is almost the same with different high pressure IMEP values.

Table 3.4 – Comparison between 0 and 80 CA deg of reOpening phase with 3.0 mm as maximum lift – 1000 RPM X 2 bar BMEP [89]

		reOpening phase = 0 CA	reOpening phase = 80 CA
IMEP ₃₆₀	bar	3.37	3.49
PMEP	bar	0.07	0.16
ISFC ₃₆₀	bar	219.7	220.0

Transient analysis

The WLTC evaluation was carried out considering the iEGR-only configuration with the best single-step solution. The trade-off between delta exhaust temperature and delta BSFC shows that the best configuration is 3.0 mm (maximum lift) X 80 CA (reOpening phase) for the secondary open of the EV. The results are shown in Figure 3.50, Figure 3.51 and Figure 3.52.

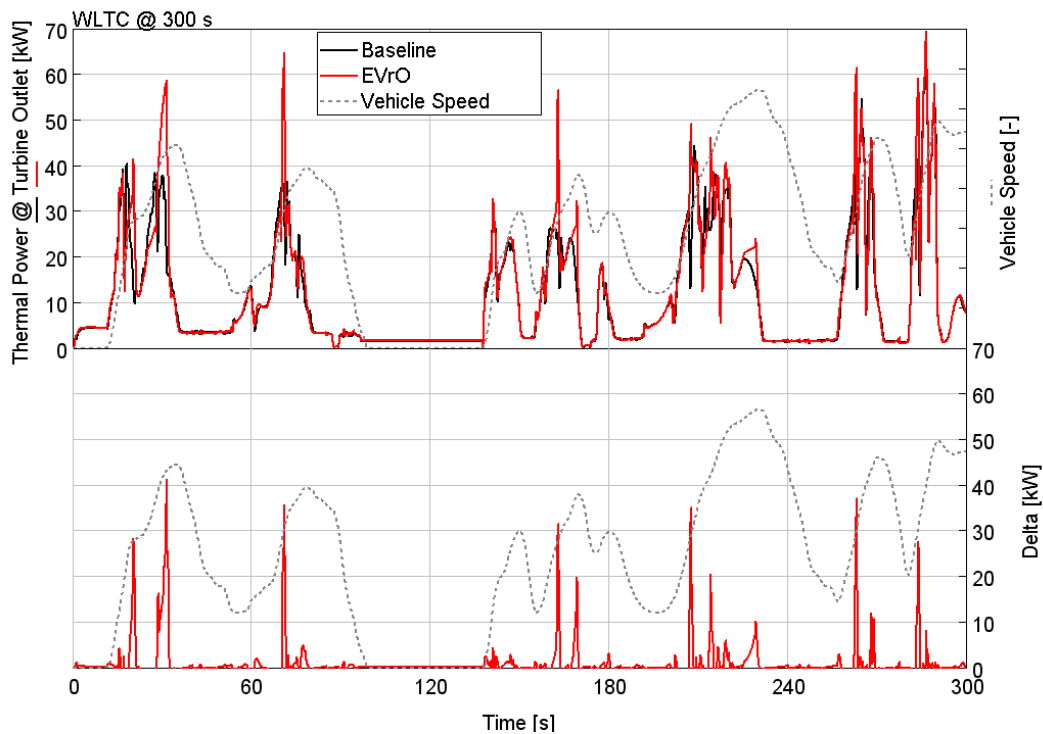


Figure 3.50 – Top: thermal exhaust power at turbine outlet in transient simulations for baseline (black) and EVrO 3.0 mm X 80 CA (red) actuations. Bottom: relative delta between VVA and baseline thermal power – First 300 s of WLTC [89]

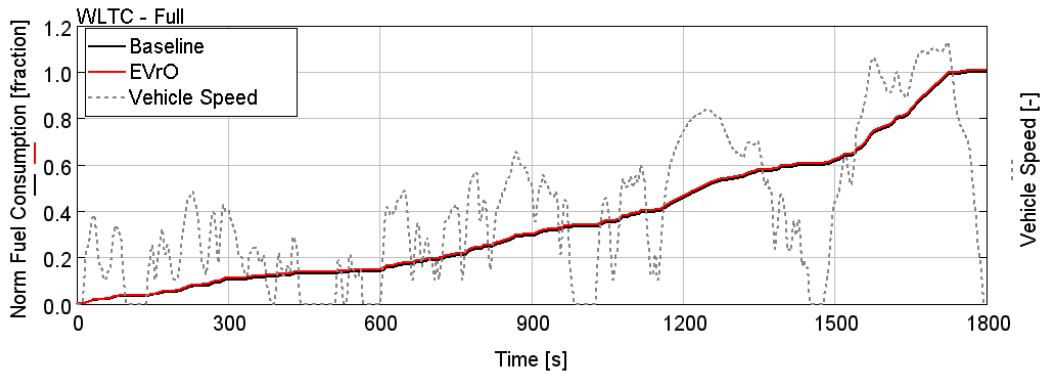


Figure 3.51 – Normalized cumulated fuel consumption respect to the baseline value, in transient simulations for baseline (black) and EVrO 3.0 mm X 80 CA (red) actuations. [89]

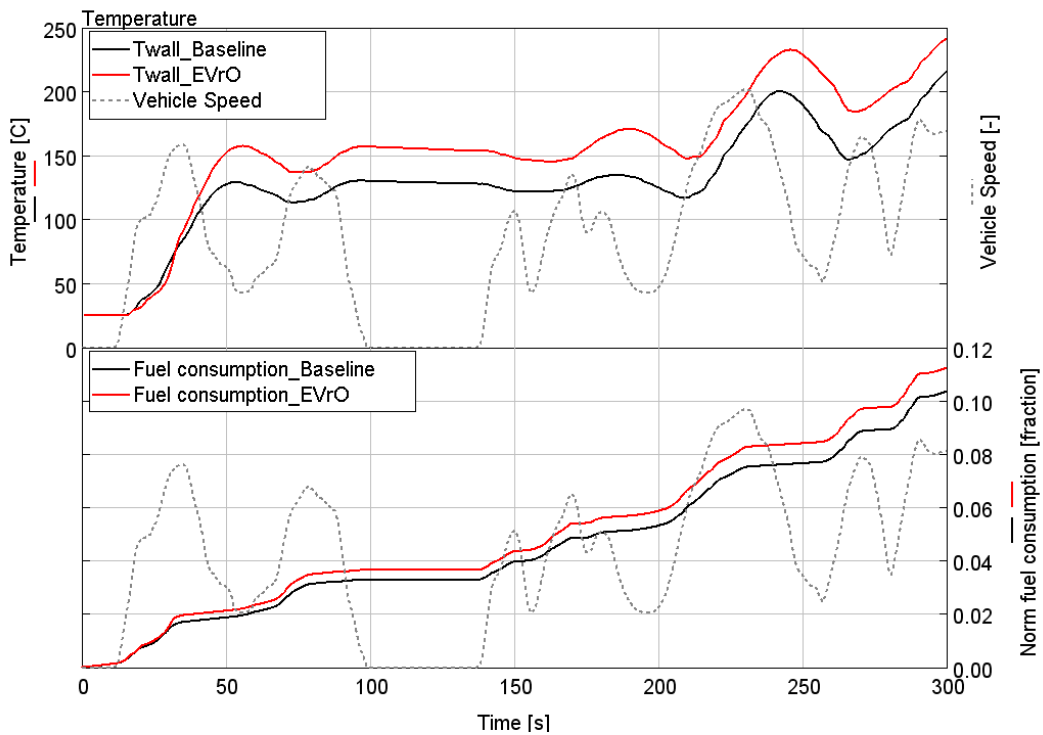


Figure 3.52 – Top: DOC monolith temperature in transient simulations for baseline (black) and EVrO 3.0 mm X 80 CA (red) actuations. Bottom: normalized cumulated fuel consumption respect to the baseline value, in transient simulations for baseline (black) and VVAs (red) actuations – First 300 s of WLTC

From Figure 3.50, it can be observed that EVrO can provide very high peaks of exhaust thermal power due to the high iEGR fraction that is hotter respect to the external one with a limited fuel consumption penalty (about 1% at the end of WLTC in Figure 3.52) without exceeding NO_x emission levels. More specifically, after 300 s, considering only the part of cycle where EVrO works, the fuel penalty is about 8.5%. The AT system simulation in Figure 35 shows that after the first 300 s of the WLTC it is possible to increase the DOC monolith temperature of about 28°C. This result confirms the steady state outcomes, where the EVrO appears to be the most promising technique for obtaining high value of exhaust gas temperature.

3.3 Summary of the results

The simulation study presented in this chapter was carried out in order to evaluate and identify the best VVA strategies to be implemented in a passenger car Diesel engine in order to both increase the engine efficiency and accelerate the aftertreatment system warm up.

Regarding the CO₂ reduction aim, the following 3 different techniques were scrutinized under steady-state operating conditions:

- Late Intake Valve Opening (LIVC) – This strategy allows efficiency improvements only at lower load and the larger the lift profile, the higher the BSFC benefit. However, the trend becomes opposite at higher load as shown in Figure 3.53, where the BSFC trend was shown on the engine map considering the most retarded simulated valve lift.
- Late Exhaust Valve Opening (LEVO) – LEVO strategy does not lead to significant benefits in BSFC reduction with any of the investigated valve lift profiles. A retarded opening of the EV causes an increase in pressure inside the cylinder during the initial part of the exhaust stroke that results in an increment of pumping losses.
- Exhaust Phasing (VVT) – No significant benefits could be achieved in terms of BSFC reduction with any of the investigated valve lift phasings, nor by advancing the EVO, nor retarding the EVO. More specifically, the higher expansion work is offset by the increase of the pumping work at the beginning of the exhaust stroke.

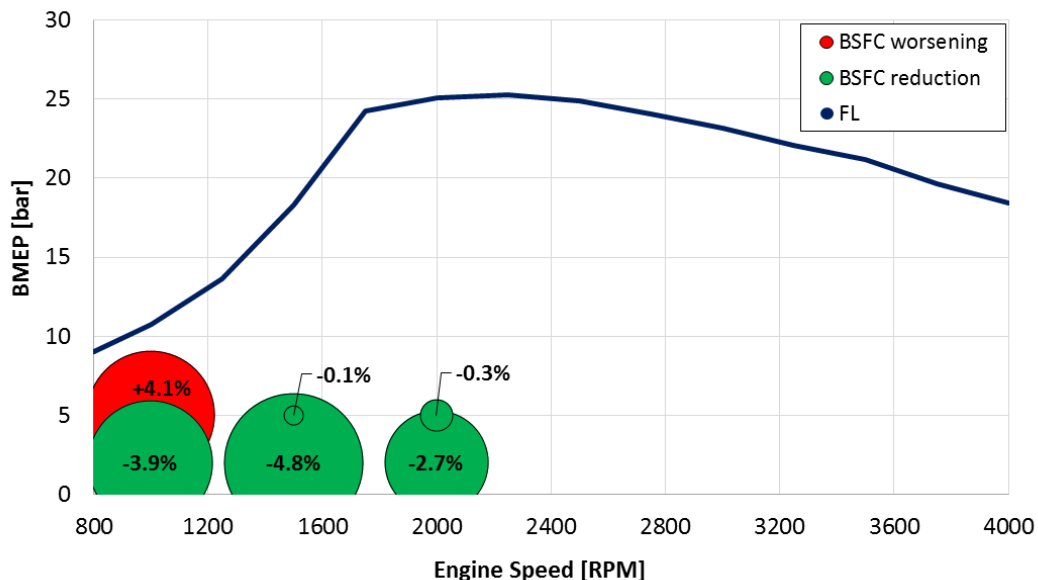


Figure 3.53 – LIVC60 steady state results in terms of BSFC difference on the engine map

Since only LIVC showed significant reduction in terms of fuel consumption (up to 5% at low engine loads) without exceeding the baseline Brake Specific

engine-out NO_x emissions, the actuation was simulated under transient conditions, for evaluating its BSFC reduction potential over the whole WLTC. Results showed that even if LIVC leads to significant efficiency improvements in steady-state analysis, its actuation is limited to a part load zone that has a low impact on the total fuel consumption.

As far as the aftertreatment warmup improvement is concerned, the following 3 different techniques were scrutinized both in steady state and in transient conditions:

- Early Exhaust Valve Opening (EEVO) – advancing the EVO, the exhaust temperature increases due to the reduced expansion in the cylinder. However, the lower expansion work collected by the piston gives higher BSFC. EEVO60 with CR 15.5 was chosen as best EEVO technique for the WLTC simulation since it gives the best compromise between temperature increment and BSFC worsening.

The EEVO60 steady state results in terms of exhaust temperature difference respect to the conventional actuation are shown in Figure 3.54.

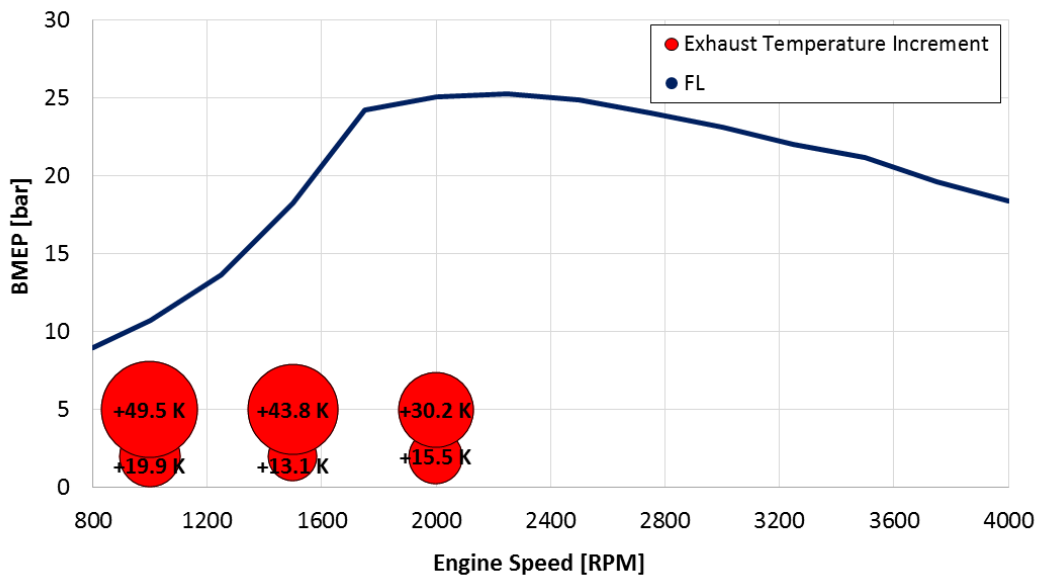


Figure 3.54 – EEVO60 steady state results in terms of exhaust temperature difference on the engine map

- Exhaust Phasing (VVT) - Thanks to an exhaust phasing variation, higher exhaust temperatures could be obtained linked to a not negligible BSFC penalt. The highest values are obtained with the most advanced and most retarded timing. VVT-30 and VVT+56 (sign ‘-’ means that the profile was rigidly advanced, ‘+’ retarded) were chosen for WLTC simulations. It is worth to point out that the most retarded one is not feasible with the actual combustion chamber because it would require a 5 mm valve pocket in the piston head.

The VVT-30 steady state results in terms of exhaust temperature difference respect to the conventional actuation are shown in Figure 3.55.

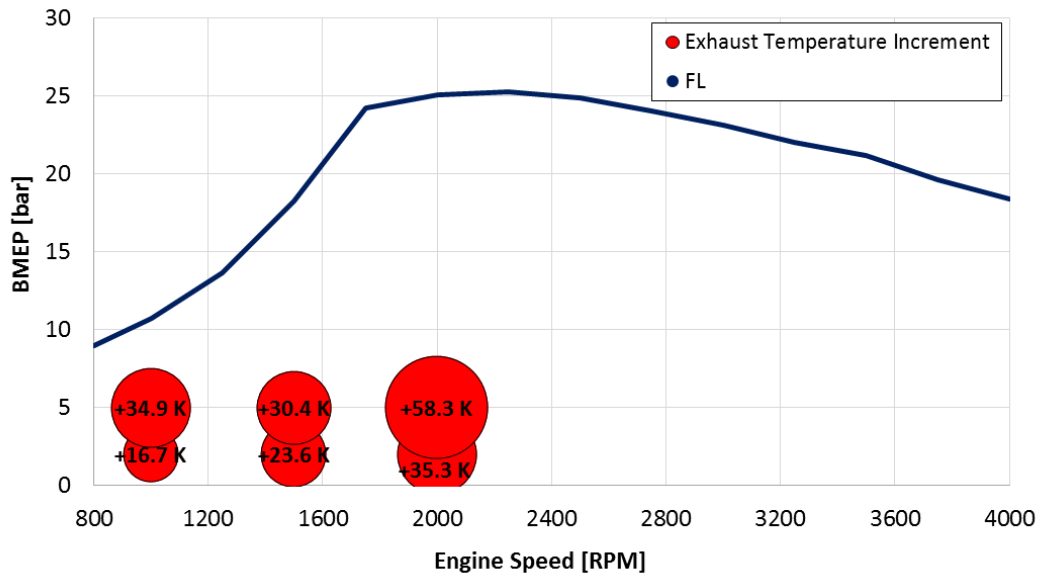


Figure 3.55 – VVT-30 steady state results in terms of exhaust temperature difference on the engine map

- Exhaust Valve reOpening (EVrO) – in order to properly evaluate the effect of EVrO, two different EGR configurations were simulated: one considering the iEGR provided by the ReOpening, the other one with iEGR in combination with a low pressure EGR to extend the zone in the engine map where EVrO could be helpful. Moreover, 36 different combinations of maximum lift of EV reOpening and phasing respect to the main EV closure timing were analysed. The results show an increment in terms of exhaust temperature by using the EV re-breathing that is always linked to an higher BSFC. The BSFC worsening effect could be mitigate by blending the external and internal EGR, but a lower exhaust temperature increment would be obtained. The WLTC evaluation was carried out considering the iEGR-only configuration with the best single-step solution. The trade-off between delta exhaust temperature and delta BSFC shows that the best configuration is 3.0 mm (maximum lift) X 80 CA deg (reopening phase) for the secondary open of the EV.

The EVrO (3.0 mm X 80 CA deg) steady state results in terms of exhaust temperature difference respect to the conventional actuation are shown in Figure 3.56.

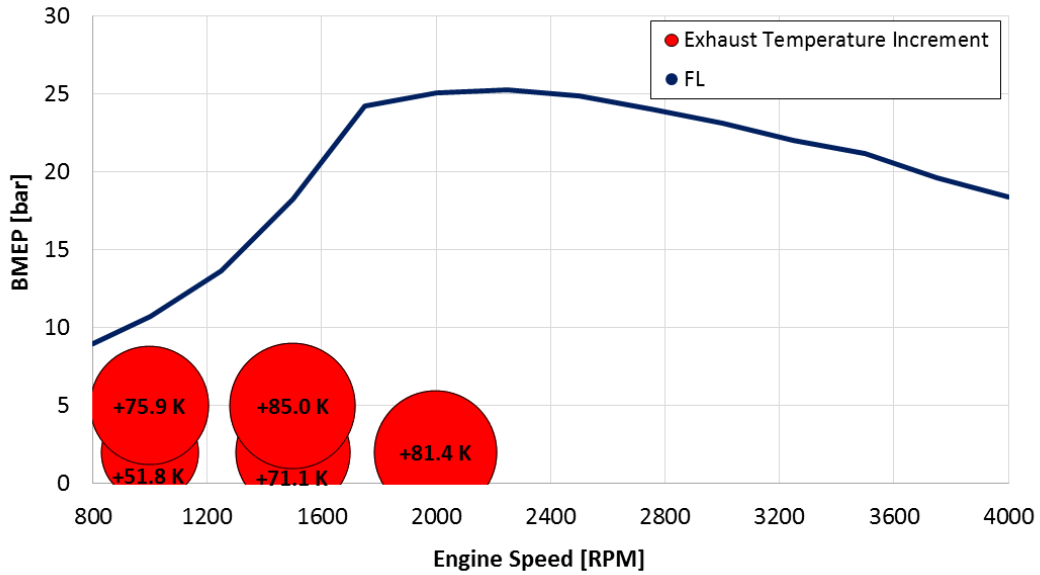


Figure 3.56 – EVrO (3.0 mm X 80 CA deg) steady state results in terms of exhaust temperature difference on the engine map

Regarding the transient analysis, all the 3 abovementioned VVA strategies allowed achieving significant increases in the exhaust gas temperature after cold start, with generally negligible or acceptable fuel penalties (lower than 1% on WLTC). Confirming the steady state results (Figure 3.54, Figure 3.55, Figure 3.56), the most promising technique was EVrO, with which a monolith temperature increment of about 30°C could be achieved at 300 s after the start of the WLTC.

A resume of the results is shown in the histogram in Figure 3.57.

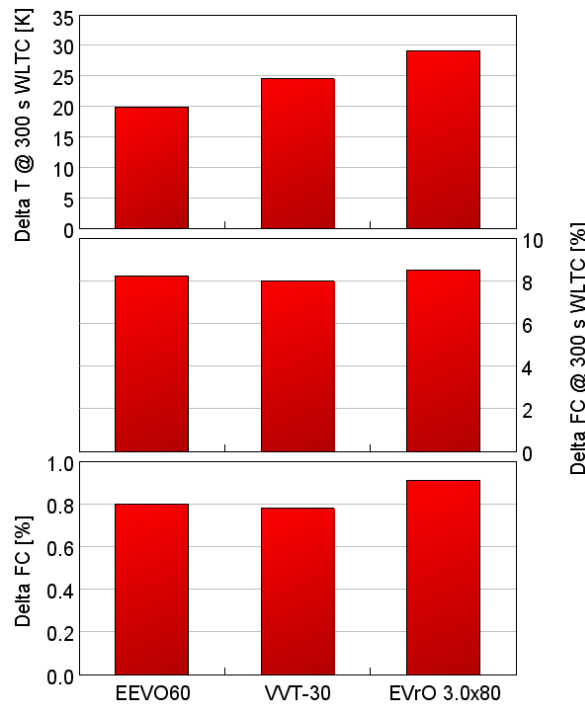


Figure 3.57 – WLTC results for warmup improvement strategies: aftertreatment monolith temperature @ 300 s WLTC (top), delta fuel consumption difference @ 300 s (center) and @ end of WLTC (bottom)

Regarding the EVrO application further investigations would be focused on the control point of view since EVrO could achieve a reduction in transport time when iEGR is used compared with external EGR. This could provide a faster control response during transient operation, with some emissions reductions. Moreover, a secondary EV lift during the main IV event could realize scavenging, with direct flow from the intake to the exhaust side, allowing a significant increase in the low-end torque.

Chapter 4

II part: Fuel injection system optimization

Part of the work described in this Chapter was also previously published in the following publications.

- Sapio, F., Piano, A., Millo, F., and Pesce, F., "Digital Shaping and Optimization of Fuel Injection Pattern for a Common Rail Automotive Diesel Engine through Numerical Simulation," SAE Technical Paper 2017-24-0025, 2017, <https://doi.org/10.4271/2017-24-0025>.
- Piano, A., Millo, F., Sapio, F., and Pesce, F., "Multi-Objective Optimization of Fuel Injection Pattern for a Light Duty Diesel Engine through Numerical Simulation," SAE Technical Paper 2018-01-1124, 2018, <https://doi.org/10.4271/2018-01-1124>.

Common Rail Fuel Injection Systems (FIS), in conjunction with multiple injection strategies, have proven to be very effective in reducing fuel consumption, combustion noise and emissions, when applied to Compression Ignition (CI) engines [96–105]. Latest developments in FIS have allowed an increase in the number of injection events per engine cycle, leading to a more accurate control of the combustion process. Although, the efficient calibration and management of such technologies represent a real engineering challenge due to the large number of parameters involved. Injection timing and quantity for up to 10 injection events per engine cycle need to be properly calibrated, in addition to other engine parameters, in order to reduce both fuel consumption and combustion noise without exceeding the target emissions level. In order to fully exploit the potential of the abovementioned fuel injection strategy optimization, numerical simulation can play a fundamental role by allowing the creation of a kind of a virtual test rig, where the input is the fuel injection rate and the optimization targets are the combustion outputs, such as the burn rate, the pollutant emissions and the combustion noise.

With this aim, a numerical fuel injection optimization process was carried out on the selected engine presented in Chapter 1 (Table 2.1). 3 different optimization approaches were evaluated with the aim of identifying the ideal fuel injection strategies which should be performed in order to minimize BSFC, Combustion Noise without exceeding the BSNO_x baseline value.

The numerical analysis was carried out considering 3 steady state engine operating conditions in the low-medium speed and low-medium load range (reported in Table 4.1), which can be considered representative of a typical type approval driving cycle engine conditions.

Table 4.1 – Selected key-points for injection optimization

Engine Speed [RPM]	BMEP [bar]
1500	2.0
1500	5.0
2000	8.0

4.1 Simulation setup

In order to fully exploit the potential of the fuel injection strategy digitalization, a kind of virtual test rig was developed in GT-SUITE environment. The main characteristics are briefly summarized as follows

Reduced engine model

A detailed model includes all the engine's subsystems such as the turbocharger, the EGR circuit, all the pipes and volumes from the airbox to the exhaust pipe, with all the cylinders and injectors. In this configuration, shown in Figure 4.1, the model is able to reproduce the engine's behaviour accurately, however the required computational time is not suitable for simulations characterized by a large number of cases.

Figure 4.2 represents the developed simplified configuration, based on a single cylinder with valves, injection system and intake/exhaust ports, in order to reduce computational time. Information about intake and exhaust temperature, pressure and EGR rate were collected from the abovementioned detailed model and given as boundary conditions for the simulation. The previously introduced Injection Rate Map was integrated into the model as well as the calibrated predictive DIPulse: as already pointed out, the Injection Rate Map is not able to capture the dynamic pulse-to-pulse interaction effect. For this reason, the fuel injection strategy obtained from the optimization process can be defined 'ideal', since the constraints and limitations of the real hardware were not taken into account.

A control unit able to manage engine load, injection timing and duration, swirl level and MFB50 position was implemented into the model.

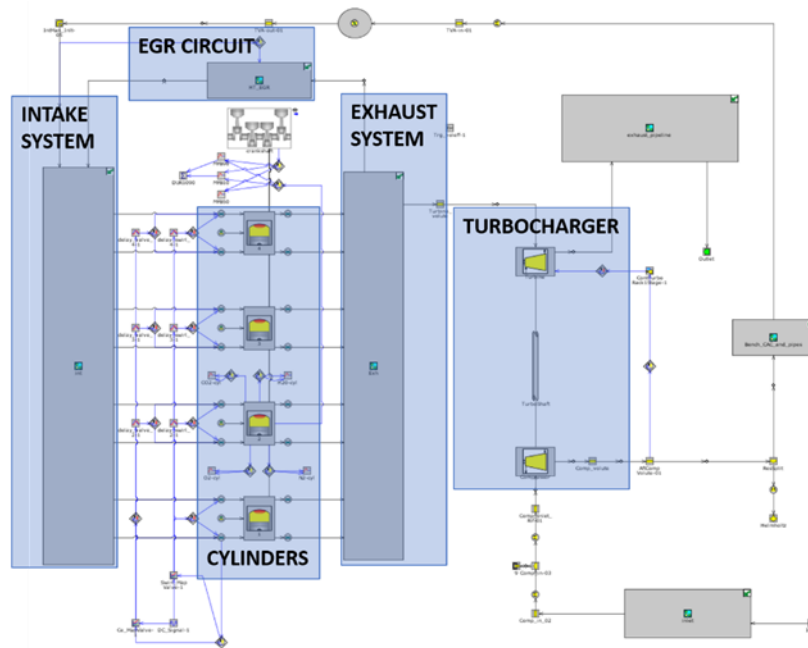


Figure 4.1 – Detailed engine model [106]

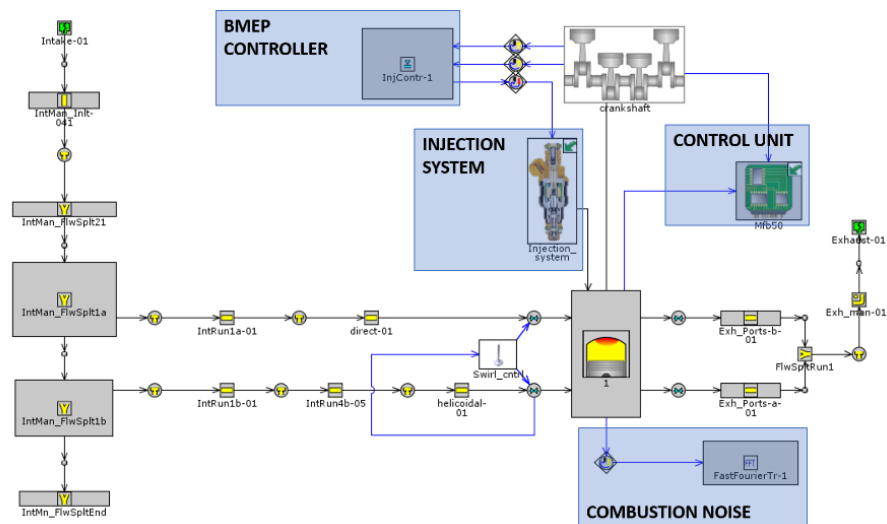


Figure 4.2 – Reduced engine model [106]

With this configuration, turbocharging system, detailed injector model, EGR circuit and part of intake and exhaust systems were no longer required, significant improvements in computational time were obtained while maintaining a satisfactory agreement with the detailed model results, as shown in Figure 4.3 – right. The average CPU time required to the detailed model in order to run the 3 key-points was reduced of an order of magnitude with the simplified configuration (Figure 4.3 – left).

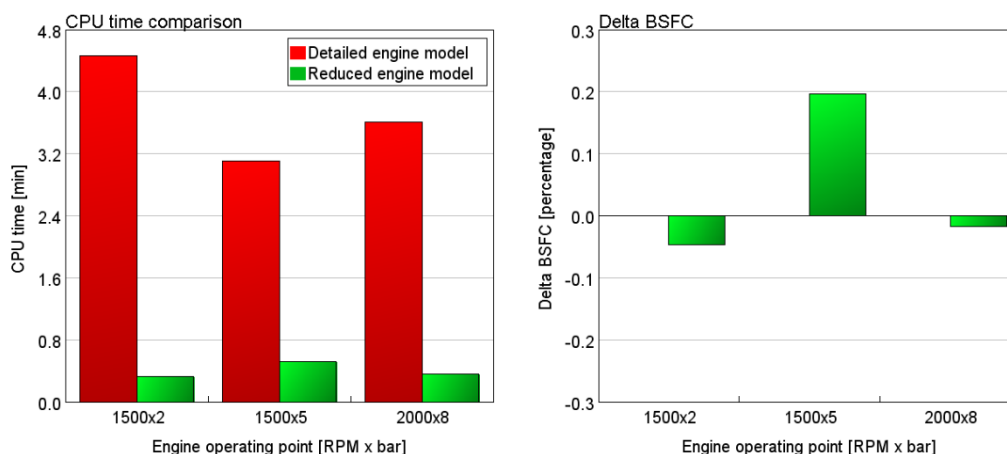


Figure 4.3 – Detailed (red) and reduced (green) engine model configuration comparison for selected key-points: CPU time (left), BSFC (right)

Combustion noise evaluation

Since in GT-SUITE combustion noise was not available directly as a simulation result, a user subroutine has been developed and validated over a large set of experimental data.

First, the power spectrum of the cylinder pressure signal was obtained through a Fast Fourier Transform. A digital low pass filter was applied to clean the signal from the high-frequency content, related to normal modes of the gas and acquisition's noise, which is not meaningful as far combustion noise is concerned [107]. At this end, GT-SUITE provides different digital filters [107]. In this analysis, the 24th order one was used, which provides full attenuation for frequencies higher than half of the maximum one in the spectrum. The power spectrum of the signal was divided in octave bands and the attenuation, introduced from the engine structure and the human ear, was applied according to the AVL [108,109] and A weighting curves respectively.

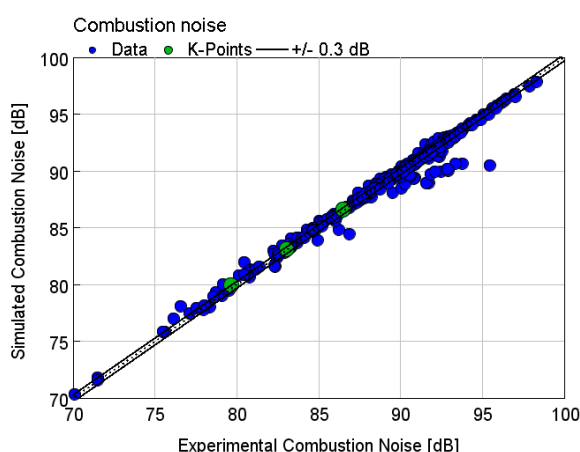


Figure 4.4 – GT-SUITE and experimental combustion noise comparison. Engine map points in blue, key-points in red [106]

Results were validated over the whole engine map, which consists of 337 different operating points. Experimental in-cylinder pressure traces were given as inputs for the subroutine obtaining a more than satisfactory agreement with the experimental data, as shown in Figure 4.4. The obtained average error lies within the ± 0.3 dB band.

4.2 Optimization process

Since the aim of this work is to find an ideal trend of injection strategies in order to optimize the combustion process by minimizing the BSFC, BSNO_x and Combustion Noise, several optimization processes were considered. First of all, the input variables and the design space, in which they can be optimized during the process, were defined. In Table 4.2, the injection parameter inputs are highlighted: it is clear that the very high number of independent variables increases the complexity of the optimization problem.

Several optimization approaches can be found in literature and they can be summarized as follows:

- DoE – It is a powerful tool for problems with multiple input variables that can be manipulated, determining their effect on the chosen outputs.
- Single-Objective (SO) – The objective of an optimizer is to minimize or maximize a so-called objective function, which can be a single output, such as, for instance, fuel consumption, or a combination of a certain number of outputs such as, for instance, fuel consumption and combustion noise.
- Multi-Objective (MO) – Differently from the Single-optimization study, in this approach the optimizer takes into account multiple dependent variables that can be simultaneously minimized or maximized.

Each approach relies on different methods, the selection of which is a fundamental step in the optimization process. The optimization methods can briefly be categorized in local or global optimizers, depending on the solution provided by the process. More specifically, when the output function $f(x)$ is multimodal, local optimizer, using steepest gradient search direction, could converge to a local optimum. Moreover, its performance will strongly depend on the process initialization. On the other hand, the stochastic methods, used by global optimizer, will search the solution in the entire design space and will be independent from the initial conditions of the process [110].

4.2.1 DoE approach

In order to identify, for each of the 3 selected operative points, the injection rate that offers the best performance in terms of brake specific fuel consumption, NO_x emissions and combustion noise, a Full Factorial DoE approach was chosen.

Full Factorial DoE is a procedure through which all combinations of variables levels are explored: in other words, if the idea is to estimate the effect by varying

the independent variables X_1 (on a levels) and X_2 (on b levels), $N = a \cdot b$ combinations must be analysed. The advantage of this approach is that the resulted exploration of the domain is organic and the multiple dependent variables can be manipulated, determining their effect on the chosen outputs.

According to this procedure [110,111], input variables are divided in a user-defined number of levels and then all the possible combinations between levels are produced and tested through the previously introduced virtual test-rig. The accuracy of a full factorial analysis increases with the number of levels defined for each input variable as well as the computational time required for the simulation.

The number of levels for each variable was defined carefully in an attempt to provide both the highest accuracy and a reasonable computational time. Table 4.2 shows the minimum, maximum and number of levels chosen for each variable.

Table 4.2 – Full Factorial DoE settings [106]

Parameter name		Minimum value	Maximum value	Number of levels
Number of Pilot	-	0	5	6
Injected mass	<i>mg</i>	0.4	1.5	5
Dwell time	<i>ms</i>	0.0	3.0	6
Rail pressure	<i>bar</i>	200	2000	10
Delta SOI Main (wrt baseline)	<i>deg</i>	-4.0	+4.0	5
EGR rate	<i>fraction</i>	0.0	0.5	6

Results

As a result, an average of 500'000 different injection patterns were produced and tested, for each of the mentioned operating points. These patterns were evaluated in terms of BSFC, BSNOx and CN outcomes, through the virtual test-rig. In order to provide a baseline reference to compare results, outcomes for experimental injection profiles were also calculated through the same test-rig model. The results of the analysis were normalized with respect to the baseline value, by the definition of the following 3 factors.

- BSFC factor

$$f_{BSFC} = \frac{BSFC_{optimized}}{BSFC_{baseline}}$$

- BSNOx factor

$$f_{BSNOx} = \frac{BSNOx_{optimized}}{BSNOx_{baseline}}$$

- Combustion noise factor

$$f_{CN} = 10^{\frac{(dB_{optimized} - dB_{baseline})}{20}}$$

The large number of results produced can be represented in a 3D space, as depicted in Figure 4.5, defined by normalized BSFC, BSNO_x and CNF axis. Each red point in the space refers to the outcomes of a different injection profile. The more promising patterns, in terms of fuel consumption and combustion noise, were selected fixing NO_x emissions within the range defined by $\pm 5\%$ of the baseline value. As a result, a 2D contour surface defined by BSFC and CNF axis was obtained. The black rectangular area of the 2D contour surface depicted in Figure 4.6, is representative of patterns which fuel consumption and combustion noise outcomes are lower compared to the baseline, but comparable in terms of NO_x emissions.

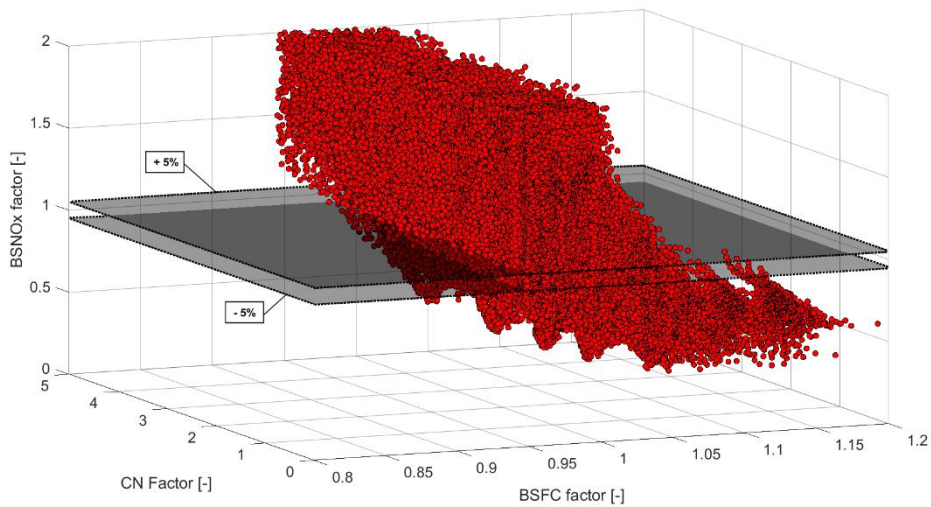


Figure 4.5 – DoE results in normalized BSFC – BSNO_x – CN space. Grey planes represents the maximum and minimum BSNO_x level allowed. [106]

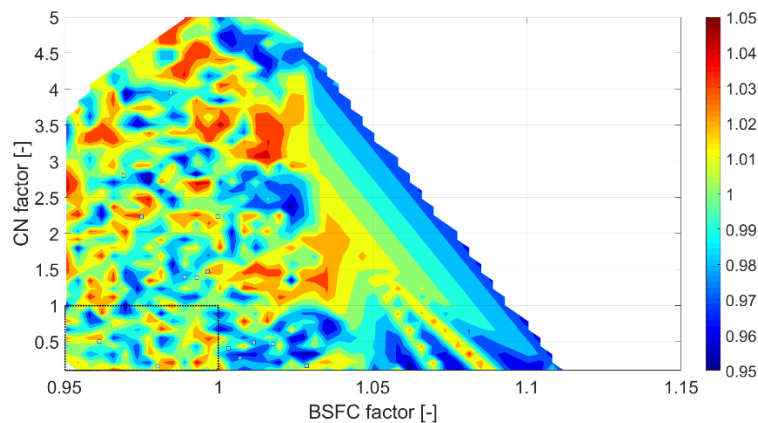


Figure 4.6 – DoE post-processed results: BSNO_x level within 5% of the baseline value [106]

The obtained multiple injection patterns were demonstrated to be dramatically effective in achieving CN and BSFC reduction while not exceeding the target NO_x emissions level, in accordance with previous research findings [102,112,113]. In Figure 4.7 the most promising pattern is depicted, for each of the analyzed engine operating points, in terms of in-cylinder pressure (top), burn rate (center) and

injection rate (bottom). Results highlighted some common trends between optimized injection patterns. First, best results were obtained splitting the fuel injection in a large number of close events, thanks to high injection pressures and short dwell times. This injection digitalization trend led to a progressive burn rate and a smooth pressure outcome was observed in most of the cases.

As can be noticed from Figure 4.7 – right, in the medium load engine operating point 2000 RPM X 8 bar BMEP the optimized pattern led to a more intense premixed combustion and to a progressive burn rate, thanks to the large number of pilot injections. With this optimized pattern, a maximum 4% BSFC improvement was obtained, thanks to the anticipated crank angle of MFB50 and to the higher peak pressure, while reducing significantly combustion noise, thanks to the smooth obtained pressure signal. The effect of shorter combustion duration allows a BSFC improvements up to 4%, compensating the friction losses worsening due to the increase in maximum pressure.

In reduced load conditions such as 1500 RPM X 2 bar BMEP (Figure 4.7 – left) and 1500 RPM X 5 bar BMEP (Figure 4.7 – center) operating points, the optimized patterns led to combustion processes characterized by a smoothed premixed phase, a progressively increasing burn rate and a peak pressure lower than the baseline. This led to lower frictions which, combined with lower heat transfer losses and a lower exhaust enthalpy, allowed a maximum BSFC improvement of 5%. Nevertheless, a lower level of combustion noise was observed, in each case, thanks to the smooth pressure rise obtained through the large number of pilot injections.

A summary of the results, in terms of BSFC and CN factors comparison for each engine operating key-points is shown in Figure 4.8.

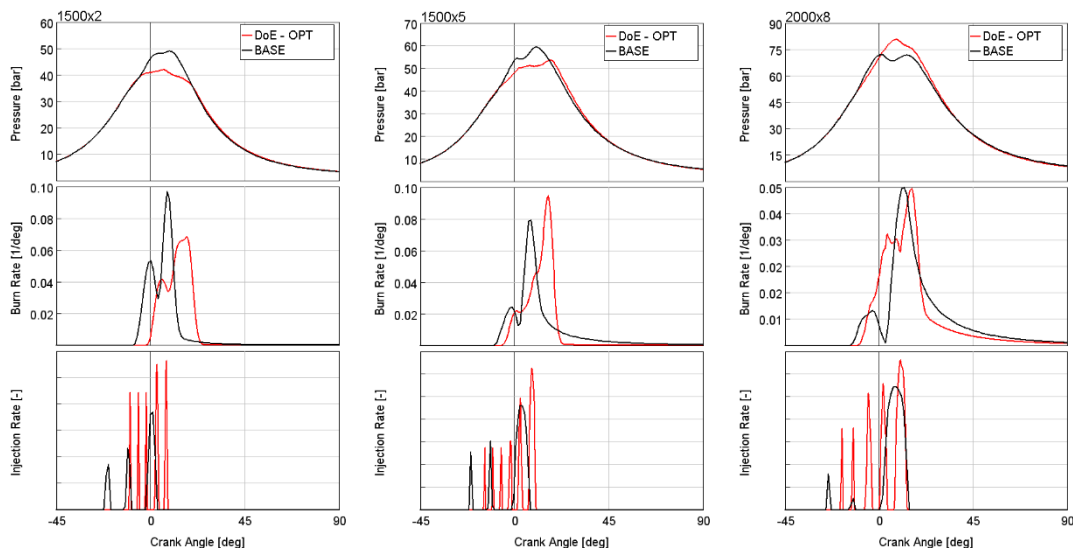


Figure 4.7 – DoE results: baseline (black) and optimized (red) in-cylinder pressure (top), burn rate (center) and injection rate (bottom) – Left column: 1500 RPM X 2 bar BMEP; Center column: 1500 RPM X 5 bar BMEP, Right column: 2000 RPM X 8 bar BMEP

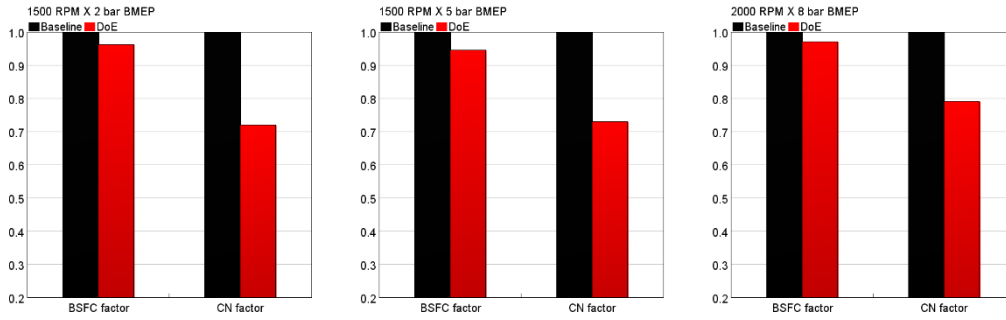


Figure 4.8 – DoE results: baseline (black) and optimized (red) BSFC factor and CN factor – Left column: 1500 RPM X 2 bar BMEP; Center column: 1500 RPM X 5 bar BMEP, Right column: 2000 RPM X 8 bar BMEP

4.2.2 Single-Objective approach

The first step of an optimization process is the definition of an objective function, that generally can be defined as Equation 24 shows.

$$f(x) = f(G(x)) \quad \text{Eq. 24}$$

Where x is the independent variable, and G is the dependent variable or, in other words, the output that must be optimized. With the optimizer, the function f could be minimized or maximized, within a space delimited by the upper and lower values of x and a precise set of constrains which define the allowable working range.

In literature, several objective functions could be found and they are reported as follows. Montgomery and Reitz in [114,115] proposed the maximization of the function in Equation 25:

$$f(x) = \frac{1000}{\left[\frac{NO_x + HC}{(NO_x + HC)_t} \right]^2 + \left(\frac{PM}{PM_t} \right)^2 + \left(\frac{BSFC}{BSFC_t} \right)} \quad \text{Eq. 25}$$

Where NO_x , HC and PM are the brake specific emission levels, and the subscript t is referred to the target value for each dependent variables. The power of 2 for the emission levels means that the penalty in terms of objective function value is bigger, the more the target level is exceeded. On the other hand, when the target value is reached, or the emission level is lower respect to the target, the power of 2 does not produce any significant reduction in terms of objective function value, giving more importance into BSFC improvements. In terms of optimization approach, Equation 25 could be manipulate and the result is expressed in Equation 26 , that represents an objective function that must be minimized.

$$f'(x) = \left[\frac{NO_x + HC}{(NO_x + HC)_t} \right]^2 + \left(\frac{PM}{PM_t} \right)^2 + \left(\frac{BSFC}{BSFC_t} \right) \quad \text{Eq. 26}$$

Desantes et al. in [116] introduced the objective function presented in Equation 27.

$$f(x) = \frac{BSFC}{BSFC_t} + e^{\left[k_1 \left(\frac{NO_x - NO_{x,t}}{NO_{x,t}}\right)\right]} + e^{\left[k_2 \left(\frac{PM - PM_t}{PM_t}\right)\right]} \quad \text{Eq. 27}$$

Where k_1 and k_2 are 2 calibration constants with the aim to properly calibrate the emissions weight in the value of the objective function. As it can be easily seen from Equation 27, the emissions terms are included in 2 exponential terms: in this way, when the targets are reached, the emissions weight on the objective function value becomes rapidly negligible, and vice versa.

Mallamo in [117] proposed the following objective function (Equation 28).

$$f(x) = \frac{BSFC}{BSFC_t} + k_1 \left(\frac{NO_x}{NO_{x,t}}\right)^{m_1} + k_2 \left(\frac{PM}{PM_t}\right)^{m_2} k_3 \cdot 10^{\left(\frac{dB - dB_t}{20}\right)} \quad \text{Eq. 28}$$

Where the k_i , m_i allow the calibration of the emissions terms in the objective function. Moreover, in Equation 28 a term related to the combustion noise (in decibel) was added although it is not subject to any limitation according to current regulations.

In this analysis, in order to identify through numerical simulation, the optimal injection rate to achieve the best trade-off among BSFC, BSNOx and Combustion Noise, an appropriate objective function was defined (Equation 29).

$$f(x) = k_1 f_{BSFC} + k_2 f_{CN} \quad \text{Eq. 29}$$

Where, k_1 and k_2 are the calibration constants to weigh the terms of the function (BSFC and Combustion Noise factors). In this case, $k_1 = k_2 = 1$. The term related to the BSNOx was not added in the objective function because it was considered as a constraint in the optimization process. More specifically, the BSNOx output must be within the band $\pm 5\%$ with respect to the baseline value ($0.95 \leq f_{BSNOx} \leq 1.05$).

Differently from other objective functions that can be found in literature [114–117], Eq. 29 does not consider the Soot term. This is due to the fact that 1D soot model cannot provide accurate quantitative values of soot emission (as clearly shown in Figure 2.37), and a 3D-CFD approach is required to fully investigate the soot formation process.

The algorithm NSGA-III was used for the optimization study [110,118]. This algorithm, specifically optimized for multimodal and non-linear problems, was tested in several conditions demonstrating its effectiveness in very complex optimizations. A simple genetic algorithm can be defined by the following pillars found in [119,120]:

- ‘Individuals’ are generated through random selection of the parameter space for each control factor, and a ‘population’ is then produced from the set of individuals.
- A model (which may be empirical or multi-dimensional) is used to evaluate the fitness of each individual.
- The fittest individuals are allowed to ‘reproduce’, resulting in a new ‘generation’ through combining the characteristics from two sets of individuals. A ‘Mutations’ are also allowed through random changes to a small portion of the population.
- The fitness criteria thins out the population by ‘killing off’ less suitable solutions. The characteristics of the individuals tend to converge to the most-fit solution over successive generations.

The optimizer settings are shown in Table 4.3. By using this settings, the total number of iterations required to the GA is 5’000 (defined by the product between population size and number of generations), for each engine operating point, which results in a computational time reduction of 2 orders of magnitude compared to the Factorial DoE approach (which consisted in 500’000 simulation runs per engine operating point).

Table 4.3 – Genetic Algorithm settings [121]

Population size	50
Number of generations	100
Crossover rate	1
Mutation rate	0.091

The population size depends directly from the independent variables involved in the optimization process. In addition, the number of generations was increased with respect to the suggested value in order to obtain a stable solution for each optimized output [110].

Results

The maximum number of iterations was set equal to 5’000, at the end of which the objective function resulted minimized respect to the baseline value for the 3 analyzed engine points.

In Figure 4.9, the blue dots show the results of the optimization in terms of objective function value for each iteration; while the dashed black line represents the baseline value. As it can be seen, the optimizer found a combination of the injection parameters that minimizes the objective function for each key-point.

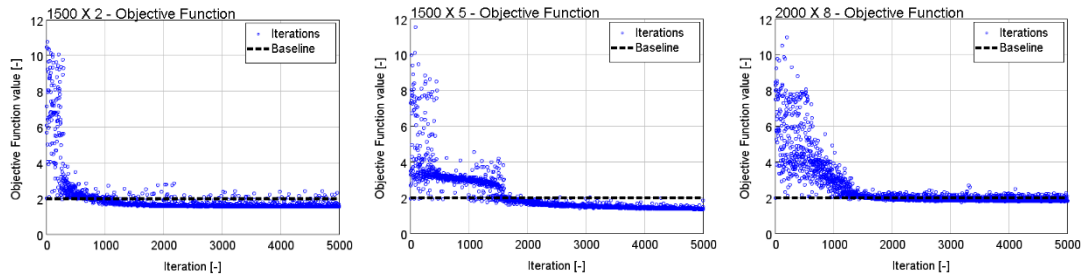


Figure 4.9 – Single-Objective results: objective function values for each iteration [121]

Figure 4.10 shows the comparison between baseline (black) and optimized (blue) configuration in terms of in-cylinder pressure (top), burn rate (center) and injection rate (bottom) for the analyzed 3 engine points. As it can be noted from Figure 4.10, the optimized strategies are characterized by a higher number of injection events with very short dwell time: this feature allows a smoother pressure trace reducing the combustion noise. Moreover, the reduction in peak pressure in Figure 4.10 – left (1500 RPM x 2 bar BMEP), led to a lower friction losses with consequent benefit in terms of fuel consumption.

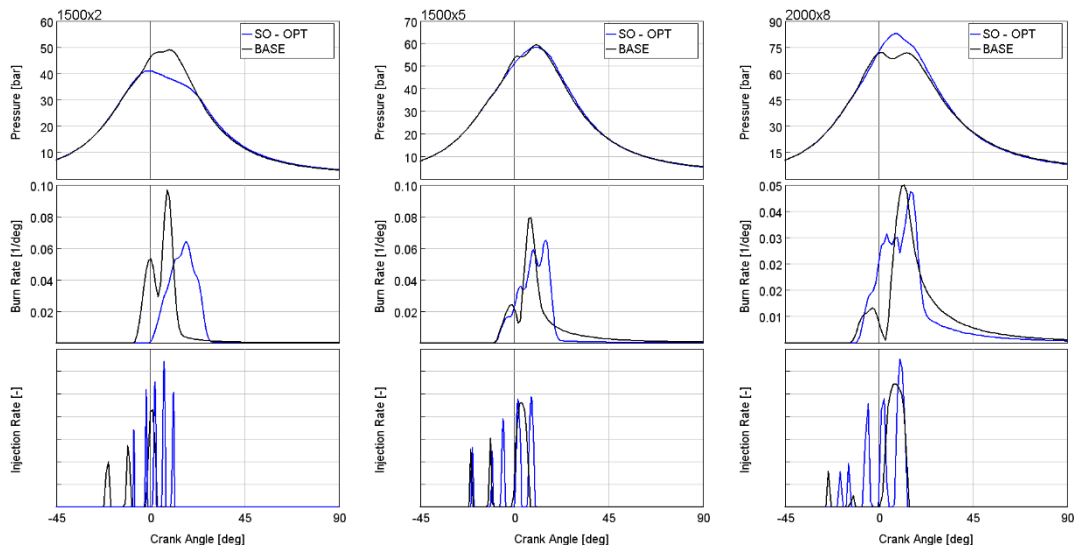


Figure 4.10 – Single-Objective results: baseline (black) and optimized (blue) in-cylinder pressure (top), burn rate (center) and injection rate (bottom) – Left column: 1500 RPM X 2 bar BMEP; Center column: 1500 RPM X 5 bar BMEP, Right column: 2000 RPM X 8 bar BMEP [121]

As already stated and as it can be seen in Figure 4.9, the optimizer minimized the defined objective function (Equation 29), obtaining significant improvement mainly in terms of combustion noise. A more detailed analysis of the results of the optimization process is shown in Figure 4.11, where the last 1,000 iterations for the engine point 2000 RPM X 8 bar BMEP are reported. Figure 4.11 shows that even if the objective function is minimized, for most of the points the combustion noise is reduced maintaining the BSFC value almost equal to the baseline, or even worse than the baseline value. This result suggests that a sensitivity analysis on the calibration constants k_1 , k_2 should be done in order to properly weigh the two terms of the Eq. 29.

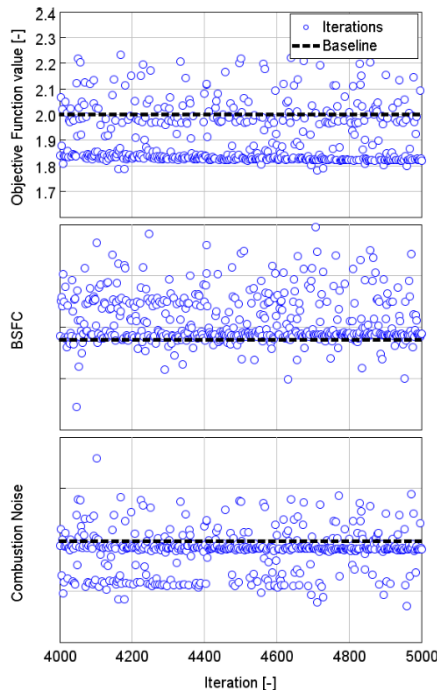


Figure 4.11 – Detail on objective function results. Top: objective function value; Center: BSFC; Bottom: Combustion Noise – 2000 RPM X 8 bar BMEP [121]

A summary of the results, in terms of BSFC and CN factors comparison for each engine operating key-points is shown in Figure 4.12, where the black bars are related to baseline injection pattern calibration and blue bars are referred to the optimized one.

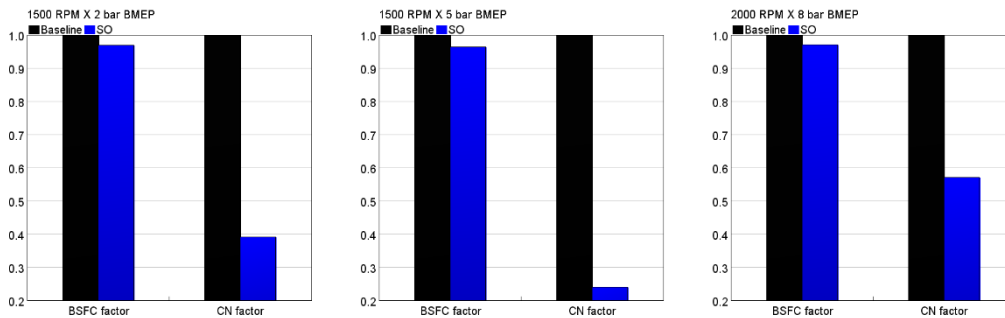


Figure 4.12 – Single-Objective results: baseline (black) and optimized (blue) BSFC factor and CN factor – Left column: 1500 RPM X 2 bar BMEP; Center column: 1500 RPM X 5 bar BMEP, Right column: 2000 RPM X 8 bar BMEP

4.2.3 Multi-Objective approach

Differently from the Single-Optimization study, in the Multi-Objective approach the optimizer takes into account multiple dependent variables that can be simultaneously minimized or maximized. Weighted-sum and Pareto are the 2 main approaches in the Multi-Objective optimization field: the weighted-sum technique is based on a single objective function, in which each response has different sign in order to differentiate between minimization and maximization. However, the

majority of complex optimization processes in engine design consists of trade-offs among several objectives, and the weighted-sum approach has not the capability to allow trade-offs analysis. By means of the definition of the Pareto front, it is possible to see the results in a space defined by 2 (or even more) dependent variables. Pareto front is not an optimal point that minimizes/maximizes an objective function, but it is a continuum with several solutions that are considered to be equally good, without any other information. Since the Multi-Objective studies introduce complex relationship among dependent and independent variables, they are usually resolved by using metaheuristic algorithms, as Genetic Algorithm [110].

The use of Genetic Algorithm in conjunction with a computational model for engine calibration was extensively studied by Hiroyasu et al. in [122]. Thanks to the adoption of the Neighborhood Cultivation Genetic Algorithm NCGA, the authors obtained a Pareto front optimum solutions, which show that it is possible to reduce emissions without increasing the fuel consumption by the optimization of EGR and multiple injections.

In [120], Senecal et al. defined a methodology for internal combustion engine design that incorporates multi-dimensional modelling and experiments to optimize the engine performance and emissions levels. This methodology, applied for a heavy-duty Diesel truck engine, simultaneously investigated the effect and of 6 inputs parameters (SOI, injection pressure, EGR rate, boost pressure and injection rate shape) on emissions and performance and optimized them by means of a GA optimization process. The optimum results showed a significant reduction in terms of NO_x and SOOT emissions, together with improved fuel consumption respect to the baseline configuration.

Also in this case, the algorithm NSGA-III was used the optimization study [110,118], without changing the optimizer settings, already shown in Table 4.3, since the population size strictly depends from the number of independent variables involved in the optimization process.

Results

Figure 4.13 show the results of the GA optimization in BSFC-CN space where black cross is related to the baseline configuration. Regarding the GA results, the complete iteration results are highlighted in white dots, while the Pareto front is shown in black. As it can be seen from Figure 4.13, the GA found solutions that improve the best result obtained through DoE approach, both in terms of BSFC and CN.

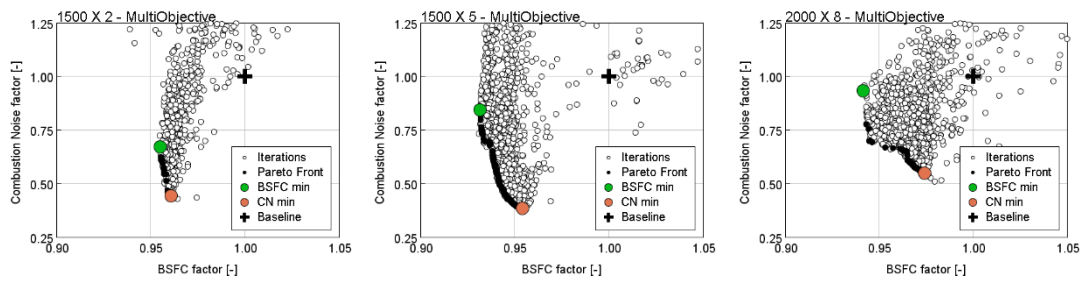


Figure 4.13 – Multi-Objective optimization results in the BSFC-Combustion Noise space – Left column: 1500 RPM X 2 bar BMEP; Center column: 1500 RPM X 5 bar BMEP, Right column: 2000 RPM X 8 bar BMEP [121]

The best configurations in the Pareto front in terms of minimum BSFC (green dot in Figure 4.13) and minimum Combustion Noise (orange dot in Figure 4.13) were simulated and are shown in Figure 4.14 where baseline (black) and optimized (green for minimum BSFC configuration and orange for minimum Combustion Noise configuration) in-cylinder pressure (top), burn rate (center) and injection rate (bottom) are reported. Also in this case, the optimized strategies are characterized by an higher number of injection events with very short dwell time, that allow a smoother pressure trace reducing the combustion noise.

A summary of the results, in terms of BSFC and CN factors comparison for each engine operating key-points is shown in Figure 4.15, comparing the baseline with minimum BSFC and minimum CN optimized calibrations resulted from the Multi-Objective approach.

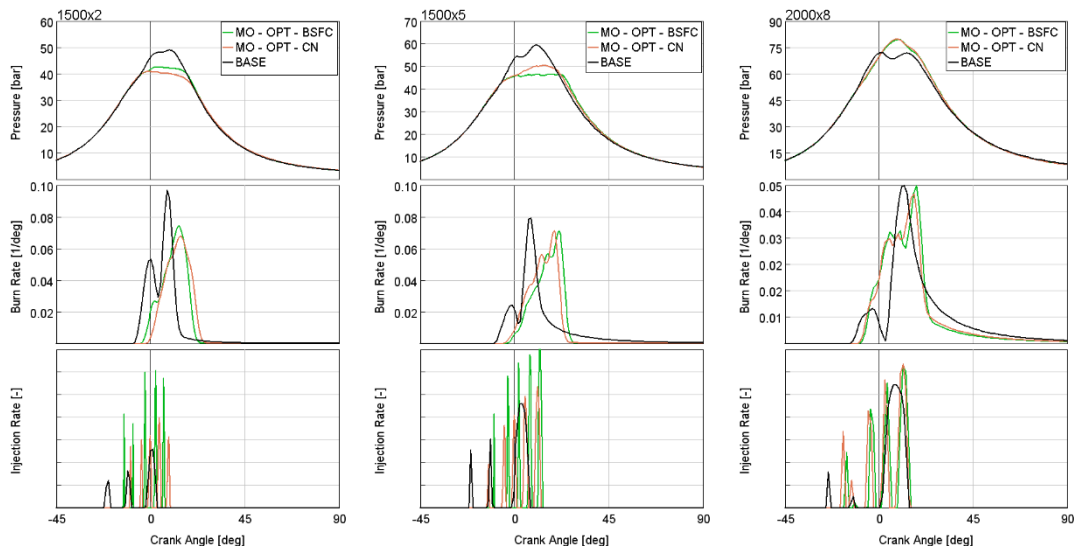


Figure 4.14 – Multi-Objective results: baseline (black) and optimized (green for minimum BSFC, orange for minimum combustion noise) in-cylinder pressure (top), burn rate (center) and injection rate (bottom) – Left column: 1500 RPM X 2 bar BMEP; Center column: 1500 RPM X 5 bar BMEP, Right column: 2000 RPM X 8 bar BMEP [121]

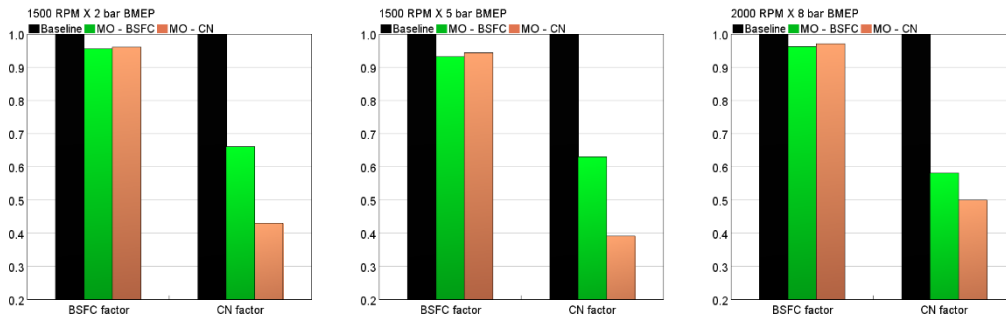


Figure 4.15 – Multi-Objective results: baseline (black) and optimized (green for minimum BSFC, orange for minimum combustion noise) BSFC factor and CN factor – Left column: 1500 RPM X 2 bar BMEP; Center column: 1500 RPM X 5 bar BMEP, Right column: 2000 RPM X 8 bar BMEP

4.2.4 Summary of the results

A numerical optimization analysis aiming to minimize Brake Specific Fuel Consumption (BSFC) and Combustion Noise (CN) without exceeding the Brake Specific NOx (BSNOx) baseline value, was presented for 3 engine operating conditions. Starting from a previously developed 1D-CFD single cylinder engine model, coupled with a 1D-CFD injector model, 3 different optimization processes were evaluated:

- Full Factorial DoE – A detailed space of results was defined thanks to a complete definition of dependent variables domain.
- Single-Objective – A proper objective function, taking into account BSFC and Combustion Noise, was firstly defined and then minimized by the optimizer.
- Multi-Objective – The optimizer took into account multiple dependent variables (BSFC and Combustion Noise) that were simultaneously minimized defining a Pareto front of solutions.

Promising results were obtained for the abovementioned optimization processes. Similar trends could be highlighted: the optimized injection rates are characterized by multiple and dense pilot injection patterns, obtained thanks to high injection pressures and short ET/DT. They led to a significant BSFC improvement up to 7% and combustion noise reduction higher than 70% thanks to a regular and progressive burn rate, while not exceeding the target level of NOx emissions.

Moreover, the optimization process provided more accurate results with significant improvements in terms of BSFC and Combustion Noise with respect to the DoE approach, as the histograms in Figure 4.16 shows. More in detail, the black bars correspond to the normalized BSFC and Combustion Noise value (BSFC and CN factor); the red bars are related to the best results obtained with the DoE approach; the orange and green bars are representative of the results of the Multi-Objective optimization, considering in the Pareto front the minimum CN and minimum BSFC configurations, respectively; in blue the Single-Objective results. The Single- and Multi-Objective optimization processes are able to find the optimal injection strategy configuration respect to the DoE approach, obtaining very high

improvement in terms of Combustion Noise, without exceeding the baseline BSNOx emissions level.

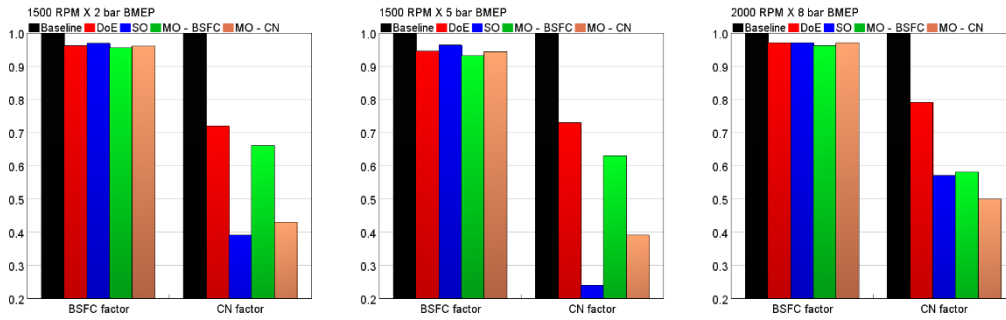


Figure 4.16 – Optimization process results: baseline (black) and optimized (red for DoE, blue for DoE, green for minimum BSFC, orange for minimum combustion noise) BSFC factor and CN factor – Left column: 1500 RPM X 2 bar BMEP; Center column: 1500 RPM X 5 bar BMEP, Right column: 2000 RPM X 8 bar BMEP [121]

As already pointed out in Paragraph 4.2.2, the actual calibration constants values of the proposed objective function (Equation 29) led to a significant reduction in terms of combustion noise, as shown by the blue bars in Figure 4.16.

For the sake of clarity, the numeric value of the optimization factors are summarized in Table 4.4.

Table 4.4 – Optimization results [121]

Engine key-point	Optimization approach	f_{BSFC}	f_{CN}
1500 RPM X 2 bar BMEP	DoE	0.96	0.73
	Single-Objective	0.97	0.39
	Multi-Objective – Min BSFC	0.95	0.66
	Multi-Objective – Min CN	0.96	0.43
1500 RPM X 5 bar BMEP	DoE	0.95	0.73
	Single-Objective	0.96	0.24
	Multi-Objective – Min BSFC	0.93	0.63
	Multi-Objective – Min CN	0.94	0.39
2000 RPM X 8 bar BMEP	DoE	0.97	0.79
	Single-Objective	0.97	0.57
	Multi-Objective – Min BSFC	0.96	0.58
	Multi-Objective – Min CN	0.97	0.50

Regarding the thermodynamic analysis of the impact of the optimized injection strategies on the overall engine efficiency, a split losses for each operating key-point is presenting evaluating the different optimization approaches.

Engine Point - 1500 RPM X 2 bar BMEP

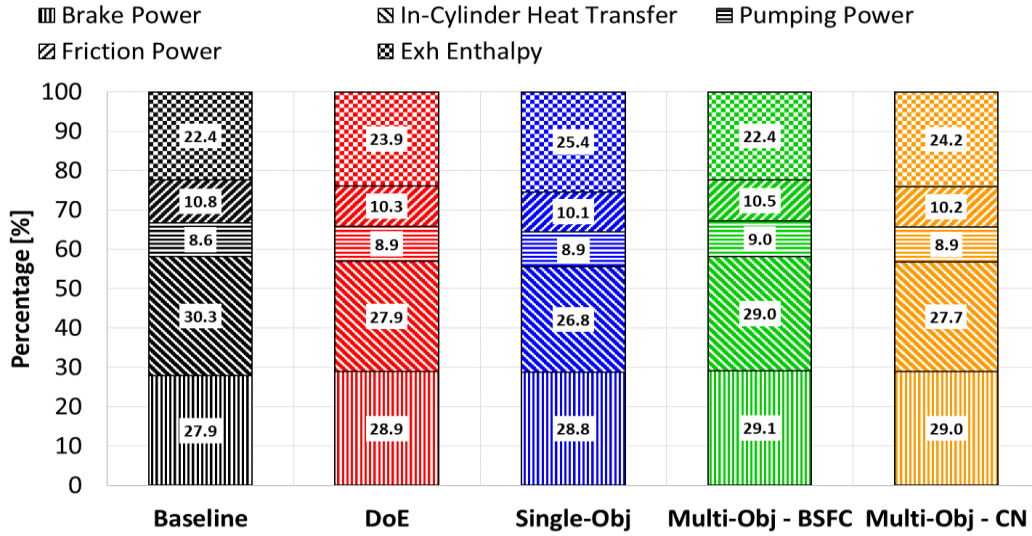


Figure 4.17 – Split power losses for the best injection strategy for each optimization approach. Engine operating point: 1500 RPM X 2 bar BMEP [121]

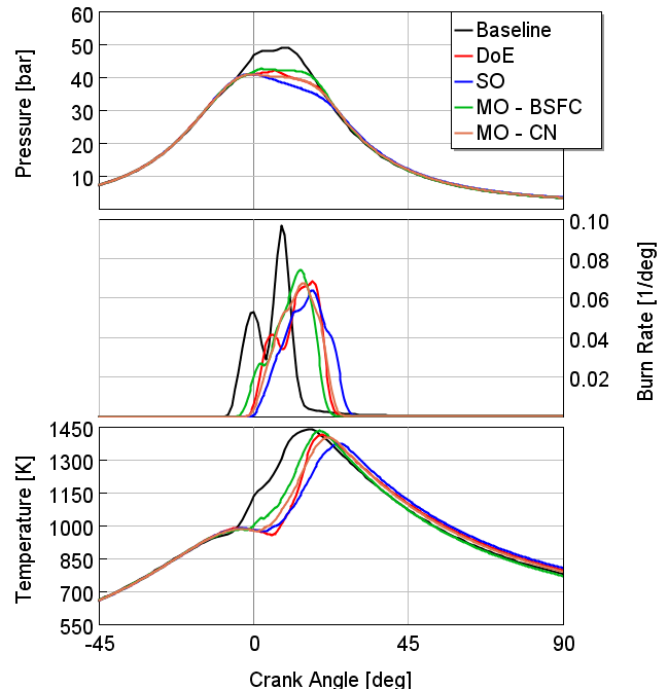


Figure 4.18 – In-cylinder pressure (top), burn rate (center) and in-cylinder temperature (bottom) comparisons for the best injection strategy for each optimization approach. Engine operating point: 1500 RPM X 2 bar BMEP [121]

Figure 4.17 shows that the benefit in engine efficiency is related to a friction reduction (due to the reduced peak pressure as shown in Figure 4.18 – top) and to an heat transfer reduction (due to the reduced peak temperature in Figure 4.18 – bottom). Both the effects are obtained thanks to a retarded combustion, as highlighted by the burn rates in Figure 4.18 – center.

Engine Point - 1500 RPM X 5 bar BMEP

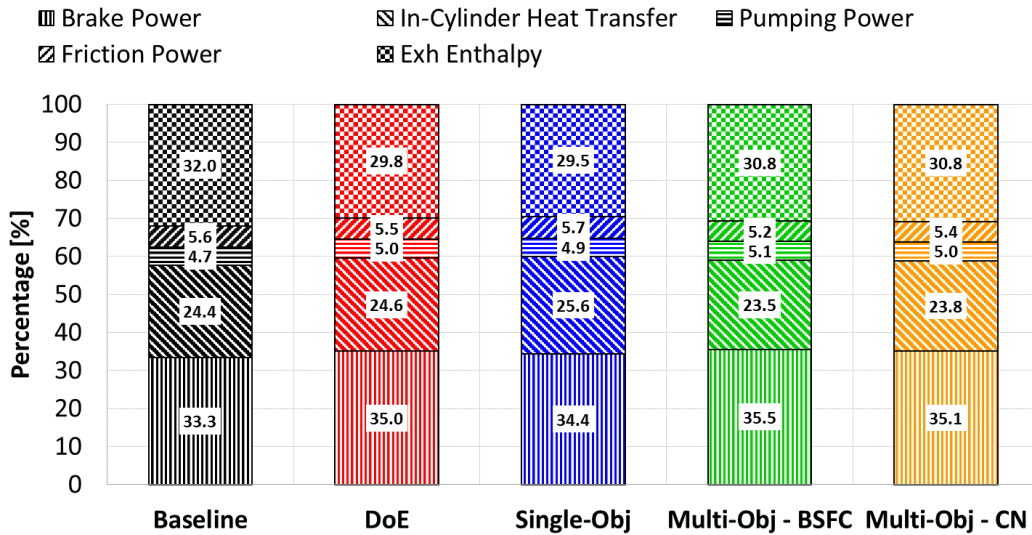


Figure 4.19 – Split power losses for the best injection strategy for each optimization approach. Engine operating point: 1500 RPM X 5 bar BMEP [121]

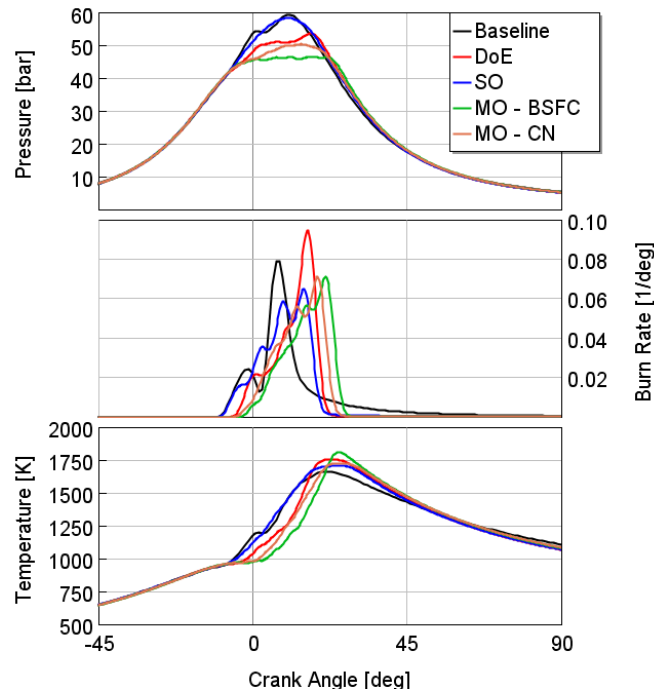


Figure 4.20 – In-cylinder pressure (top), burn rate (center) and in-cylinder temperature (bottom) comparisons for the best injection strategy for each optimization approach. Engine operating point: 1500 RPM X 5 bar BMEP [121]

Figure 4.20 – center show that the all optimized injection strategies lead to a retarded combustion process with respect to the baseline configuration. However, as shown by the split losses in Figure 4.19 this effect does not produce an increment in terms of exhaust enthalpy, which is on the contrary reduced for all the optimization approaches, thanks to the shorter combustion duration.

Engine Point - 2000 RPM X 8 bar BMEP

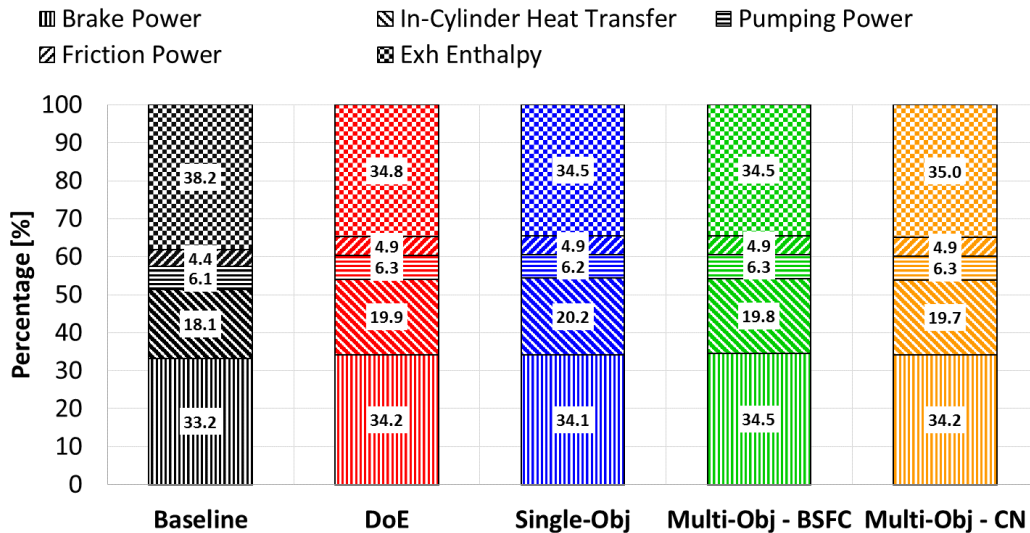


Figure 4.21 – Split power losses for the best injection strategy for each optimization approach. Engine operating point: 2000 RPM X 8 bar BMEP [121]

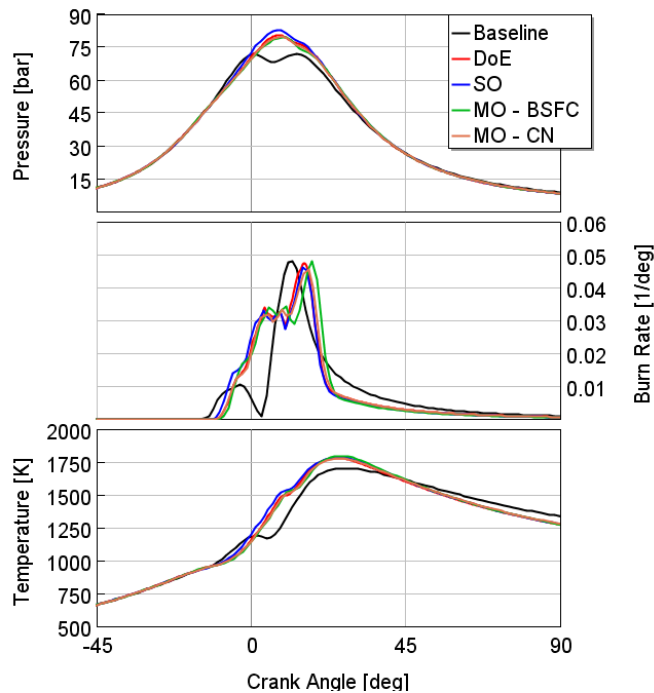


Figure 4.22 – In-cylinder pressure (top), burn rate (center) and in-cylinder temperature (bottom) comparisons for the best injection strategy for each optimization approach. Engine operating point: 2000 RPM X 8 bar BMEP [121]

The 3 different optimization approaches produce almost identical pressure traces (Figure 4.22 – top), with a comparable effects in terms of friction and heat transfer losses, which are both higher than the baseline (as shown in Figure 4.21) due to higher peak pressure and temperature values. However, the dominating effect is the shorter combustion duration, which leads, for all the optimized injection strategies, to a significant reduction of the exhaust enthalpy.

It is worth to point out that the requested computational time has been reduced of 2 orders of magnitude adopting the optimizer instead of the Full Factorial DoE

approach, as shown in Figure 4.23 (where 22 seconds are considered as the average required time for a single simulation run).

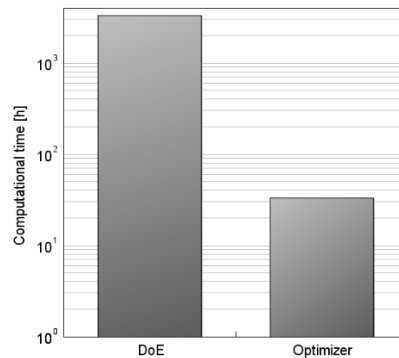


Figure 4.23 – Computational time for the optimization process considering Full Factorial DoE and Multi-Objective (or Single-Objective) optimization approaches (referred to simulations distributed on a single core, Intel i7-6700 3.4 GHz processor) [121]

The Single-Optimization approach highlighted an issue related to the calibration constants within the objective function: the objective function minimization was linked to a combustion noise reduction maintaining the BSFC value almost equal to the baseline, or even worse than the baseline value. This result suggests that a further sensitivity analysis on the calibration constants should be done in order to properly estimate the two terms of the objective function. Further analysis may be focused on a detailed quantification of soot emission by means of 3D-CFD approach, as well as the experimental assessment of the best injection parameters configurations for evaluating the effects of such innovative injection strategies in real engine operation.

Conclusions

The increasing stringency of pollutant emission regulations, aiming to fuel neutral NO_x limits along with the challenging future CO₂ targets, is expected to foster the implementation of new technologies in terms of aftertreatment (AT), air management and fuel injection systems (FIS). In order to fully exploit the potential of the innovative technologies, numerical simulation can play a fundamental role by allowing the creation of reliable and computationally efficient simulation models where evaluating the impact of design modifications, or in order to support the optimization of such complex sub-systems through their reduced time and cost expenses.

In the current work, an optimization analysis of the air management and fuel injection systems through numerical simulation was carried out. A 1D-CFD engine model of a 1.6l 4-cylinder EURO 6 diesel engine was coupled with a latest generation solenoid Common Rail injector model in a commercially available software, GT-SUITE. The predictive combustion model developed by Gamma Technologies, DIPulse, was calibrated and validated on a wide range of operating engine condition showing a high accuracy in replicating the combustion phenomena.

The developed 1D-CFD model, capable to run both in steady state and in transient conditions, was used as a virtual test rig where evaluating the potential of the application of a fully flexible valve actuation and the fuel injection pattern optimization.

Firstly, the analysis was focused on the identification of the best Variable Valve Actuation (VVA) strategies to be implemented in a passenger car diesel engine with the aim of fuel consumption reduction. Three different techniques (Late Intake Valve Closure LIVC, Late Exhaust Valve Opening LEVO, Variable Exhaust Valve Timing VVT) were scrutinized under steady state operating conditions. Among them, only LIVC showed significant reduction in terms of fuel consumption (up to 5% at low engine loads) without exceeding the baseline Brake Specific engine-out NO_x emissions. For this reason, LIVC actuation was evaluated under transient

conditions, for quantifying its BSFC reduction potential over the whole Worldwide harmonized Light vehicles Test Cycle (WLTC). Results showed that even if LIVC leads to efficiency improvements in steady state analysis, its actuation is limited to a part load zone that has a low impact on the total fuel consumption (lower than 10%).

The potential of VVA in order to optimize the thermal management of the aftertreatment system was also evaluated scrutinizing three different strategies (Early Exhaust Valve Opening EEVO, VVT and Exhaust Valve reopening EVrO). Since all the simulated VVA strategies allowed achieving significant increases in the exhaust gas temperature in steady state analysis, they were simulated in transient condition over the entire WLTC. The most promising technique was EVrO, with which a aftertreatment monolith temperature increment of about 30°C could be achieved at 300 s after the start of the WLTC, with generally negligible or acceptable fuel penalties (lower than 1%).

After that, a numerical optimization analysis of fuel injection pattern for the selected test case diesel engine was carried out. The aim of this is to identify the target or “ideal” fuel injection strategies, which should be performed in order to minimize both Brake Specific Fuel Consumption and Combustion Noise, regardless of the constraints and limitations due to a specific fuel injection system. Starting from the detailed 1D-CFD engine model, a single cylinder engine model was developed in GT-SUITE, allowing a reduction of an order of magnitude in terms of computational time, while maintaining an high accuracy in replicating the real engine operating conditions. Several independent variables were introduced into the optimization process, mainly related to the injection pattern (number of injection events, Start of Injection SOI, Energizing Time ET, Dwell Time DT, rail pressure), as well as the EGR rate. Three optimization approaches were used in this analysis, Full Factorial DoE, Single- and Multi-objective. Promising results were obtained with multiple and dense pilot injection patterns, obtained thanks to high injection pressures and short ET/DT. A BSFC improvement up to 7%, significant combustion noise reduction were obtained through a regular and progressive burn rate, while not exceeding the target level of NO_x emissions. Moreover, for Single- and Multi-Objective problems the Non-dominated Sorting Genetic Algorithm (NSGA-III) was used highlighting relevant computational time savings for the optimization process with respect to the Full Factorial DoE.

Concluding, I would like to echo Dr. Volkmar Denner’s (Bosch CEO) words, *“There’s a future for diesel. Today, we want to put a stop, once and for all, to the debate about the demise of diesel technology. [...] A combination of advanced fuel-injection technology, a newly developed air management system, and intelligent temperature management has made such low readings possible. NO_x emissions can now remain below the legally permitted level in all driving situations, irrespective of whether the vehicle is driven dynamically or slowly, in freezing conditions or in summer temperatures, on the freeway or in congested city traffic. [...] Diesel will remain an option in urban traffic, whether drivers are tradespeople or commuters.”* [123].

Even in this context, where mass media are pushing public opinion to an often irrational run towards electrification, modern Diesel engines can still represent, from a sound and rational engineering perspective, a cornerstone in the quest for sustainable transport systems, thanks to their so-far unparalleled fuel conversion efficiency.

Thermodynamics laws tell us that room for improvement still exists, and from our side, as a researcher community, we have the moral duty to achieve it.

References

1. Epa, U., of Transportation, O., Quality, A., and Division, C., “VW Notice of Violation, Clean Air Act (September 18, 2015),” 2009.
2. Audi 2010 Green Car Super Bowl Commercial - YouTube, https://www.youtube.com/watch?v=O_MuqoSsuTQ, Apr. 2018.
3. “Dirty diesels” – your easy guide to the new clean air strategy, <https://www.telegraph.co.uk/cars/advice/dirty-diesels-everything-need-know-new-emissions-rules/>, Apr. 2018.
4. Poliscanova, J., “Diesel: The True (Dirty) Story,” 1–63, 2017.
5. The death of diesel: has the one-time wonder fuel become the new asbestos? | Cities | The Guardian, <https://www.theguardian.com/cities/2017/apr/13/death-of-diesel-wonder-fuel-new-asbestos>, Apr. 2018.
6. German Carmakers Criticized for Emissions Research on Monkeys - The New York Times, <https://www.nytimes.com/2018/01/28/business/german-carmakers-diesel-monkeys.html>, Apr. 2018.
7. VW condemned for testing diesel fumes on humans and monkeys | Business | The Guardian, <https://www.theguardian.com/business/2018/jan/29/vw-condemned-for-testing-diesel-fumes-on-humans-and-monkeys>, Apr. 2018.
8. VW, Audi, Porsche, BMW und Daimler bildeten über Jahre ein Kartell – eines der größten der deutschen Wirtschaftsgeschichte DER SPIEGEL 2017/30, <https://magazin.spiegel.de/SP/2017/30/152270400/index.html>, Apr. 2018.
9. Lesermeinungen zum SPIEGEL 40/2015 - SPIEGEL ONLINE, <http://www.spiegel.de/spiegel/spiegelblog/lesermeinungen-zum-spiegel-40-2015-a-1055889.html>, Apr. 2018.
10. Şenzeybek, M., Tietge, U., and Mock, P., “CO₂ emissions from new passenger cars in the EU: Car manufacturers’ performance in 2016,” 2017.
11. ICCT, “Shifting Gears: The Effects of a Future Decline in Diesel Market Share on Tailpipe CO₂ and NO_x emissions in Europe,” (X), 2017.
12. Mock, P. and Tietge, U., “Diesel car sales decline will have negligible impact on attainment of European CO₂ emission standards,” 2018.
13. No improvements on average CO₂ emissions from new cars in 2017 — European Environment Agency, <https://www.eea.europa.eu/highlights/no-improvements-on-average-co2>, Apr. 2018.

14. CO2 from new cars up as petrol overtakes diesel, 2017 data shows | ACEA - European Automobile Manufacturers' Association, <http://www.acea.be/press-releases/article/co2-emissions-from-new-cars-up-as-petrol-overtakes-diesel-2017-data-shows>, Apr. 2018.
15. Sanguedolce, A. and Mallamo, F., "INTERNAL COMBUSTION ENGINES Passenger cars with diesel powertrain are approx . 15 - 20 % more efficient compared to gasoline powertrain , overall diesel market share at 50 %," 2018.
16. Tomorrow's Vehicles – A projection of transportation fuel demand through 2025, Apr. 2018.
17. ICCT, "Diesel Technology Developments," 2017.
18. Sanchez, F.P., Bandivadekar, A., and German, J., "Estimated cost of emission reduction technologies for LDVs," *Int. Counc. Clean Transp.* (March):1–136, 2012.
19. Opel introducing new 1.6L diesel engine family; fuel consumption reduced by up to 10%, Euro 6 compliant, <http://www.greencarcongress.com/2013/01/opel-20130116.html>, 2013.
20. Borgia, L., "An example of Diesel Engine right-sizing: the 1.6 liter Engine Family from General Motors," *CO2 Reduction for Transportation Systems*, Turin, 2016.
21. Common-rail injection systems - CRS2-25 diesel common-rail system with solenoid valve injectors and 2500bar, *Robert Bosch GmbH*, 2015.
22. Mobasher, R., Peng, Z., and Mirsalim, S.M., "Analysis the effect of advanced injection strategies on engine performance and pollutant emissions in a heavy duty DI-diesel engine by CFD modeling," *Int. J. Heat Fluid Flow* 33(1):59–69, 2012, doi:10.1016/j.ijheatfluidflow.2011.10.004.
23. Dhar, A. and Agarwal, A.K., "Experimental investigations of the effect of pilot injection on performance, emissions and combustion characteristics of Karanja biodiesel fuelled CRDI engine," *Energy Convers. Manag.* 93:357–366, 2015, doi:10.1016/j.enconman.2014.12.090.
24. Mohan, B., Yang, W., and Chou, S.K., "Fuel injection strategies for performance improvement and emissions reduction in compression ignition engines - A review," *Renew. Sustain. Energy Rev.* 28(x):664–676, 2013, doi:10.1016/j.rser.2013.08.051.
25. Heywood, J.B., "Internal Combustion Engine Fundamentals," ISBN 007028637X, 1988, doi:10987654.
26. Ferrari, A., Paolicelli, F., and Pizzo, P., "The new-generation of solenoid injectors equipped with pressure-balanced pilot valves for energy saving and dynamic response improvement," *Appl. Energy* 151:367–376, 2015, doi:http://dx.doi.org/10.1016/j.apenergy.2015.03.074.
27. Leonhard, R., Warga, J., Pauer, T., Rückle, M., and Schnell, M., "Solenoid common-rail injector for 1800 bar," *MTZ Worldw.* 71(2):10–15, 2010, doi:10.1007/BF03227003.
28. Salvador, F.J., Carreres, M., and Jaramillo, D., "An Investigation on the Dynamic Behaviour at Different Temperatures of a Solenoid Operated Common-Rail Ballistic Injector by means of a One-Dimensional Model," 2014, doi:10.4271/2014-01-1089.Copyright.
29. Salvador, F.J., Gimeno, J., La Morena, J. De, and Carreres, M., "Using one-dimensional modeling to analyze the influence of the use of biodiesels on the dynamic behavior of solenoid-operated injectors in common rail systems: Results of the simulations and discussion," *Energy Convers. Manag.* 54(1):122–132, 2012, doi:10.1016/j.enconman.2011.10.007.

30. Payri, R., Salvador, F.J., Carreres, M., and La Morena, J. De, "Fuel temperature influence on the performance of a last generation common-rail diesel ballistic injector. Part II: 1D model development, validation and analysis," *Energy Convers. Manag.* 114:376–391, 2016, doi:10.1016/j.enconman.2016.02.043.
31. Piano, A., Millo, F., Postriotti, L., Biscontini, G., Cavicchi, A., and Pesce, F.C., "Numerical and Experimental Assessment of a Solenoid Common-Rail Injector Operation with Advanced Injection Strategies," *SAE Int. J. Engines* 9:565–575, 2016, doi:10.4271/2016-01-0563.
32. Salvador, F.J., Carreres, M., Crialesi-Esposito, M., and Plazas, A.H., "Determination of critical operating and geometrical parameters in diesel injectors through one dimensional modelling, design of experiments and an analysis of variance," *Proc. Inst. Mech. Eng. Part D J. Automob. Eng.* 95440701773526, 2017, doi:10.1177/0954407017735262.
33. Payri, R., Salvador, F.J., Gimeno, J., and Morena, J. De, "Influence of injector technology on injection and combustion development – Part 1 : Hydraulic characterization," *Appl. Energy* 88(4):1068–1074, 2011, doi:10.1016/j.apenergy.2010.10.012.
34. Payri, R., Climent, H., Salvador, F.J., Favennec, A.G., Termicos, C., Polite, U., and Valencia, D., "Diesel injection system modelling . Methodology and application for a rst-generation common rail system," 218:81–91, 2004.
35. Payri, R., Morena, J. De, Pagano, V., Hussain, A., Sammut, G., and Smith, L., "One-dimensional modeling of the interaction between close-coupled injection events for a ballistic solenoid injector," 2018, doi:10.1177/1468087418760973.
36. Salvador, F.J., Gimeno, J., Morena, J. De, and Carreres, M., "Comparison of Different Techniques for Characterizing the Diesel Injector Internal Dimensions," 2018.
37. Macian, V., Bermudez, V., Payri, R., and Gimeno, J., "New Technique for Determination of Internal Geometry of a Diesel Nozzle With the Use of Silicone Methodology," *Exp. Tech.* 27(2):39–43, 2003, doi:10.1111/j.1747-1567.2003.tb00107.x.
38. Hessler, J., "Industrial CT scanning," <https://www.sae.org/news/2014/03/industrial-ct-scanning>, 2014.
39. Carmignato, S., "Computed tomography as a promising solution for industrial quality control and inspection of castings," 30:5–14, 2012.
40. Postriotti, L., Malaguti, S., Bosi, M., Buitoni, G., Piccinini, S., and Bagli, G., "Experimental and numerical characterization of a direct solenoid actuation injector for Diesel engine applications," *FUEL* 118:316–328, 2014, doi:10.1016/j.fuel.2013.11.001.
41. Postriotti, L., Buitoni, G., Pesce, F.C., and Ciaravino, C., "Zeuch method-based injection rate analysis of a common-rail system operated with advanced injection strategies," *FUEL* 128:188–198, 2014, doi:10.1016/j.fuel.2014.03.006.
42. ISO 4113:2010 - Road vehicles -- Calibration fluids for diesel injection equipment, 2010.
43. Piano, A., Boccardo, G., Millo, F., Torino, P., Cavicchi, A., Postriotti, L., and Pesce, F.C., "Experimental and Numerical Assessment of Multi-Event Injection Strategies in a Solenoid Common-Rail Injector," 2017, doi:10.4271/2017-24-0012.
44. GT-SUITE - Flow Theory Manual - VERSION 2017, 2017.

45. GT-SUITE - Engine Performance Application Manual - VERSION 2017, 2017.
46. Kuensberg Sarre, C. von, Kong, S.-C., and Reitz, R.D., "Modeling the Effects of Injector Nozzle Geometry on Diesel Sprays," (724), 1999, doi:10.4271/1999-01-0912.
47. GT-SUITE - Fuel Injection Manual - VERSION 2017, 2017.
48. Jung, D. and Assanis, D.N., "Multi-Zone DI Diesel Spray Combustion Model for Cycle Simulation Studies of Engine Performance and Emissions," 2001, doi:10.4271/2001-01-1246.
49. Hiroyasu, H. and Arai, M., "Structures of Fuel Sprays in Diesel Engines," 1990, doi:10.4271/900475.
50. Aggarwal, S.K. and Peng, F., "A Review of Droplet Dynamics and Vaporization Modeling for Engineering Calculations," *J. Eng. Gas Turbines Power* 117(3):453, 1995, doi:10.1115/1.2814117.
51. Prommersberger, K., Maier, G., and Wittig, S., Validation and application of a droplet evaporation model for real aviation fuel, 1999.
52. Morel, T. and Keribar, R., "Heat Radiation in D.I. Diesel Engines," 1986, doi:10.4271/860445.
53. Morel, T. and Wahiduzzaman, S., "Modeling of diesel combustion and emissions," *XXVI FISITA Congress*, Prague, Czech Republic, 1996.
54. Tai, C., Tsao, T.-C., Schörn, N.A., and Levin, M.B., "Increasing Torque Output from a Turbodiesel with Camless Valvetrain," *SAE Technical Paper*, SAE International, 2002, doi:10.4271/2002-01-1108.
55. Lancefield, T., Methley, I., Rase, U., and Huhn, T., "The application of variable event valve timing to a modern diesel engine," *SAE World Congr. Exhib. 2000(724)*, 2000, doi:10.4271/2000-01-1229.
56. Xin, Q., "Diesel Engine System Design," ISBN 9781845697150, 2013, doi:10.1533/9780857090836.4.909.
57. Miller, R., "High-pressure supercharging system," US patent No. 2670595, United States of America, 1954.
58. Miller, R., "High expansion, spark ignited, gas burning, internal combustion engines," US patent No. 2773490, United States of America, 1956.
59. Miller, R., "Supercharged engine," US patent No. 2817322, United States of America, 1957.
60. Yang, B. and Keller, P., "Analysis of Diesel Engine Emissions Reduction by Late Intake Valve Close and VTG Turbocharger Using 1-D Simulation," 2008, doi:10.4271/2008-01-2444.
61. Leet, J.A., Simescu, S., Froelund, K., Dodge, L.G., and Roberts, C.E., "Emissions Solutions for 2007 and 2010 Heavy-Duty Diesel Engines," 2004, doi:10.4271/2004-01-0124.
62. Millo, F., Mallamo, F., Arnone, L., Bonanni, M., and Franceschini, D., "Analysis of Different Internal EGR Solutions for Small Diesel Engines," *SAE Technical Paper*, SAE International, 2007, doi:10.4271/2007-01-0128.
63. Fessler, H. and Genova, M., "An Electro-Hydraulic 'Lost Motion' VVA System for a 3.0 Liter Diesel Engine," 2004, doi:10.4271/2004-01-3018.
64. Benajes, J., Reyes, E., and Luján, J.M., "Intake Valve Pre-lift Effect on the Performance of a Turbocharged Diesel Engine," *SAE Technical Paper*, SAE International, 1996, doi:10.4271/960950.
65. Babajimopoulos, A., Lavoie, G.A., and Assanis, D.N., "Modeling HCCI Combustion With High Levels of Residual Gas Fraction - A Comparison of Two VVA Strategies," *SAE Technical Paper*, SAE International, 2003,

- doi:10.4271/2003-01-3220.
66. Ren, S., Wang, Z., Xiang, S., Zhao, H., and Wang, J., “Numerical Study of Gasoline Homogeneous Charge Induced Ignition (HCII) by Diesel with a Multi-Component Chemical Kinetic Mechanism,” 2016, doi:10.4271/2016-01-0784.
 67. Homogeneous Charge Compression Ignition (HCCI) Engines, <https://www.sae.org/publications/books/content/pt-94/>, Apr. 2018.
 68. Gonzalez D, M.A. and Nunno, D. Di, “Internal Exhaust Gas Recirculation for Efficiency and Emissions in a 4-Cylinder Diesel Engine,” *SAE Tech. Pap.*, 2016, doi:10.4271/2016-01-2184.
 69. Brauer, M., Pohlke, R., Berndt, R., Manns, J., Elicker, M., Brands, C., and Scheidt, M., “Variable valve train as key technology for compliance with future emission limits and further downsizing,” *SIA Powertrain International Conference*, Rouen, 2016.
 70. Brauer, M., Diezemann, M., Pohlke, R., Rohr, J., Severin, C., and Werler, A., “Variable Valve Train - Measure for Active Exhaust Temperature management in Diesel Engine,” *5. MTZ Fachtagung Ladungswechsel im Verbrennungsmotor*, Stuttgart, 2012.
 71. Mavinahally, N., Kamo, R., Bryzik, W., Reid, M., and Wong, V., “SAE TECHNICAL PAPER SERIES961050 Insulated Miller Cycle Diesel Engine,” (412), 2018.
 72. Kamo, R., Mavinahally, N.S., Kamo, L., Bryzik, W., Reid, M., and Army, U.S., “SAE TECHNICAL Emissions Comparisons of an Insulated Turbocharged Multi-Cylinder Miller Cycle Diesel Engine,” (724), 2018.
 73. Wang, Y., Zeng, S., Huang, J., He, Y., Huang, X., Lin, L., and Li, S., “Experimental Investigation of Applying Miller Cycle to Reduce NO_x Emission From Diesel Engine,” *Proc. Inst. Mech. Eng. Part A J. Power Energy* 219(8):631–638, 2006, doi:10.1243/095765005X31289.
 74. Imperato, M., Antila, E., Sarjovaara, T., Kaario, O., Larmi, M., Kallio, I., and Isaksson, S., “NO_x Reduction in a Medium-Speed Single-Cylinder Diesel Engine using Miller Cycle with Very Advanced Valve Timing,” *SAE Technical Paper*, Consiglio Nazionale delle Ricerche, 2009, doi:10.4271/2009-24-0112.
 75. Gonca, G., Sahin, B., Parlak, A., Ust, Y., and Ayhan, V., “Theoretical and experimental investigation of the Miller cycle diesel engine in terms of performance and emission parameters,” 138:11–20, 2015, doi:10.1016/j.apenergy.2014.10.043.
 76. Millo, F., Mallamo, F., and Mego, G.G., “The Potential of Dual Stage Turbocharging and Miller Cycle for HD Diesel Engines,” *SAE Technical Paper*, SAE International, 2005, doi:10.4271/2005-01-0221.
 77. Stebler, H. and Weisser, G., “Reduction of NO_x Emissions of D . I . Diesel Engines by Application of the Miller-System : An Experimental and Numerical Investigation,” (41 2), 1996.
 78. Schutting, E., Neureiter, A., Fuchs, C., Schatzberger, T., and Klell, M., “Miller- and Atkinson-Cycle on a Turbocharged Diesel Engine Authors :,” 68:21–23, 2007.
 79. Rinaldini, C., Mattarelli, E., and Golovitchev, V.I., “Potential of the Miller cycle on a HSDI diesel automotive engine,” *Appl. Energy* 112(x):102–119, 2013, doi:10.1016/j.apenergy.2013.05.056.
 80. Guan, W., Pedrozo, V., Zhao, H., Ban, Z., and Lin, T., “Investigation of EGR and Miller Cycle for NO_x Emissions and Exhaust Temperature Control of a

- Heavy-Duty Diesel Engine,” 2018, doi:10.4271/2017-01-2227.Copyright.
81. Piano, A., Millo, F., Nunno, D. Di, and Gallone, A., “Numerical Assessment of the CO₂ Reduction Potential of Variable Valve Actuation on a Light Duty Diesel Engine,” *CO₂ Reduction for Transportation Systems Conference*, 2018.
 82. Gallo, W.L.R., “Thermodynamic Evaluation of Variable Valve Timing,” 1992, doi:10.4271/921479.
 83. Pischinger, M., Salber, W., Staay, F. Van Der, Baumgarten, H., and Kemper, H., “Benefits of the Electromechanical Valve Train in Vehicle Operation,” 2000, doi:10.4271/2000-01-1223.
 84. Edwards, S.P., Frankle, G.R., Wirbeleit, F., and Raab, A., “The Potential of a Combined Miller Cycle and Internal EGR Engine for Future Heavy Duty Truck Applications,” 1998, doi:10.4271/980180.
 85. Sakono, T., Nakai, E., Kataoka, M., and Takamatsu, H., “MAZDA SKYACTIV-D 2.2L Diesel Engine,” *20. Aachener Kolloquium Fahrzeug- und Motorentechnik*, Aachen, 2011.
 86. Busch, H., Jones, A., Higgins, D., Page, G., Deppenkemper, K., Honardar, S., Rohs, H., and Holderbaum, B., “Ingenium: Jaguar Land Rover’s all New 4-Cylinder Diesel Engine,” *24. Aachener Kolloquium Fahrzeug- und Motorentechnik*, Aachen, 2015.
 87. Deppenkemper, K., Özyalcin, C., Ehrly, M., Schoenen, M., Bergmann, D., and Pischinger, S., “1D Engine Simulation Approach for Optimizing Engine and Exhaust Aftertreatment Thermal Management for Passenger Car Diesel Engines by Means of Variable Valve Train (VVT) Applications,” 2018, doi:10.4271/2018-01-0163.
 88. Au, T.H., Rs, O., Deppenkemper, K., Günther, M., and Pischinger, S., “Potential of Valve Train Variabilities on Gas Exchange of Diesel Engines II,” Apr. 2018.
 89. Piano, A., Millo, F., Nunno, D. Di, and Gallone, A., “Numerical Analysis on the Potential of Different Variable Valve Actuation Strategies on a Light Duty Diesel Engine for Improving Exhaust System Warm Up,” *SAE Technical Paper*, SAE International, 2017.
 90. Millo, F., Rafigh, M., Andreata, M., Vlachos, T., Arya, P., and Miceli, P., “Impact of high sulfur fuel and de-sulfation process on a close-coupled diesel oxidation catalyst and diesel particulate filter,” *Fuel* 1–10, 2017, doi:10.1016/j.fuel.2017.01.006.
 91. Rafigh, M., “Exhaust Aftertreatment Modeling for Efficient Calibration in Diesel Passenger Car Applications,” Politecnico di Torino, 2017.
 92. Arya, P., “Modelling od Fulfur Poisoning for Diesel Oxidation Catalyst,” Politecnico di Torino, 2015.
 93. Schwoerer, J., Dodi, S., Fox, M., Huang, S., and Yang, Z., “Internal EGR Systems for NO_x Emission Reduction in Heavy-Duty Diesel Engines,” *SAE Technical Paper*, SAE International, 2004, doi:10.4271/2004-01-1315.
 94. Parvate-Patil, G.B., Hong, H., and Gordon, B., “Analysis of Variable Valve Timing Events and Their Effects on Single Cylinder Diesel Engine,” *SAE Technical Paper*, SAE International, 2004, doi:10.4271/2004-01-2965.
 95. Benajes, J., Reyes, E., and Luján, J.M., “Modelling Study of the Scavenging Process in a Turbocharged Diesel Engine with Modified Valve Operation,” *Proc. Inst. Mech. Eng. Part C J. Mech. Eng. Sci.* 210(4):383–393, 1996, doi:10.1243/PIME_PROC_1996_210_210_02.
 96. Minami, T., Takeuchi, K., and Shimazaki, N., “Reduction of Diesel Engine

- NOx Using Pilot Injection,” *SAE Technical Paper*, SAE International, 1995, doi:10.4271/950611.
97. Zhang, L., “A Study of Pilot Injection in a DI Diesel Engine,” *SAE Technical Paper*, SAE International, 1999, doi:10.4271/1999-01-3493.
 98. Schommers, J., Duvinage, F., Stotz, M., Peters, A., Ellwanger, S., Koyanagi, K., and Gildein, H., “Potential of Common Rail Injection System for Passenger Car DI Diesel Engines,” *SAE Technical Paper*, SAE International, 2000, doi:10.4271/2000-01-0944.
 99. Nehmer, D.A. and Reitz, R.D., “Measurement of the Effect of Injection Rate and Split Injections on Diesel Engine Soot and NOx Emissions,” *SAE Technical Paper*, SAE International, 1994, doi:10.4271/940668.
 100. Corcione, F.E., Vaglieco, B.M., Corcione, G.E., Lavorgna, M., and Lanzafame, R., “Study of the Combustion System of a New Small DI Diesel Engine with Advanced Common Rail Injection System,” *SAE Technical Paper*, SAE International, 2003, doi:10.4271/2003-01-1782.
 101. Corcione, F.E., Vaglieco, B.M., Corcione, G.E., and Lavorgna, M., “Potential of Multiple Injection Strategy for Low Emission Diesel Engines,” *SAE Technical Paper*, SAE International, 2002, doi:10.4271/2002-01-1150.
 102. Badami, M., Mallamo, F., Millo, F., and Rossi, E.E., “Influence of Multiple Injection Strategies on Emissions, Combustion Noise and BSFC of a DI Common Rail Diesel Engine,” *SAE Technical Paper*, SAE International, 2002, doi:10.4271/2002-01-0503.
 103. Ricaud, J.C. and Lavoisier, F., “Optimizing the Multiple Injection Settings on an HSDI Diesel Engine,” in: Whitelaw, J. H., Payri, F., Arcoumanis, C., and Desantes, J. M., eds., *Thermo- and Fluid Dynamic Processes in Diesel Engines 2: Selected Papers from the THIESEL 2002 Conference, Valencia, Spain, 11--13 September 2002*, Springer Berlin Heidelberg, Berlin, Heidelberg, ISBN 978-3-662-10502-3: 199–234, 2004, doi:10.1007/978-3-662-10502-3_11.
 104. Atzler, F., Kastner, O., Rotondi, R., and Weigand, A., “Multiple injection and rate shaping Part 1: Emissions reduction in passenger car Diesel engines,” *SAE Technical Paper*, Consiglio Nazionale delle Ricerche, 2009, doi:10.4271/2009-24-0004.
 105. Boggavarapu, P. and Singh, S., “Computational Study of Injection Rate-Shaping for Emissions Control in Diesel Engines,” *SAE Technical Paper*, The Automotive Research Association of India, 2011, doi:10.4271/2011-26-0081.
 106. Sapio, F., Piano, A., Millo, F., Torino, P., and Pesce, F.C., “Digital Shaping and Optimization of Fuel Injection Pattern for a Common Rail Automotive Diesel Engine through Numerical Simulation,” 2017, doi:10.4271/2017-24-0025. Copyright.
 107. GT-SUITE - Acoustic Application Manual - VERSION 2017, 2017.
 108. AVL, “Operative Instructions AVL 450 Combustion Noise Meter,” 1986.
 109. AVL, “Noise and Vibrations Training Program,” 1986.
 110. GT-SUITE - Optimization Manual - VERSION 2017, 2017.
 111. Emery, a F. and Nenarokomov, A. V, “Optimal experiment design,” *Meas. Sci. Technol.* 9:864–876, 1998, doi:10.1088/0957-0233/9/6/003.
 112. Mallamo, F., Badami, M., and Millo, F., “Analysis of Multiple Injection Strategies for the Reduction of Emissions, Noise and BSFC of a DI CR Small Displacement Non-Road Diesel Engine,” *SAE Technical Paper*, SAE International, 2002, doi:10.4271/2002-01-2672.

113. Han, Z., Uludogan, A., Hampson, G.J., and Reitz, R.D., "Mechanism of Soot and NOx Emission Reduction Using Multiple-injection in a Diesel Engine," *SAE Technical Paper*, SAE International, 1996, doi:10.4271/960633.
114. Montgomery, D.T. and Reitz, R.D., "Effects of Multiple Injections and Flexible Control of Boost and EGR on Emissions and Fuel Consumption of a Heavy-Duty Diesel Engine," *SAE Technical Paper*, SAE International, 2001, doi:10.4271/2001-01-0195.
115. Montgomery, D.T. and Reitz, R.D., "Optimization of Heavy-Duty Diesel Engine Operating Parameters Using A Response Surface Method," *SAE Technical Paper*, SAE International, 2000, doi:10.4271/2000-01-1962.
116. Desantes, J.M., López, J.J., García, J.M., and Hernández, L., "Application of Neural Networks for Prediction and Optimization of Exhaust Emissions in a H.D. Diesel Engine," *SAE Technical Paper*, SAE International, 2002, doi:10.4271/2002-01-1144.
117. Mallamo, F., "Ottimizzazione delle Strategie di Iniezione in Motori Diesel Common Rail," Politecnico di Torino, 2004.
118. Deb, K. and Jain, H., "An evolutionary many-objective optimization algorithm using reference-point-based nondominated sorting approach, Part I: Solving problems with box constraints," *IEEE Trans. Evol. Comput.* 18(4):577–601, 2014, doi:10.1109/TEVC.2013.2281535.
119. Pilley, A.D., Beaumont, A.J., Robinson, D.R., and Mowell, D., "Design of experiments for optimization of engines to meet future emissions targets," *27th International Symposium on Automotive Technology Automation - ISATA*, 1994.
120. Senecal, P.K., Montgomery, D.T., and Reitz, R.D., "A methodology for engine design using multi-dimensional modelling and genetic algorithms with validation through experiments," *Int. J. Engine Res.* 1(3):229–248, 2000, doi:10.1243/1468087001545155.
121. Piano, A., Millo, F., Sapio, F., and Pesce, F.C., "Multi-Objective Optimization of Fuel Injection Pattern for a Light Duty Diesel Engine through Numerical Simulation," 2018, doi:10.4271/2018-01-1124.
122. Hiroyasu, H., Miao, H., Hiroyasu, T., Miki, M., Kamiura, J., and Watanabe, S., "Genetic Algorithms Optimization of Diesel Engine Emissions and Fuel Efficiency with Air Swirl, EGR, Injection Timing and Multiple Injections," *SAE Technical Paper*, SAE International, 2003, doi:10.4271/2003-01-1853.
123. Breakthrough: new Bosch diesel technology provides solution to NOx problem - Bosch Media Service, <http://www.bosch-presse.de/pressportal/de/en/breakthrough-new-bosch-diesel-technology-provides-solution-to-nox-problem-155524.html>, Apr. 2018.

Appendix A1

Combustion process modelling: sensitivity analysis to DIPulse calibration parameters

In order to highlight the effects of the calibration parameters of the DIPulse Predictive Combustion model, which are reported in Equation 13, 15, 16 and 17 a sensitivity analysis was performed. The analysis was carried out considering, for each parameter, variations of $\pm 10\%$ and $\pm 30\%$ with respect to the optimized values, while keeping all the other parameters constant.

The results are shown in Figure A1.1 and Figure A1.2 for two selected engine operating conditions:

- 2000 RPM X 2 bar BMEP
- 3000 RPM X FL

For the low load engine operating point (Figure A1.1), Entrainment Rate Multiplier and Ignition Delay Multiplier were shown to have a dramatic impact on the burn rate, while on the other hand Premixed Combustion Rate Multiplier and Diffusion Combustion Rate Multiplier had a limited impact on burn rates.

For the full load engine operating condition, (Figure A1.2) the Premixed Combustion Rate Multiplier and the Ignition Delay Multiplier showed a significant effect on the combustion of the pilot injection, while the Diffusion Combustion Rate Multiplier was the most influent parameter on the combustion process of the main injection.

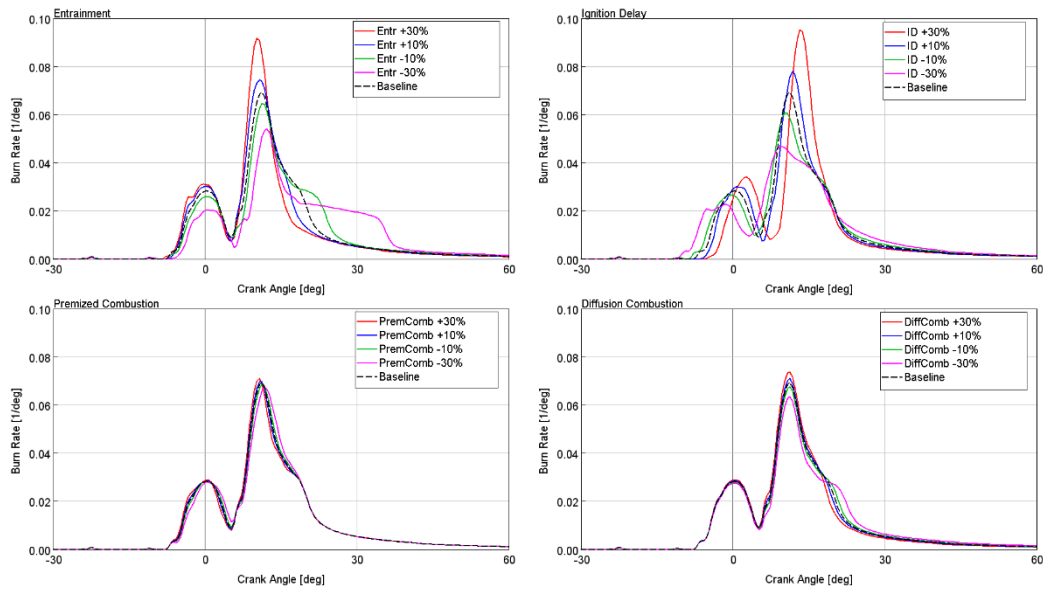


Figure A1.1 – Sensitivity analysis for different multipliers values using predictive DIPulse combustion model: Entrainment Rate Multiplier (top left), Ignition Delay Multiplier (top right), Premixed Combustion Rate Multiplier (bottom left), Diffusion Combustion Rate Multiplier (bottom right) – Engine operating point: 2000 RPM X 2 bar BMEP

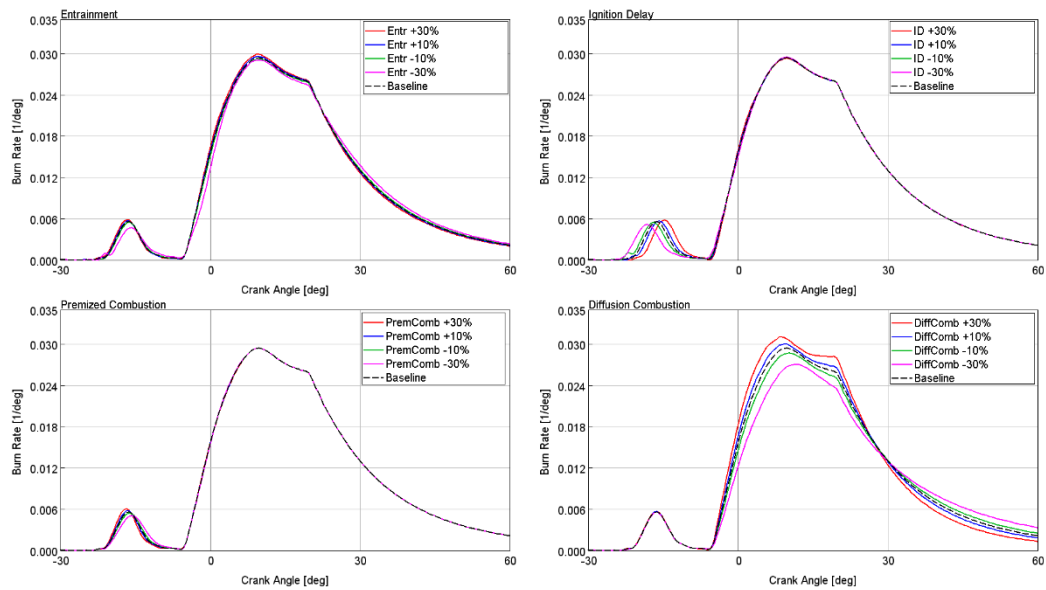


Figure A1.2 - Sensitivity analysis for different multipliers values using predictive DIPulse combustion model: Entrainment Rate Multiplier (top left), Ignition Delay Multiplier (top right), Premixed Combustion Rate Multiplier (bottom left), Diffusion Combustion Rate Multiplier (bottom right) – Engine operating point: 3000 RPM X FL bar BMEP

Appendix A2

Combustion process modelling: sensitivity analysis to engine control parameters

As mentioned in Chapter 1, the complete experimental dataset contained a set of operating points covering the entire engine map (337 engine points), a set of EGR, rail pressure, start of injection and boost pressure sweeps measured in 7 operating points representative of a typical driving cycle.

EGR Rate sweep

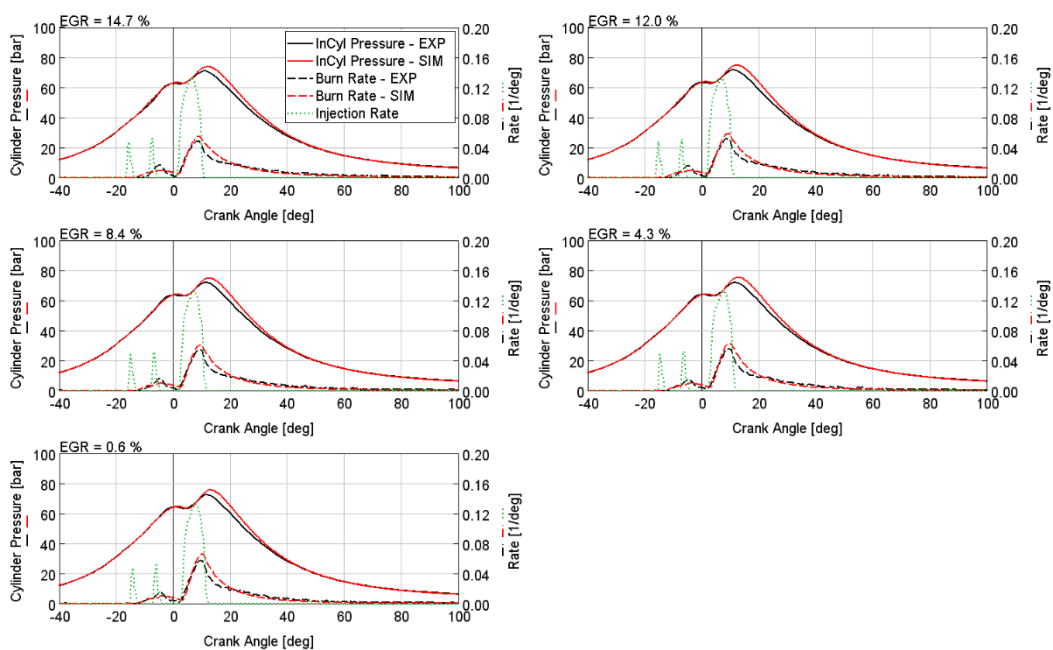


Figure A2.1 – DIPulse combustion model results @ 5 different EGR rates – Experimental (black) and predicted (red) in-cylinder (solid) and burn rate (dashed) comparisons, injection mass flow rate (green dashed) – 1500 RPM X 8 bar BMEP

SOI sweep

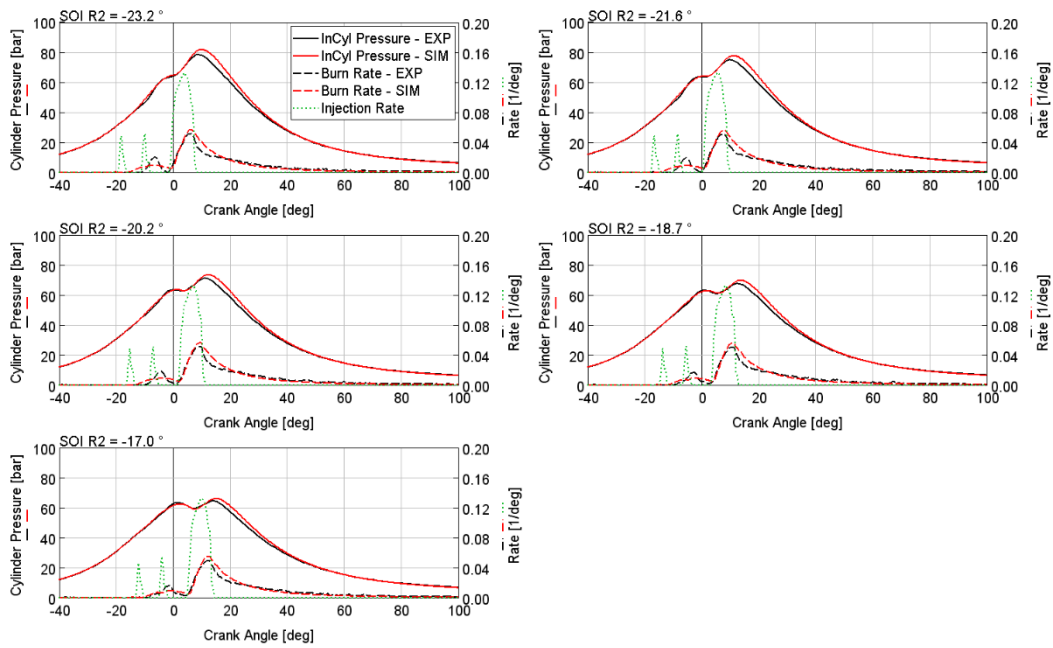


Figure A2.2 – DIPulse combustion model results @ 5 different SOI – Experimental (black) and predicted (red) in-cylinder (solid) and burn rate (dashed) comparisons, injection mass flow rate (green dashed) – 1500 RPM X 8 bar BMEP

Boost Pressure sweep

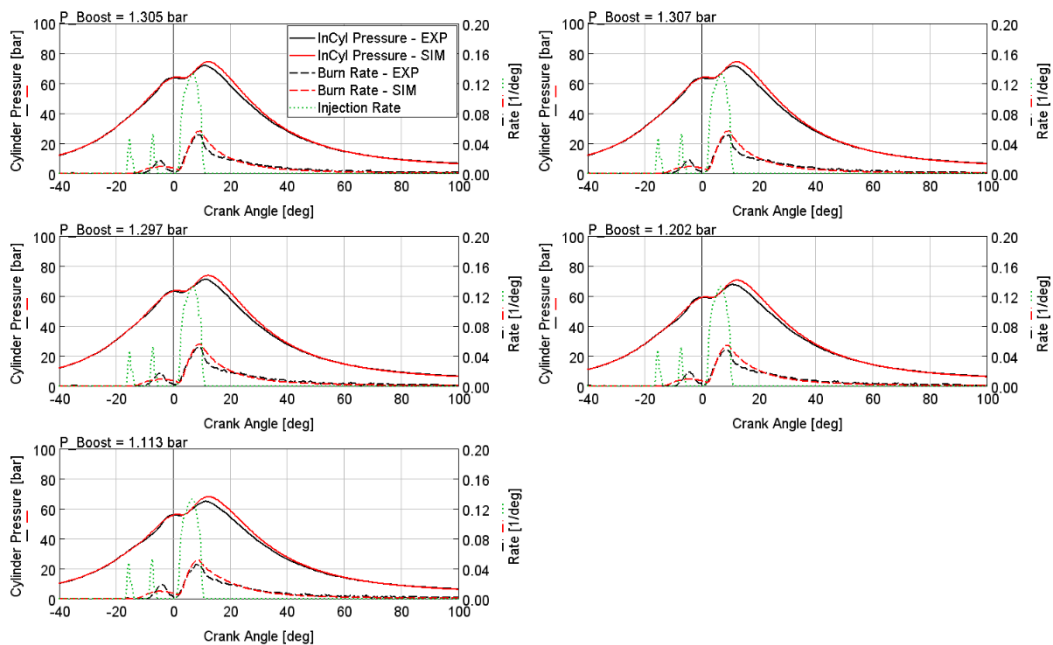


Figure A2.3 – DIPulse combustion model results @ 5 different Boost Pressure levels – Experimental (black) and predicted (red) in-cylinder (solid) and burn rate (dashed) comparisons, injection mass flow rate (green dashed) – 1500 RPM X 8 bar BMEP

The instantaneous plots are related to the engine condition 1500 RPM X 8 bar BMEP (Figure A2.1 for EGR sweep, Figure A2.2 for SOI sweep, Figure A2.3 for boost pressure sweep). As it can be seen from Figure A2.1, Figure A2.2, and Figure A2.3, a satisfactory agreement between the predicted (red line) and experimental (black line) in-cylinder pressure and burn rate can be observed for each of the sweep analysis. The pilot injections and main injection pulse is well captured by the DIPulse combustion model.

This good agreement is also confirmed from the results in terms of main combustion parameters shown in Figure A2.4. The DIPulse model can satisfactorily reproduce the combustion process with errors which are lower than 5 bar of maximum cylinder pressure, 5 degrees on MFB50 and on crank angle of maximum cylinder pressure.

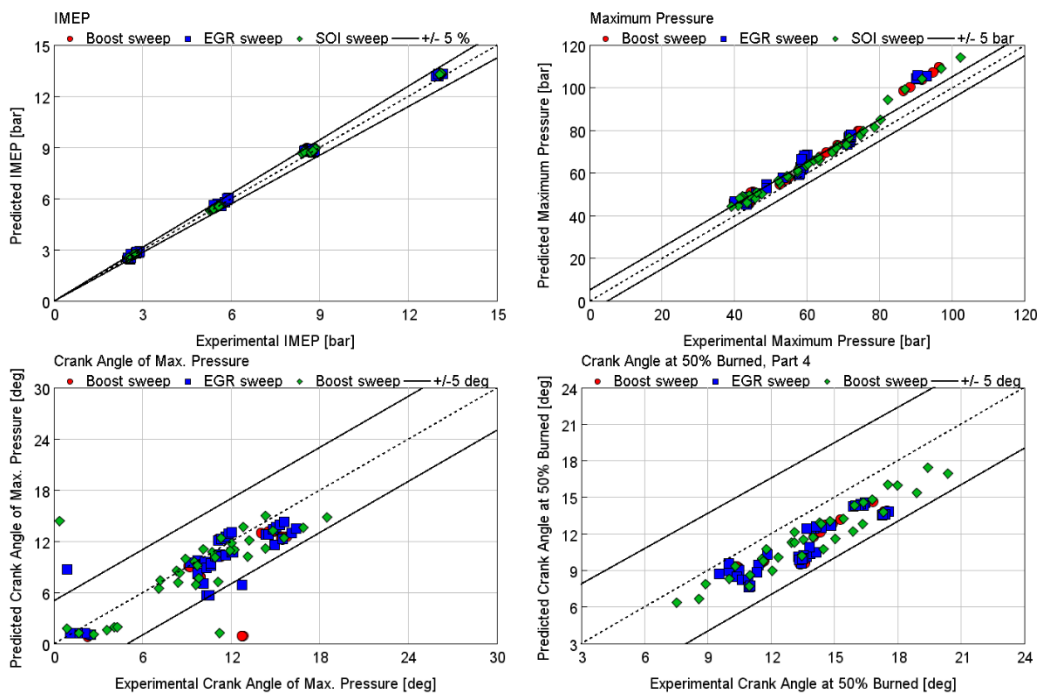


Figure A2.4 – DIPulse combustion model results - Combustion parameters: IMEP (top-left), in-cylinder maximum pressure (top-right), crank angle of maximum pressure (bottom-left), crank angle at 50% fuel burned (bottom-right) for boost pressure (red circle), EGR rate (blue square) and SOI (green diamond) sweeps

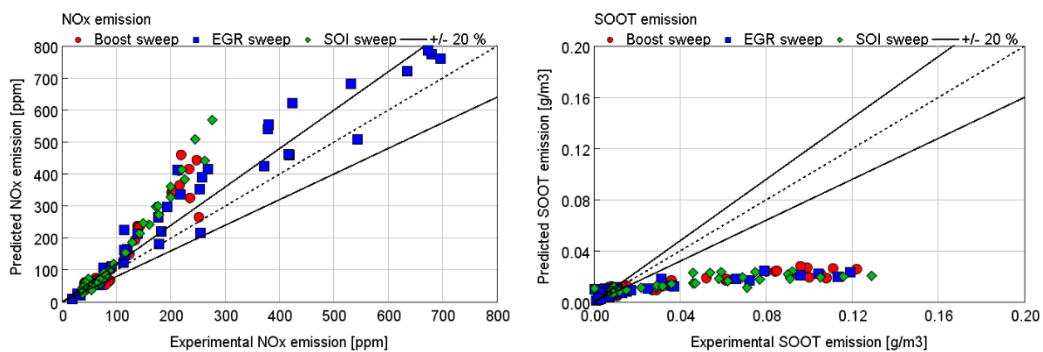


Figure A2.5 – DIPulse combustion model results – NOx (left) and SOOT emission (right) comparison for boost pressure (red circle), EGR rate (blue square) and SOI (green diamond) sweeps

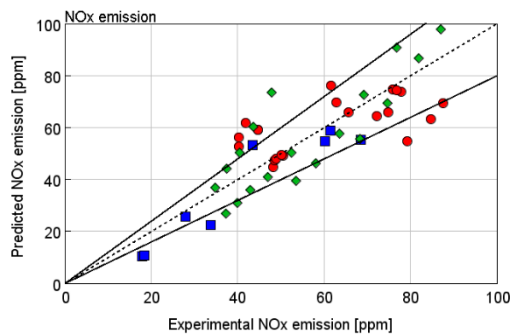


Figure A2.6 – NOx emission comparison – Zoom on low NOx zone

Also the emissions level can be well predicted by the DIPulse Figure A2.5 – left (and more in detail, Figure A2.6) shows a more than satisfactory accuracy in the prediction of the NOx concentration. Same accuracy was not obtained for SOOT emission prediction: this is due to the fact that a 1D model cannot provide an accurate quantitative values of SOOT emissions, requiring a more detailed 3D-CFD approach for fully investigating the emission formation process.